



Universitat Autònoma de Barcelona

ADVERTIMENT. L'accés als continguts d'aquesta tesi queda condicionat a l'acceptació de les condicions d'ús establertes per la següent llicència Creative Commons:  http://cat.creativecommons.org/?page_id=184

ADVERTENCIA. El acceso a los contenidos de esta tesis queda condicionado a la aceptación de las condiciones de uso establecidas por la siguiente licencia Creative Commons:  <http://es.creativecommons.org/blog/licencias/>

WARNING. The access to the contents of this doctoral thesis it is limited to the acceptance of the use conditions set by the following Creative Commons license:  <https://creativecommons.org/licenses/?lang=en>



**Universitat Autònoma
de Barcelona**

Controlled Nanotherapies Using Magneto-plasmonic Nanodomes

Zhi Li

Doctoral Thesis

Doctoral Program in Materials Science

Borja Sepúlveda (Director)

Josep Nogués (Director)

Eva Pellicer Vilà (Tutor)

Department of Physics

Faculty of Science

2019



Universitat Autònoma de Barcelona

Memòria presentada per aspirar al Grau de Doctor per

Zhi Li

Vist i plau

Dr. Borja Sepúlveda
(Director)

Prof. Josep Nogués
(Director)

Dra. Eva Pellicer Vilà
(Tutor)

Bellaterra, 3th July 2019

Acknowledgments

Before the end of the Thesis and the four beautiful years of research in ICN2, I would like to express my personal appreciations to everyone who has brought me supports, helps, inspirations and happiness.

My great gratitude goes to my Thesis directors and tutor: Dr. Borja Sepúlveda, Prof. Josep Nogués and Dra. Eva Pellicer. Without your careful supervision of daily work and patient guidance in the Thesis preparation, I couldn't have gone so smoothly on the way. I always remember the inspiring answer of Borja about how can you balance so well the heavy scientific work and the family daily life: I LOVE MY WORK. Simple but it is true that you will only be happy, motivated and successful by doing what you really like. You teach me not only the most valuable characters for doing research: enthusiasm, carefulness, efficiency and broaden vision, but also positive attitude and strong responsibility towards life, from which I will benefit in the rest of my life.

I will never forget the days I have shared with my super fancy groupmates. It is a great pleasure to have the big smile of Alex, black humour of "Javier", "Magic" talents (photography, programming, sports...) of Pau, elegancy and cleverness of Yue, warmness of Nour and genuineness of Guba as a part of my daily life.

Many thanks should be given to the collaborators and co-authors of my research work. It is your invaluable supports and suggestions that make me progress and eventually stand at the door of the PhD defense.

The financial supports from Chinese Scholarship Council are gratefully acknowledged as well as the frequent favours from the department divisions in ICN2 including Nanofabrication, Microscopy (SEM, TEM, XPS and FTIR) and Mechanical workshop.

Lastly, I would like to express my sincere gratitude to my friends (Daijun, Chao, Yu, Jie, Jose "Flan", Jose de la "Real" and...) and my family. It is not easy to go oversea for a PhD degree, but your consistent encouragement and unconditional supports make me confident, brave and strong to move forward.

All of you deserve a big hug from me. ¡Muchas Gracias!

Abstract

One of the main challenges of current nanotherapies is improving the concentration of the therapeutic agents inside the tumours and to maximize their therapeutic effects. Externally controlled stimuli-responsive nanomaterials offer a promising path to improve the delivery and accumulation efficiency as well as the control and amplification of the therapeutic effects. However, biomedical applications impose several constraints in the nanomaterials, such as the size, colloidal stability, toxicity and biodegradability, and in the safeness of the external actuators.

Under this context, this Thesis has focused on developing highly tunable magneto-plasmonic nanomaterials externally actuated and controlled by light and magnetic fields for efficient nanotherapy activation, amplification and control.

To achieve highly controlled magnetic and optical properties of nanostructures, but keeping cost-effectiveness and scalability, in this Thesis we have focused on the development of multifunctional nanostructures by combining bottom-up (self-assembly) and top-down (physical vapour deposition) processes to develop novel versatile magneto-plasmonic nanodomains (i.e. dielectric nanoparticles with metallic and ferromagnetic semi-shells). This nanofabrication strategy enables combining magnetic and optical nanomaterials that could be hardly achieved by standard chemical synthesis. Moreover, it offers high size and composition tunability to finely modulate the magnetic and optical properties, straightforward functionalization on the substrate without laborious phase transfer processes typical required in chemical synthesis, and direct dispersion in water solutions under mild ultrasonication.

With an aim of merging and fine tuning the magnetic and optical properties, in the first part of the Thesis we have developed magneto-plasmonic Fe/Au nanodomains with fluorescent polystyrene core (100 nm in diameter) for their application in magnetically amplified photothermal therapy and multimodal imaging. By varying the thickness of the Fe and Au layers, we observed that colloidally stable single domain or vortex ferromagnetic structures can be achieved. At the same time, the optical properties can be adjusted from pure plasmonic resonances with well-defined absorption bands to broadband absorbance in the whole visible and near-infrared spectral ranges. Interestingly, we have shown that the scattering cross section of the

nanodomains can be highly suppressed while keeping high absorption when the Fe ratio increases. These features allow keeping very high photothermal conversion efficiency (ca. 65%) even for high Fe content, which is similar to the most efficient plasmonic nanoheaters. Moreover, the capacity to magnetically concentrate the nanodomains at the illumination region can enhance even further the local heating efficiency. The Fe/Au semi-shell and the fluorescent polymer core also provide non-invasive multimodal imaging features due to their intense contrasts in T_2 nuclear magnetic resonance (larger than commercial iron oxide nanoagents), X-ray absorption, and fluorescence. The *in vitro* results demonstrate low cytotoxicity and strong capacity to locally amplify the photothermal therapy effects in HeLa cancer cells by the magnetic concentration at the illumination region, which highlights their biomedical potential.

In the second part of the Thesis, one of the challenges of the photothermal therapies has been addressed, *i.e.* detecting and monitoring the temperature rise during optical heating to achieve controlled cell deaths, by developing a novel simultaneous nano-heating/thermometry concept. To develop this concept, we have designed new Co/Au nanodomains exhibiting highly anisotropic out-of-plane magnetization and plasmonic resonances in an almost spherical nanoparticle. This combination enables very efficient magnetic rotation of the nanodomains in fluids under low amplitude and low frequency magnetic fields, and the generation of intense optical modulation in the near-infrared. By monitoring and analyzing the nanodomains rotation as a function of the magnetic frequency, we have been able to quantify and monitor the viscosity reduction in the fluid surrounding the nanodomains while they are optically heated as novel and accurate temperature nanodetectors. This nanothermometry concept shows a low detection limit of 0.05 °C, independence on nanodomains concentration and much simpler and cost-effective setup than standard luminescent nanothermometers. The capacity to integrate heating and thermometry in a single nanostructure and to use the same laser for detection and heating are relevant advantages that have been demonstrated even in highly concentrated cell dispersions. Therefore, detection of the nanodomains rotation under an alternating magnetic field provides a very useful tool to monitor and control photothermal therapies.

The final goal of the Thesis have been maximizing the biomedical potential of the nanodomains as cancer nanotherapies by developing fully biodegradable drug loaded

PLGA@Fe/SiO₂ magneto-plasmonic nanocapsules. These nanocapsules simultaneously enable: **i)** improving the biodegradability, **ii)** reinforcing the magnetic actuation due to their mass reduction (actuation strength equivalent to 10³ superparamagnetic iron oxide nanoparticles), **iii)** keeping high photothermal conversion efficiency in both near-infrared biological windows (63- 67%) as a result of the further suppression of the light scattering, **iv)** showing higher T_2 contrast in nuclear magnetic resonance, and **v)** retaining high magnetic and optical anisotropies for opto-magnetic nanothermometry and biosensing. Importantly, the unloaded nanocapsules have shown very low toxicity *in vitro* in long-term cell cultures, and *in vivo* in mice. The high T_2 contrast has been exploited to non-invasively monitor the *in vivo* biodistribution of the nanocapsules after intravenous injection, which shows accumulation in the liver 1 h after the injection, and almost total recovery after 96h. These preliminary results are encouraging for their application in multi-active local therapies.

In conclusion, in this Thesis we have shown how the hybrid nanofabrication strategy can be exploited to develop nanostructures with unprecedented strong ferromagnetic and plasmonic properties enabling external control and non-invasive visualization. The *in vitro* and preliminary *in vivo* results encourage further technological development of this novel nanotechnology to maximize its local nanotherapeutic performance and fabrication scalability for clinical applications.

Table of Contents

Acknowledgments	V
Abstract	VII
Introduction	1
1 Cancer therapy	1
2 Nanotherapies for cancer treatment	5
2.1 Fabrication of therapeutic nanostructures	5
2.2 Nanotherapy enhanced drug delivery	8
2.3 Nanocontrolled drug release	10
2.4 Nanostructures as therapeutic agents	10
2.5 Nanomaterials as contrast agents for bioimaging	13
2.6 Challenges of cancer nanotherapies	14
3 Externally controlled nanotherapies	15
3.1 Photothermal nanotherapy	16
3.1.1 Material dependent heating mechanisms	17
3.1.2 Light dependent effects (continuous wave vs. pulsed laser)	20
3.1.3 Photothermal conversion efficiency of nanomaterials	23
3.1.4 Optimization of the photothermal nanoagents	29
3.2 Nanothermometry	38
3.2.1 Luminescence nanothermometry	39
3.2.2 Bioimaging based nanothermometry	40
3.3 Magnetic nanotherapies	41
3.3.1 Magnetic actuation mechanisms	42
3.3.2 Magnetically actuated nanotherapy	44
3.3.3 Magnetically enhanced phototherapies	47
4 Objectives of the Thesis	51
5 Bibliography	53

Chapter 1	65
1.1 Magnetically amplified photothermal therapies and multimodal imaging with magneto-plasmonic nanodomes	65
1.2 Personal Contribution	67
Chapter 2	90
2.1 Simultaneous local heating/thermometry based on plasmonic magnetochromic nanoheaters	93
2.2 Personal Contribution	95
Chapter 3	117
3.1 Biodegradable ferromagnetic-plasmonic nanocapsules for externally controlled and non-invasively monitored nanotherapies	117
3.2 Personal Contribution	119
Chapter 4: General discussion	143
Chapter 5: Conclusion	147
Chapter 6: Future Perspectives	149
Chapter 7: Appendix	151

Introduction

1 Cancer therapy

Cancer is a group of diseases resulting from genetic mutations that induce uncontrollable cell growth and division with strong capability of generating metastasis. According to the estimation of the World Health Organization (WHO) in 2015, cancer was the first or second leading cause of death before 70 years age in 91 out of 172 countries. The latest global cancer data released by the International Agency for Research on Cancer (IARC) estimated 18.1 million new cancer cases and 9.6 million cancer deaths in 2018.^[1] Only in the EU, cancer treatment related services costs in 2014 were estimated to be nearly 83.2 billion euros, compared to 35.7 billion in 1995.^[2] These data clearly show how cancer has become a heavy burden for both for patients and society.

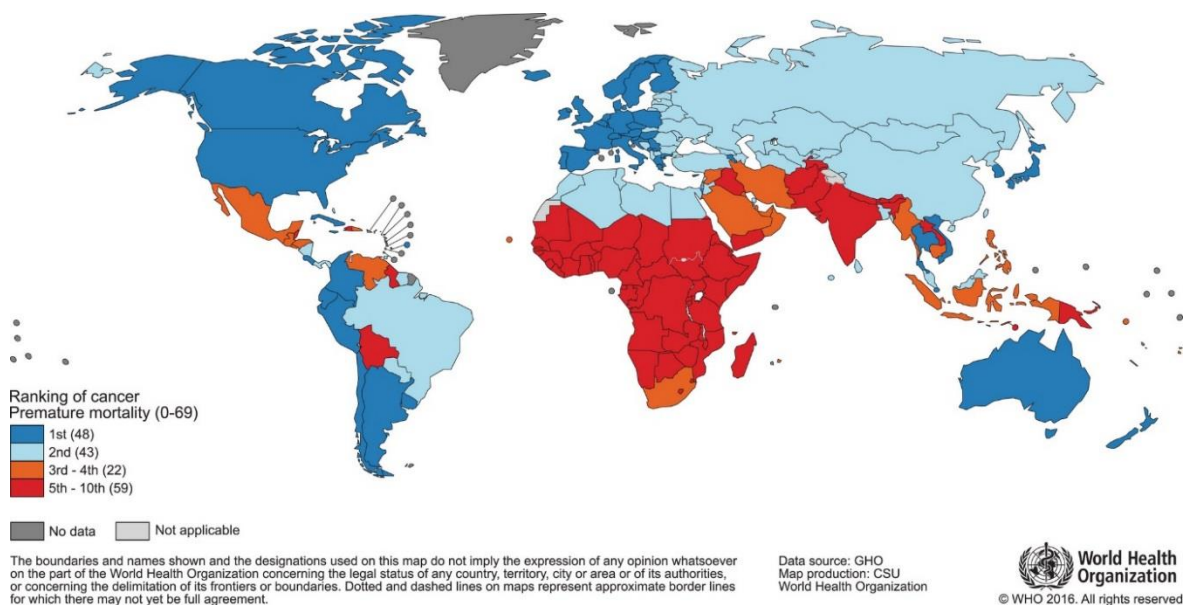


Figure 1. Global map presenting the national ranking of cancer as a cause of death at ages below 70 years in 2015. Figure extracted from ref^[1].

The difficulties for treating cancer mostly arise from the complex diagnostic and the low efficacy of current therapies. Conventional therapies, including surgery operation, chemotherapy and radiotherapy, have been proved to be invasive, nonspecific, inefficient and generate serious systemic side effects. Thus, novel cancer therapies need to be developed. Motivated by several successful cases of cured cancer, biological therapies (immunotherapy and gene therapy) are acquiring a wide interest and are currently showing a fast development.^[3-7] However, there is still a long way before their extended

clinical use due to threats related to the complex immune responses, off-target toxicity, autoimmunity and some ethical problems.

Other interesting alternative treatments, which can reduce the systemic side effects are photodynamic or local hyperthermia therapies.

Photodynamic therapy (PDT) is a minimally invasive photochemotherapy, based on the production of reactive oxygen species (reactive oxygen species such as singlet O_2 , $O_2^{\cdot-}$, H_2O_2 , $HO\cdot$, by exposing photosensitizers to light irradiation. Through strong oxidation effects, photodynamic therapy triggers several therapeutic actions, including tumor vasculature destruction, DNA damage and host immune system recovery and activation, which together contribute to the strong and long-term anti-tumor effects.^[8-12] Initially, photodynamic therapy typically involved ultraviolet (UV) photosensitizers. However, the use of UV light rises concerns due to the genotoxicity and low penetration of the UV light. However, currently photodynamic therapy employs nontoxic photosensitizers with absorption peaks in the visible or near infrared range, which generate efficient, but spatially limited cytotoxic effects (biological diffusion radius 10- 20 nm, reactive oxygen species lifetime 0.01 to 0.04 μs),^[13-15] which indicates a great improvement of intrinsic safety and specificity. Although photodynamic therapy is considered as a promising cancer therapy with minimal systemic toxicity and invasiveness, its application is still limited by three elements: **i)** the photosensitizer, **ii)** the activating light wavelength, and **iii)** the tissue oxygen. Tremendous efforts had been made to improve the reactive oxygen species production efficiency, aqueous solubility, photostability and targeting specificity of photosensitizers,^[9,16-20] but highly efficient photosensitizer using near infrared, in the range from 800 nm to 1300 nm (i.e., with the largest penetration in tissues) are still required.^[21,22] However, the fabrication of efficient photosensitizers in this range is difficult since the activating light energy should at least be larger than the energy of the resultant singlet oxygen ($94 kJ mol^{-1}$ at 1270 nm) for efficient energy transfer.^[9] To overcome this problem, photosensitizers for two-photo excitation are being developed, although involving the use of expensive high power pulsed lasers.^[23] The hypoxia environmental condition is another restriction for photodynamic therapy. Although, many efforts have been done since the launch of the first photosensitizer Photofrin®, photodynamic therapy is still far from a wide clinical

use due to some practical problems, such as subsequent photo-sensitisation, inability for treating solid tumors and lack of cell targeting.

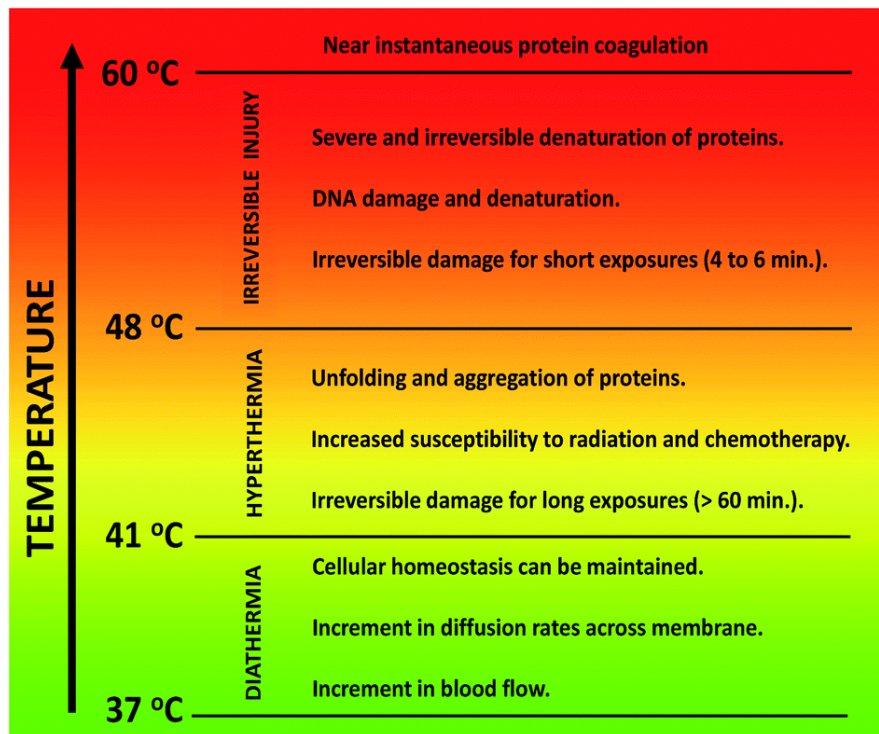


Figure 2. Schematic diagram of thermal induced biological effects under different operating temperature. Figure extracted from ref^[24].

In contrast to drug-based therapies, **local hyperthermia treatments** can cause tumour cell death in response to the biological thermal effects when the local temperature increases. Depending on the reached temperature, three different levels of biological effects could be triggered (Figure 2):^[24]

- 1) A slight temperature increase up to 41 °C can induce physiological changes, such as decrease of intracellular pH, and improvement of oxygenation and blood flow.^[25] This is mostly used in physiotherapy to treat rheumatic diseases, since muscles and joints under this temperature for less than an hour can accelerate the cell healing or metabolic rates.^[26]
- 2) Temperature rise over 48 °C induces serious and irreversible thermal destruction of healthy and cancer cells. This high temperature range is useful for tumour thermal ablation.^[27] Necrotic cell death is generally induced in this temperature range, which can cause important side effects due to induced inflammatory responses.

3) Temperatures in the range from 41 °C to 48 °C cause moderate hyperthermia effects. Within the temperature range from 41 °C to 43 °C, beneficial biological changes could enhance the efficiency of drug delivery and radiation thermo-sensitisation to generate synergistic effects when combined with chemotherapy or radiation therapy as an adjuvant therapy.^[28,29] When the temperature increases above 43 °C, for several minutes, the induced heat shock is able to independently trigger selective tumour cells eradication, as tumours are relatively more sensitive to heating than normal tissues,^[30,31] while keeping healthy cells largely unaffected.^[24,32] Generally, tumours are poorly vascularized and show lower order than healthy tissue. As a result, local heat can be easily accumulated in tumours and reach higher temperatures than in healthy tissues due to the slower blood flow and more inefficient heat dissipation.

Although hyperthermia therapy shows several advantages over conventional treatments such as accessibility, selectivity and repeatability without causing large systemic side effects, it presents several shortcomings related to the technologies employed to generate the local heat. Conventional local hyperthermia is typically performed by focusing waves such as ultrasound,^[33] or electromagnetic radiation (*e.g.* light, microwave^[34] and RF),^[35,36] at the region of interest. However, the power-to-heat energy conversion efficiency of external radiation or sound is rather limited for achieving a sufficiently high therapeutic level, whereas implanted antennas for treating deep located tumours bring huge invasiveness. Moreover, efficient hyperthermia treatments require very accurate spatial control of the focused radiation and the reached temperature during the actuation, which is technologically challenging. Consequently, local hyperthermia must be combined with complex and expensive imaging techniques to localize the actuating region and to monitor the therapeutic actuation for minimizing the negative effects of excessive heating and the damage of healthy tissue.

Therefore, innovative therapeutic ways with higher specificity, lower invasiveness, less side effects and higher efficacy should be further developed. The impressive development of nanotechnology in the last two decades have brought new tools which could be applied in the biomedical fields for cancer treatment. In the following sections of the introduction we first give a brief overview of the advantages and limitations of current nanotherapies. We then discuss the necessities and possible approaches of novel nanotherapies enabling external control with light or magnetic fields.

2 Nanotherapies for cancer treatment

Cancer nanotherapies involve the uses of “nanostructures” and “nanotechnologies” in cancer treatment, with the aim of efficiently confining the therapeutic effects at the tumour sites and avoiding the systemic side effects commonly occurred in conventional treatments.^[37–41] With the help the nanomaterials, antitumor agents could be specifically delivered, released and activated sequentially at the sites of action. Precise monitoring and control of the therapeutic effects with bioimaging tools are also enabled by exploiting the properties of nanomaterials as contrast agents.

2.1 Fabrication of therapeutic nanostructures

The development of nanotherapies has been closely related to the advances of nanofabrication technologies. Any nanofabrication method for nanotherapy applications should meet several requirements, including low cost, high yield, and facile control of size, shape and morphology and physicochemical properties. Two main nanofabrication approaches can be differentiated: bottom-up and top-down (Figure 3).^[42]

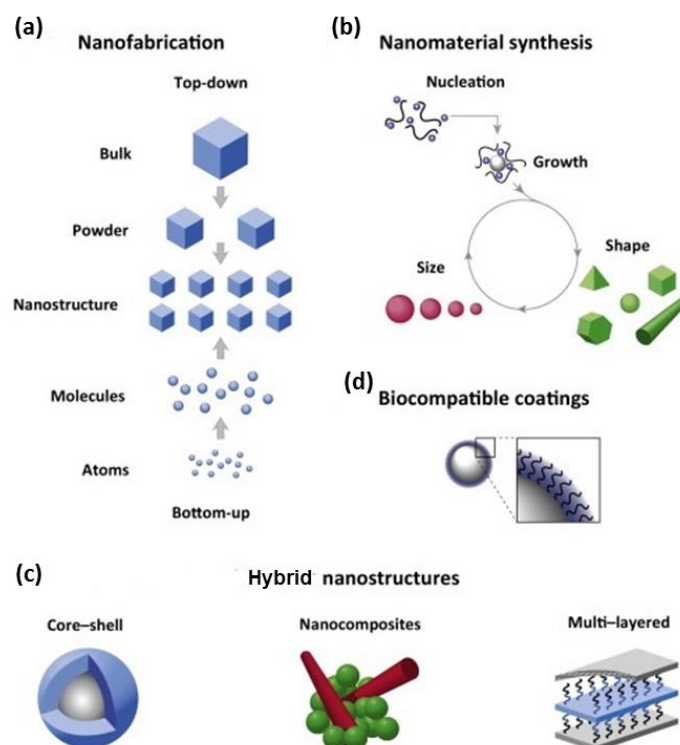


Figure 3. Schematic of biomedical nanomaterial preparation. (a) Top-down and bottom-up nanofabrications. (b) Nucleation growth of nanomaterial. (c) Assembly patterns of hybrid nanostructures. (d) Surface biofunctionalization. Figure adapted from ref^[43].

The **bottom-up** approach, which provides a broad size, composition and even shape tunability, is the dominant synthetic method for the majority of therapeutic nanoagents, such as polymeric, plasmonic, metal chalcogenides, or magnetic nanomaterials. Generally, the bottom-up nanofabrication starts from basic atoms and molecules to form larger and more organized systems under a physically- or chemically-driven force. It includes gas phase (*e.g.* physical or chemical vapor deposition) and liquid phase methods (*e.g.* self-assembly, sol-gel synthesis, hydrothermal method, electrochemical deposition and so on). Bottom-up nanomaterial synthesis often follows an initial stage of nucleus formation and subsequent growth (Figure 3).^[44,45] Therefore, by modulating the growth-driven force, such as temperature, pressure, ambient gas, solvent or precursors concentration, it is possible to achieve size, shape, crystalline phase and morphology control in the nanomaterials. In the particular case of simple nanomaterials, bottom-up can show high mass production, low cost and simple equipment requirements, which is promising for industrialization.

There are countless examples of bottom-up approaches employed for nanotherapeutic nanostructures fabrication. Firstly, **polymeric nanoparticles** are mostly prepared *via* bottom-up method. Conjugated polymers nanoparticles, *e.g.* polyaniline, polypyrrole and poly(3,4-ethylenedioxythiophene):poly(4-styrenesulfonate) (PEDOT:PSS),^[46] are typical examples, which are commonly prepared sequentially through molecular polymerization and subsequent formation of nanoparticles through nano-precipitation, mini-emulsion or self-assembly based on hydrophobic or electrostatic interactions between polymers.^[46] By controlling the synthetic parameters, such as type, molecular weights, amphiphaticity, charge potential, polymer concentration, solvent polarity and surfactant additives, the size of the particles can be controlled. Post-synthetic surface modifications to add functional groups can be conducted for specific cell targeting. Polymer nanoparticles exhibit excellent photostability, low toxicity and strong light energy harvesting and translating capacity, which indicate great capabilities for photoinduced theranostic applications. Despite the outstanding optical properties and easy synthetic steps, the size distribution during the chemical reactions in solution is rather poor and difficult to control, and better synthetic regulation methods should be proposed.

Inorganic nanomaterials are also gaining a significant nanomedical relevance. For instance, Au **plasmonic nanomaterials** with outstanding optical properties and chemical stability have been synthesized through solution based methods.^[47-49] The boost of Au nanomaterials should be attributed to the discovery of modern-concept of seed mediated growth synthesis,^[50] which leads to anisotropic Au nanostructures with well controlled size, shape, morphology and high yields.^[51-53] Compared to spherical Au nanoparticles, the anisotropic Au nanorods,^[54] nanoshells,^[55] nanocages^[56] and nanotriangles^[57] with the red-shift plasmonic absorption band towards the near-infrared region, have become highly attractive for biomedical diagnostics and photothermal therapies.^[58-62] **Magnetic nanomaterials**, especially iron oxides with excellent magnetic properties and biocompatibility, have also shown a wide range of biomedical applications.^[63] The magnetic properties of nanomaterials are strongly dependent on their size and shape. Magnetite or maghemite iron oxides with size lower than 20 nm exhibit superparamagnetism, which are very beneficial for achieving colloidally stable dispersions for bioimaging and magnetic hyperthermia therapy. In general, small size magnetic nanomaterials prepared *via* bottom-up routes, such as co-precipitation, thermal decomposition, microemulsion and hydrothermal synthesis.^[63] However, due to the magnetic dipole-dipole interaction, oxidation susceptibility and difficulty to control the chemical driving force, chemical synthesis of nanomaterials exhibiting high magnetic strength and good colloidal stabilities is very challenging. Usually, protection strategies, such as coating with inert organic ligands or inorganic layers are employed to chemically stabilize the magnetic nanoparticles during or after the preparation. However, these coatings reduce the net magnetization of the nanostructure, and achieving high control in solution without losing colloidal stability is still complicated.

In contrast, **top-down** nanofabrication is a cutting down process from bulk materials to nanoscale structures including mechanical ball milling, anodizing and lithography. The latter is a reproducible nanofabrication method and especially suitable for fabricating complex nanostructures. However, the high-quality resultant nanostructures with high size and shape precision strongly rely on expensive supporting facilities. Generally, the high cost and low yield of highly controlled standard nanolithographic techniques (*e.g.* electron beam lithography, focused ion beam lithography and so on) prevent their extended biomedical application.

Therefore, although bottom-up methods are quite suitable to synthesize therapeutic nanoagents, the combination of complicated experimental conditions, poor reproducibility and complex solvent transfer for biomedical applications make it difficult to achieve high quality and high yield controllable nanomaterials. Additionally, to accomplish the nanomaterial synthesis for biological applications, post-synthetic modifications with biocompatible coatings and specific bioconjugates might also be necessary. Moreover, in the search of novel multifunctional nanobiomedical tools, complex multi-material nanostructures are needed, whose bottom up fabrication can be too complex. As a result, novel nanofabrication strategies that could combine the versatility and low cost of bottom up approaches and the high control of the top-down strategies are still needed.

2.2 Nanotherapy enhanced drug delivery

Initially, nanostructures were introduced as drug carriers for local cytotoxicity generation to improve the circulation time, solubility, delivery specificity and efficacy of the drug.^[38,64-66] Traditional chemotherapies commonly fail due to the nonspecific drug distribution and their associated systemic side effects and multidrug resistance. Instead of free drug delivery, nanotherapies pack drug in nanostructures such as micelles, liposomes and polymer nanoparticles for a better delivery control. (Figure 4).^[38] Due to the leaky vascular structures and dysfunctional lymph vessels, tumour tissues possess larger capillary fenestrae as compared to normal tissues. Nanotherapies can exploit this feature for the specific accumulation of nanostructures in tumour tissues, the so-called **Enhanced Permeability and Retention** (EPR) effects.^[67-70] Extending the blood circulation lifetime of the nanostructures is beneficial for acquiring higher possibilities to encounter tumour sites and enhance the EPR effects, which can be modulated by the nanostructures physiochemical properties. Nanostructures with moderate size (10-200 nm),^[37,41] antifouling polymer coating (PEG^[71,72] or PVP^[73]), hydrophilic surface with neutral charge and biocompatible composition, are more likely to possess a longer circulation lifetime and higher EPR efficiency.^[37,38,74] A great improvement of specific retention of nanostructures in tumour largely decreases the drug exposure to healthy tissues and, thereby, the systemic side effects. Nevertheless, the EPR only favours tumour accumulation of the drug nanovehicles, and approaches for improving intratumoral distribution and cell uptake should also be incorporated.

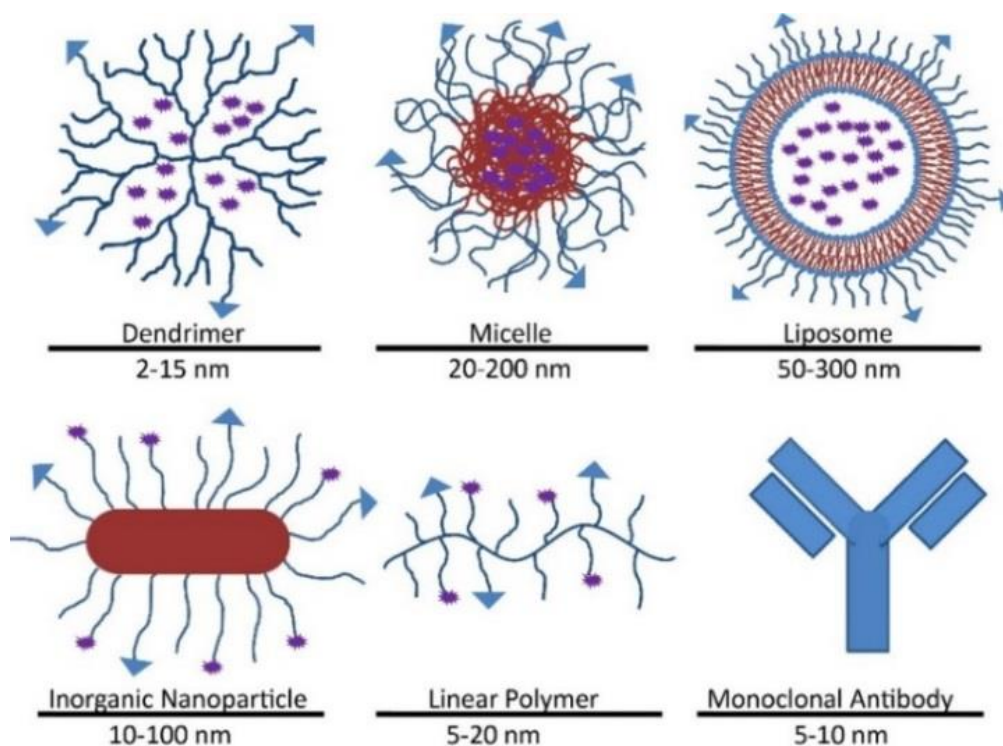


Figure 4. Nanostructures as drug carriers in nanotherapy. Figure extracted from ref^[38].

Active cell targeting was proposed to assist in the intratumoral drug delivery processes by improving intratumoral diffusion and cell internalization. Cell targeting strategy is mainly based on specific receptor-acceptor recognitions between nanostructures and tumour cells.^[75-77] For intratumoral distribution, nanostructures have to go through the highly dense and crosslinked extracellular matrix where tumour cells are closely packed and disorganized. Targeting moieties might be capable of creating a "green channel" for nanostructures to go through by interacting with the specific receptors of tumour cells. This strategy promotes a deeper intratumoral diffusion of nanostructures.^[78] More importantly, cell targeting is able to improve the specificity and efficiency of drug-cell internalization process. The cell membrane is a barrier that drugs have to cross through to enter tumour cells and generate the therapeutic effects. Many small molecule drugs are able to spontaneously diffuse and go through this lipid bilayer membrane.^[79] However, free drug treatment could induce the development of drug resistance of cancer cell by overexpressing membrane pumps, typically P-glycoprotein to actively remove drug molecules out of the cells.^[80,81] This is how cancer can develop multidrug resistance. Well-designed drug carriers are able to decrease the possibilities of drug exposure to overcome drug resistance. However, unlike small and hydrophobic drug molecules, hydrophilic drug carriers with large size have a more complex pathway into

tumour cells and often lower internalization efficiency.^[82-84] The surface modification with known specific tumour receptors enable nanostructures to be actively internalized by tumour cells *via* receptor mediated endocytosis or pinocytosis,^[78] which allows a specific and efficient cell uptake and drug localization. Typical targeting moieties, which are complementary to specific receptors of tumour cells, are antibodies, peptides or aptamers.^[85]

2.3 Nanocontrolled drug release

As we have seen above, nano-sized drug carriers can achieve specific drug localization with high efficiency. However, to generate local effects, proper drug release should be controlled. The drug release can be passively or actively triggered.^[86-89] **Passive drug release** mainly relies on drug diffusion associated to the response of nanocarriers to various tumour microenvironment parameters, such as concentration, osmotic potential gradients or pH. However, passive drug release is not well regulated due to these uncontrollable inherent parameters inside tumours. In contrast, **active drug release** with an artificially controllable “power button” is more attractive. According to different responsive nanostructures, active drug release could be remotely triggered by different mechanisms such as light,^[90,91] ultrasonic waves^[92] or magnetic field,^[93] which have been comprehensively reviewed.^[87,89] For instance, ultrasounds with proper intensity, frequency and duration could be employed for drug release from polymer nanoparticles and liposomes through the thermal or mechanical effects generated by cavitation phenomena or radiation forces. Optical heating can also trigger the swelling and collapse of thermosensitive hydrogels for drug release. Moreover, active drug release could be performed in a pulsatile manner, contrasting the sustained diffusion mostly occurred in passive release processes, thereby enabling easier control of the therapeutic concentration level and the therapeutic effects.^[94]

2.4 Nanostructures as therapeutic agents

So far in this introduction, nanostructures have been considered as drug carriers to largely improve the efficiency and specificity of cancer drugs. However, with the development of nanomaterials and nanotechnologies, nanostructures as therapeutic agents for treating cancer have gained tremendous attention.^[95,96] In particular, nanostructures could be employed as **heat mediators for generating local**

hyperthermia, thereby promoting a heating mode transformation from “out-inside” to “inside out” (Figure 5) to revolutionize hyperthermia therapeutic applications.^[97] The “inside out” hyperthermia induces amplified and localized thermal destruction by concentrating and remotely heating nanoparticles, while minimizing the collateral side effects in nearby tissues. Nanomaterials mediated hyperthermia demonstrate many advantages, such as higher heating efficiency and specificity, non-invasiveness and intrinsic selectivity by exploiting both EPR and cell targeting.

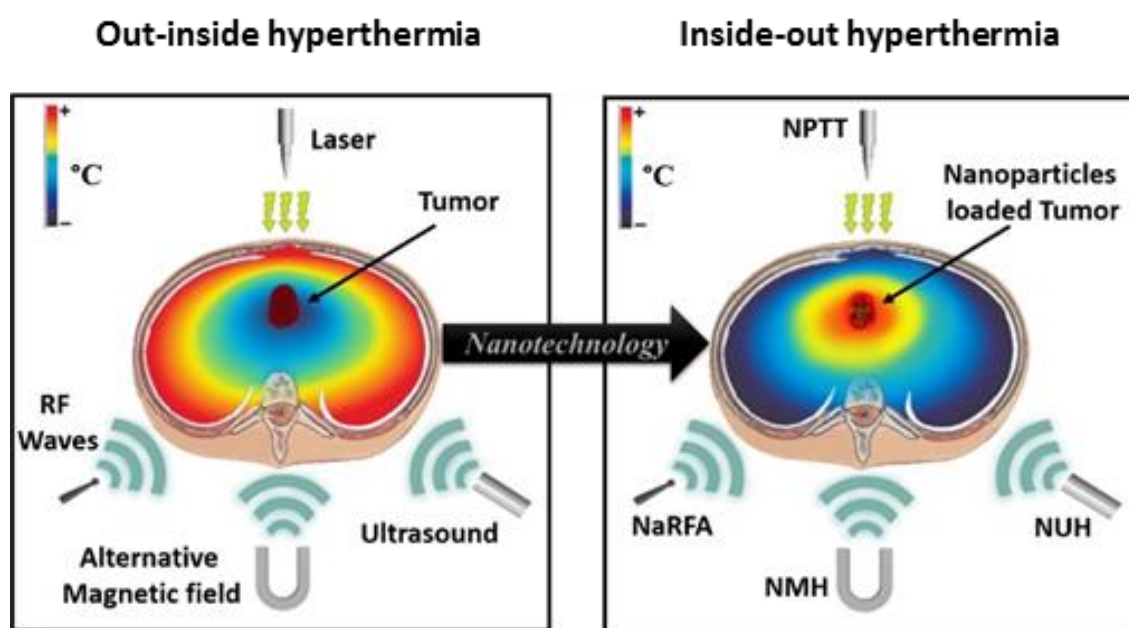


Figure 5. Transformation and enhancement of hyperthermia by involving nanoparticles as nanoheaters. Figure adapted from ref^[97]. Abbreviations; NPTT: Nano-photothermal therapy. NMH: Nano-magnetic hyperthermia. NaRFA: Nano-radio-frequency ablation. NUH: Nano-ultrasound hyperthermia.

Hyperthermia responsive nanomaterials are distinctly categorized according to the power sources used to induce the heating (Figure 5),^[97] such as ultrasounds^[98] or electromagnetic fields (*i.e.*, light,^[99] microwaves, radiofrequency^[100] and alternating magnetic field^[101]). **Nano-ultrasound hyperthermia** is due to the enhanced attenuation of ultrasonic wave and thermal lattice vibration effects. The accompanying acoustic cavitation effects may trigger synergistic therapeutic effects. Nanomaterials with large ultrasound attenuation coefficient and high thermal conductivity, such as Au or Si nanoparticles, are preferred as ultrasound heating agents. **Nano-photothermal therapy** is based on light activated electronic excitation and non-irradiative relaxation. Nanomaterials with large light optical absorption cross sections are required to achieve

high therapeutic efficiency, such as plasmonic metals, carbon based nanomaterials and conjugated polymers. **Nano-radio-frequency ablation** induces Joule heating effects from eddy current loss. Au, Pt and carbon nanotubes are often used as the heating agents. In contrast, **nano-magnetic hyperthermia** is based on the heating capability of magnetic nanomaterials by harvesting power from alternating magnetic fields. Superparamagnetic, ferrimagnetic and ferromagnetic nanomaterials are frequently employed as magnetic hyperthermia agents and the nanomaterials properties, such as size, dispersion stability, hysteresis loop area and magnetic anisotropy are crucial for optimizing the magnetic heating.

Interestingly, as be observed in Figure 6, **plasmonic metals** (Au or Pt) and **iron based nanomaterials** are multi-responsive materials, which exhibit great potentials to be used for multimodal hyperthermia modalities with synergistic thermal effects.

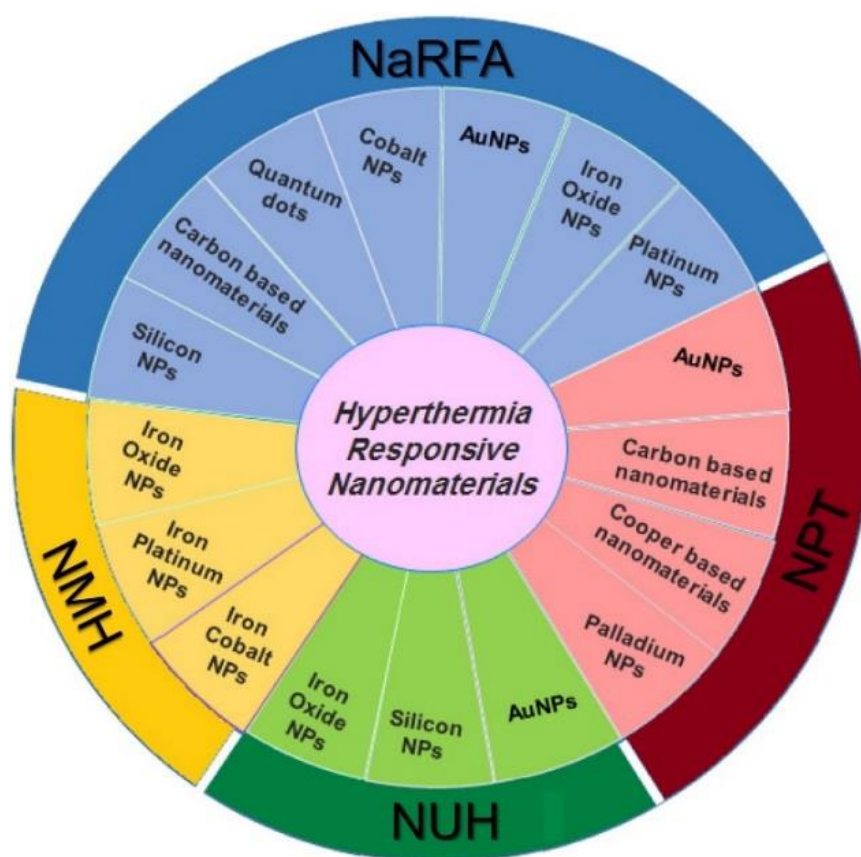


Figure 6. Hyperthermia responsive nanomaterials. Abbreviations; NPTT: Nano-photothermal therapy. NMH: Nano-magnetic hyperthermia. NaRFA: Nano-radio-frequency ablation. NUH: Nano-ultrasound hyperthermia. Note: Some nanomaterials listed in the chart are multi-parameters responsive and utilized for different hyperthermia modalities. Figure extracted from ref^[97].

2.5 Nanomaterials as contrast agents for bioimaging

In addition to therapeutic applications, nanomaterials can also be employed for bioimaging for diagnostics and for visualizing and evaluating the therapeutic effects. Traditional bioimaging techniques, such as optical imaging,^[102-106] X-ray tomography,^[107] ultrasound imaging^[108] and magnetic resonance imaging^[109,110] are widely used in biomedicine. **Optical imaging** exhibits excellent spatial resolution and provides biochemical information by detecting responses under light activation, for example by fluorescence molecular labels. **Magnetic resonance imaging (MRI)** is a non-invasive imaging technology which is able to show three dimensional anatomical images with detailed functional information of the structure.^[111-114] It is exceptionally suitable for imaging soft tissue, such as ligaments or organs. On the other hand, **X-ray tomography** and **ultrasonic imaging** are serving as complementary imaging approaches, although suffering from relatively low resolution and poor tissue functional information, due to their lower costs, rapid processing and accessibility.

To improve the imaging resolution and acquire more the biochemical information, nanomaterials are currently extensively studied as **contrast nanoagents**.^[115] Nanomaterials showing fluorescence emission or direct band gap semiconductors (e.g. quantum dots) can provide larger intensities and reduction of the inherent photobleaching instability of the fluorescence molecules. In addition, nanomaterials with large extinction (absorption and scattering) cross section, such as plasmonic metals and carbon based nanomaterials, are often employed to enhance the optical imaging effects. Importantly, nanomaterials with optical absorption/emission in the near infrared (NIR), i.e. from 700 nm to 1300 nm, show improved bioimaging capabilities due to the decreased attenuation and larger light penetration depth of light in physiological tissue.^[116,117]

Nanomaterials with high atomic number and high X-ray absorption coefficient such as iodine, Au or lanthanide based nanomaterials, can locally increase the X-ray absorption, thus generating higher X-ray imaging contrast.^[118-120]

Due to their large magnetic susceptibilities, magnetic nanomaterials (paramagnetic, superparamagnetic or ferromagnetic) can be used either as T_1 (e.g. gadolinium (Gd)-, europium (Eu), neodymium (Nd), and manganese (Mn) containing

materials) or T_2 contrast agents (e.g. maghemite $\gamma\text{-Fe}_2\text{O}_3$, magnetite Fe_3O_4). The enhanced imaging effects are achieved through the interaction with surrounding protons and enhance the T_1 or T_2 relaxation process.^[121,122] Although Gd-type T_1 contrast agents are commercially available, some potential adverse effects related with compromised renal function have been discovered. Ultra-small superparamagnetic iron oxides (iron supplement Ferumoxytol) are biocompatible and were approved by the FDA.^[123-125] However, it was recently recommended by FDA to reconsider them as magnetic resonance imaging contrast agents due to some long-term health risks.^[126] Therefore, it is still necessary to minimize current disadvantages and to integrate different imaging tools. Multimodal imaging with wider application, higher resolution and biocompatibility is currently pursued for future contrast nanoagents.

2.6 Challenges of cancer nanotherapies

Although nanotherapies show promising performance for treating cancer, the *in-vivo* results show that there is still a huge gap between the concept and the implementation of nanotherapies. For instance, nanostructures as drug carriers have been employed to enhance the drug delivering efficiency. However, according to the results (based on mouse model) published from 2005 to 2015, only 0.7% (median per gram of tissue) of the administered dose of nanoparticles are delivered to the tumour site, which indicates rather low overall delivery efficiency.^[127] The reasons behind the low delivery efficiency could be various, such as aggregation of nanostructures in blood stream, low possibilities to encounter tumours in a huge body system, high clearance by immune system, decreased extravasation efficiency by elevated interstitial tumour pressure, and non-accessible tumour area.^[38] Moreover, active cell targeting strategies with live animals demonstrate no significant increase of nanoparticles uptake efficiency compared to Enhanced Permeability Retention passive delivery, which may suggest that active cell targeting does not efficiently work *in vivo*.^[127-131] The low delivery efficiency limits the number of nanoparticles in local tumour sites, which sets a limit in the resultant therapeutic effects. Current delivery strategies should be further optimized and targeting approaches with higher *in-vivo* efficiency should be carried out. As a consequence, only very few nanomedicines have been clinically approved (e.g. thermosensitive liposomes and iron oxide nanoparticles), which is also related to the difficulties of preparation, stability and biocompatibility of the nanomaterials.^[87]

In conclusion, although nanotherapies with virtually limitless versatility have shown promising potentials to assist in different therapeutic processes (e.g. specific drug delivery, controlled drug release, selective therapy activation and bioimaging monitoring), there is still a long journey to achieve successful clinical approval. Benefiting from ideal tunability in size, shape, composition and surface chemistry, novel multi-responsive nanostructures might be developed to improve current therapeutic nanotools. Multiple external actuation and control mechanisms could be combined to improve the performance of current nanotherapies.

3 Externally controlled nanotherapies

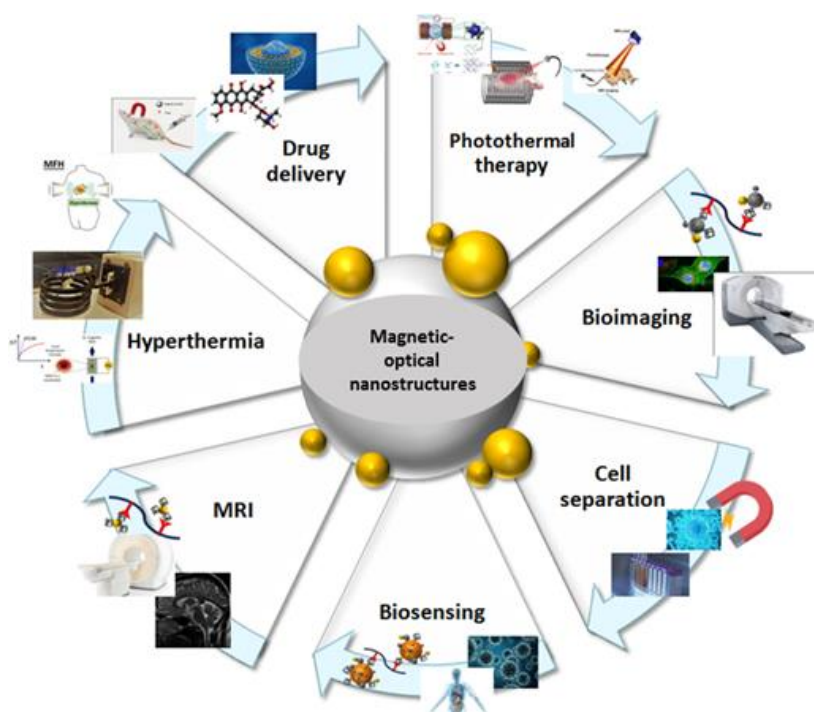


Figure 7. Potential biomedical applications of magnetic and -optical nanostructures. Adapted from ref^[132].

Multi-responsive multi-functional nanomaterials are bringing new ways to improve nanotherapies to a higher level. In particular, high tunable magnetic and optical nanostructures demonstrate high versatility as multifunctional platforms in biomedical applications, such as photothermal therapy, magnetically controlled drug delivery, magnetic hyperthermia or magneto-mechanical therapies, but also for magnetic resonance or optical imaging and biosensing (Figure 7).^[132] Apart from the promising features inherited from nanotherapies, such as high specificity, selectivity, efficiency and non-invasiveness, the combination of optical and magnetic effects in nanotherapies

brings extra external assistance and control, including synergistic therapeutic effects, therapy self-monitoring and self-confirming bioimaging capabilities. In the next sections, we will discuss how optical and magnetic nanostructures can help nanotherapies to improve their efficacy and control.

3.1 Photothermal nanotherapy

Light triggered nanotherapies have been boosted by the development of versatile light responsive nanostructures, such as plasmonic, carbon-based, semiconducting and up-converting nanoparticles. Upon light irradiation, light responsive nanomaterials either absorb or scatter light. Light absorption is followed by electronic relaxation through both radiative (luminescence or fluorescence emission) or non-radiative (heat or reactive oxygen species) pathways (Figure 8).^[24] These specific and efficient nanoparticle-light interactions can be exploited and applied in several nanobiomedical areas, such as photothermally triggered drug release, photodynamic therapy, photothermal therapy (PTT), biosensing or bioimaging.

As mentioned in section 1, photodynamic therapies, which are based on the local generation of cytotoxic reactive oxygen species, are commonly limited by the low photostability, poor solubility, limited absorption band and low reactive oxygen species quantum yield of the photosensitizers, the limited light penetration and the hypoxia in the tumor environment.

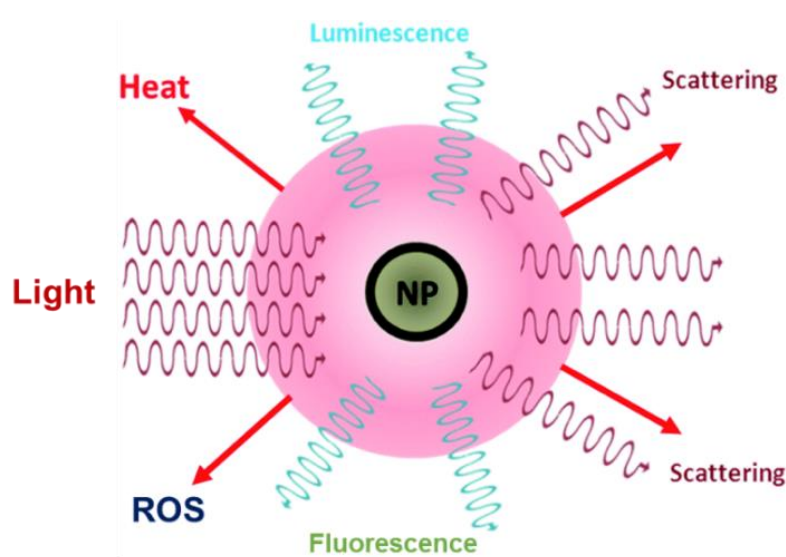


Figure 8. Multiple responses of nanoparticle to light irradiation. Figure adapted from ref^[24].

In contrast, photothermal therapy using nanomaterials shows less limitations and better therapeutic performance due to their excellent water solubility, high photostability, strong and tunable absorption bands, high heating efficiency and biocompatibility. Moreover, there is a wider range of nanomaterials which are eligible as photothermal agents, such as plasmonic metals,^[133] carbon-based materials or quantum dots^[134] among others. Their versatile fabrication and surface modification approaches can also enable achieving specific cell targeting during the delivery process. Another important aspect is the possibility to develop optically based nanothermometers and contrast agents for the *in-situ* temperature detection during photothermal therapies, which is crucial for controlling the therapeutic effect. To further improve the theranostic capacity, light responsive nanomaterials can also be used as multimodal imaging contrast agents. Since light induced and controlled photothermal therapies demonstrate plenty of promising application potentials, we discuss in depth in the next sections the main features of photothermal therapy and nanothermometry.

Photothermal nanotherapy is based on the optically induced heating of nanostructures.^[135,136] Due to the high light-to-heat energy conversion capacity, photothermal nanoagents could largely improve the specificity and efficiency of “outside-in” hyperthermia therapies (Figure 5). Nevertheless, this energy translating process is complex and it strongly depends on the type of nanomaterials and light actuating conditions, thereby resulting in different photothermal effects. Optical heating of nanomaterials generally consists of three steps: **i)** electronic excitation, **ii)** atomic lattice heating up, and **iii)** outward heat diffusion. The former two steps account for the nanoparticles heating up, while the last one is the heat dissipation to the surrounding environment.

3.1.1 Material dependent heating mechanisms

Nanomaterials can be optically heated by different mechanisms (Figure 9).^[137,138] Plasmonic metals, such as Au, Ag, Pt and Pd, generate heat under light irradiation by the **localized surface plasmonic resonance** as follows.^[139,140] The incident light induces an oscillation of metal conduction electrons. When the light frequency meets the natural frequency of the conduction electrons, which is given by the size, shape and composition of the nanoparticle, a coherent collective electronic oscillation is triggered. Such electronic movement generates heat *via* electron-electron scattering and electron-

phonon coupling, which warm up the whole metal lattice structure.

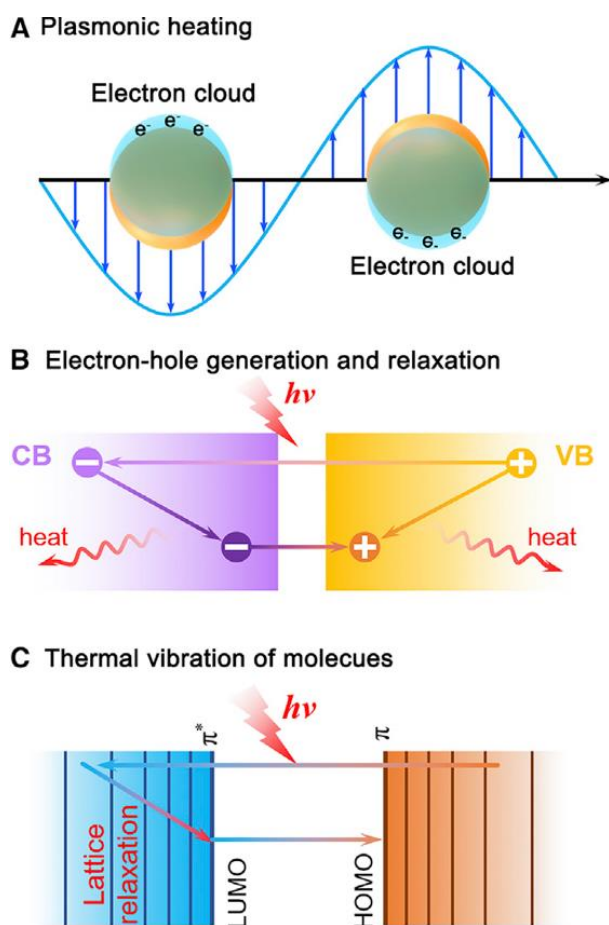


Figure 9. Photothermal mechanisms of different photothermal nanomaterials. (A) plasmonic heating, (B) electron-hole generation and relaxation, (C) thermal vibration of molecules. Figure extracted from ref^[137].

In contrast, semiconductors including quantum dots and metal oxides, produce photothermal effects through the generation of **electron-hole pairs and their non-irradiative relaxation**.^[141] When the light energy is larger than the band gap energy of the semiconductor, electrons in the valence band are excited to the conduct band, thus generating electron-hole pairs. Heat is produced through a thermalization process when the excited electrons and holes relax and decay to the band edges.^[142]

On the other hand, carbon-based nanomaterials^[143,144] (*e.g.* carbon nanodots, nanotubes and graphene based nanomaterials) or organic polymers (*e.g.* NIR dyes or conjugated polymers), also employed as photothermal nanoagents, are heated up through **electron transition from a π orbital** (highest occupied molecular orbital, HOMO) **to a π^* orbital** (lowest unoccupied molecular orbital, LUMO) under light excitation, and the subsequent generation of lattice thermal vibrations.

The majority of nanomaterials generate heat through one of these three mechanisms, and their heating efficiency is highly dependent on the heating mechanism. Generally, **nanomaterials with large absorption coefficient and small optical emission quantum yield show strong photothermal heating efficiency.**^[24] For instance, Au nanoparticles, as a typical plasmonic metal, combine high light absorption and minimum radiative emission (fluorescence and phosphorescence), thereby being considered as excellent photothermal nanoagents. Comparatively, fluorescent nanomaterials (*e.g.* organic dyes or fluorescent quantum dots^[145]) or broad bandgap semiconductors (*e.g.* bulk TiO₂^[141,146] or SiO₂) with high emission quantum yield exhibit low photothermal capability, as the absorbed energy dissipates mainly through radiative photon emission. However, semiconducting nanomaterials with narrow bandgap (*e.g.* Cu_{2-x}S^[147] or WO_{3-x}^[148]) can be attractive photothermal agents. This is due to the capacity to generate more above-bandgap electron-hole pairs, whose extra energy is converted into heat through the thermalization process when relaxing to the band edge. In addition, the lower bandgap enables heating with longer wavelengths, falling within the NIR transparent biological window showing deeper light penetration in tissues. Recently, graphene based nanomaterials^[149] and novel conjugated polymers^[46] demonstrate rather competitive photothermal capabilities, based on their high absorption cross section and excellent thermal conductivity.

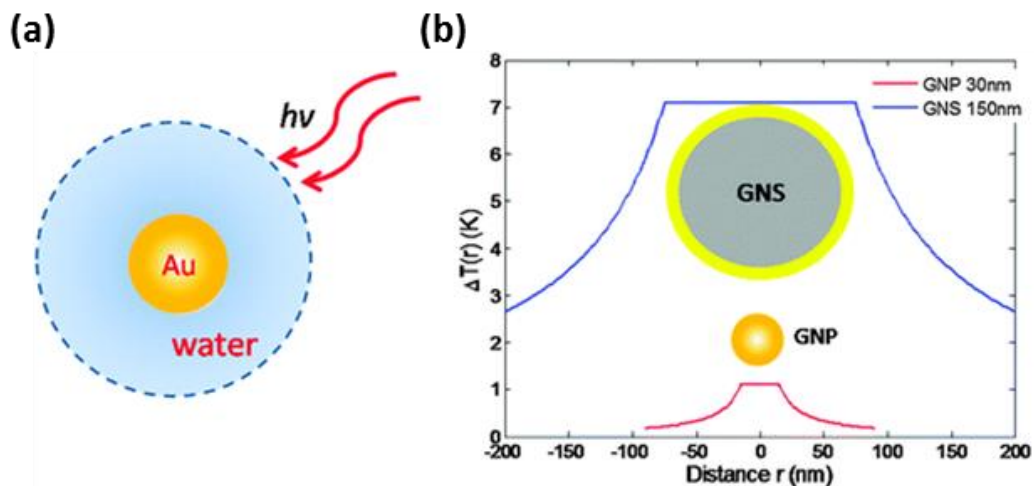


Figure 10. A typical steady photothermal heating process. (a) Schematic of gold nanoparticle with water medium under light irradiation. (b) The steady state temperature profile around the nanoparticle for two nanoparticles with different sizes, 30 nm gold nanosphere and 150 nm gold nanoshell under laser fluence 10^4 W/cm². Figure extracted and adapted from ref^[150,151].

3.1.2 Light dependent effects (continuous wave vs. pulsed laser)

To achieve photothermal effects for cancer therapy, the heat diffusion from the nanoparticles to the surrounding tissue plays a crucial role, and this process depends on how the light is delivered to the nanomaterial.

Figure 10 shows a typical steady photothermal heating process with a **continuous wave (CW) laser irradiation**. Once exposed to CW laser, the absorbing nanoparticles are rapidly heated up and elevate their temperature. Driven by the induced temperature gradient, heat spontaneously flows from the hot nanoparticle surface to the cold surrounding medium, which is warmed up through phonon-phonon coupling until the thermal equilibrium is reached. CW laser illumination induces a gradual temperature elevation of the whole system through the accumulative and spreading thermal effects.^[152] CW laser induced photothermal effects are attractive due to the highly controllable hyperthermia process. However, CW laser heating can show limitations related to the low nanoparticle delivery efficiency and the maximum permissible light exposure. Tumor overheating due to large nanoparticles doses or high light intensity can generate collateral damage to the surrounding healthy tissues through heat diffusion. Therefore, spatially and quantitatively controlling the induced thermal effects are important for adjusting the therapeutic efficacy and to minimize the side effects.

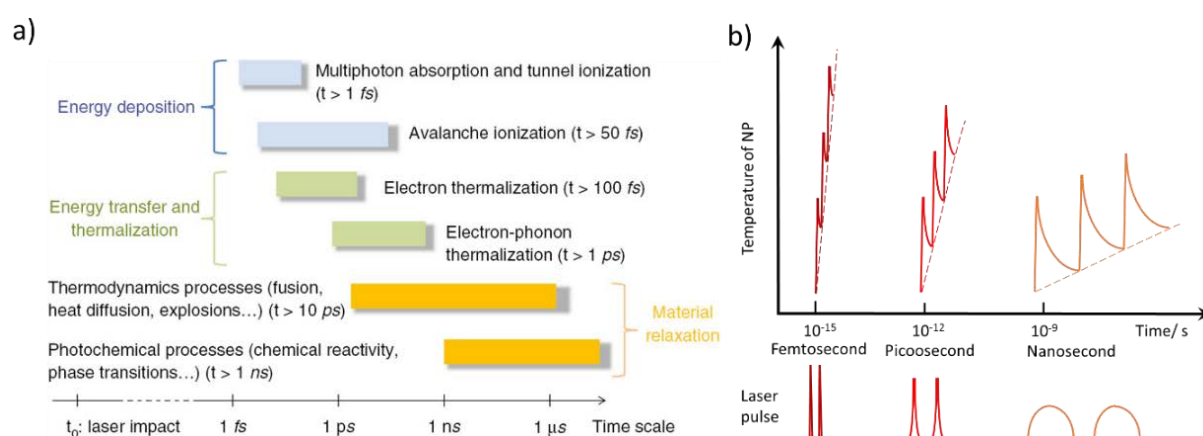


Figure 11. (a) Timescales of the physical phenomena involved in laser-material interactions. Figure extracted from ref^[153]. (b) Schematic of nanoparticle temperature elevation under different pulsed laser heating.

In contrast, **pulsed laser heating** can provide phototherapies with more confined thermal effects, by reducing the pulse duration to minimize the heat flow from the

nanomaterial. To understand the mechanism behind, it is necessary to go deeper to clarify the transient thermal dynamic processes during the pulsed laser heating. As mentioned above, although heating mechanisms are distinct for different nanomaterials, a complete heating cycle commonly includes three identical processes: **i)** energy delivery, **ii)** energy transfer and thermalization, and **iii)** material relaxation.^[153,154]

However, as observed in Figure 11 (a), the aforementioned processes take place in very different timescales. Energy deposition and thermalization within the nanoparticles require much less time (< 1 ps) compared to material relaxation (> 10 ps), which indicates rapid heating-up but slow cooling-down regimes. When exposed to a pulsed laser with ultra-short pulse duration, nanoparticles are able to readily absorb light photons and reach a high temperature level within single pulse interval. Under multi-pulse laser excitation, pulse-after-pulse effects might cause a rapid temperature increase in the nanoparticles with minimal thermal release to the surrounding environment (Figure 11b), since there is not enough time for heat dissipation to completely cool down the nanoparticle. Such thermal confinement with negligible heat diffusion can only be achieved when the laser pulse duration (t_P) is substantially lower than the thermal relaxation time (τ_T), i.e, $t_P < \tau_T$.^[155,156] For spherical nanoparticles with diameter D ,

$$\tau_T = D^2/27k \quad (1)$$

, where k is thermal diffusivity of surrounding medium. Typically, for nanoparticles with diameter of 20 nm in water, $k = 1.44 \times 10^{-3} \text{ cm}^2/\text{sec}$, and $\tau_T \sim 1 \text{ ns}$. Therefore, ultra-short pulsed lasers showing high peak intensity are able to induce high local thermal effects and heat nanoparticles to much higher temperature level during the same irradiation time. These amplified nanoscale thermal effects are confined within the nanoparticles. The highly localized therapeutic effect ensure high local efficiency for photothermal therapy with minimal risks of spreading thermal influences toward adjacent tissues.

However, the ultra-intense pulsed-laser heating can also induce uncontrollable effects in the nanoparticles and its surrounding material (Figure 12).^[151,154,157] For instance, a low power pulsed laser is able to melt ice around Au nanoparticles.^[150] With the increase of laser power, the temperature of Au surface is high enough to cause protein denaturation, thereby being within the hyperthermia range.^[158] Higher laser power might heat nanoparticles and induce a volume expansion with acoustic wave formation,

which is very interesting for photoacoustic imaging applications.^[159,160] A further increase of laser power might promote water boiling around the Au surface and generate a vapor layer around nanoparticles, which acts as a thermal insulator layer and enhances the thermal confinement in the nanoparticles.^[161–164] The resultant cavitation effects can lead to efficient cell destruction (mechanical stress) or improved photoacoustic imaging.^[156,159,164,165] Once heat accumulates and local temperature exceeds the melting (1063 °C) or vaporization points (2660 °C) of Au, nanoparticles may even deform, melt or collapse into small NP pieces, which could be used for reshaping^[166–168] and fabricating ultra-small nanoparticles^[169,170] or promote nanotherapeutic effects^[171].

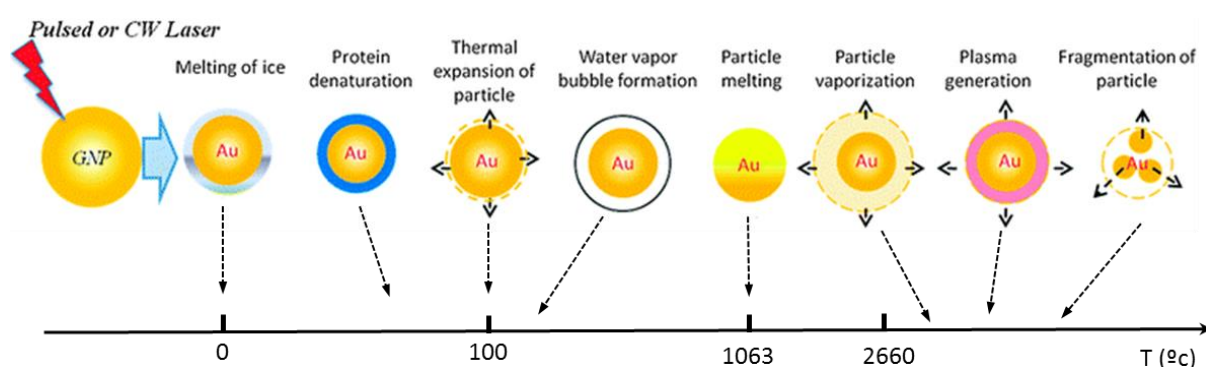


Figure 12. Schematic for thermophysical responses of laser Au nanoparticles heating. According to the Laser power increases from left to right, the particle surface temperature increases and leads to different thermophysical responses. Figure is extracted and adapted from ref^[151].

These tunable light responsive effects can find many biomedical applications (*e.g.* selective protein inactivation,^[172] DNA analysis,^[173] molecular delivery^[174,175] or thermal release^[176,177]), but careful control of the maximum temperature acquired by the nanoparticles is required to avoid tissue overheating, which is very complex with pulsed lasers. As a result, for common photothermal therapy, CW laser is still a better option due to a more controllable heating process, higher overall therapeutic effects and larger working area. Comparatively speaking, a CW laser induces moderate, accumulative and spreading thermal effects centered on the nanoparticles within the laser spot. It enables macroscale heating effects and the therapeutic efficiency strongly depends on the irradiation time, light fluence and nanoparticles concentration. The CW laser induced temperature increase could be more easily estimated and modulated by phase change^[150,178] or thermal imaging. In contrast, determining the transient temperature distribution around the nanoparticles under pulse laser heating is more complicated due to the ultrafast and nanoscale thermal dynamics. Expensive time-resolved

microscopy^[179,180] is required for the complex local temperature detection. On the other hand, pulsed laser heating only affects the substances or cells which are directly in contact to the nanoparticles. Thus, the overall effects are quite restricted by the number of nanoparticles at the sites of action. These amplified thermal effects can probably induce unwanted necrosis rather than apoptosis cell deaths,^[181,182] with the subsequent release of intracellular contents into the extracellular milieu, which might cause undesirable side effects, such as inflammatory or immunogenic responses in adjacent healthy tissues.^[183,184] In contrast, CW laser can better control the light intensity to trigger apoptotic cell deaths and spread the thermal effects over a larger volume, which is more attractive for solid tumor eradication.

Although CW laser induced photothermal therapy have been extensively studied, improving the therapeutic efficacy and controlling the thermal effects are becoming the critical issues. In this sense, the photothermal nanoagents are crucial factors for treatment control. Their tunable composition, morphology and surface state offer great possibilities to achieve ideal photothermal effects through nanomaterial optimization.

3.1.3 Photothermal conversion efficiency of nanomaterials

An ideal photothermal nanoagent should meet several requirements according to different therapeutic objectives including (Table 1): safety, specificity, efficiency, multifunctionality and industrialization capability. Compared to other factors, the photothermal therapy efficiency in the NIR region with higher penetration in tissues is a major factor for therapy optimization. Only nanomaterials with high photothermal therapy efficiency will be considered for further optimization to achieve the other objectives. Therefore, it is necessary and significant to discuss how to evaluate and optimize the photothermal therapy efficiency of nanomaterials.

The photothermal conversion efficiency represents the light-to-heat energy translating efficiency of a nanomaterial, and it is commonly regarded as a quantitative and numerical index of the photothermal conversion efficacy. As previously described, nanomaterials are able to absorb and scatter light, and then emit fluorescence, luminescence or release heat. Since the photothermal conversion efficiency is closely correlated with the absorption process and the non-radiative relaxation path,

nanomaterials with large absorption and high non-radiative relaxation yields are the most promising photothermal nanoagents.

Table 1. Requirements for ideal photothermal nanoagents.

Objectives	Target related properties	Necessary improvements
1. Safety	Biocompatible compositions	Long-term toxicity
2. NIR (I or II) activating	High extinction cross section	Maximum penetration depth
3. Specific targeting	Desirable surface modification	<i>In-vivo</i> targeting mechanism
4. <i>In-vitro</i> and <i>in-vivo</i> PTT efficacy	High light-to-heat conversion efficiency	Nanomaterials optimization
5. Multimodal imaging and combined therapies	Multi-responsive properties for imaging, drug delivery, drug release and therapies.	Nanomaterial hybridization
6. Facile synthesis and high cost-effectiveness	High availability of materials and facility; Standard synthesis conditions	Quality and quantity control

Based on steady state heating process of nanoparticles dispersion under CW laser illumination, the photothermal conversion efficiency (η) can be calculated by:

$$\eta = \frac{Q_{output}}{Q_{input}} \quad (2)$$

, where Q_{input} is the incident light power and Q_{output} is the generated heat. To get accurate values of Q_{input} and Q_{output} , standard optical heating tests with certain conditions related to the light and nanoparticle dispersions should be carried out (Figure 13).

Briefly, to calculate the photothermal conversion efficiency a certain volume of nanoparticle dispersion is placed inside a transparent cuvette. By turning the laser on, the whole colloidal dispersion is heated up through heat radiation, conduction and convection effects between the nanoparticles and the solvent medium (Figure 13c region (i)). Due to the energy balance of light energy input and thermal dissipation of the colloidal dispersion, a steady stabilization will be reached (Figure 13c region (ii)). When

the laser is turned off, the dispersion cools down to the ambient temperature (Figure 13c region (ii)). During the whole heating/cooling process, the temperature of the colloidal dispersion must be recorded in real-time.

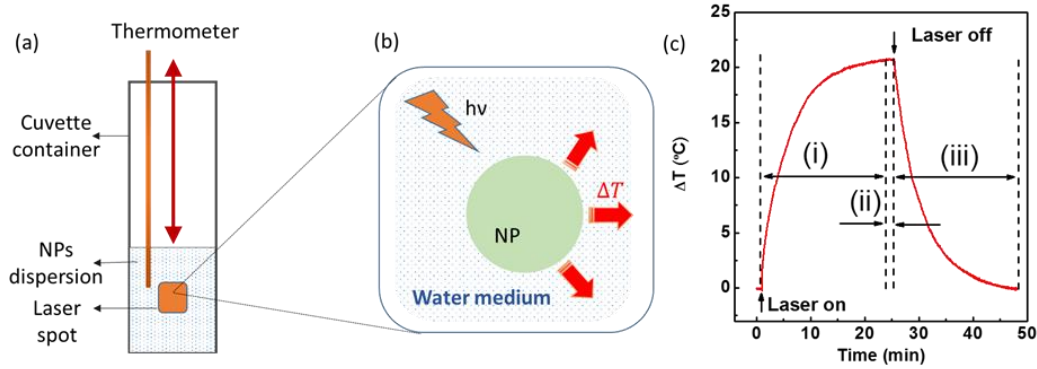


Figure 13. Experimental schematic and heating curve of photothermal conversion efficiency measurement. (a) Schematic of experimental setup. (b) Schematic of nanoparticles heating and heat diffusion. (c) A typical temperature evaluation curve: heating up (i), thermal stabilization (ii) and cooling down (iii).

According to the Beer-Lambert law, Q_{input} can be derived as:

$$Q_{input} = I(1 - 10^{-E_{\lambda}}) \quad (3)$$

, where I is incident laser intensity, E_{λ} is the light extinction of the nanoparticles dispersion at the illumination wavelength λ , which can be obtained through UV-vis spectroscopy measurement. To acquire the value of Q_{output} , the relationship of the thermal energy transfer between the colloidal dispersion and the surrounding environment should be determined. According to the work of Roper *et al.*,^[185-188] the general photothermal conversion efficiency calculation formula is:

$$\eta = \frac{hS(T_{max} - T_{amb}) - Q_{water}}{I(1 - 10^{-E_{\lambda}})} \quad (4)$$

, where h is a heat transfer coefficient between the nanoparticle dispersion and the surrounding ambient, S is the surface area of the cuvette container, T_{max} is the temperature of the nanoparticle dispersion during the thermalization process (ii) and T_{amb} is the ambient temperature. Q_{water} represents heat induced by light in the solvent without nanoparticles, which is acquired through heating of the solvent without nanoparticles under the equivalent experimental conditions. The value of hS could be obtained by analyzing the temperature decrease in the cooling down process. Detailed information of the calculation process is included in the Appendix at the end of the Thesis.

To conclude, this model represents a standard, concise and experimentally simple approach for photothermal conversion efficiency calculation, which is becoming a common criterion for photothermal therapy evaluation.

By measuring photothermal conversion efficiency, the photothermal capacity of different nanomaterials can be easily compared and optimized. According to previous investigations, appealing nanomaterials, such as plasmonic metals, carbon based nanomaterials, metal chalcogenide, 2D MXenes, quantum dots, metal-oxides, conjugated polymers and NIR dyes, can exhibit high optical heating capacity. A comparison of the different nanomaterials with their most relevant features is shown in Table 2.

Plasmonic metals, such as Au,^[189,190] Ag,^[191] Pd,^[192] Pt^[193] and Cu^[194] show quite large absorption coefficients (10^9 - 10^{10} M⁻¹cm⁻¹) due to their intense localized surface plasmon resonance (LPSR). In particular, Au shows highly tunable morphology, absorption band and good biocompatibility, and it has been extensively explored for photothermal therapy. However, Au^[195,196] and other plasmonic metal nanoparticles,^[197] are very ductile and can easily melt, deform and irreversibly lose their NIR-absorption properties under strong, repeated or long-time laser illumination. Moreover, although Pt and Pd seem very efficient for optical heating, their complex synthesis and high cost largely hinder their wide biomedical application.

Owing to the large absorption cross section and high thermal conductivity, **carbon based nanomaterials** such as carbon nanodots,^[198,199] nanotubes,^[200-205] graphene^[206-208] based nanomaterials and fullerenes,^[209] generally demonstrate high photothermal therapy capacity. The optical heating is based on the photoinduced excitation of electronic orbital transition and non-radiative relaxation by thermal lattice vibration. Although post-synthetic modifications with hydrophilic moieties, can provide improved water solubility and biocompatibility, their stability and functionalization properties need further improvements for therapeutic uses.

Metal chalcogenides comprising transition metal (Cu, Mo, W and Mn) and chalcogenides (S, Se and Te) are also attractive optical heating agents. Metal chalcogenides show similar localized surface plasmon resonance induced absorption^[210-212] as plasmonic metals, in which the intensity and peak of the absorption strongly depend on the composition, shape, size, and crystalline structure.^[147,210,213-215] However,

unlike plasmonic metals, metal chalcogenides are rather stable under laser irradiation. The main concerns of these nanomaterials are related to their toxicity and high hydrophobicity derived from the organic synthesis, as well as their complex biofunctionalization routes.

MXenes are a new class of 2D materials composed of transition metal carbides/ carbonitrides, which were introduced by Gogotsi's group in 2011.^[216,217] MXenes allow negligible electromagnetic wave emission and ultimate energy dissipation in the form of heat, which inspired the thought attractive light-to-heat mediators.^[218] The NIR light absorption and photothermal behaviour of Ti_3C_2 MXenes might be also attributed to localized surface plasmon resonance effects.^[219] Although the synthesis with controlled uniform morphology and dispersion stability is complicated, their strong heating capacity is promising for photothermal therapy applications.

Quantum dots (QDs) exhibit unique tunable absorbing properties and good photostability owing to the quantum confinement effects. The strong light absorption extinction coefficient (10^5 - $10^6 \text{ M}^{-1}\text{cm}^{-1}$) of QDs indicates large light harvesting capability. However, due to a high radiative emission (fluorescence) quantum yield, QDs show slightly lower photothermal efficiency than other nanomaterials but enable integrating photothermal therapy and optical bioimaging. Traditional QDs with heavy metal ions, such as Cd^{2+} possess high toxicity and are not suitable for biological uses.^[220,221] Novel black phosphorous QDs with intrinsic safe composition, morphology dependent band gap, strong and wide absorption from the UV to the visible region, and biological degradability seem more attractive for photothermal therapy.^[222]

Semiconducting metal-oxides, such as TiO_{2-x} ,^[223] WO_{3-x} ,^[148,224,225] and iron oxides,^[226-228] also show strong light-to-heat converting capability. The stoichiometric oxides are quite weak NIR absorbers due to their very wide bandgap. For instance, bulk TiO_2 with a bandgap around 3.2 eV commonly works as agents for light harvesting and reactive oxygen species based applications.^[229] However, it requires an excitation wavelength within the ultraviolet (UV) region, typically below 385 nm, which is inapplicable for biomedical applications due to high cytotoxicity of the UV light. Efforts for fabricating hybrid nanocomposites with metal or organic dyes have been made to narrow the band gaps.^[230] Alternatively, up-converting nanomaterials can convert NIR to UV light.^[231] However, the cytotoxicity and low abundance of the required rare-earth

materials are the biggest problem for clinical use. Interestingly, magnetite Fe_3O_4 can become an interesting photothermal nanoagent due to their proved biocompatibility, semi-metal behaviour and increased NIR absorbance.^[232]

Table 2. Typical photothermal nanoagents.

Category	Type	PTT mechanism	Advantages	Disadvantages	Necessary Improvements
Plasmonic metals	Au, Ag, Pt, Pd, Ni, Cu	LSPR	tunable morphology and absorption, biocompatibility, easy modification, high PTT efficiency	undesirable absorption band, poor photo-mechanical stability, expensive synthesis	assembly of small NPs, nanocomposites
Carbon based nano-materials	Carbon Graphene Fullerene	thermal lattice vibration	flat absorption, high photostability, cheap synthesis	nonspecific absorption, poor biodegradability, surface dependent toxicity	reproducible synthesis with uniform size, biocompatibility surface modification
Metal chalcogenide	CuS, CuSe, MoSe, MoS, Bi ₂ Se ₃	LSPR	tunable composition, morphology and absorption, high photostability, low cost	poor hydrophilicity, unknown toxicity	multifunctional surface modification
2D MXenes	Ti ₃ C ₂ , Nb ₂ C	LSPR	high NIR absorption, high photostability, high PTT efficiency	polydispersity, laborious synthesis	reproducible synthesis with uniform size, nanocomposites
Quantum Dots	Black Phosphorus, CdSe/ Bi ₂ Se ₃	non-radiative recombination	tunable composition and morphology, bioimaging capacity	poor hydrophilicity, potential toxicity (not for Black Phosphorus)	biocompatibility surface modification
Metal-Oxides	FeO _x , TiO _x , SiO ₂ , WO _x	non-radiative recombination	tunable absorption by doping, high photostability	undesirable absorption band, toxicity	biocompatibility surface modification, nanocomposites
Conjugated polymers	Polypyrrole Porphyrin Polyaniline Dopamine	thermal lattice vibration	high NIR absorption, low-toxicity, high photostability biodegradability,	polydispersibility, expensive synthesis	reproducible synthesis with uniform size
NIR Dyes	Prussian blue, ICG, BODIPY, IR825/ 780,	thermal lattice vibration	high NIR absorption, biocompatibility, biodegradability, bioimaging capacity	poor photostability, low PTT efficiency	nanocomposites photostability PTT efficiency

Conjugated polymers (CPs) are macromolecules with extended π -bonding structures showing band gaps in the 1-3 eV range,^[233,234] which covers a wide spectrum from the blue to the NIR. The delocalized electronic structure and efficient coupling between optoelectronic segments of the CPs (e.g. polypyrrole (PPy),^[235–238] polydopamine^[239] and polyaniline^[240,241]) within the nanoparticles enables rapid exciton

transfer along the confined backbone structure, thereby endowing strong light absorption and thermal conductivity for photothermal therapy applications. Different types of CP nanoparticles can be fabricated to narrow the band gap and enhance the absorption for NIR applications.^[165,242,243] The excellent photostability and good biodegradability make them promising for clinical uses. Lastly, there is still room to improve the synthesis and polydispersity of the resultant products.

NIR dyes with high NIR absorbance are rather attractive for phototherapy and bioimaging applications. For photothermal cancer treatment, NIR dyes can be conjugated *via* covalent interactions to form nanoparticles for improving the delivery efficiency through Enhanced Permeability Retention effects. NIR dyes nanoparticles exhibit several advantages including facile synthesis, large yields, high biological affinity and good biocompatibility. Due to the high emission quantum yield, clinical organic dyes, such as ICG or some cyanine derivatives show high fluorescence imaging performances, but low photothermal therapy efficiency.^[244-247] Therefore, some NIR dyes with higher photothermal therapy capacity by reducing the emission quantum yield have been synthesized, including IR825,^[248] IR780,^[249] RC-BSA^[250] and BODIPY derivatives^[251]. Interestingly, prussian blue nanoparticles were employed as photothermal nanoagents (20.5%),^[252] and their magnetic properties could be employed to achieve MRI guided photothermal therapies.^[253-255] Nowadays, the introduction of multifunctional monomers or the combination with more stable inorganic nanomaterials are becoming popular methods to improve their efficiency and multi-functionality.^[256,257]

3.1.4 Optimization of the photothermal nanoagents

For clinical photothermal therapy, the following elementary features are required in nanomaterials: good aqueous solubility, low toxicity and high NIR absorption. Therefore, improvement of photothermal conversion efficiency should be mainly focused on the optimization of the nanomaterials properties in the NIR. According to the related publications, the photothermal conversion efficiency is strongly dependent on the size, shape, composition, and assembly-state of the nanostructures.^[258,259] Even though there are difficulties to precisely compare photothermal conversion efficiency of different samples under different synthetic and experimental detection conditions, the following relevant conclusions can be extracted after careful analysis of the photothermal conversion efficiency of different nanomaterials.

- **Size dependence**

Size is a crucial factor in the optical properties and have complex effects on the photothermal conversion efficiency of nanomaterials. Firstly, size determines the absorbing and scattering properties of nanomaterials. According to Mie theory, nanoparticles with large size exhibit enhanced light absorption and scattering cross sections, but decreased absorption to scattering ratio, which might cause a reduction of the photothermal conversion efficiency. For example, the size dependence of photothermal conversion efficiency for Au nanoparticles has been elaborately analyzed. As shown in Figure 14, a negative correlation between the size and photothermal conversion efficiency is clearly observed.^[186] The same tendency is also observed with Au NRs^[260] and nanobipyramid.^[259] As a result, at similar mass concentration and identical resonance wavelength, smaller colloidal nanoparticles will induce much stronger thermal effects due to their minimal scattering.

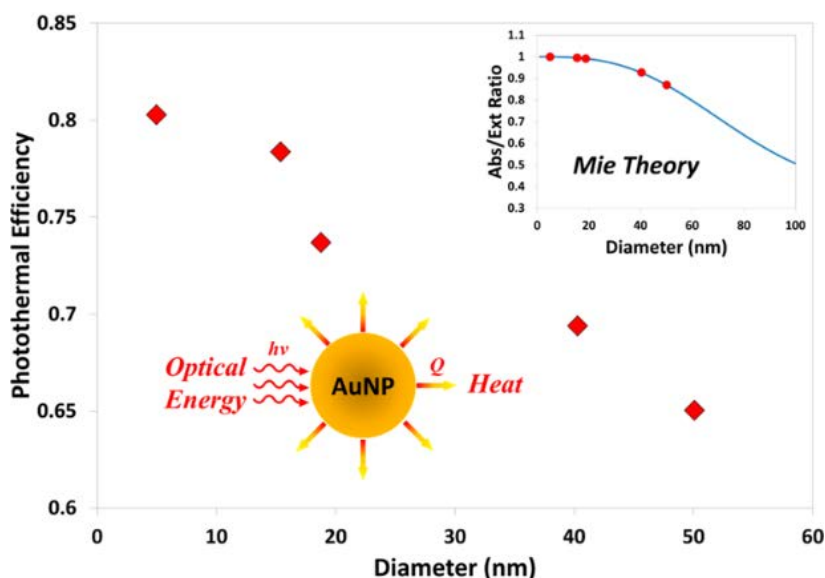


Figure 14. Photothermal conversion efficiency (PCE) of Au NPs with different sizes. Figure adapted from ref^[186].

Therefore, the size influence on both the Absorption/Scattering ratio and the absorption wavelength should be simultaneously considered for photothermal conversion efficiency optimization. Moreover, size is also playing a crucial role in the nanoparticles delivery process, as it is reported that a size range from 10 nm to around 200 nm can combine benefits from longer blood circulation lifetime and higher cell internalization efficiency.

- **Shape dependence**

Nanomaterials can be fabricated into different shapes with zero, one, two, three dimensions (0D, 1D, 2D and 3D). Shape influences on the photothermal conversion efficiency are mainly attributed to the morphology dependence of the optical properties. Compared to the size, shape could be more efficient to optimize the photothermal conversion efficiency due to its higher tunability freedom. All shapes including 0D (quantum dots or nanodots), 1D (*e.g.* nanorods, nanowires or nanotubes), 2D (*e.g.* nanosheets or nanoflakes), 3D (nanotriangles, nanocages, nanostars, nanoflowers) nanomaterials are able to modulate the absorption and scattering spectra. In particular, 3D nanomaterials here represent those with three or more dimensional degrees of freedom in nanoscale.

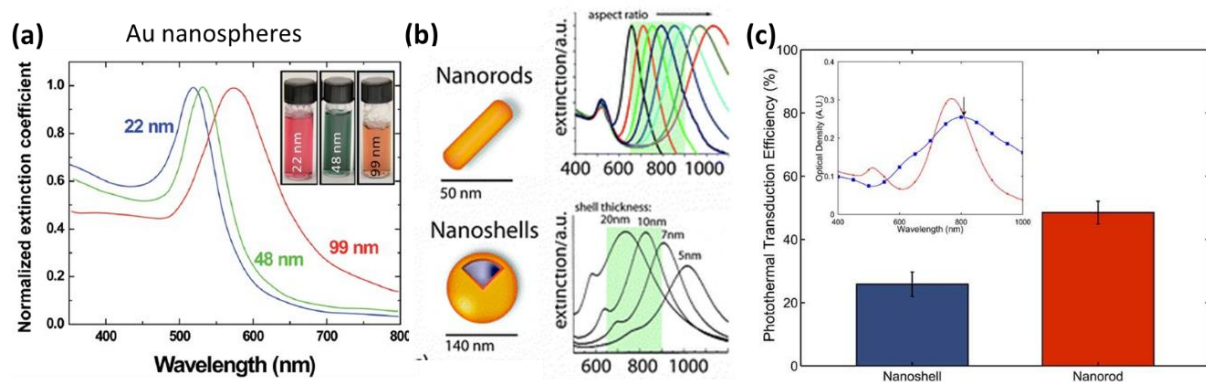


Figure 15. (a) Normalized extinction coefficients of gold nanospheres with different size. (b) Tunable extinction spectrum of nanorods and nanoshells (c) Extinction spectra and photothermal transduction efficiency of nanoshell (blue) and nanorod (red). Figure (a), (b), (c) adapted from ref[261][262][263], respectively.

Firstly, the shape of the nanomaterials can be tuned to modify the intensity and wavelength of the absorption peak to obtain desirable photothermal conversion efficiency in the NIR. For instance, Au nanospheres with absorption band falling in visible range (500- 550 nm) are not eligible for photothermal therapy. Increasing the size is unable to fully tune the resonance towards the NIR region without drastically increasing the detrimental scattering (Figure 15a). However, fabrication of Au nanorods and nanoshells enable a facile achievement of strong NIR absorption bands by just adjusting the aspect ratio and the shell thickness without large volume changes (Figure 15b). As a result, Au nanoshells and, especially, Au nanorods can exhibit interesting photothermal

conversion efficiency (25% and 50%) (Figure 15c). However, in the case of highly anisotropic materials, such as nanorods and nanowires or 2D nanomaterials, the absorption cross section is highly dependent on the orientation of the nanoparticles with respect to the polarization of the incident light. As the nanoparticles are in general randomly oriented in photothermal therapy applications, an overall decrease of the photothermal conversion efficiency can be observed.

Table 3. Photothermal heating results of Au nanomaterials with sharp edges.

Year	Sample	Size (nm)	Laser λ (nm)	PTT efficiency (%)
2018	Au Nanospikes	58	980	78.8
2014	Hollow Au_Ag Nanourchins	80	808	80.4
2014	Au Bellflowers	144.6/ 123.3/ 10	808	74
2015	Hollow Au nanoflowers		800	52
2018	Au nanooctopods		660	83

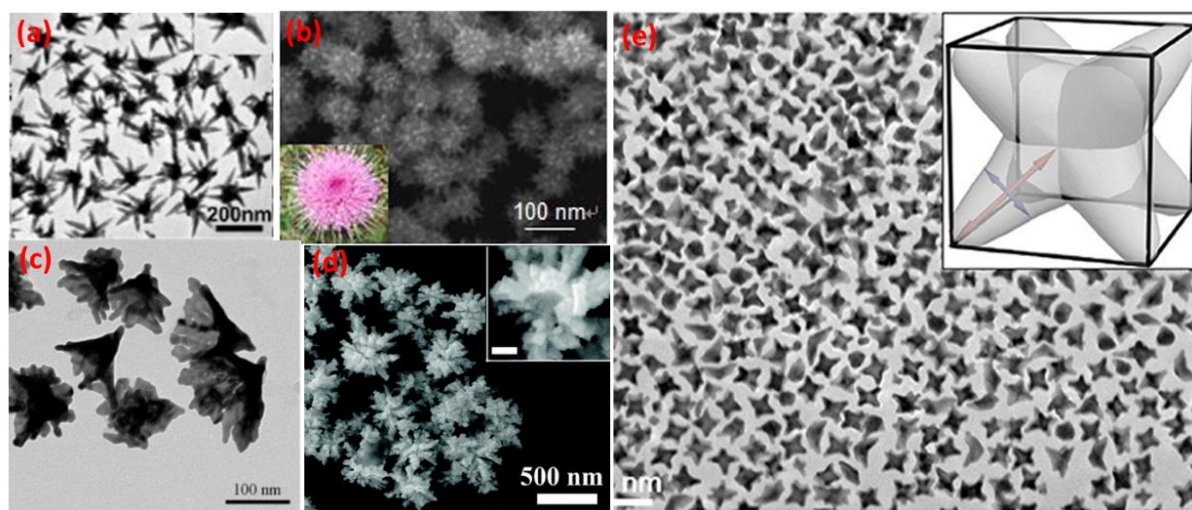


Figure 16. SEM images of nanomaterials involved in Table 3. (a) Au Nanospikes, (b) Hollow Au_Ag Nanourchins, (c) Au Bellflowers, (d) Hollow Au nanoflowers, (e) Au nanooctopods. Figures extracted and reproduced from ref^[264–268], respectively.

To achieve high photothermal conversion efficiency, nanomaterials with sharp edges in different directions are becoming popular for photothermal heating. Especially

for plasmonic metals, such as Au or Ag, the nanotips in different directions can simultaneously help to red-shift the resonance to the NIR without largely increasing the scattering and to get quasi-isotropic structures (Figure 16) without polarization dependence, thus largely enhancing the LOCALIZED SURFACE PLASMON RESONANCE INDUCED absorption and heating (Table 3).

Nevertheless, these complex 3D nanostructures are difficult to synthesize with high quality and reproducibility. Most of them are rather fragile and are susceptible to thermal deformation and mechanical stress. The laborious synthetic approaches and solution stability need also to be improved.

- **Composition dependence**

Different nanomaterial compositions show diverse photothermal heating mechanisms and photothermal therapy capacities. In general, plasmonic metals, conjugated polymers, metal chalcogenides, carbonaceous nanomaterials and 2D Mxenes show relatively higher photothermal conversion efficiency and stronger photothermal therapy capability compared to quantum dots and NIR dyes.

For nanomaterials composed of multi atomic elements, modulating their compositions by tuning the ratio of each element enable altering their absorption properties and photothermal conversion efficiency. Typical examples are self-doped nanomaterials,^[269] such as the nonstoichiometric metal oxides (TiO_{2-x} , WO_{3-x} or iron oxide) and binary copper chalcogenides (CuS or CuSe). For common semiconducting nanomaterials, such as TiO_{2-x} , the photothermal heating efficiency is essentially determined by the population of above-bandgap electron-hole pairs, which accounts for the subsequent thermalization when relaxing to the band edges. Therefore, a narrow band-gap should be preferable for increasing both the interband electronic transitions and the density of above-bandgap electron-hole pairs under low-energy NIR light irradiation. Nonstoichiometric metal oxides with heavy self-doping levels possess numerous crystallographic defects that contribute to narrow the band gaps, which is desirable for generating photothermal effects. As an archetypical example, bulk TiO_2 shows a large band gap of 3.2eV. However, decreasing the O/Ti ratio via reduction approaches, such as Ti_2O_3 (0.1 eV),^[144] Ti_8O_{15} (0.66 eV)^[270] and black H- TiO_2 (typically from 1.54 eV^[271] to 1.85 eV^[272]) increases the defects concentration including Ti^{5+} ,

oxygen vacancies, TiOH or TiH,^[229] thus largely reducing the bandgap to improve the photothermal capacity.^[272]

Regarding multi-element nanomaterials with localized surface plasmon resonance-like absorbing properties, such as binary copper chalcogenides or WO_{3-x} , adjusting the stoichiometric ratio allows modulating the intensity and wavelength peak of the localized surface plasmon resonance, and tuning the hole density generated from the metal vacancies to maximize their photothermal conversion efficiency. For instance, $Cu_{2-x}S$ experiences red-shift of the localized surface plasmon resonance band with the increase of Cu ions ratio (Figure 17a).^[272] Actually, nonstoichiometric $Cu_{2-x}S$, such as Cu_9S_5 , $Cu_{7.2}S_4$ and Cu_7S_4 have shown remarkable photothermal conversion efficiency, as summarized in the Table 4.

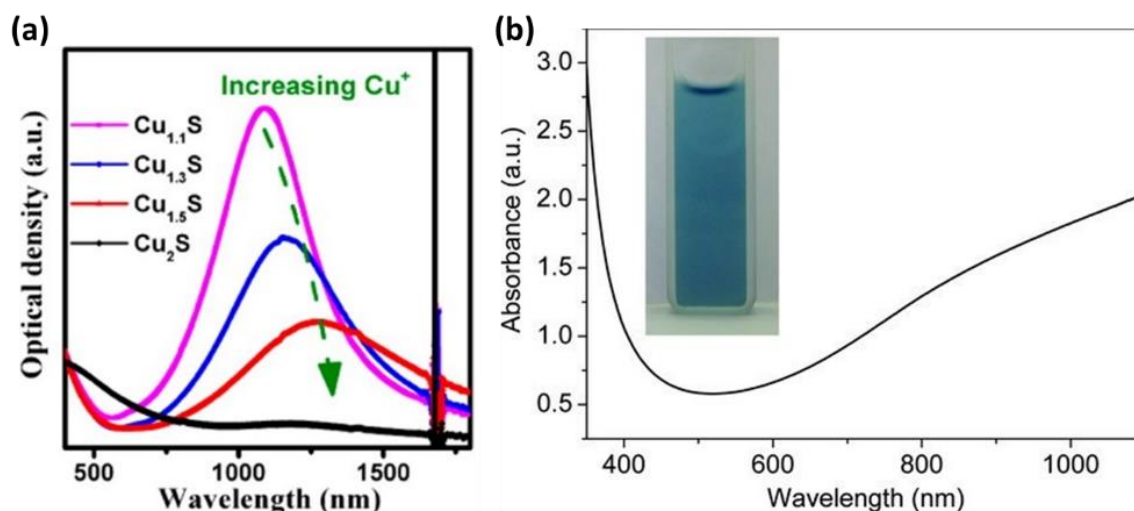


Figure 17. (a) Evolution of the optical extinction spectra of $Cu_{2-x}S$. (b) Optical extinction spectra of an aqueous dispersion $W_{18}O_{49}$ nanowires. Figure (a), (b) adapted from ref^{[214][273]}, respectively.

In the particular case of WO_3 (bulk band gap of 2.6 eV)^[148], a variety of oxygen-deficient stoichiometries can be generated and WO_{3-x} undergoes a metal-insulator transition when $x = 0.1$.^[274] For $x > 0.1$, the electrical and optical properties of WO_{3-x} are dominated by free electrons which contributes to get localized surface plasmon resonance induced absorption bands in the NIR (Figure 17b).^[148,273] Actually, $W_{18}O_{49}$ nanowires,^[273] $WO_{2.9}$ nanorods,^[225] WO_{3-x} nanodots^[224] and WO_{3-x} hierarchical nanostructures^[275] show intense NIR absorption and relevant photothermal performance. Another proof of the stoichiometry effects on photothermal effects is related to iron oxides. Magnetite (Fe_3O_4) could be easily oxidized to maghemite

(Fe₂O₃),^[232] which results in a large decrease of the NIR absorption with subsequently hampered photothermal effects.

Table 4. Photothermal conversion efficiency of Cu_{2-x}S and WO_{3-x}.

Year	Sample	Size (nm)	Laser λ (nm)	PTT efficiency (%)
2011 ^[276]	Cu ₉ S ₅ NCs	70/ 13	980	25.7
2014 ^[277]	Cu _{7.2} S ₄ NCs	20	980	56.7
2015 ^[278]	Cu ₇ S ₄ NCs	25	808	48.62
2015 ^[279]	Cu ₇ S ₄ NCs	61	808	52.9
2016 ^[280]	Cu ₇ S ₄ NRs	50/ 30	808	57.8
2014 ^[275]	WO _{3-x} hierarchical nanostructures	700-1400	915	28.1

NRs: nanorods, NCs: nanocrystals.

Lastly, the crystallographic phase of the nanomaterials is also strongly correlated with the photothermal efficacy. For instance, there are three main crystal phases of TiO₂: stable rutile (tetragonal), metastable anatase (tetragonal), and brookite (rhombohedral). Anatase generally shows the highest photocatalytic activity, followed by rutile, while the brookite and amorphous TiO₂ have no apparent photocatalytic activity, but shows increased photothermal conversion efficiency.^[281]

- **Nanostructures assembly state**

The assembly of nanostructures could be considered as a combination of size and shape effects. By using assembly methods, a large number of small nanostructures can be conjugated to form clusters or vesicles with larger size and extended shape. Generally, nanostructures assembly or aggregation results in a red-shift in the absorption band towards the NIR region compared to the original building blocks due to the near-field electromagnetic coupling.^[282] Consequently, it can bring positive influence on the photothermal capacity.

A systematic study of nanoplasmonic micelles composed of small Au nanoparticles cores and amphiphilic block copolymers tethers.^[283] shows that fine control over the

assembly micelles is able to modulate the plasmon coupling to achieve strong NIR absorption. Through a similar method, Huang and coworkers reported plasmonic gold nanovesicles (diameter~200nm) composed of poly(ethylene glycol)-bpoly(ϵ -caprolactone) (PEG-b-PCL)-tethered Au nanoparticles (diameter 27nm) with intense NIR absorbance and reasonably high photothermal conversion efficiency (37%).^[284] Another rather facile synthesis of tube-like Au-attapulgite nanocomposites has been achieved by electrostatic binding of Au nanoparticles (diameter ~15 nm) to the surface of a nanosized mineral attapulgite.^[285] The resulting composites exhibit a longitudinal absorption mode shifted to the NIR region (~670 nm) and possess a photothermal conversion efficiency of 25.6%.

Nanoclusters composed of nonmetallic nanoparticles, such as Fe_3O_4 ,^[226] carbon nanodots^[286] and Cu_7S_4 ^[278] have been also reported interesting photothermal heating results. Typically, supra- carbon nanodots (5- 25 nm) are fabricated by assembling the surface charge-confined carbon nanodots (1- 5 nm) through electrostatic interactions and hydrogen bonds. These clusters display strong visible–NIR absorption band (500-900 nm) and high photothermal conversion efficiency of 53.2%. Another solid proof was reported by Cui and coworkers. By tuning the surface properties of Cu_7S_4 nanocrystals, rod-like alignments or nanosuperlattices could be obtained, which accounts for a large increase of photothermal conversion efficiency from 48.62% to 56.32% and 65.7%. In conclusion, nanomaterials with small size and resonances in the visible can benefit from the self-assembly to enhance their NIR absorbance to improve the photothermal heating capacity.

- **Multimaterial effects in nanocomposites**

According to Table 2, although a wide variety of nanomaterials are eligible as photothermal nanoagents, all of them possess advantages and limitations. Nanocomposites composed of several nanomaterials components can merge merits and avoid shortcomings of each component and achieve synergistic effects. Several relevant types of nanocomposites for photothermal heating have been summarized in Table 5.

Table 5. Typical nanocomposites with extremely high photothermal conversion efficiency.

Category	Type	Year	Sample	Size (nm)	Laser λ (nm)	PTT efficiency (%)
Au	Au_CuS	2018 ^[287]	coreshell_Au/ Cu _{2-x} S	17/29 / 13.5	808	52.1
		2016 ^[288]	coreshell_Au/ Cu _{2-x} S	50	808	59.01
		2018 ^[288]	coreshell Au NRs/ Cu ₇ S ₄	36/ 84	808	62
			dumbbell Au NRs/ Cu ₇ S ₄	61/ 20		56
	2015 ^[289]	coreshell_Au/ Cu ₇ S ₄	88.5	980	63	
	Au_Iron oxides	2015 ^[290]	Au Nanopopcorn_Iron oxide cluster	158	808	61
		2015 ^[291]	Au/ PPy_Fe ₃ O ₄	200	808	23.9
	Au_Carbon	2016 ^[292]	Carbon NPs_Patchy Au	100	808	31.6
		2016 ^[293]	Carbon nanotubes_Au NPs		808	76
	Conjugated polymers (CPs)	CPs_Fe ₃ O ₄	2015 ^[294]	Fe ₃ O ₄ / PEDOT		808
2015 ^[295]			Fe ₃ O ₄ / PDA	237	808	13.1
2014 ^[296]			PPy/ Fe ₃ O ₄	60.8	808	49
CPs_MoSe ₂		2016 ^[297]	MoSe ₂ _PDA	314	808	44.5
CPs_/ Au or Pd		2014 ^[298]	PPy/ Au Chains	14.5/ 14	808	66.1
		2016 ^[299]	Pd NPs/ PPy	29	808	96

To summarize, photothermal therapy has received increasing attentions as a non-invasive, highly efficient hyperthermia cancer therapy with minimal side effects. However, there are many unsolved problems lying in front, such as unoptimized photothermal therapy nanoagents and uncontrollable heating effects. photothermal conversion efficiency optimization of the nanomaterials should be continued due to the limited biological light penetration and nanoparticles delivery efficiency. In addition, the control of the induced thermal effects is another troublesome problem that remains to be addressed. Developing nanothermometric tools that are accessible to the site of action is critical for enabling therapy self-monitoring and modulation.

3.2 Nanothermometry

To avoid overheating and to minimize the side effects, precise temperature control at the nanoscale level is crucial in thermally controlled drug release and photothermal therapy applications. Nanothermometers for biological applications should meet several fundamental conditions, including non-contact, nanoscale size, thermal specificity, biocompatibility and independence of the biological targets, such as cells or tissue. The different applications also impose specific requirements for the temperature detection.

For controlling the drug release, there is only need for continuous monitoring over a determined temperature range when a specific temperature threshold is reached. Therefore, long-term stability, large dynamic range and good repeatability are important requirements, while temperature sensitivity and thermal response time are less relevant for the nanothermometry design.

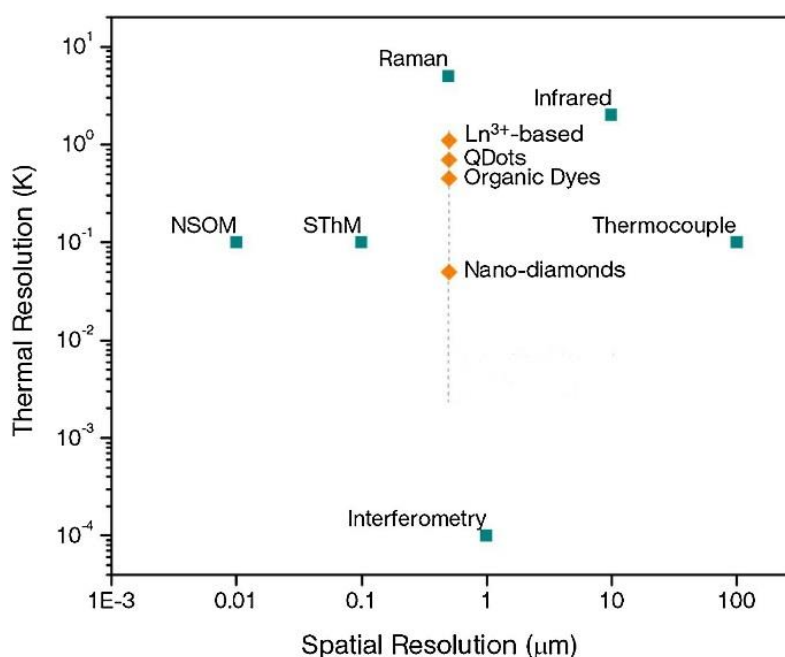


Figure 18. Typical thermal resolution and spatial resolution for various thermometry techniques. Figure extracted from ref^[300]. Note that NSOM: Near-field scanning optical microscopy, SThM: Scanning Thermal Microscopy.

In contrast, photothermal therapy demands fast and precise thermal control in real-time. By modifying the therapy actuation conditions, the local temperature should be finely adjusted during a small effective hyperthermia temperature range (43 °C- 48 °C). In addition, to trigger tumour cell death by the apoptotic pathway instead of cell necrosis

with the undesirable side effects, moderate temperature increases within a safe range is extremely necessary. Generally, for photothermal therapy, good temperature sensitivity (at the order of 0.1 °C) and fast thermal equilibrium are essential. Owing to the radiative temperature distribution centred at the nanoagents, a high spatial resolution ($\sim\mu\text{m}$) of temperature detection is also needed to visualize and control the whole heating volume.

As shown in Figure 18,^[300] traditional thermometers, such as calorimeters,^[301,302] or IR detectors show poor spatial and temporal resolution, and they are not applicable for current biological applications at subcellular level. Thermocouples are invasive and not suitable for mapping temperature with high spatial resolution. For biological thermometry applications, novel nanothermometers based on nanomaterials, such as fluorophores, up-converting nanoparticles, Au nanoparticles, carbon-based nanomaterials and quantum dots, are raising a wide interests.^[300,303-307] By exploiting the versatile properties of nanomaterials, nanothermometers based on different mechanisms have been proposed.

3.2.1 Luminescence nanothermometry

Luminescence is the emission of light from a material when it experiences an electronic transition followed by radiative relaxation. Due to its strong susceptibility to the local temperature, luminescent fluorophores and nanomaterials can be exploited for temperature detection. There are many luminescence parameters that can be employed to develop nanothermometers, such as the intensity, band-shape, polarization and lifetime. According to the different correlation with the temperature, these nanothermometers show distinct characteristics.^[303,308]

Luminescence intensity nanothermometry is based on the thermally induced luminescence quenching or the non-radiative relaxation enhancement with temperature. It is a simple and popular nanothermometry method. However, its application is rather restricted due to concentration variation artefacts. Therefore, concentration independent thermometers are preferable. **Band-shape nanothermometry** detects the relative intensity variations of different emission bands in response to the temperature changes. By correlating the intensity ratios of different bands with temperature, ratiometric nanothermometers can be developed. Moreover, the polarization state of the luminescence can be a highly sensitive temperature indicator. **Polarization**

nanothermometry is based on the anisotropy of the luminescence polarization and its temperature dependence due to the variations of the emitter Brownian motion when the temperature changes. Polarization luminescence nanothermometry is concentration independent and shows high temperature sensitivity in the biological temperature range (20- 50 °C),^[309] thus gaining biomedical interest. Finally, **luminescence lifetime** is another parameter that is strongly influenced by temperature.

Nevertheless, there are still several drawbacks that should be addressed in luminescent nanothermometers. For example, organic fluorophores suffer from photobleaching and their stability under heat and light irradiation should be improved. This can be improved with quantum dots whose tuneable excitation and emission bands are interesting for luminescence nanothermometers. In particular, the linear temperature response of the emission intensity is valuable for thermal sensing.^[310,311] However, quantum dots exhibit blinking problems,^[312,313] in addition to potential long-term cytotoxicity and relatively low thermal sensitivity. Up-converting nanoparticles are popular for thermal sensing by exploiting some intrinsic advantages, which include zero background due to the anti-stokes shift^[314] and ratiometric readout based on the intensity ratios between multiple emission bands. However, they require laborious preparation process and fine optimization of size and composition, their quantum yields needed to be largely improved, and the required rare earth materials have high cost and potential toxicity. In addition, luminescent nanothermometers working in the NIR biological window should be further developed to maximize the probing depth.^[315-318] Finally, luminescence nanothermometry requires complex and expensive optical detection tools.

3.2.2 Bioimaging based nanothermometry

Apart from the direct measurement by thermal nanoprobess, bioimaging methods based on the thermal responses under ultrasound or electromagnetic radiation (X-ray, light and magnetic field) can be employed for temperature detection. With the assistance of bioimaging tools, the presence of photo-absorbers could be identified in advance, and the temperature variations could be monitored in real-time. **Ultrasound thermometry**^[319,320] is based on the linear changes of ultrasound propagating properties in response to local thermal effects. In order to enhance the ultrasound signal, contrast agents with high ultrasonic attenuation coefficient are commonly involved. Ultrasound

thermometry exhibits unlimited penetration depth, but low temperature sensitivity, and therefore it is not suitable for photothermal therapy. **X-ray computed tomography**^[321] can be employed to visualize thermally induced density changes to infer the temperature variations. However, likewise ultrasounds, the sensitivity of CT thermometry is low, and there are safety concerns related to the X-ray exposure.

Photoacoustic (PA) nanothermometry^[105,322] based on the photoacoustic effects produced by pulsed photothermal heating is a new method for temperature sensing. It is a hybrid modality merging optical and ultrasound imaging. By checking the dimensionless Grueneisen coefficient, which is a function of the thermal expansion coefficient and significantly depends on the temperature, it is possible to obtain the specific temperature value.^[323] PA nanothermometry can be ideally combined with photothermal treatment, thereby simplifying the therapeutic setup. More advantages, such as rapid and high temperature sensitivity, large penetration depth and wide dynamic range endow promising features for future thermal sensing applications. However, the spatial resolution (~mm) of PA nanothermometry is still low to achieve precise temperature control at the nanoscale or microscale. Moreover, the translational applications of PA faces many challenges related to the high requirements of the actuation and detection system, such as expensive pulsed lasers, high acquisition speed, highly sensitive detectors and low capability for real-time recording.

Magnetic resonance imaging is also feasible for local thermometry^[324,325] based on the temperature dependence of: T_1/T_2 relaxation times, diffusion coefficient, magnetization or proton resonant frequency. Due to the higher temperature sensitivity and linear temperature dependence, proton resonant frequency based nanothermometry is the preferred choice for *in-vivo* applications.^[326,327] It is the only FDA approved method for temperature measurement in thermal therapies.^[328,329] However, the drawbacks of magnetic resonance imaging thermometry are also clear. Slow response time, low spatial resolution and expensive facilities limit the accessibility for common treatments.

3.3 Magnetic nanotherapy

Although photothermal treatments with nanoparticles are promising for local nanotherapies with high efficacy and minimal side effects, they still need to be improved

for efficient cancer eradication, especially in solid tumours, due to the limited light penetration and low nanoparticle delivery efficiency. Magnetically responsive nanostructures could help in addressing these major drawbacks to achieve higher level of control on the therapeutic effects. By exploiting the magnetic actuation, magnetic nanostructures could travel across biological barriers, penetrate into deep locations and target the site of action. This active navigation process can be tracked and regulated with the aid of magnetic resonance imaging. In addition to the delivery improvement, the therapeutic efficacy could also be enhanced by other magnetic assistances, such as magnetic concentration, magnetic hyperthermia and magneto-mechanical effects. These capabilities are based on the following actuation mechanisms.

3.3.1 Magnetic actuation mechanisms

The magnetic field actuation on nanoparticles exhibits many advantages including remote wireless control, non-invasiveness, unlimited penetration, no power attenuation and minimal side effects. It is thus significant to analyse how magnetic nanostructures can be actuated under external magnetic fields and employed as nanotherapeutic tools.

Different magnetic field amplitude and frequency trigger distinct magnetic responses on nanoparticles (Table 6).^[330] Firstly, a uniform magnetic field exerts magnetic torque (T_{NP}) on the magnetic nanoparticles that tend to align their magnetization parallel to the field:

$$T_{NP} = (V_{NP}M_{NP}) \times B \quad (5)$$

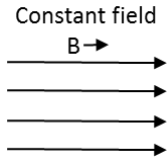
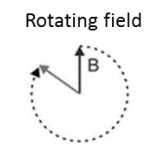

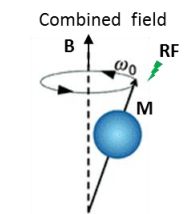
, where B is the magnetic induction, V_{NP} is the volume of the magnetic nanoparticle and M_{NP} is the volumetric magnetization. The magnetic torque is exerted until the nanoparticle M_{NP} is collinear with B . Therefore, when the magnetic field slowly changes its direction, the nanoparticle will correspondingly follow this change.

On the other hand, a static but spatially inhomogeneous magnetic field can induce the translational motion of magnetic nanoparticles towards the strongest field due to the generation of magnetophoretic forces F_m , which can be described as:

$$F_m = V_{NP} (M_{NP}\nabla)B \quad (6)$$

, where $M_{NP}\nabla = M_{NP}(\partial/\partial x)$ represents the magnetic dipole moment in the x direction when exposed to a magnetic field gradient (dB/dx).^[331]

Table 6. Summary of magnetic actuation methods.

Field type		Actuation mechanism	Bioapplications
Uniform magnetic field	Constant field 	Magnetic torque	Magnetic alignment
	Magnetic field gradient		
Alternating magnetic fields (low frequency)	Rotating field 	Magnetic torque	Magnetic nanomotor, magneto-mechanical therapy
Alternating magnetic fields (high frequency)	Oscillating field 	Néel relaxation/ Brownian relaxation/ Hysteresis loss	Magnetic hyperthermia
Superimposed magnetic field	Combined field 	Nuclear magnetic resonance, magnetization relaxation	MRI

In contrast, **alternating magnetic fields** trigger a complex actuation on the nanoparticles, which is highly dependent on the amplitude and frequency of the field. With low amplitude and low frequency, rotating or oscillating magnetic fields generate a continuously alternating magnetic torque that triggers the physical rotation or flipping of the nanoparticles. Conversely, under high amplitude and frequency magnetic field, magnetic heating could be induced by the combination of spin friction of the magnetic

moment (Néel relaxation), physical rotation of nanoparticles (Brownian relaxation), or reconstruction of domain walls (Hysteresis loss). As observed in Table 6, the different magnetic actuation methods enable the development of diverse nanotherapeutic applications that we discuss below.

Finally, an **ultrahigh and uniform magnetic field** combined with **orthogonal RF pulses** is employed to generate the nuclear magnetic resonance in different atoms, and particularly in hydrogen, by inducing the precession of the nuclear magnetic momentum, which is the basis for the widely extended magnetic resonance imaging. Three different imaging modalities can be distinguished: proton-density-weighted, T_1 spin-lattice relaxation or T_2 spin-spin relaxation weighted imaging. They enable 3D imaging of the whole body with high contrast because of the widespread distribution of protons and their distinct distribution in biological tissues.

3.3.2 Magnetically actuated nanotherapy

- **Magnetically guided drug delivery**

Guided by magnetophoretic forces, magnetic nanocarriers can be remotely actuated, controlled and concentrated at the tumour sites to improve the low efficacy of passive delivery. Efficient magnetic guidance imposes several requirements for both magnetic nanocarriers and magnetic field.^[332] The nanocarriers should possess high magnetization, high loading efficiency, low coercivity, moderate size (10- 200 nm) and good biocompatibility to achieve high delivery efficiency while being biologically safe. However, it is very difficult to simultaneously acquire high magnetization nanoparticles and good colloidal stability due to the strong magnetic dipole-dipole interactions, which leads to particle aggregation. Superparamagnetic iron oxides with zero magnetic remanence are preferred as drug carriers owing to their intrinsic stability under magnetic field, but their small size (< 20 nm) and low magnetization considerably reduce the possibility to achieve high drug loading and efficient actuation.

Accurate and intense magnetic guidance also requires adequate magnetic fields with precise gradient distribution in 3D space for a well-controlled delivery process. However, the fast decay of field with the distance from the magnet makes it rather difficult to acquire strong enough magnetic force for remote manipulation. To address this problem, some studies proposed surgical implantation of internal magnets in the

vicinity of the targeted tissue to avoid the field decaying effects of external magnets, thereby enhancing the magnetic targeting efficiency, but at the cost of the high invasiveness and medical risks.^[333,334]

Although many promising preclinical results of magnetic drug delivery have been shown since the first trial was conducted in 1970s,^[335] few magnetic carriers have been approved for clinical use due to their insufficient *in vivo* efficiency. Therefore, research on new nanomaterials and *in vivo* delivering process should be conducted.

- **Magnetic hyperthermia**

As already mentioned above, magnetic nanomaterials are able to act as magnetic energy harvesters under alternating magnetic field with high amplitude and frequency, to induce local magnetic hyperthermia (MHT). Magnetic hyperthermia nanotherapy effects, generated via Néel relaxation, Brownian relaxation and hysteresis loss, can be quantitatively evaluated by the specific absorption rate (SAR) coefficient. SAR is commonly determined as the power absorption per unit mass of iron (W/g):

$$SAR = \frac{C_{water}m_s}{m_{Fe}} \frac{dT}{dt} \quad (7)$$

, where C_{water} is the specific heat capacity of the sample, m_s is the total mass of the sample, m_{Fe} is the iron mass in the sample. The value of dT/dt is extracted by calculating the initial slope of the temperature variation curve.

The SAR value strongly depends on the applied magnetic field conditions (frequency (f) and amplitude (H)), hysteresis loop area, magnetic anisotropy, size and aggregation degree of the magnetic nanomaterials.^[336] Due to limitations in the applicable magnetic field imposed by safety reasons ($f \cdot H < 5 \times 10^9 \text{ Am}^{-1}\text{s}^{-1}$),^[337] magnetic hyperthermia nanotherapy requires carefully optimizing the magnetic nanomaterials, which is still unclear as a result of the complex interplay between the heating mechanisms.

Magneto hyperthermia nanotherapy as a single therapy modality is still restricted due to the rather low magnetic heating efficiency of the magnetic nanomaterials, thereby imposing very high nanomaterial dosage and unsafe magnetic fields.^[338] Alternatively, magnetic hyperthermia nanotherapy can be used for magnetically triggered drug

delivery by combining magnetic and thermally responsive materials.^[339] Taking advantage of the magnetic heating of nanoparticles, efficient drug release could be externally triggered. Some relevant studies have been summarized and listed in Table 7.

Table 7. Magnetic hyperthermia (MHT) triggered drug release.

Year	Sample	Size (nm)	Magnetic field	Improvement
2013 ^[340]	MNP/DOX_nanofibers		166 kHz/ 480A/ 362 W	MHT induces 'on' and 'off' switches DOX release
2014 ^[341]	Fe ₃ O ₄ /DOX NPs	70	230 kHz/ 8 kA m ⁻¹	SAR (487W/g) compared with Resovist (236 W/g)
2010 ^[342]	FA-CD-SPIONs	12,4	230 kHz/ 100 Oe	SAR (132W/g)
2013 ^[343]	Iron oxide NPs	13	332.5 kHz/ 11.3 kAm ⁻¹	SAR (49W/g)
2010 ^[344]	Zinc-doped iron oxide nanocrystals	40,63	500 kHz/ 37.4 kAm ⁻¹	50 °C of 1 mL dispersion; 1 min MHT caused 40% release of rhodamine B dye

Abbreviation: MNP (Magnetic nanoparticles), SPIONs (superparamagnetic iron oxides).

- **Magneto-mechanical nanotherapies**

Unlike magnetic hyperthermia, which works under high strength (tens of mT) and frequency (> 100 kHz) magnetic fields, magneto-mechanical nanotherapy can be more efficiently activated with low field strength (few mT) and frequencies of few tens of Hzs. In these conditions, the magnetic nanostructures can rotate by the induced magnetic torque. The generated magneto-mechanical effects can affect the cell-membrane integrity, promote cell rupture, break down cellular constructs and signalling pathways, thereby inducing apoptotic or necrotic cell deaths.^[345] A significant example was showed by Novosad and co-workers, who successfully fabricated colloiddally-stable magnetic-vortex permalloy microdiscs (thickness 60 nm, diameter 1 μm) with a 5 nm thick gold coating.^[346] The *in vitro* tests showed 90% cell death after 10-min exposure to a low amplitude (9 mT) and low frequency (10- 20 Hz) magnetic field. Magneto-mechanical nanotherapy exhibits lower particle concentration and field dependence than magnetic hyperthermia nanotherapy, and can show higher therapeutic efficiency.

Although magneto-mechanical nanotherapy seems a facile alternative for efficient tumour eradication, some insufficiencies and contradictory requirements should be

highlighted. Efficient magneto-mechanical nanotherapy requires large magnetic torque for manipulation, and large particle sizes for amplified destruction. Therefore, micron-sized magnetic microstructures with high magnetization are needed. However, from the biological perspective, micron-size particles will be fast removed from blood and will retain very low delivery efficiency. Moreover, the high magnetization could induce magnetic agglomeration that hampers the rotation dynamics of the microstructures. To avoid this problem, structures with magnetic vortex have been fabricated to simultaneously show high saturation magnetization^[347] and low magnetic remanence for achieving high magnetic manipulation capacity and colloidal stability. But still intense efforts for cutting down the structure size while keeping spin vortex arrangement should be made. In addition, as the efficiency of the magneto-mechanical therapy is closely related the rotation dynamics of magnetic nanostructures, the complicated biological environment with high rotation impedance should be considered in *in vivo* applications. Finally, similar with other nanotherapies, specific targeting of tumour sites has also to be improved.

3.3.3 Magnetically enhanced phototherapies

Nowadays, combined synergistic nanotherapies are becoming a popular trend to integrate the advantages and to avoid the insufficiencies of different therapeutic modalities. Based on the promising theranostic features, compatibility and external actuation capabilities, magnetic therapies and phototherapies could be directly combined to achieve synergistic effects. Therefore, to end this introduction we will analyse currently emerging nanotherapeutic tools that combine magnetic and optical actuations to achieve better control and higher efficacy by overcoming their separated limitations.

- **Magnetically enriched phototherapies**

Phototherapies suffer from low *in vivo* efficiency due to the low concentration of the passively delivered nanoagents and the limited light dose in deep tissues. Inspired by the magnetic guidance of nanomaterials under magnetic field gradients, phototherapy nanoagents with magnetic properties could be guided to the site of action to locally increase the concentration to develop magnetically enriched phototherapies.

Table 8. Examples of magnetically enriched photothermal heating.

Year	Sample	Size (nm)	Laser λ (nm)	PTT efficiency (%)	Improvement
2015 ^[348]	IONP_Au nanopopcorns	158	808	61	<i>In vitro</i> Enhanced PTT+PDT
2015 ^[349]	Fe ₃ O ₄ cluster NPs	200	1064	20,8	<i>In vitro</i> <i>T</i> ₂ -MRI+OCT_enhanced PTT
2012 ^[350]	GO-IONP	(5-10)/ (50-300)	808	-	<i>In vitro</i> <i>T</i> ₂ -MRI_enhanced PTT
2014 ^[351]	ZnFe ₂ O ₄ -rGO	20/ (500-1000)	808	-	<i>In vitro</i> Enhanced PTT
2015 ^[352]	Rattle-type Fe ₃ O ₄ @CuS	146,9	808	15,7	<i>In vitro/in vivo</i> <i>T</i> ₂ -MRI+UCL_enhanced PTT
			1064	19,2	<i>In vitro/in vivo</i> <i>T</i> ₂ -MRI+UCL_enhanced PTT
2016 ^[353]	Cu ₉ S ₅ /mSiO ₂ /Fe ₃ O ₄	~50	980	-	<i>In vitro/in vivo</i> <i>T</i> ₂ -MRI_enhanced PTT
2019 ^[354]	FeCUPs	216	808	47,4	<i>In vitro/in vivo</i> <i>T</i> ₂ -MRI+UCL_enhanced PTT

Abbreviation: IONP (iron oxide NPs), rGO (reduced graphene oxide), FeCUPs (FeC up-converting NPs), OCT (optical coherence tomography), UCL (up-converting luminescence imaging).

Table 8 shows that the introduction of magnetic elements in hybrid nanomaterials endows photothermal nanoagents, not only enhancing *in vitro* and *in vivo* the photothermal hyperthermia efficiency, but also adding magnetic resonance imaging capabilities for non-invasive therapy evaluation. For example, rattle-type Fe₃O₄@CuS photothermal nanoagents show moderate photothermal conversion efficiency around 15.7% and 19.2% under 808 nm and 1064 nm laser illumination.^[352] Enriched by magnetic attraction, the cell survival rate decreased from 63% to 7% under 1064 nm laser irradiation. The *in vivo* magnetic resonance imaging results reconfirmed the increase in the nanoparticles accumulation through magnetic concentration, which subsequently resulted in more efficient tumour inhibition. In another interesting example, upconversion-magnetic nanoagents (FeCUPs) were fabricated to combine luminescence imaging, magnetic resonance imaging and magnetic concentration enhanced photothermal therapy. In the presence of a magnetic field gradient, FeCUPs could be visualized *in vivo* by magnetic resonance imaging and optical imaging concentrated in tumours after magnetic enrichment, and the photothermal therapy efficacy was synergistically enhanced.^[354] Therefore, magnetically actuated nanoagents under an

external magnetic field gradient could help to overcome the biological barriers which are unavoidable in passive delivery to enrich nanoagents at local sites, thereby opening a promising path to improve phototherapies.

- **Synergistic magnetic/optical hyperthermia nanotherapies**

Currently, photothermal therapy with highly efficient nanoagents are eligible for treating superficial skin cancers. However, magnetic nanotherapies are better options for deep located tumours, due to the non-attenuation properties of magnetic field when penetrating through biological tissues, although high nanomaterial concentrations are required to reach the therapeutic level. By integrating magnetic hyperthermia nanotherapy and photothermal therapy, the hyperthermia effects induced by each of them could be superimposed to improve the overall therapy efficiency by reducing the necessary particle concentration and increasing the actuation depth.

Table 9. Combined magnetic hyperthermia (MHT) and photothermal therapy (PTT).

Year	Sample	Size (nm)	Light condition	Magnetic field	Improvement
2016 ^[355]	Iron oxide nanocubes	20	808 nm/ (0,3-2,5) W/cm ²	(320-900) kHz/ 25mT	MHT alone (900 kHz, 25mT), SAR (700-900W/g); MHT+PTT (2.5 W/cm ²), SAR (4850W/g)
2016 ^[356]	Ag/Fe ₃ O ₄ nanoflowers	40/22	442 nm/ (0,13-1,6) W/cm ²	310 kHz/ (10-80) mT	MHT alone (310 kHz, 20mT), SAR (10W/g); MHT+PTT (0.93 W/cm ²), SAR (130W/g)
2018 ^[357]	MNP@PES-Cy7/2-DG	94	808 nm/ 0,75 W/cm ²	200 kHz/ 38 kA m ⁻¹	MHT alone, SAR(704,5W/g); MHT+PTT, SAR (2371,5W/g)

For instance, Wilhelm and co-workers reported a DUAL-mode hyperthermia therapy based on combined magnetic hyperthermia nanotherapy and photothermal therapy by using iron oxide nanocubes as hyperthermia nanoagents.^[355] An ultrahigh combined optical-magnetic SAR value (4850 W/g) was achieved compared to a 2- to 5-fold lower SAR value (700-900 W/g) in magnetic hyperthermia nanotherapy alone. *In vivo* tests show that single-mode treatments (magnetic or laser hyperthermia) enable reduced tumour growth, while DUAL-mode treatment resulted in complete tumour regression with even lower iron dose and tolerable magnetic field strength. Although iron oxides could be employed for triggering magnetic hyperthermia and photothermia

simultaneously, the photothermal heating efficiency is rather limited compared with other photothermal nanoagents, such as plasmonic metal or conjugated polymers nanoparticles, due to their low NIR absorption. Magnetic-optical nanocomposites embedded with light antennas can be used to enhance the NIR absorption and the combined magnetic hyperthermia nanotherapy and photothermal therapy (Table 9). However, taking a closer look at the results from Table 9, it is obvious that photothermal therapy showed dominant contributions to the overall therapeutic effects compared to magnetic hyperthermia nanotherapy, which was corroborated by other studies.^[338,358] Therefore, the synergistic effects of combined magnetic hyperthermia nanotherapy and photothermal therapy are highly dependent on photothermal therapy efficiency of nanomaterials. Nevertheless, the advantages of magnetic hyperthermia nanotherapy, such as remote induction, unlimited penetration, non-invasiveness and desirable biocompatibility will continually encourage the development of optimization studies for more efficient hybrid actuations.

- **Synergistic magneto-mechanical/ photothermal nanotherapies**

Magneto-mechanical nanotherapies^[346,347,359–361] can also be combined with photothermal therapy to achieve even higher therapeutic efficiencies. Chen and co-workers reported colloidally stable hedgehog-like microspheres (diameter 1.5 μm) composed of needle-like Fe_3O_4 nanoparticles with carbon and gold double shells. They exhibited strong magneto-mechanical force of 35.79 pN (400 mT, 3 Hz) combined with promising photothermal conversion efficiency of 30.1% at 808 nm. *In vitro* results showed a large decrease in cell viability when switching from the single therapeutic modality to the dual-modality. The synergistic effects of combined therapy caused complete tumour elimination compared to only tumour growth inhibition under single magneto-mechanical nanotherapy.^[362] Moreover, a multimodal nanotherapy with synergistic effects of magneto-mechanical nanotherapy, photothermal therapy, photodynamic therapy and chemotherapy was explored by Wo and co-workers using core-shell composites (Magnetic nanoparticles/ SiO_2 /graphene quantum dots-DOX).^[363] Significant cell killing efficiency was achieved by the therapeutic combination. The low field requirements of magneto-mechanical nanotherapy and the high therapeutic effects by the combination with optical therapies might provide interesting developments in the near future.

4 Objectives of the Thesis

Cancer treatment is still challenging due to the lack of efficient therapeutic tools. The conventional cancer therapies suffer from high invasiveness, serious side effects, lack of efficacy and high multidrug resistance. The main aim of nanotherapies is confining the local therapeutic effects at the site of action to achieve higher specificity and minimal side effects. However, the low delivery efficiency and subsequent limited therapeutic effects of the therapeutic nanoagents largely restrict their further clinical use. Therefore, there is an urgent need for developing multiparameter-responsive nanomaterials with external actuation capacities to improve the delivery efficiency and to externally control the therapeutic effects.

To achieve these goals, magneto-plasmonic nanomaterials could provide a promising path due to their external and non-invasive multi-actuation capabilities, with synergistic effects for combined nanotherapies. However, merging magnetic and plasmonic nanomaterials together with current bottom-up fabrication methods is highly challenging for highly efficient advanced nanotherapeutic applications.

Therefore, the main objectives of the Thesis are summarized in the following list:

1. Developing a simple, cost-effective, scalable and highly controllable nanofabrication method to merge ferromagnetic and optically responsive nanomaterials for efficient externally controlled therapeutic applications.
2. Achieving highly tunable ferromagnetic nanostructures which are able to merge high colloidal stability, strong magnetic manipulation and efficient optical heating in the near-infrared biological windows.
3. Providing the required physiochemical properties for biomedical applications, such as nontoxicity, biocompatibility, biodegradability, suitable size (10- 200 nm) and easy functionalization.
4. Demonstrating *in-vitro* and *in-vivo* the local therapeutic efficacy of the ferromagnetic-plasmonic nanomaterials in magnetically controlled photothermal therapies.
5. Demonstrating the multimodal imaging capabilities to enable non-invasive

visualization of the nanotherapeutic agents and to monitor their effects.

6. Developing a novel nano-heating/thermometry concept for improving the control in local photothermal therapies.
7. Merging the multi-therapeutic, imaging and sensing capabilities in totally biodegradable ferromagnetic-plasmonic nanocapsules to achieve enhanced opto-magnetic drug delivery and local therapeutic control.

5 Bibliography

- [1] F. Bray, J. Ferlay, I. Soerjomataram, R. L. Siegel, L. A. Torre, A. Jemal, *CA. Cancer J. Clin.* **2018**, *68*, 394.
- [2] B. Jönsson, T. Hofmarcher, P. Lindgren, N. Wilking, *Eur. J. Cancer* **2016**, *66*, 162.
- [3] S. L. Ginn, A. K. Amaya, I. E. Alexander, M. Edelstein, M. R. Abedi, *J. Gene Med.* **2018**, *20*, 1.
- [4] J. R. Brahmer, S. S. Tykodi, L. Q. M. Chow, W.-J. Hwu, S. L. Topalian, P. Hwu, C. G. Drake, L. H. Camacho, J. Kauh, K. Odunsi, H. C. Pitot, O. Hamid, S. Bhatia, R. Martins, K. Eaton, S. Chen, T. M. Salay, S. Alaparthi, J. F. Grosso, A. J. Korman, S. M. Parker, S. Agrawal, S. M. Goldberg, D. M. Pardoll, A. Gupta, J. M. Wigginton, *N. Engl. J. Med.* **2012**, *366*, 2455.
- [5] D. W. Lee, J. N. Kochenderfer, M. Stetler-Stevenson, Y. K. Cui, C. Delbrook, S. A. Feldman, T. J. Fry, R. Orentas, M. Sabatino, N. N. Shah, S. M. Steinberg, D. Stroncek, N. Tschernia, C. Yuan, H. Zhang, L. Zhang, S. A. Rosenberg, A. S. Wayne, C. L. Mackall, *Lancet* **2015**, *385*, 517.
- [6] O. Hamid, C. Robert, A. Daud, F. S. Hodi, W.-J. Hwu, R. Kefford, J. D. Wolchok, P. Hersey, R. W. Joseph, J. S. Weber, R. Dronca, T. C. Gangadhar, A. Patnaik, H. Zarour, A. M. Joshua, K. Gergich, J. Ellassaiss-Schaap, A. Algazi, C. Mateus, P. Boasberg, P. C. Tumei, B. Chmielowski, S. W. Ebbinghaus, X. N. Li, S. P. Kang, A. Ribas, *N. Engl. J. Med.* **2013**, *369*, 134.
- [7] A. Snyder, V. Makarov, T. Merghoub, J. Yuan, J. M. Zaretsky, A. Desrichard, L. A. Walsh, M. A. Postow, P. Wong, T. S. Ho, T. J. Hollmann, C. Bruggeman, K. Kannan, Y. Li, C. Elipenahli, C. Liu, C. T. Harbison, L. Wang, A. Ribas, J. D. Wolchok, T. A. Chan, *N. Engl. J. Med.* **2014**, *371*, 2189.
- [8] A. P. Castano, T. N. Demidova, M. R. Hamblin, *Photodiagnosis Photodyn. Ther.* **2004**, *1*, 279.
- [9] R. Bonnett, *Chem. Soc. Rev.* **1995**, *24*, 19.
- [10] S. Yano, S. Hirohara, M. Obata, Y. Hagiya, S. ichiro Ogura, A. Ikeda, H. Kataoka, M. Tanaka, T. Joh, *J. Photochem. Photobiol. C Photochem. Rev.* **2011**, *12*, 46.
- [11] S. O. Gollnick, B. Owczarczak, P. Maier, *Lasers Surg. Med.* **2006**, *38*, 509.
- [12] C. A. Robertson, D. H. Evans, H. Abrahamse, *J. Photochem. Photobiol. B Biol.* **2009**, *96*, 1.
- [13] J. MOAN, K. BERG, *Photochem. Photobiol.* **1991**, *53*, 549.
- [14] R. W. Redmond, I. E. Kochevar, *Photochem. Photobiol.* **2006**, *82*, 1178.
- [15] M. Niedre, M. S. Patterson, B. C. Wilson, *Photochem. Photobiol.* **2010**, *75*, 382.
- [16] J. Zhang, C. Jiang, J. P. Figueiró Longo, R. B. Azevedo, H. Zhang, L. A. Muehlmann, *Acta Pharm. Sin. B* **2018**, *8*, 137.
- [17] S. S. Lucky, K. C. Soo, Y. Zhang, *Chem. Rev.* **2015**, *115*, 1990.
- [18] H. Abrahamse, M. R. Hamblin, *Biochem. J.* **2016**, *473*, 347.
- [19] A. E. O'Connor, W. M. Gallagher, A. T. Byrne, *Photochem. Photobiol.* **2009**, *85*, 1053.
- [20] D. K. Chatterjee, L. S. Fong, Y. Zhang, *Adv. Drug Deliv. Rev.* **2008**, *60*, 1627.
- [21] S. Luo, E. Zhang, Y. Su, T. Cheng, C. Shi, *Biomaterials* **2011**, *32*, 7127.
- [22] S. L. Jacques, *Phys. Med. Biol.* **2013**, *58*, 5007.
- [23] K. Ogawa, Y. Kobuke, *Anticancer. Agents Med. Chem.* **2008**, *8*, 269.
- [24] D. Jaque, L. Martínez Maestro, B. del Rosal, P. Haro-Gonzalez, A. Benayas, J. L. Plaza, E. Martín Rodríguez, J. García Solé, *Nanoscale* **2014**, *6*, 9494.
- [25] H. I. Bicher, F. W. Hetzel, T. S. Sandhu, S. Frinak, P. Vaupel, M. D. O'Hara, T. O'Brien, *Radiology* **2014**, *137*, 523.
- [26] I. Mellal, A. Oukaira, E. Kengene, A. Lakhssassi, *Int. J. Appl. Sci. - Res. Rev.* **2017**, *04*, 1.
- [27] C. J. Diederich, *Int. J. Hyperth.* **2005**, *21*, 745.

- [28] W. C. Dewey, L. E. Hopwood, S. A. Sapareto, L. E. Gerweck, *Radiology* **2014**, *123*, 463.
- [29] M. Urano, M. Kuroda, Y. Nishimura, *Int. J. Hyperth.* **1999**, *15*, 79.
- [30] H. G. Streffer C, Vaupel P, *Biological Basis of Oncologic Thermootherapy*, Springer Berlin Heidelberg, Berlin, Heidelberg, **1990**.
- [31] B. Emami, C. W. Song, *Int. J. Radiat. Oncol.* **1984**, *10*, 289.
- [32] S. A. Sapareto, W. C. Dewey, *Int. J. Radiat. Oncol.* **1984**, *10*, 787.
- [33] C. A. Cain, S. I. Umemura, *IEEE Trans. Microw. Theory Tech.* **1986**, *34*, 542.
- [34] J. Mendecki, E. Friedenthal, C. Botstein, R. Paglione, F. Sterzer, *Int. J. Radiat. Oncol.* **1980**, *6*, 1583.
- [35] M. H. Stauffer, P. R., Diederich, C. J., Seegenschmiedt, *Thermoradiotherapy and Thermochemotherapy*, Springer Berlin Heidelberg, Berlin, Heidelberg, **1995**.
- [36] M. Hiraoka, S. Jo, K. Akuta, Y. Nishimura, M. Takahashi, M. Abe, *Cancer* **1987**, *60*, 128.
- [37] J. A. Barreto, W. O'Malley, M. Kubeil, B. Graham, H. Stephan, L. Spiccia, *Adv. Mater.* **2011**, *23*, H18.
- [38] J. W. Nichols, Y. H. Bae, *Nano Today* **2012**, *7*, 606.
- [39] A. Ediriwickrema, W. M. Saltzman, *ACS Biomater. Sci. Eng.* **2015**, *1*, 64.
- [40] I. Brigger, C. Dubernet, P. Couvreur, *Adv. Drug Deliv. Rev.* **2012**, *64*, 24.
- [41] G. J. Kim, S. Nie, *Mater. Today* **2005**, *8*, 28.
- [42] P. Iqbal, J. A. Preece, P. M. Mendes, in *Supramol. Chem.*, John Wiley & Sons, Ltd, Chichester, UK, **2012**.
- [43] A. Care, P. L. Bergquist, A. Sunna, *Trends Biotechnol.* **2015**, *33*, 259.
- [44] N. T. K. Thanh, N. Maclean, S. Mahiddine, *Chem. Rev.* **2014**, *114*, 7610.
- [45] V. K. LaMer, R. H. Dinegar, *J. Am. Chem. Soc.* **1950**, *72*, 4847.
- [46] L. Xu, L. Cheng, C. Wang, R. Peng, Z. Liu, *Polym. Chem.* **2014**, *5*, 1573.
- [47] M. Faraday, *Philos. Trans. R. Soc. London* **1857**, *147*, 145.
- [48] J. Turkevich, P. C. Stevenson, J. Hillier, *Discuss. Faraday Soc.* **1951**, *11*, 55.
- [49] M. Brust, J. Fink, D. Bethell, D. J. Schiffrin, C. Kiely, *J. Chem. Soc. Chem. Commun.* **1995**, 1655.
- [50] N. R. Jana, L. Gearheart, C. J. Murphy, *Adv. Mater.* **2001**, *13*, 1389.
- [51] T. K. Sau, C. J. Murphy, *J. Am. Chem. Soc.* **2004**, *126*, 8648.
- [52] N. Li, P. Zhao, D. Astruc, *Angew. Chemie Int. Ed.* **2014**, *53*, 1756.
- [53] M. Grzelczak, J. Pérez-Juste, P. Mulvaney, L. M. Liz-Marzán, *Chem. Soc. Rev.* **2008**, *37*, 1783.
- [54] P. Pérez-Juste, J., Pastoriza-Santos, I., Liz-Marzán, L.M. and Mulvaney, *Coord. Chem. Rev.* **2005**, *249*, 1870.
- [55] L. M. Liz-Marzán, M. Giersig, P. Mulvaney, *Langmuir* **1996**, *12*, 4329.
- [56] S. E. Skrabalak, J. Chen, Y. Sun, X. Lu, L. Au, C. M. Copley, Y. Xia, *Acc. Chem. Res.* **2008**, *41*, 1587.
- [57] S. P. Chandran, M. Chaudhary, R. Pasricha, A. Ahmad, M. Sastry, *Biotechnol. Prog.* **2006**, *22*, 577.
- [58] S. Balakrishnan, F. A. Bhat, A. Jagadeesan, in *Biomed. Eng. (NY)*, IGI Global, **2018**, pp. 780–808.
- [59] C. M. Copley, J. Chen, E. C. Cho, L. V. Wang, Y. Xia, *Chem. Soc. Rev.* **2011**, *40*, 44.
- [60] L. Dykman, N. Khlebtsov, *Chem. Soc. Rev.* **2012**, *41*, 2256.
- [61] M. Hu, J. Chen, Z.-Y. Li, L. Au, G. V. Hartland, X. Li, M. Marquez, Y. Xia, *Chem. Soc. Rev.* **2006**, *35*, 1084.
- [62] Y.-C. Yeh, B. Creran, V. M. Rotello, *Nanoscale* **2012**, *4*, 1871.
- [63] A.-H. Lu, E. L. Salabas, F. Schüth, *Angew. Chemie Int. Ed.* **2007**, *46*, 1222.

- [64] K. Cho, X. Wang, S. Nie, Z. Chen, D. M. Shin, *Clin. Cancer Res.* **2008**, *14*, 1310.
- [65] T. M. Allen, *Science*. **2004**, *303*, 1818.
- [66] J. B. C. Vasant V. Ranade, *Drug Delivery Systems, Third Edition*, CRC Press, **2011**.
- [67] H. Maeda, *Adv. Drug Deliv. Rev.* **2015**, *91*, 3.
- [68] H. Maeda, *Bioconjug. Chem.* **2010**, *21*, 797.
- [69] H. Maeda, K. Tsukigawa, J. Fang, *Microcirculation* **2016**, *23*, 173.
- [70] A. K. Iyer, G. Khaled, J. Fang, H. Maeda, *Drug Discov. Today* **2006**, *11*, 812.
- [71] V. P. Torchilin, V. G. Omelyanenko, M. I. Papisov, A. A. Bogdanov, V. S. Trubetskoy, J. N. Herron, C. A. Gentry, *Biochim. Biophys. Acta - Biomembr.* **1994**, *1195*, 11.
- [72] S. Moffatt, *MOJ Proteomics Bioinforma.* **2015**, *2*, 27.
- [73] A. N. Lukyanov, V. P. Torchilin, *Adv. Drug Deliv. Rev.* **2004**, *56*, 1273.
- [74] S. M. Moghimi, A. C. Hunter, J. C. Murray, *Long-Circulating and Target-Specific Nanoparticles : Theory to Practice*, American Society For Pharmacology And Experimental Therapeutics, **2001**.
- [75] A. Z. Wang, F. Gu, L. Zhang, J. M. Chan, A. Radovic-Moreno, M. R. Shaikh, O. C. Farokhzad, *Expert Opin. Biol. Ther.* **2008**, *8*, 1063.
- [76] S. D. Perrault, C. Walkey, T. Jennings, H. C. Fischer, W. C. W. Chan, *Nano Lett.* **2009**, *9*, 1909.
- [77] R. Singh, J. W. Lillard, *Exp. Mol. Pathol.* **2009**, *86*, 215.
- [78] M. Juweid, R. Neumann, C. Paik, M. J. Perez-Bacete, J. Sato, W. van Osdol, J. N. Weinstein, *Cancer Res.* **1992**, *52*, 5144.
- [79] S. Ong, H. Liu, C. Pidgeon, *J. Chromatogr. A* **1996**, *728*, 113.
- [80] P. D. W. Eckford, F. J. Sharom, *Chem. Rev.* **2009**, *109*, 2989.
- [81] M. M. Gottesman, *Cancer Res.* **1993**, *53*, 747.
- [82] M. G. Qaddoumi, H. Ueda, J. Yang, J. Davda, V. Labhasetwar, V. H. L. Lee, *Pharm. Res.* **2004**, *21*, 641.
- [83] D. B. Chithrani, M. Dunne, J. Stewart, C. Allen, D. A. Jaffray, *Nanomedicine Nanotechnology, Biol. Med.* **2010**, *6*, 161.
- [84] A. Verma, F. Stellacci, *Small* **2010**, *6*, 12.
- [85] J. Y. Wong, *Science*. **1997**, *275*, 820.
- [86] K. E. Uhrich, S. M. Cannizzaro, R. S. Langer, K. M. Shakesheff, *Chem. Rev.* **1999**, *99*, 3181.
- [87] S. Mura, J. Nicolas, P. Couvreur, *Nat. Mater.* **2013**, *12*, 991.
- [88] J. Blanchard, *J. Am. Chem. Soc.* **1998**, *120*, 4554.
- [89] R. Langer, *Science*. **1990**, *249*, 1527.
- [90] S. Sortino, *J. Mater. Chem.* **2012**, *22*, 301.
- [91] C. Alvarez-Lorenzo, L. Bromberg, A. Concheiro, *Photochem. Photobiol.* **2009**, *85*, 848.
- [92] W. G. Pitt, G. A. Husseini, B. J. Staples, *Expert Opin. Drug Deliv.* **2004**, *1*, 37.
- [93] D. Mertz, O. Sandre, S. Bégin-Colin, *Biochim. Biophys. Acta - Gen. Subj.* **2017**, *1861*, 1617.
- [94] A. Kikuchi, T. Okano, *Adv. Drug Deliv. Rev.* **2002**, *54*, 53.
- [95] L. Zhang, F. Gu, J. Chan, A. Wang, R. Langer, O. Farokhzad, *Clin. Pharmacol. Ther.* **2008**, *83*, 761.
- [96] R. A. Petros, J. M. DeSimone, *Nat. Rev. Drug Discov.* **2010**, *9*, 615.
- [97] J. Beik, Z. Abed, F. S. Ghoreishi, S. Hosseini-Nami, S. Mehrzadi, A. Shakeri-Zadeh, S. K. Kamrava, *J. Control. Release* **2016**, *235*, 205.
- [98] J. W. Hand, C. C. Vernon, M. V. Prior, *Int. J. Hyperth.* **1992**, *8*, 587.

- [99] L. Cheng, C. Wang, Z. Liu, *Chinese J. Clin. Oncol.* **2014**, *41*, 18.
- [100] C. H. Moran, S. M. Wainerdi, T. K. Cherukuri, C. Kittrell, B. J. Wiley, N. W. Nicholas, S. A. Curley, J. S. Kanzius, P. Cherukuri, *Nano Res.* **2009**, *2*, 400.
- [101] Z. Hedayatnasab, F. Abnisa, W. M. A. W. Daud, *Mater. Des.* **2017**, *123*, 174.
- [102] B. A. Kairdolf, A. M. Smith, T. H. Stokes, M. D. Wang, A. N. Young, S. Nie, *Annu. Rev. Anal. Chem.* **2013**, *6*, 143.
- [103] Z. Guo, S. Park, J. Yoon, I. Shin, *Chem. Soc. Rev.* **2014**, *43*, 16.
- [104] H. Ke, S. Tai, L. V. Wang, *J. Biomed. Opt.* **2014**, *19*, 026003.
- [105] J. Shah, S. Park, S. Aglyamov, T. Larson, L. Ma, K. Sokolov, K. Johnston, T. Milner, S. Y. Emelianov, *J. Biomed. Opt.* **2008**, *13*, 034024.
- [106] S. C. Ray, A. Saha, N. R. Jana, R. Sarkar, *J. Phys. Chem. C* **2009**, *113*, 18546.
- [107] U. Hampel, in *Ind. Tomogr.*, Elsevier, **2015**, pp. 175–196.
- [108] A. Fenster, D. B. Downey, H. N. Cardinal, *Phys. Med. Biol.* **2001**, *46*, R67.
- [109] R. K. Hobbie, B. J. Roth, in *Intermed. Phys. Med. Biol.*, Springer International Publishing, Cham, **2015**, pp. 535–565.
- [110] V. M. Ferreira, M. D. Robson, T. D. Karamitsos, M. M. Bissell, D. J. Tyler, S. Neubauer, in *Adv. Card. Imaging*, Elsevier, **2015**, pp. 127–169.
- [111] K. K. Kwong, J. W. Belliveau, D. A. Chesler, I. E. Goldberg, R. M. Weisskoff, B. P. Poncelet, D. N. Kennedy, B. E. Hoppel, M. S. Cohen, R. Turner, *Proc. Natl. Acad. Sci.* **1992**, *89*, 5675.
- [112] S. Ogawa, T. M. Lee, A. R. Kay, D. W. Tank, *Proc. Natl. Acad. Sci.* **1990**, *87*, 9868.
- [113] T. D. Karamitsos, J. M. Francis, S. Myerson, J. B. Selvanayagam, S. Neubauer, *J. Am. Coll. Cardiol.* **2009**, *54*, 1407.
- [114] M. D. Fox, M. E. Raichle, *Nat. Rev. Neurosci.* **2007**, *8*, 700.
- [115] B. R. Smith, S. S. Gambhir, *Chem. Rev.* **2017**, *117*, 901.
- [116] G. Hong, A. L. Antaris, H. Dai, *Nat. Biomed. Eng.* **2017**, *1*, 0010.
- [117] S. Luo, E. Zhang, Y. Su, T. Cheng, C. Shi, *Biomaterials* **2011**, *32*, 7127.
- [118] W. A. Kalender, *Phys. Med. Biol.* **2006**, *51*, R29.
- [119] H. Lusic, M. W. Grinstaff, *Chem. Rev.* **2013**, *113*, 1641.
- [120] J. F. Hainfeld, D. N. Slatkin, T. M. Focella, H. M. Smilowitz, *Br. J. Radiol.* **2006**, *79*, 248.
- [121] G.-P. Yan, L. Robinson, P. Hogg, *Radiography* **2007**, *13*, e5.
- [122] H. Bin Na, I. C. Song, T. Hyeon, *Adv. Mater.* **2009**, *21*, 2133.
- [123] J. Salanitri, S. Tutton, E. E. Dunkle, J. R. Schneider, L. N. Pierchala, P. M. Jacobs, R. R. Edelman, **2007**, *242*, 873.
- [124] W. Li, S. Tutton, A. T. Vu, L. Pierchala, B. S. Y. Li, J. M. Lewis, P. V. Prasad, R. R. Edelman, *J. Magn. Reson. Imaging* **2005**, *21*, 46.
- [125] B. Turkbey, H. K. Agarwal, J. Shih, M. Bernardo, Y. L. McKinney, D. Daar, G. L. Griffiths, S. Sankineni, L. Johnson, K. B. Grant, J. Weaver, S. Rais-Bahrami, M. Harisinghani, P. Jacobs, W. Dahut, M. J. Merino, P. A. Pinto, P. L. Choyke, *Am. J. Roentgenol.* **2015**, *205*, 64.
- [126] H. E. Daldrup-Link, *Radiology* **2017**, *284*, 616.
- [127] S. Wilhelm, A. J. Tavares, Q. Dai, S. Ohta, J. Audet, F. Harold, W. C. W. Chan, *Nat. Rev. Mater.* **2016**, *1*, 1.
- [128] S. Kunjachan, R. Pola, F. Gremse, B. Theek, J. Ehling, D. Moeckel, B. Hermanns-Sachweh, M. Pechar, K. Ulbrich, W. E. Hennink, G. Storm, W. Lederle, F. Kiessling, T. Lammers, *Nano Lett.* **2014**, *14*, 972.
- [129] E. A. Sykes, J. Chen, G. Zheng, W. C. W. Chan, *ACS Nano* **2014**, *8*, 5696.

- [130] R. Li, K. Zheng, C. Yuan, Z. Chen, M. Huang, *Nanotheranostics* **2017**, *1*, 346.
- [131] X. Huang, X. Peng, Y. Wang, Y. Wang, D. M. Shin, M. A. El-Sayed, S. Nie, *ACS Nano* **2010**, *4*, 5887.
- [132] S. Shams, M. Ghazanfari, C. Schmitz-Antoniak, *Nanomaterials* **2019**, *9*, 97.
- [133] R. Vankayala, A. Sagadevan, P. Vijayaraghavan, C.-L. Kuo, K. C. Hwang, *Angew. Chemie Int. Ed.* **2011**, *50*, 10640.
- [134] A. C. S. Samia, X. Chen, C. Burda, *J. Am. Chem. Soc.* **2003**, *125*, 15736.
- [135] X. Huang, I. H. El-Sayed, W. Qian, M. A. El-Sayed, *J. Am. Chem. Soc.* **2006**, *128*, 2115.
- [136] X. Huang, P. K. Jain, I. H. El-Sayed, M. A. El-Sayed, *Lasers Med. Sci.* **2008**, *23*, 217.
- [137] C. Chen, Y. Kuang, L. Hu, *Joule* **2019**, *3*, 683.
- [138] M. Gao, L. Zhu, C. K. Peh, G. W. Ho, *Energy Environ. Sci.* **2019**, *12*, 841.
- [139] G. Baffou, R. Quidant, *Laser Photon. Rev.* **2013**, *7*, 171.
- [140] P. K. Jain, X. Huang, I. H. El-Sayed, M. A. El-Sayed, *Plasmonics* **2007**, *2*, 107.
- [141] J. Wang, Y. Li, L. Deng, N. Wei, Y. Weng, S. Dong, D. Qi, J. Qiu, X. Chen, T. Wu, *Adv. Mater.* **2017**, *29*, 1603730.
- [142] M. Umlauff, J. Hoffmann, H. Kalt, W. Langbein, J. M. Hvam, M. Scholl, J. Söllner, M. Heuken, B. Jobst, D. Hommel, *Phys. Rev. B* **1998**, *57*, 1390.
- [143] G. Hong, S. Diao, A. L. Antaris, H. Dai, *Chem. Rev.* **2015**, *115*, 10816.
- [144] Z. Liu, J. T. Robinson, S. M. Tabakman, K. Yang, H. Dai, *Mater. Today* **2011**, *14*, 316.
- [145] D. A. Hanifi, N. D. Bronstein, B. A. Koscher, Z. Nett, J. K. Swabeck, K. Takano, A. M. Schwartzberg, L. Maserati, K. Vandewal, Y. van de Burgt, A. Salleo, A. P. Alivisatos, *Science*. **2019**, *363*, 1199.
- [146] M. Wang, Z. Hou, A. A. Al Kheraif, B. Xing, J. Lin, *Adv. Healthc. Mater.* **2018**, *7*, 1800351.
- [147] Y. Liu, D. Zhu, Y. Hu, M. T. Swihart, W. Wei, *Langmuir* **2018**, *34*, 13905.
- [148] K. Manthiram, A. P. Alivisatos, *J. Am. Chem. Soc.* **2012**, *134*, 3995.
- [149] Y. W. Chen, Y. L. Su, S. H. Hu, S. Y. Chen, *Adv. Drug Deliv. Rev.* **2016**, *105*, 190.
- [150] H. H. Richardson, Z. N. Hickman, A. O. Govorov, A. C. Thomas, W. Zhang, M. E. Kordesch, *Nano Lett.* **2006**, *6*, 783.
- [151] Z. Qin, J. C. Bischof, *Chem. Soc. Rev.* **2012**, *41*, 1191.
- [152] P. Hernandez, P. J. Tandler, A. O. Govorov, M. T. Carlson, H. H. Richardson, *Nano Lett.* **2009**, *9*, 1139.
- [153] Y. Petit, S. Danto, T. Guérineau, A. Abou Khalil, A. Le Camus, E. Fargin, G. Duchateau, J.-P. Bérubé, R. Vallée, Y. Messadeg, T. Cardinal, L. Canioni, *Adv. Opt. Technol.* **2018**, *7*, 291.
- [154] S. Hashimoto, D. Werner, T. Uwada, *J. Photochem. Photobiol. C Photochem. Rev.* **2012**, *13*, 28.
- [155] R. Anderson, J. Parrish, *Science*. **2006**, *220*, 524.
- [156] C. M. Pitsillides, E. K. Joe, X. Wei, R. R. Anderson, C. P. Lin, *Biophys. J.* **2003**, *84*, 4023.
- [157] V. K. Pustovalov, A. S. Smetannikov, V. P. Zharov, *Laser Phys. Lett.* **2008**, *5*, 775.
- [158] G. Hüttmann, R. Birngruber, *IEEE J. Sel. Top. Quantum Electron.* **1999**, *5*, 954.
- [159] V. P. Zharov, V. Galitovsky, M. Viegas, *Appl. Phys. Lett.* **2003**, *83*, 4897.
- [160] R. R. Letfullin, C. Joenathan, T. F. George, V. P. Zharov, *Nanomedicine* **2006**, *1*, 473.
- [161] D. Lapotko, *Int. J. Heat Mass Transf.* **2009**, *52*, 1540.
- [162] A. Siems, S. A. L. Weber, J. Boneberg, A. Plech, *New J. Phys.* **2011**, *13*, 043018.
- [163] R. Lachaine, É. Boulais, M. Meunier, *ACS Photonics* **2014**, *1*, 331.
- [164] D. Lapotko, *Nanomedicine* **2009**, *4*, 813.

- [165] V. P. Zharov, K. E. Mercer, E. N. Galitovskaya, M. S. Smeltzer, *Biophys. J.* **2006**, *90*, 619.
- [166] D. Werner, S. Hashimoto, T. Uwada, *Langmuir* **2010**, *26*, 9956.
- [167] X. Chen, Y. Chen, M. Yan, M. Qiu, *ACS Nano* **2012**, *6*, 2550.
- [168] A. Plech, V. Kotaidis, S. Grésillon, C. Dahmen, G. Von Plessen, *Phys. Rev. B - Condens. Matter Mater. Phys.* **2004**, *70*, 1.
- [169] D. Werner, A. Furube, T. Okamoto, S. Hashimoto, *J. Phys. Chem. C* **2011**, *115*, 8503.
- [170] T. Nakamura, Y. Mochidzuki, S. Sato, *J. Mater. Res.* **2008**, *23*, 968.
- [171] R. R. Letfullin, C. Joenathan, T. F. George, V. P. Zharov, *Nanomedicine* **2006**, *1*, 473.
- [172] G. Huettmann, B. Radt, J. Serbin, R. Birngruber, in *Ther. Laser Appl. Laser-Tissue Interact.* (Ed.: R.W. Steiner), **2003**, p. 88.
- [173] J. Stehr, C. Hrelescu, R. A. Sperling, G. Raschke, M. Wunderlich, A. Nichtl, D. Heindl, K. Kürzinger, W. J. Parak, T. A. Klar, S. J. Feldmann, *Nano Lett.* **2008**, *8*, 619.
- [174] P. Chakravarty, W. Qian, M. A. El-Sayed, M. R. Prausnitz, *Nat. Nanotechnol.* **2010**, *5*, 607.
- [175] M. Babincová, P. Sourivong, D. Chorvát, P. Babinec, *J. Magn. Magn. Mater.* **1999**, *194*, 163.
- [176] T. S. Troutman, S. J. Leung, M. Romanowski, *Adv. Mater.* **2009**, *21*, 2334.
- [177] A. S. B. Breaking, N. R. Branda, **2010**, *4*, 6395.
- [178] A. Kyrsting, P. M. Bendix, D. G. Stamou, L. B. Oddershede, *Nano Lett.* **2011**, *11*, 888.
- [179] S. Link, M. A. El-Sayed, *Int. Rev. Phys. Chem.* **2000**, *19*, 409.
- [180] M. Hu, G. V Hartland, *J. Phys. Chem. B* **2003**, *107*, 1284.
- [181] X. Huang, B. Kang, W. Qian, M. A. Mackey, P. C. Chen, A. K. Oyelere, I. H. El-Sayed, M. A. El-Sayed, *J. Biomed. Opt.* **2010**, *15*, 058002.
- [182] S. A. Sapareto, W. C. Dewey, *Int. J. Radiat. Oncol. Biol. Phys.* **1984**, *10*, 787.
- [183] S. J. Martin, C. M. Henry, S. P. Cullen, *Mol. Cell* **2012**, *46*, 387.
- [184] J. R. Melamed, R. S. Edelstein, E. S. Day, *ACS Nano* **2015**, *9*, 6.
- [185] D. K. Roper, W. Ahn, M. Hoepfner, *J. Phys. Chem. C* **2007**, *111*, 3636.
- [186] K. Jiang, D. A. Smith, A. Pinchuk, *J. Phys. Chem. C* **2013**, *117*, 27073.
- [187] H. Chen, L. Shao, T. Ming, Z. Sun, C. Zhao, B. Yang, J. Wang, *Small* **2010**, *6*, 2272.
- [188] H. H. Richardson, M. T. Carlson, P. J. Tandler, P. Hernandez, A. O. Govorov, *Nano Lett.* **2009**, *9*, 1139.
- [189] X. Huang, M. A. El-Sayed, *J. Adv. Res.* **2010**, *1*, 13.
- [190] V. P. Zharov, K. E. Mercer, E. N. Galitovskaya, M. S. Smeltzer, *Biophys. J.* **2006**, *90*, 619.
- [191] S. Boca-Farcau, M. Potara, T. Simon, A. Juhem, P. Baldeck, S. Astilean, *Mol. Pharm.* **2014**, *11*, 391.
- [192] X. Huang, S. Tang, X. Mu, Y. Dai, G. Chen, Z. Zhou, F. Ruan, Z. Yang, N. Zheng, *Nat. Nanotechnol.* **2011**, *6*, 28.
- [193] X.-M. Zhu, H.-Y. Wan, H. Jia, L. Liu, J. Wang, *Adv. Healthc. Mater.* **2016**, *5*, 3165.
- [194] K.-C. Li, H.-C. Chu, Y. Lin, H.-Y. Tuan, Y.-C. Hu, *ACS Appl. Mater. Interfaces* **2016**, *8*, 12082.
- [195] S. Link, C. Burda, M. B. Mohamed, B. Nikoobakht, M. A. El-Sayed, *J. Phys. Chem. A* **2002**, *103*, 1165.
- [196] P. Zhang, J. Wang, H. Huang, K. Qiu, J. Huang, L. Ji, H. Chao, *J. Mater. Chem. B* **2017**, *5*, 671.
- [197] X. Huang, S. Tang, B. Liu, B. Ren, N. Zheng, *Adv. Mater.* **2011**, *23*, 3420.
- [198] M. Zheng, Y. Li, S. Liu, W. Wang, Z. Xie, X. Jing, *ACS Appl. Mater. Interfaces* **2016**, *8*, 23533.
- [199] J. Ge, Q. Jia, W. Liu, L. Guo, Q. Liu, M. Lan, H. Zhang, X. Meng, P. Wang, *Adv. Mater.* **2015**, *27*, 4169.

- [200] N. W. Shi Kam, M. O'Connell, J. A. Wisdom, H. Dai, *Proc. Natl. Acad. Sci.* **2005**, *102*, 11600.
- [201] P. Chakravarty, R. Marches, N. S. Zimmerman, A. D.-E. Swafford, P. Bajaj, I. H. Musselman, P. Pantano, R. K. Draper, E. S. Vitetta, *Proc. Natl. Acad. Sci.* **2008**, *105*, 8697.
- [202] L. J. Carlson, T. D. Krauss, *Acc. Chem. Res.* **2008**, *41*, 235.
- [203] J. Zhou, J. Li, D. Wu, C. Hong, in *Adv. Bioinspired Biomed. Mater. Vol. 2*, **2017**, pp. 169–192.
- [204] S. Ghosh, S. Dutta, E. Gomes, D. Carroll, R. D'Agostino, J. Olson, M. Guthold, W. H. Gmeiner, *ACS Nano* **2009**, *3*, 2667.
- [205] J. W. Fisher, S. Sarkar, C. F. Buchanan, C. S. Szot, J. Whitney, H. C. Hatcher, S. V. Torti, C. G. Rylander, M. N. Rylander, *Cancer Res.* **2010**, *70*, 9855.
- [206] O. Akhavan, E. Ghaderi, *Small* **2013**, *9*, 3593.
- [207] Y. Xuan, R.-Y. Zhang, X.-S. Zhang, J. An, K. Cheng, C. Li, X.-L. Hou, Y.-D. Zhao, *Nanotechnology* **2018**, *29*, 355101.
- [208] M. Sinha, G. Gollavelli, Y.-C. Ling, *RSC Adv.* **2016**, *6*, 63859.
- [209] V. Krishna, A. Singh, P. Sharma, N. Iwakuma, Q. Wang, Q. Zhang, J. Knapik, H. Jiang, S. R. Grobmyer, B. Koopman, B. Moudgil, *Small* **2010**, *6*, 2236.
- [210] S. Hsu, K. On, A. R. Tao, *J. Am. Chem. Soc.* **2011**, *133*, 19072.
- [211] Y. Zhao, H. Pan, Y. Lou, X. Qiu, J. Zhu, C. Burda, *J. Am. Chem. Soc.* **2009**, *131*, 4253.
- [212] M. Liu, X. Xue, C. Ghosh, X. Liu, Y. Liu, E. P. Furlani, M. T. Swihart, P. N. Prasad, *Chem. Mater.* **2015**, *27*, 2584.
- [213] A. Comin, L. Manna, *Chem. Soc. Rev.* **2014**, *43*, 3957.
- [214] Y. Xie, A. Riedinger, M. Prato, A. Casu, A. Genovese, P. Guardia, S. Sottini, C. Sangregorio, K. Miszta, S. Ghosh, T. Pellegrino, L. Manna, *J. Am. Chem. Soc.* **2013**, *135*, 17630.
- [215] Y. Xie, L. Carbone, C. Nobile, V. Grillo, S. D'Agostino, F. Della Sala, C. Giannini, D. Altamura, C. Oelsner, C. Kryschi, P. D. Cozzoli, *ACS Nano* **2013**, *7*, 7352.
- [216] B. Anasori, M. R. Lukatskaya, Y. Gogotsi, *Nat. Rev. Mater.* **2017**, *2*, 16098.
- [217] M. Naguib, M. Kurtoglu, V. Presser, J. Lu, J. Niu, M. Heon, L. Hultman, Y. Gogotsi, M. W. Barsoum, *Adv. Mater.* **2011**, *23*, 4248.
- [218] F. Shahzad, M. Alhabeab, C. B. Hatter, B. Anasori, S. Man Hong, C. M. Koo, Y. Gogotsi, *Science*. **2016**, *353*, 1137.
- [219] G. Liu, J. Zou, Q. Tang, X. Yang, Y. Zhang, Q. Zhang, W. Huang, P. Chen, J. Shao, X. Dong, *ACS Appl. Mater. Interfaces* **2017**, *9*, 40077.
- [220] N. Chen, Y. He, Y. Su, X. Li, Q. Huang, H. Wang, X. Zhang, R. Tai, C. Fan, *Biomaterials* **2012**, *33*, 1238.
- [221] R. Hardman, *Environ. Health Perspect.* **2006**, *114*, 165.
- [222] Z. Sun, H. Xie, S. Tang, X. Yu, Z. Guo, J. Shao, H. Zhang, H. Huang, H. Wang, P. K. Chu, *Angew. Chemie* **2015**, *127*, 11688.
- [223] M. Wang, Z. Hou, A. A. Al Kheraif, B. Xing, J. Lin, *Adv. Healthc. Mater.* **2018**, *7*, 1800351.
- [224] L. Wen, L. Chen, S. Zheng, J. Zeng, G. Duan, Y. Wang, G. Wang, Z. Chai, Z. Li, M. Gao, *Adv. Mater.* **2016**, *28*, 5072.
- [225] Z. Zhou, B. Kong, C. Yu, X. Shi, M. Wang, W. Liu, Y. Sun, Y. Zhang, H. Yang, S. Yang, *Sci. Rep.* **2015**, *4*, 3653.
- [226] S. Shen, S. Wang, R. Zheng, X. Zhu, X. Jiang, D. Fu, W. Yang, *Biomaterials* **2015**, *39*, 67.
- [227] Z. Zhou, Y. Sun, J. Shen, J. Wei, C. Yu, B. Kong, W. Liu, H. Yang, S. Yang, W. Wang, *Biomaterials* **2014**, *35*, 7470.
- [228] M. E. Sadat, M. Kaveh Baghbador, A. W. Dunn, H. P. Wagner, R. C. Ewing, J. Zhang, H. Xu, G. M. Pauletta, D. B. Mast, D. Shi, *Appl. Phys. Lett.* **2014**, *105*, 091903.

- [229] Y. Lan, Y. Lu, Z. Ren, *Nano Energy* **2013**, *2*, 1031.
- [230] R. Daghrrir, P. Drogui, D. Robert, *Ind. Eng. Chem. Res.* **2013**, *52*, 3581.
- [231] F. Auzel, *Chem. Rev.* **2004**, *104*, 139.
- [232] J. Tang, M. Myers, K. A. Bosnick, L. E. Brus, *J. Phys. Chem. B* **2003**, *107*, 7501.
- [233] A. Pron, P. Rannou, *Prog. Polym. Sci.* **2002**, *27*, 135.
- [234] R. H. Friend, R. W. Gymer, A. B. Holmes, J. H. Burroughes, R. N. Marks, C. Taliani, D. D. C. Bradley, D. A. Dos Santos, J. L. Brédas, M. Lögdlund, W. R. Salaneck, *Nature* **1999**, *397*, 121.
- [235] K. M. Au, M. Chen, S. P. Armes, N. Zheng, *Chem. Commun.* **2013**, *49*, 10525.
- [236] S. Wang, Z. Zhou, G. Yu, N. Lu, Y. Liu, Y. Dai, X. Fu, J. Wang, X. Chen, *ACS Appl. Mater. Interfaces* **2018**, *10*, 28382.
- [237] X. Wang, Y. Ma, X. Sheng, Y. Wang, H. Xu, *Nano Lett.* **2018**, *18*, 2217.
- [238] M. Chen, X. Fang, S. Tang, N. Zheng, *Chem. Commun.* **2012**, *48*, 8934.
- [239] Y. Liu, K. Ai, J. Liu, M. Deng, Y. He, L. Lu, *Adv. Mater.* **2013**, *25*, 1353.
- [240] J. Yang, J. Choi, D. Bang, E. Kim, E. Lim, H. Park, J. Suh, K. Lee, K. Yoo, E. Kim, Y. Huh, S. Haam, *Angew. Chemie Int. Ed.* **2011**, *50*, 441.
- [241] J. Zhou, Z. Lu, X. Zhu, X. Wang, Y. Liao, Z. Ma, F. Li, *Biomaterials* **2013**, *34*, 9584.
- [242] Y. Jiang, J. Li, X. Zhen, C. Xie, K. Pu, *Adv. Mater.* **2018**, *30*, 1705980.
- [243] Y. Jiang, P. K. Upputuri, C. Xie, Z. Zeng, A. Sharma, X. Zhen, J. Li, J. Huang, M. Pramanik, K. Pu, *Adv. Mater.* **2019**, *31*, 1808166.
- [244] S. Luo, E. Zhang, Y. Su, T. Cheng, C. Shi, *Biomaterials* **2011**, *32*, 7127.
- [245] J. O. Escobedo, O. Rusin, S. Lim, R. M. Strongin, *Curr. Opin. Chem. Biol.* **2010**, *14*, 64.
- [246] A. Yuan, J. Wu, X. Tang, L. Zhao, F. Xu, Y. Hu, *J. Pharm. Sci.* **2013**, *102*, 6.
- [247] L. J. Hennings, E. R. Siegel, R. Friedman, M. A. Moreno, G. Shafirstein, W. Ba, J. Webber, C. Jackson, R. J. Griffin, **2012**, *1215*, 1208.
- [248] L. Cheng, W. He, H. Gong, C. Wang, Q. Chen, Z. Cheng, Z. Liu, *Adv. Funct. Mater.* **2013**, *23*, 5893.
- [249] C. Yue, P. Liu, M. Zheng, P. Zhao, Y. Wang, Y. Ma, L. Cai, *Biomaterials* **2013**, *34*, 6853.
- [250] B. Zhou, Y. Li, G. Niu, M. Lan, Q. Jia, Q. Liang, *ACS Appl. Mater. Interfaces* **2016**, *8*, 29899.
- [251] J. Zou, P. Wang, Y. Wang, G. Liu, Y. Zhang, Q. Zhang, J. Shao, W. Si, W. Huang, X. Dong, *Chem. Sci.* **2019**, *10*, 268.
- [252] H. A. Hoffman, L. Chakrabarti, M. F. Dumont, A. D. Sandler, R. Fernandes, *RSC Adv.* **2014**, *4*, 29729.
- [253] Z. Li, Y. Zeng, D. Zhang, M. Wu, L. Wu, A. Huang, H. Yang, X. Liu, J. Liu, *J. Mater. Chem. B* **2014**, *2*, 3686.
- [254] M. Shokouhimehr, E. S. Soehnlén, J. Hao, M. Griswold, C. Flask, X. Fan, J. P. Babilion, S. Basu, S. D. Huang, *J. Mater. Chem.* **2010**, *20*, 5251.
- [255] M. Shokouhimehr, E. S. Soehnlén, A. Khitrin, S. Basu, S. D. Huang, *Inorg. Chem. Commun.* **2010**, *13*, 58.
- [256] Y. Deng, L. Huang, H. Yang, H. Ke, H. He, Z. Guo, T. Yang, A. Zhu, H. Wu, H. Chen, *Small* **2017**, *13*, 1602747.
- [257] F. Zhao, B. Hu, *Sci. Bull.* **2015**, *60*, 279.
- [258] D. Melo-Diogo, C. Pais-Silva, D. R. Dias, A. F. Moreira, I. J. Correia, *Adv. Healthc. Mater.* **2017**, *6*, 1700073.
- [259] H. Chen, L. Shao, T. Ming, Z. Sun, C. Zhao, B. Yang, J. Wang, *Small* **2010**, *6*, 2272.
- [260] R. Jiang, S. Cheng, L. Shao, Q. Ruan, J. Wang, *J. Phys. Chem. C* **2013**, *117*, 8909.

- [261] D. Jaque, L. Martínez Maestro, B. del Rosal, P. Haro-Gonzalez, A. Benayas, J. L. Plaza, E. Martín Rodríguez, J. García Solé, *Nanoscale* **2014**, *6*, 9494.
- [262] D. Jaque, L. Martínez Maestro, B. del Rosal, P. Haro-Gonzalez, A. Benayas, J. L. Plaza, E. Martín Rodríguez, J. García Solé, *Nanoscale* **2014**, *6*, 9494.
- [263] V. P. Pattani, J. W. Tunnell, *Lasers Surg. Med.* **2012**, *44*, 675.
- [264] C. Bi, J. Chen, Y. Chen, Y. Song, A. Li, S. Li, Z. Mao, C. Gao, D. Wang, H. Möhwald, H. Xia, *Chem. Mater.* **2018**, *30*, 2709.
- [265] Z. Liu, L. Cheng, L. Zhang, Z. Yang, Z. Liu, J. Fang, *Biomaterials* **2014**, *35*, 4099.
- [266] Y. Chang, H. Gao, N.-N. Zhang, X. Tao, T. Sun, J. Zhang, Z.-Y. Lu, K. Liu, B. Yang, *Front. Chem.* **2018**, *6*, 1.
- [267] S. Li, L. Zhang, T. Wang, L. Li, C. Wang, Z. Su, *Chem. Commun.* **2015**, *51*, 14338.
- [268] P. Huang, P. Rong, J. Lin, W. Li, X. Yan, M. G. Zhang, L. Nie, G. Niu, J. Lu, W. Wang, X. Chen, *J. Am. Chem. Soc.* **2014**, *136*, 8307.
- [269] T. Liu, J. Conde, T. Lipiński, A. Bednarkiewicz, C. Huang, *NPG Asia Mater.* **2016**, *8*, e295.
- [270] G. Ou, Z. Li, D. Li, L. Cheng, Z. Liu, H. Wu, *Nano Res.* **2016**, *9*, 1236.
- [271] X. Chen, L. Liu, P. Y. Yu, S. S. Mao, *Science*. **2011**, *331*, 746.
- [272] W. Ren, Y. Yan, L. Zeng, Z. Shi, A. Gong, P. Schaaf, D. Wang, J. Zhao, B. Zou, H. Yu, G. Chen, E. M. B. Brown, A. Wu, *Adv. Healthc. Mater.* **2015**, *4*, 1526.
- [273] Z. Chen, Q. Wang, H. Wang, L. Zhang, G. Song, L. Song, J. Hu, H. Wang, J. Liu, M. Zhu, D. Zhao, *Adv. Mater.* **2013**, *25*, 2095.
- [274] E. Salje, B. Güttler, *Philos. Mag. B* **1984**, *50*, 607.
- [275] B. Li, Y. Zhang, R. Zou, Q. Wang, B. Zhang, L. An, F. Yin, Y. Hua, J. Hu, *Dalt. Trans.* **2014**, *43*, 6244.
- [276] Q. Tian, F. Jiang, R. Zou, Q. Liu, Z. Chen, M. Zhu, S. Yang, J. Wang, J. Wang, J. Hu, *ACS Nano* **2011**, *5*, 9761.
- [277] B. Li, Q. Wang, R. Zou, X. Liu, K. Xu, W. Li, J. Hu, *Nanoscale* **2014**, *6*, 3274.
- [278] J. Cui, R. Jiang, S. Xu, G. Hu, L. Wang, *Small* **2015**, *11*, 4183.
- [279] J. Cui, S. Xu, C. Guo, R. Jiang, T. D. James, L. Wang, *Anal. Chem.* **2015**, *87*, 11592.
- [280] G. Hu, T. Xu, X. Chen, D. James, S. Xu, *RSC Adv.* **2016**, *6*, 103930.
- [281] S. M. Gupta, M. Tripathi, *Chinese Sci. Bull.* **2011**, *56*, 1639.
- [282] J. Nam, N. Won, H. Jin, H. Chung, S. Kim, *J. Am. Chem. Soc.* **2009**, *131*, 13639.
- [283] J. He, X. Huang, Y. Li, Y. Liu, T. Babu, M. A. Aronova, S. Wang, Z. Lu, X. Chen, Z. Nie, *J. Am. Chem. Soc.* **2013**, *135*, 7974.
- [284] P. Huang, J. Lin, W. Li, P. Rong, Z. Wang, S. Wang, X. Wang, X. Sun, M. Aronova, G. Niu, R. D. Leapman, Z. Nie, X. Chen, *Angew. Chemie Int. Ed.* **2013**, *52*, 13958.
- [285] P. Wu, D. Deng, J. Gao, C. Cai, *ACS Appl. Mater. Interfaces* **2016**, *8*, 10243.
- [286] D. Li, D. Han, S. Qu, L. Liu, P. Jing, D. Zhou, W. Ji, X. Wang, T.-F. Zhang, D.-Z. Shen, *Light Sci. Appl.* **2016**, *5*, e16120.
- [287] H. Zhu, Y. Wang, C. Chen, M. Ma, J. Zeng, S. Li, Y. Xia, M. Gao, *ACS Nano* **2017**, *11*, 8273.
- [288] M. Ji, M. Xu, W. Zhang, Z. Yang, L. Huang, J. Liu, Y. Zhang, L. Gu, Y. Yu, W. Hao, P. An, L. Zheng, H. Zhu, J. Zhang, *Adv. Mater.* **2016**, *28*, 3094.
- [289] J. Zhang, G. Liu, F. He, L. Chen, Y. Huang, *RSC Adv.* **2015**, *5*, 87903.
- [290] S. Bhana, G. Lin, L. Wang, H. Starring, S. R. Mishra, G. Liu, X. Huang, *ACS Appl. Mater. Interfaces* **2015**, *7*, 11637.
- [291] W. Feng, X. Zhou, W. Nie, L. Chen, K. Qiu, Y. Zhang, C. He, *ACS Appl. Mater. Interfaces* **2015**, *7*, 4354.

- [292] X. Wang, D. Cao, X. Tang, J. Yang, D. Jiang, M. Liu, N. He, Z. Wang, *ACS Appl. Mater. Interfaces* **2016**, *8*, 19321.
- [293] J. Song, F. Wang, X. Yang, B. Ning, M. G. Harp, S. H. Culp, S. Hu, P. Huang, L. Nie, J. Chen, X. Chen, *J. Am. Chem. Soc.* **2016**, *138*, 7005.
- [294] C. J. Jeong, S. M. Sharkar, I. In, S. Y. Park, *ACS Appl. Mater. Interfaces* **2015**, *7*, 9469.
- [295] R. Zheng, S. Wang, Y. Tian, X. Jiang, D. Fu, S. Shen, W. Yang, *ACS Appl. Mater. Interfaces* **2015**, *7*, 15876.
- [296] X. Zhang, X. Xu, T. Li, M. Lin, X. Lin, H. Zhang, H. Sun, B. Yang, *ACS Appl. Mater. Interfaces* **2014**, *6*, 14552.
- [297] C. Wang, J. Bai, Y. Liu, X. Jia, X. Jiang, *ACS Biomater. Sci. Eng.* **2016**, *2*, 2011.
- [298] M. Lin, C. Guo, J. Li, D. Zhou, K. Liu, X. Zhang, T. Xu, H. Zhang, L. Wang, B. Yang, *ACS Appl. Mater. Interfaces* **2014**, *6*, 5860.
- [299] Y. Liu, D. Wang, L. Zhao, M. Lin, H.-Z. Sun, H. Sun, B. Yang, *RSC Adv.* **2016**, *6*, 15854.
- [300] M. Quintanilla, L. M. Liz-Marzán, *Nano Today* **2018**, *19*, 126.
- [301] Y. Feng, Z. Luo, S. Qu, C. Zeng, H. Xu, *Thermochim. Acta* **1997**, *303*, 203.
- [302] H. Böttcher, P. Fürst, *Baillieres. Clin. Endocrinol. Metab.* **1997**, *11*, 739.
- [303] B. del Rosal, E. Ximendes, U. Rocha, D. Jaque, *Adv. Opt. Mater.* **2017**, *5*, 1600508.
- [304] M. Nakano, T. Nagai, *J. Photochem. Photobiol. C Photochem. Rev.* **2017**, *30*, 2.
- [305] C. D. S. Brites, P. P. Lima, N. J. O. Silva, A. Millán, V. S. Amaral, F. Palacio, L. D. Carlos, *Nanoscale* **2012**, *4*, 4799.
- [306] J. Lee, N. A. Kotov, *Nano Today* **2007**, *2*, 48.
- [307] H. Zhou, M. Sharma, O. Berezin, D. Zuckerman, M. Y. Berezin, *ChemPhysChem* **2016**, *17*, 27.
- [308] D. Jaque, F. Vetrone, *Nanoscale* **2012**, *4*, 4301.
- [309] G. Baffou, M. P. Kreuzer, F. Kulzer, R. Quidant, *Opt. Express* **2009**, *17*, 3291.
- [310] B. Han, W. L. Hanson, K. Bensalah, A. Tuncel, J. M. Stern, J. A. Cadeddu, *Ann. Biomed. Eng.* **2009**, *37*, 1230.
- [311] G. W. Walker, V. C. Sundar, C. M. Rudzinski, A. W. Wun, M. G. Bawendi, D. G. Nocera, *Appl. Phys. Lett.* **2003**, *83*, 3555.
- [312] A. L. Efros, M. Rosen, *Phys. Rev. Lett.* **1997**, *78*, 1110.
- [313] M. Nirmal, B. O. Dabbousi, M. G. Bawendi, J. J. Macklin, J. K. Trautman, T. D. Harris, L. E. Brus, *Nature* **1996**, *383*, 802.
- [314] G. Chen, H. Qiu, P. N. Prasad, X. Chen, *Chem. Rev.* **2014**, *114*, 5161.
- [315] I. E. Kolesnikov, E. V. Golyeva, M. A. Kurochkin, E. Lähderanta, M. D. Mikhailov, *Sensors Actuators B Chem.* **2016**, *235*, 287.
- [316] U. Rocha, K. U. Kumar, C. Jacinto, I. Villa, F. Sanz-Rodríguez, M. Del Carmen Iglesias De La Cruz, A. Juarranz, E. Carrasco, F. C. J. M. Van Veggel, E. Bovero, J. G. Solé, D. Jaque, *Small* **2014**, *10*, 1141.
- [317] E. N. Cerón, D. H. Ortgies, B. del Rosal, F. Ren, A. Benayas, F. Vetrone, D. Ma, F. Sanz-Rodríguez, J. G. Solé, D. Jaque, E. M. Rodríguez, *Adv. Mater.* **2015**, *27*, 4781.
- [318] M. Kamimura, T. Matsumoto, S. Suyari, M. Umezawa, K. Soga, *J. Mater. Chem. B* **2017**, *5*, 1917.
- [319] M. A. Lewis, R. M. Staruch, R. Chopra, *Int. J. Hyperth.* **2015**, *31*, 163.
- [320] I. Rivens, A. Shaw, J. Civale, H. Morris, *Int. J. Hyperth.* **2007**, *23*, 121.
- [321] B. G. Fallone, P. R. Moran, E. B. Podgorsak, *Med. Phys.* **1982**, *9*, 715.
- [322] L. Gao, L. Wang, C. Li, Y. Liu, H. Ke, C. Zhang, L. V. Wang, *J. Biomed. Opt.* **2013**, *18*, 026003.

- [323] M. W. Sigrist, *J. Appl. Phys.* **1986**, *60*, R83.
- [324] B. Quesson, J. A. de Zwart, C. T. W. Moonen, *J. Magn. Reson. Imaging* **2000**, *12*, 525.
- [325] V. Rieke, K. Butts Pauly, *J. Magn. Reson. Imaging* **2008**, *27*, 376.
- [326] J. C. Hindman, *J. Chem. Phys.* **2005**, *44*, 4582.
- [327] N. McDannold, *Int. J. Hyperth.* **2005**, *21*, 533.
- [328] US Food and Drug Administration Office of In Vitro Diagnostic Device Evaluation and Safety, *Test, K063841 NMR Profiler and NMR Lipo Profile*, **2008**.
- [329] N. J. Rankin, D. Preiss, P. Welsh, K. E. V. Burgess, S. M. Nelson, D. A. Lawlor, N. Sattar, *Atherosclerosis* **2014**, *237*, 287.
- [330] K. E. Peyer, L. Zhang, B. J. Nelson, *Nanoscale* **2013**, *5*, 1259.
- [331] J. Lim, S. A. Majetich, *Nano Today* **2013**, *8*, 98.
- [332] B. B. Yellen, Z. G. Forbes, D. S. Halverson, G. Fridman, K. A. Barbee, M. Chorny, R. Levy, G. Friedman, *J. Magn. Magn. Mater.* **2005**, *293*, 647.
- [333] A. J. Rosengart, M. D. Kaminski, H. Chen, P. L. Caviness, A. D. Ebner, J. A. Ritter, *J. Magn. Magn. Mater.* **2005**, *293*, 633.
- [334] B. B. Yellen, Z. G. Forbes, D. S. Halverson, G. Fridman, K. A. Barbee, M. Chorny, R. Levy, G. Friedman, *J. Magn. Magn. Mater.* **2005**, *293*, 647.
- [335] K. J. Widder, A. E. Senyei, D. G. Scarpelli, *Exp. Biol. Med.* **1978**, *158*, 141.
- [336] A. E. Deatsch, B. A. Evans, *J. Magn. Magn. Mater.* **2014**, *354*, 163.
- [337] R. Hergt, S. Dutz, *J. Magn. Magn. Mater.* **2007**, *311*, 187.
- [338] A. Espinosa, J. Kolosnjaj-Tabi, A. Abou-Hassan, A. Plan Sangnier, A. Curcio, A. K. A. Silva, R. Di Corato, S. Neveu, T. Pellegrino, L. M. Liz-Marzán, C. Wilhelm, *Adv. Funct. Mater.* **2018**, *28*, 1803660.
- [339] C. S. Brazel, *Pharm. Res.* **2009**, *26*, 644.
- [340] Y.-J. Kim, M. Ebara, T. Aoyagi, *Adv. Funct. Mater.* **2013**, *23*, 5753.
- [341] K. Hayashi, M. Nakamura, H. Miki, S. Ozaki, M. Abe, T. Matsumoto, W. Sakamoto, T. Yogo, K. Ishimura, *Theranostics* **2014**, *4*, 834.
- [342] K. Hayashi, K. Ono, H. Suzuki, M. Sawada, M. Moriya, W. Sakamoto, T. Yogo, *ACS Appl. Mater. Interfaces* **2010**, *2*, 1903.
- [343] T. T. T. N'Guyen, H. T. T. Duong, J. Basuki, V. Montembault, S. Pascual, C. Guibert, J. Fresnais, C. Boyer, M. R. Whittaker, T. P. Davis, L. Fontaine, *Angew. Chemie Int. Ed.* **2013**, *52*, 14152.
- [344] C. R. Thomas, D. P. Ferris, J.-H. Lee, E. Choi, M. H. Cho, E. S. Kim, J. F. Stoddart, J.-S. Shin, J. Cheon, J. I. Zink, *J. Am. Chem. Soc.* **2010**, *132*, 10623.
- [345] Y. I. Golovin, S. L. Gribanovsky, D. Y. Golovin, N. L. Klyachko, A. G. Majouga, A. M. Master, M. Sokolsky, A. V. Kabanov, *J. Control. Release* **2015**, *219*, 43.
- [346] D.-H. Kim, E. A. Rozhkova, I. V. Ulasov, S. D. Bader, T. Rajh, M. S. Lesniak, V. Novosad, *Nat. Mater.* **2010**, *9*, 165.
- [347] Y. Cheng, M. E. Muroski, D. C. M. C. Petit, R. Mansell, T. Vemulkar, R. A. Morshed, Y. Han, I. V. Balyasnikova, C. M. Horbinski, X. Huang, L. Zhang, R. P. Cowburn, M. S. Lesniak, *J. Control. Release* **2016**, *223*, 75.
- [348] S. Bhana, G. Lin, L. Wang, H. Starring, S. R. Mishra, G. Liu, X. Huang, *ACS Appl. Mater. Interfaces* **2015**, *7*, 11637.
- [349] C.-C. Huang, P.-Y. Chang, C.-L. Liu, J.-P. Xu, S.-P. Wu, W.-C. Kuo, *Nanoscale* **2015**, *7*, 12689.
- [350] X. Ma, H. Tao, K. Yang, L. Feng, L. Cheng, X. Shi, Y. Li, L. Guo, Z. Liu, *Nano Res.* **2012**, *5*, 199.
- [351] O. Akhavan, A. Meidanchi, E. Ghaderi, S. Khoei, *J. Mater. Chem. B* **2014**, *2*, 3306.

- [352] Z.-C. Wu, W.-P. Li, C.-H. Luo, C.-H. Su, C.-S. Yeh, *Adv. Funct. Mater.* **2015**, *25*, 6527.
- [353] B. Liu, X. Zhang, C. Li, F. He, Y. Chen, S. Huang, D. Jin, P. Yang, Z. Cheng, J. Lin, *Nanoscale* **2016**, *8*, 12560.
- [354] J. Wang, C. Yao, B. Shen, X. Zhu, Y. Li, L. Shi, Y. Zhang, J. Liu, Y. Wang, L. Sun, *Theranostics* **2019**, *9*, 608.
- [355] A. Espinosa, R. Di Corato, J. Kolosnjaj-Tabi, P. Flaud, T. Pellegrino, C. Wilhelm, *ACS Nano* **2016**, *10*, 2436.
- [356] R. Das, N. Rinaldi-Montes, J. Alonso, Z. Amghouz, E. Garaio, J. A. García, P. Gorria, J. A. Blanco, M. H. Phan, H. Srikanth, *ACS Appl. Mater. Interfaces* **2016**, *8*, 25162.
- [357] H. Yan, W. Shang, X. Sun, L. Zhao, J. Wang, Z. Xiong, J. Yuan, R. Zhang, Q. Huang, K. Wang, B. Li, J. Tian, F. Kang, S.-S. Feng, *Adv. Funct. Mater.* **2018**, *28*, 1705710.
- [358] A. Plan Sangnier, S. Preveral, A. Curcio, A. K. A. Silva, C. T. Lefèvre, D. Pignol, Y. Lalatonne, C. Wilhelm, *J. Control. Release* **2018**, *279*, 271.
- [359] M. F. Contreras, R. Sougrat, A. Zaher, T. Ravasi, J. Kosel, *Int. J. Nanomedicine* **2015**, *10*, 2141.
- [360] M. N. Bouchlaka, G. D. Sckisel, D. Wilkins, E. Maverakis, A. M. Monjazebe, M. Fung, L. Welniak, D. Redelman, A. Fuchs, C. A. Evrensel, W. J. Murphy, *PLoS One* **2012**, *7*, e48049.
- [361] Y. Shen, C. Wu, T. Q. P. Uyeda, G. R. Plaza, B. Liu, Y. Han, M. S. Lesniak, Y. Cheng, *Theranostics* **2017**, *7*, 1735.
- [362] Y. Chen, P. Han, Y. Wu, Z. Zhang, Y. Yue, W. Li, M. Chu, *Small* **2018**, *14*, 1802799.
- [363] F. Wo, R. Xu, Y. Shao, Z. Zhang, M. Chu, D. Shi, S. Liu, *Theranostics* **2016**, *6*, 485.

Chapter 1

1.1 Magnetically amplified photothermal therapies and multimodal imaging with magneto-plasmonic nanodomes

The main target of the Thesis has been the development of highly tunable ferromagnetic and plasmonic nanomaterials capable of being externally actuated and controlled by light and magnetic fields for efficient nanotherapy activation, amplification and regulation.

As the first Chapter of the Thesis, this article has undertaken the most fundamental work, which includes: **i)** developing the nanofabrication process; **ii)** optimizing the magnetic and optical properties; **iii)** demonstrating in vitro the biomedical applications in magnetically amplified photothermal therapies and multimodal imaging.

The combination of top-down (*e.g.* colloidal self-assembly) and bottom-up (*e.g.* physical vapor deposition) processes has been employed to fabricate multifunctional nanodomes, *i.e.* nanostructures composed of a polymer core and ferromagnetic-plasmonic semi-shell. Great efforts have been made to optimize the self-assembly of the polymer nanoparticles to achieve dense monolayers of isolated nanodomes with high yields. This fabrication strategy allows merging ferromagnetic and plasmonic materials and achieving high tunability in their properties by independently adjusting the size of the core and the thickness and composition of the semishell. Interestingly, the functionalization can be directly performed on the substrate and the functional nanodomes can be directly dispersed in water solutions by mild ultrasonication.

To merge and optimize the magnetic and plasmonic properties, (polystyrene)@Fe/Au nanodomes have been extensively studied to enable magnetic and optically controlled nanotherapies. The Fe and Au materials have been selected due to their biocompatibility and magnetic and plasmonic properties. The 100 nm polystyrene core has been chosen to enable plasmonic resonance bands in the near infrared range (700- 900 nm) and to keep a size within the preferred size range (10-200 nm) for nanotherapeutic applications.

The Fe layer offers thickness dependent tunable ferromagnetic properties with either single domain or vortex (Fe > 15 nm) magnetic structures. Despite the strong ferromagnetism, high colloidal stability of the nanodomains has been kept due to either the distance between neighbouring particles (thick Au layers and polystyrene cores) or the magnetic vortex configuration (near-zero remanence), which reduce the magnetic dipole-dipole interaction and the magnetic attraction between the nanostructures.

Interestingly, theoretical finite difference time domain (FDTD) simulations, predicted that the Fe layer induces a large reduction in the scattering cross-section of the nanodomains but it enables keeping high absorption cross-section, which are ideal properties to maximize the optical heating efficiency. The experimental results have confirmed this theoretical prediction, by showing the very high photothermal conversion efficiency with 808 nm laser (ca. 65%), even for high Fe ratios. Remarkably, the high magnetic strength of the Fe layer has been exploited to concentrate the nanodomains at the illumination region and to achieve a substantial additional local temperature increase.

The Fe/Au semishell also gathers multi-parametric bioimaging features. The high X-ray attenuation of the Au layer has been exploited to visualize the internalized nanodomains by frozen HeLa cancer cells by X-ray tomography microscopy at ALBA synchrotron. Moreover, the Fe layers yields strong T_2 contrast (relaxivity $r_2 = 266 \text{ mM}^{-1}\text{s}^{-1}$), which is substantially higher than commercial iron oxide contrast nanoagents.

The *in vitro* assays, which have been carried out in collaboration with the Cell Biology Unit of the UAB, have shown the non-toxicity of the nanodomains even in the case of high magnetic enrichment in initially high nanodomains concentrations (100 $\mu\text{g/mL}$). Moreover, the magnetic concentration at the illumination region have enabled nearly 100% reduction of the cell viability with low particle concentration (10 $\mu\text{g/mL}$) and mild NIR laser intensity (5 W/cm^2) to demonstrate the high biomedical potential of the magnetically enhanced photothermal therapies.

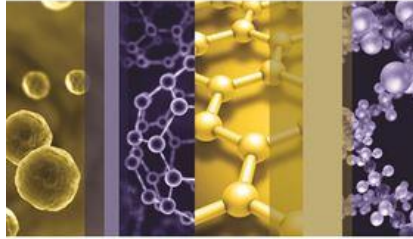
1.2 Personal Contribution

Since this work is based on a multi-disciplinary topic, this article involved collaborators from different disciplines. Thus, it is important to mention which were my contributions for this article.

My independent work included: **i)** Fe/Au nanodomes fabrication (colloidal self-assembly, electron beam evaporation, ultrasonication dispersion) and optimization, **ii)** characterizations of physiochemical properties (lithography pattern, size, surface charge) using scanning electron microscopy (SEM) and dynamic light scattering (DLS) and optical properties (extinction spectra) using vis-near infrared spectroscopy, **iii)** photothermal efficiency measurements using a custom-made optical system (built in collaboration with Borja Sepúlveda), **iv)** magnetic trapping efficiency measurements.

I participated in other experiments, where the tests were carried out mainly by some colleagues, but I was personally involved in the experiments. These include **i)** transmitted electron microscopy (TEM; Belen Ballesteros, ICN2), magnetization characterization using vibrating sample magnetometer (VSM; Jordi Sort, Universitat Autònoma de Barcelona), **ii)** theoretical calculations of optical properties using finite domain time domain (FDTD) method (Borja Sepúlveda).

Some experiments were carried out by collaborators, although I provided with the necessary nanodome samples. These include cell cultures, scanning electron microscopy of cell cultures, cell viability tests. These studies were mainly performed by the co-authors of this article (Antonio Aranda, Laia Pou and Carme Nogués, Bioscience Faculty of Universitat Autònoma de Barcelona); **or scientific services i)** mass concentration tests using inductively coupled plasma mass spectrometry (ICP-MS Service at Universitat Autònoma de Barcelona), **ii)** T_2 contrast signal detection using nuclear magnetic resonance (NMR) machine (NMR Service at Universitat Autònoma de Barcelona), **iii)** X-ray microscopy (ALBA synchrotron).



Magnetically Amplified Photothermal Therapies and Multimodal Imaging With Magneto-Plasmonic Nanodomes

Zhi Li,^{1,4} Pau Güell-Grau,¹ José Luis Tajada,¹ Alejandro Gómez Roca,¹ Josep Nogués,¹ and Borja Sepúlveda,^{1*}

Antonio Aranda-Ramos,² Laia Pou-Macayo,² Carme Nogués,²

Silvia Lope Piedrafita,³

Francesc Pi,⁴ María Dolors Baró,⁴ Jordi Sort⁴

¹ *Catalan Institute of Nanoscience and Nanotechnology (ICN2), CSIC and BIST, Campus UAB, Bellaterra, 08193 Barcelona, Spain*

² *Departament de Biologia Cel·lular, Fisiologia i Immunologia, Facultat de Biociències, Universitat Autònoma de Barcelona, Bellaterra, 08193 Barcelona, Spain.*

³ *Servei de Resonància Magnètica Nuclear, Universitat Autònoma de Barcelona, Bellaterra, 08193 Barcelona, Spain, and Centro de Investigación Biomédica en Red en Bioingeniería, Biomateriales y Nanomedicina (CIBER-BBN).*

⁴ *Departament de Física, Facultat de Ciències, Universitat Autònoma de Barcelona, Bellaterra, 08193 Barcelona, Spain.*



Magnetically amplified photothermal therapies and multimodal imaging with magneto-plasmonic nanodomains

Zhi Li^{a,e}, Antonio Aranda-Ramos^b, Pau Güell-Grau^a, José Luis Tajada^a, Laia Pou-Macayo^b, Silvia Lope Piedrafita^{c,d}, Francesc Pi^e, Alejandro G. Roca^a, María Dolors Baró^e, Jordi Sort^{e,f}, Carme Nogués^b, Josep Nogués^{a,f}, Borja Sepúlveda^{a,*}

^a Catalan Institute of Nanoscience and Nanotechnology (ICN2), CSIC and BIST, Campus UAB, Bellaterra, 08193 Barcelona, Spain

^b Departament de Biologia Cel·lular, Fisiologia i Immunologia, Facultat de Biociències, Universitat Autònoma de Barcelona, Bellaterra, 08193 Barcelona, Spain

^c Servei de Resonància Magnètica Nuclear, Universitat Autònoma de Barcelona, Bellaterra, 08193 Barcelona, Spain

^d Centro de Investigación Biomédica en Red en Bioingeniería, Biomateriales y Nanomedicina (CIBER-BBN), Spain

^e Departament de Física, Facultat de Ciències, Universitat Autònoma de Barcelona, Bellaterra, 08193 Barcelona, Spain

^f ICREA, Pg. Lluís Companys 23, 08010 Barcelona, Spain

ARTICLE INFO

Article history:

Received 15 June 2018

Received in revised form 20 July 2018

Accepted 26 July 2018

Keywords:

Magneto-plasmonic nanoparticles

Photothermal therapies

Magnetic manipulation

Contrast agents

ABSTRACT

Nanotherapies require new ways for controlling and improving the delivery of the therapeutic agents to the site of action to maximize their efficacy and minimize the side effects. This control is particularly relevant in photothermal treatments to reduce the required light intensity and amount of injected nanoparticles, and to minimize necrotic cell deaths. Here we present a novel concept for multifunctional nanobiomedical agents: magneto-plasmonic (MP) nanodomains for magnetically guided and amplified photothermal therapies and as contrast agents for multimodal imaging. The MP nanodomains are composed of a Fe/Au bilayer semi-shell deposited on a 100 nm diameter fluorescent polystyrene nanosphere, which gather a unique combination of straightforward functionalization, high colloidal stability, very strong ferromagnetic behavior and intense optical absorption, minimized scattering and low optical anisotropy. Remarkably, the effective magnetophoretic concentration of the Fe/Au nanodomains at the illumination region enables large local increase of the optically induced temperature rise. The Fe semishell also provides very intense T_2 contrast in nuclear magnetic resonance, which is at least 15-fold larger per particle than commercial iron oxide contrast agents. Moreover, the fluorescent polystyrene nanosphere and the Au semishell integrate valuable fluorescent and X-ray contrasts, respectively, which we have used to assess the nanodomains internalization by cancer cells. The MP nanodomains are nontoxic to cells even in the case of magnetophoretic local enrichment with initially high particle concentration (100 $\mu\text{g/mL}$). Remarkably, we demonstrate amplified local photothermal treatments by the magnetic enrichment of the nanodomains at the illumination region, which enables reaching nearly 100% reduction of cell viability with low particle concentration (10 $\mu\text{g/mL}$) and mild NIR laser intensity (5 W/cm^2). These results highlight the high potential of MP nanodomains for magnetically guided and amplified photothermal therapies.

© 2018 Elsevier Ltd. All rights reserved.

1. Introduction

Nanotherapies are playing an increasingly important role to create new therapies with higher efficacy and lower side effects than traditional chemical treatments, especially in diseases such

as cancer [1–4]. In addition to efficient drug carriers, nanoparticles can also be the source of efficient physical therapies, such as local hyperthermia, which can be employed to thermally destroy the tumors [5–9] or as adjuvant of chemotherapies [10–14]. Photothermal therapies are typically based on plasmonic nanoparticles due to the amplified optical absorption associated with their localized surface plasmon resonance (LSPR) [15,16], which can be tuned to the near-infrared (NIR), where the skin and capillaries show higher transparency [17]. However, the passive delivery of nanoparticles

* Corresponding author.

E-mail address: borja.sepulveda@icn2.cat (B. Sepúlveda).

<https://doi.org/10.1016/j.apmt.2018.07.008>

2352-9407/© 2018 Elsevier Ltd. All rights reserved.

hampers their control and efficient concentration at the tumor. The main obstacles that passively delivered nanoparticles encounter in cancer therapies are [18]: (i) hepatic, renal or immune system clearance, which can drastically reduce the probability to target the tumor; (ii) less pronounced enhanced permeability and retention effect in clinical tumors than in murine models, (iii) inherent elevated interstitial hydrostatic pressure in solid tumors that inhibits nanoparticle extravasation, and (iv) poor diffusion inside solid tumors due to abnormally high cross-linked extracellular matrix. An attractive way to overcome these hurdles is the external control and guidance of the nanoparticles to the site of action. The ability of magnetic nanoparticles to respond to magnetic forces has fueled the development of nanostructures to magnetically propel the nanoparticles with external magnetic fields [19–24]. Therefore, the combination of plasmonic and magnetic materials can be an interesting alternative to overcome the drawbacks associated to the passive delivery of the nanoparticles. Magneto-plasmonic nanoparticles, in addition to enhanced magneto-optic effects [25,26], could combine efficient plasmonic light absorption with magnetic manipulation [27–30].

To date, the majority of colloidal magneto-plasmonic nanostructures are based on merging plasmonic nanoparticles with small superparamagnetic iron oxide nanoparticles (SPIONs) [30–33]. However, the small size and weak magnetic moment of the SPIONs, required to minimize their magnetic interaction (which is crucial to ensure the colloidal stability), drastically limits their magnetic actuation capabilities.

Moreover, colloidal magnetic, plasmonic and magneto-plasmonic nanoparticles are generally obtained in organic solvents by chemical synthesis, in which achieving controlled optical and magnetic properties with narrow size and shape distributions can be complex. In addition, the biomedical applications require transferring the nanostructures to an aqueous medium and their functionalization, which are cumbersome processes in nanoparticles obtained from organic-based syntheses that can lead to particle aggregation, especially when heterostructures are involved. In contrast, scalable top-down methods capable of generating macroscopic amounts of colloidal nanostructures in a simple and effective way are considerably less developed. Therefore, achieving cost-effective ways to fabricate multifunctional nanostructures with highly controlled and strong optical and magnetic properties in a large scale may lead to new high-added value biomedical agents.

Here we present novel colloidal ferromagnetic/plasmonic Fe/Au nanodomains enabling: (i) excellent colloidal stability; (ii) high optical heating efficiency in the NIR, comparable to that of state-of-art plasmonic nanoparticles; (iii) strong magnetic manipulation via magnetophoretic forces, and (iv) very high contrast for fluorescence, nuclear magnetic resonance (NMR) and X-ray imaging. We show that the combination of magnetophoretic manipulation and optical heating within the magneto-plasmonic (MP) nanodomains enables a near 100% reduction of cell viability in photothermal treatments *in vitro* under demanding conditions of low MP nanodomains concentration (10 $\mu\text{g}/\text{mL}$) and mild NIR laser intensity (5 W/cm^2).

2. Experimental

2.1. Fabrication of the MP nanodomains

Unlike typical chemical synthesis methods, the MP nanodomains are fabricated by a combination of colloidal nanolithography [34] and physical vapor deposition, which are scalable and cost-effective processes that enable accurate control of their magnetic and optical properties. A schematic drawing of the different fabrication steps

can be seen in Fig. S1 in Supporting information section. Briefly, we employed four-inch silicon wafers (Siegert Wafer GmbH) cleaned with oxygen plasma (PS210, PVA Tepla America, Inc.) as substrates for the electrostatic self-assembly of the polystyrene nanospheres. The self-assembly starts by incubating the wafer surface with a solution containing positively charged polyelectrolyte [poly(diallyldimethylammonium chloride), PDDA, Sigma–Aldrich] at 2% concentration for 1 min. Then the wafer is rinsed with osmotized water and blow dried with N_2 gas, thereby yielding a monolayer of PDDA on the surface. Next, the modified wafer surface is incubated with the dispersion of sulfate functionalized polystyrene beads (100 nm diameter, concentration 0.2%, Life Technologies) for 2 min, followed by rinsing with water and drying with N_2 flow to obtain the self-assembled monolayer of nanospheres. The exposed surface of nanospheres on the wafer was then coated with Fe and Au layers using electron beam evaporator (UNIVEX 450, Leybold®) to form the Fe/Au bilayer semi-shells with a total thickness of 40 nm. The thickness of the deposited bilayers was monitored with Ångström precision by a quartz crystal microbalance during the evaporations. To improve the stability in aqueous solutions, the MP nanodomains were directly functionalized, while still on the wafer, with the negative charged polyelectrolyte [poly(sodium 4-styrenesulfonate), PSS, Sigma–Aldrich] by incubating patterned surface in at 2% concentration water solution for 3 min to deposit a monolayer on the Au surface. The wafer is rinsed with water to remove the excess of PSS and is dried with N_2 flow. The surface functionalization with proteins (e.g. for cell targeting) can also be carried out directly on the nanopatterned substrate without the need of any chemical linker. In this case we exploit the very high affinity of amine and cysteine groups of the proteins toward bare Au layers. We have actually observed the formation of uniform and stable protein monolayers on the Fe/Au nanodomains by incubating the nanopatterned substrate with a solution of 10 $\mu\text{g}/\text{mL}$ of protein in water for just 1 h (Fig. S2).

To disperse the particles in water, the wafer together with 10 mL of water was introduced into an ultrasonic bath for 1 min. The MP nanodomains were finally concentrated and redispersed through centrifugation (4000 rpm, 5 min), followed by ultrasonication to achieve highly stable dispersions at the required concentrations. The Si wafers can be reused after cleaning for 10 min in aqua regia, which efficiently dissolves the Fe and Au layers.

2.2. Morphological, optical, magnetic and colloidal characterization

To study the size and distribution of MP nanodomains on the Si wafers, scanning electron microscopy (SEM) studies were performed using Quanta SEM 650 (Field Electron and Ion Company (FEI)) at 20 kV. The density of nanospheres coated on the wafer was quantified by using ImageJ software. Transmission electron microscopy, TEM, images and electron energy loss spectroscopy (EELS) analyses were performed in a FEI Tecnai F20 equipped with a Quantum GIF EELS spectrometer.

The stability of the water dispersed MP nanodomains was studied through dynamic light scattering using Zetasizer Nano ZS (Malvern Instruments Ltd.). Both Zeta potential and average size of particles were simultaneously obtained. The visible–near infrared (vis–NIR) spectroscopy studies of the MP nanodomains dispersions were carried out using Lambda25 (PerkinElmer). For the optical measurements, the optical spectra ranged from 400 nm to 1100 nm, which covered visible light and near infrared region. The concentration of the MP dispersions was determined by ICP-OES (Perkin Elmer Optima 4300DV).

The magnetic characterization of the MP nanodomains was performed on monolayers that were transferred to adhesive tapes to eliminate the magnetic signal from the bilayer that is deposited

on the wafer surface. Magnetization loops were acquired at room temperature using a vibrating sample magnetometer (MicroSense, LOT QuantumDesign) with a maximum applied field of 20 kOe. The measurements were performed by applying the field either parallel or perpendicular to the sample, *i.e.*, in-plane or out-of-plane conditions.

2.3. Photothermal characterization

A custom-made photothermal testing system was used to determine the photothermal conversion efficiency of MP nanodomains in water (see Fig. S3), which consists of: (i) a NIR laser diode with emission wavelength at 808 nm (L808P500MM, Thorlabs) driven by a laser diode controller (LDC240C, Thorlabs) and a temperature controller (TED240C, THORLABS), (ii) an optical collimating and aligning system, (iii) an infrared thermometer (MLX90614, Melexis) to monitor the temperature variations at the liquid surface, (iv) a power meter (PM100D, Thorlabs), and (v) a computer with the data acquisition software. The laser incident power upon the samples was 166 mW. For the analysis, samples with different concentration and constant volume (400 μL) were prepared. The temperature of the solution and the power transmitted through the sample were continuously monitored during the assays. The time interval of data recording for both transmitted power and instant temperature was 1 s. The experimental photothermal conversion efficiency comparison with Au nanorods and nanoshells was carried out with Nanocomposix commercial particles, with references GRCN800 and GSPN800, respectively.

To analyze the magnetic manipulation of MP nanodomains by magnetophoretic forces, a stack of cylindrical FeNdB magnets (6 mm diameter with a 2500 Oe field at the surface) were attached at the lateral side of the cuvettes.

2.4. Nuclear magnetic resonance

^1H -magnetic resonance imaging (MRI) studies were performed in a 70 kOe Bruker BioSpec 70/30 USR (Bruker BioSpin GmbH, Ettlingen, Germany) system equipped with a mini-imaging gradient set (4000 Oe/m) and using a linear volume coil with 72 mm inner diameter. Magnetic resonance data were acquired and processed on a Linux computer using Paravision 5.1 software (Bruker BioSpin GmbH, Ettlingen, Germany). For the relaxivity measurements, phantoms containing MP nanoparticles at various concentrations in 2% agarose were prepared. Magnetic resonance images were obtained from two 2.5 mm slice thickness coronal sections with a field of view (FOV) of 9 cm \times 6 cm. Longitudinal relaxation times (T_1) were measured using a spin echo sequence with variable repetition time (TR = 300, 500, 700, 1000, 1300, 1700, 2000, 2600, 3500, and 5000 ms), echo time = 7.5 ms, and matrix size (MTX) = 128 \times 128. For transverse relaxation time (T_2) measurements, a multi-slice multi-echo sequence was used, with TR = 3 s, TE values between 10 and 600 ms in steps of 10 ms, and MTX = 128 \times 128. Data were fitted to exponential curves to obtain the T_1 and T_2 relaxation times, respectively. Longitudinal and transverse relaxivity values, r_1 and r_2 , were obtained as the slope of the linear regression of the relaxation rates (R), as the inverse of the relaxation times ($R_i = 1/T_i$, $i = 1, 2$) versus Fe concentration.

2.5. Cell culture

Human Epithelial Cervical Adenocarcinoma Cells (HeLa, ATCC) were cultured in Minimal Essential Medium (Gibco, Life Technologies) supplemented with 10% Fetal Bovine Serum (Gibco) and 2 mM L-Glutamine (Life Technologies). Cultures were maintained at 37 $^\circ\text{C}$ in a 5% CO_2 humidified atmosphere (standard culture conditions).

2.6. Scanning electron microscopy of the cell cultures

Cells were seeded in glass bottom dishes (MatTek Corporation) at a density of 3×10^4 cells/mL and incubated in standard conditions for 24 h. Two concentrations of MP nanodomains were tested: 10 and 100 $\mu\text{g}/\text{mL}$. MP nanodomains were added directly to the cell cultures and incubated in standard conditions for 3 h with or without the FeNdB spherical magnet underneath. To remove the non-internalized MP nanodomains, the cell media were replaced with fresh media and the cells were further treated with the laser according to each condition. After the MP nanodomains incubation and photothermal treatment, the cells were rinsed twice in 0.1 M sodium cacodylate buffer at pH 7.3 (SCB; TAAB), fixed in 2.5% microscopy glutaraldehyde solution for electron microscopy (Merck) in SCB for 25 min at room temperature and rinsed again twice in SCB. Cell dehydration was done in a series of ethanol washes (50, 70, 90 and twice 100%), 7 min each. Finally, cells were dried in hexamethyldisilazane (HMDS; Electron Microscope Science) for 15 min after which HMDS was withdrawn and the samples were let to dry overnight. Samples were mounted on special stubs and observed using a SEM (Zeiss Merlin).

2.7. Confocal laser scanning microscopy (CLSM)

Cells were seeded in glass bottom dishes (MatTek Corporation) at a density of 3×10^4 cells/mL and incubated in standard conditions for 24 h. Then, 10 $\mu\text{g}/\text{mL}$ of fluorescent MP nanodomains ($\lambda_{\text{excitation}} = 575$, $\lambda_{\text{emission}} = 610$ nm) were added directly to cell cultures and incubated for 3 h in standard conditions. After incubation, the cells were washed twice with saline solution and 1 mL of fresh medium was added to the sample. Finally, the cells were stained with 1 μL of CellTM Deep Red plasma membrane stain (Life Technologies), to reveal the plasma membrane, and 0.5 μL of Hoechst 33342 (Life Technologies) to expose the nucleus. Images were captured sequentially using an Olympus CLSM (Olympus FV1000). Three different lasers were used: 405, 559 and 635 nm, to visualize nucleus, MP nanodomains and plasma membrane, respectively. Stacks of images along the z-axis were obtained for a selected area using the xyz mode of the CLSM and the ImageJ (Fiji) and Bio-formats plugins were used to obtain overlapped images of all channels (nuclei, plasma membranes and MP nanodomains) and the 3D reconstructions and cross-section projections were used to confirm MP nanodomains' internalization.

2.8. Soft transmission X-ray microscopy

Cells were seeded onto gold grids covered with FORMVAR and carbon foil at a density of 5×10^4 cells/mL and incubated in standard conditions for 24 h. Then, cell cultures were incubated in the presence or absence (control cultures) of 25 $\mu\text{g}/\text{mL}$ of MP nanodomains for 3 h and afterwards, the incubation solution was discarded. The grids were subsequently rinsed in saline solution, plunge-freeze in liquid ethane chilled with liquid nitrogen and transported to the ALBA synchrotron. Finally, full field X-ray tomography was carried out at 520 eV excitation energy at the Mistral beamline of the ALBA synchrotron light source to obtain carbon compounds within the cryopreserved cells in the so-called "water-window".

2.9. Photothermal treatment and cell death evaluation

Cells were seeded in cover glass-bottom dishes (MatTek, growth area ~ 154 mm²) at a density of 6×10^4 cells/mL and kept in standard culture conditions in 500 μL of cell medium for 24 h. Next, the cell cultures were incubated in the presence or absence (control cultures) of 10 or 100 $\mu\text{g}/\text{mL}$ of MP nanodomains for 3 h. Then, the

cells were washed three times with Hank's Balanced Salt Solution to remove the dispersed nanodomains in the cell medium. The cells were finally kept in 1 mL of medium during the laser treatment and the overnight incubation after the treatment. The photothermal treatment was performed inside the incubator (HeraCell) using the light from a collimated fiber-coupled laser diode with emission wavelength at 808 nm (B1-808-1500-15A, Laser Components). The incident intensity in the sample was approximately 5 W/cm² and the treated area was a circle of 6 mm in diameter. The treatment was carried out for 30 min. To evaluate the cytotoxicity of the photothermal treatment, after irradiation, cells were incubated again in standard conditions for 24 h, and then incubated with the LIVE/DEAD[®] Viability and Cytotoxicity assay (Life Technologies) following manufacturer's guidelines. Images were acquired using the inverted fluorescence microscope Olympus IX71 (Olympus) and processed through ImageJ (Fiji). Three independent experiments were performed. The MP nanodomains photothermal effect was analyzed using Fisher's exact tests, using Graphpad Prism[®] 7.0a software (Graphpad Software). Statistical significance was considered when $P < 0.05$.

3. Results and discussion

The MP nanodomains are composed of a 100 nm diameter polystyrene core that is partially coated by a Fe/Au bilayer semi-shell. To show their tunable magnetic and optical properties, in this study we vary the relative thickness of the Fe and Au layers, but we keep a total bilayer thickness of 40 nm (Fig. 1a). The fabrication process yields a monolayer of well-separated nanodomains with a short-range order distribution and homogeneous density of 1.6×10^9 nanodomains/cm² (Fig. 1b), which is equivalent to ca. 1.3×10^{11} particles per wafer.

Mass spectrometry analyses of the MP nanodomains dispersions from different wafers concentrated in 1 mL of water have shown an average concentration of $(1.35 \pm 0.04) \times 10^{11}$ nanodomains/mL (see Supporting information Table S1). Considering the estimated amount of particles per wafer obtained by the SEM analysis, virtually 100% of the self-assembled nanodomains on the wafer are transferred to the liquid. Dynamic light scattering measurements have shown an averaged hydrodynamic diameter of 114 nm (polydispersity index – PDI = 0.09) and zeta-potential of –25 mV. After more than six months storage at room temperature the nanodomains show an averaged diameter of 116 nm and a similar PDI value,

thereby demonstrating their extremely high colloidal stability even for ferromagnetic nanodomains with high Fe content. Although the nanodomains tend to sediment with time, a process that approximately takes 36 h, gentle agitation of the container enables the recovery of a completely homogeneous dispersion.

The optical properties of the MP nanodomains in water for different Fe/Au ratios are gathered in Fig. 2a. The extinction spectrum of 40 nm thick Au nanodomains shows two peaks located at 650 nm and 850 nm wavelength, which correspond to the superposition of the complex optical resonances in the plasmonic semi-shells induced by their geometrical asymmetry. The nanodomains exhibit two different optical configurations, for the light polarized parallel to the longitudinal or transversal orientations of the nanodomains (see Fig. 2b). In the longitudinal configuration there are two main resonances of magnetic dipolar and quadrupolar character, located in the NIR and in the red part of the spectrum, respectively (Fig. S4). In contrast, two electric dipolar and quadrupolar resonances are observed in the transversal configuration that are blue shifted with respect to those in the longitudinal orientation (Fig. S4). Since the dispersed nanodomains are randomly distributed, the experimental spectrum is the convolution of these resonances averaged over all the possible orientations. The resonance band in the NIR region suits perfectly within the spectral region with higher penetration in physiological tissues (biological window) and, therefore, has high potential for photothermal applications. This resonance can be red-shifted even further by reducing the Au thickness (Fig. S5).

The introduction of the Fe layer and the reduction of the Au thickness generate remarkable spectral changes in the nanodomains. A 5 nm thick Fe layer red shifts and broadens the NIR resonant band, and blue shifts the band initially centered at 650 nm. As the Fe thickness increases, a substantial peak broadening and reduction of the extinction values are observed. For nanodomains with 20 nm Fe thickness and above, the plasmonic bands practically disappear, showing broadband extinction spectra with reduced extinction intensity. Such extinction reduction could initially suggest that the optical heating efficiency of MP nanodomains with high Fe content could substantially decrease. However, it has to be taken into account that the extinction measurements are the sum of scattering and absorption. In fact, finite difference time domain (FDTD) calculations in Fig. S4 show that increasing Fe thickness drastically reduces the scattering cross section of the nanodomains in both longitudinal and transversal orientations, nevertheless, the decrease in the absorption cross-section is considerably weaker. Consequently,

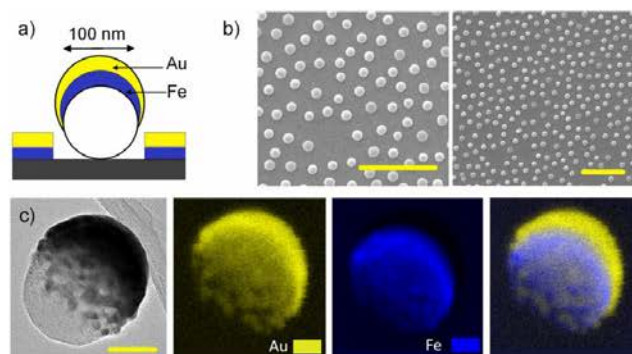


Fig. 1. Morphological and composition characterization of the MP nanodomains. (a) Schematic of the MP nanodomains composed of Fe and Au bilayers. (b) SEM image of the self-assembled nanodomains on the wafer with a density of 1.6×10^9 particles/cm². The scale bars are 1 μ m. (c) High angular annular dark field scanning transmission electron microscopy images of a MP nanodomain with 20 nm Fe and 20 nm Au together with the EELS mappings for the Au M-edge (yellow) and the Fe L-edge (blue) signal and the composed image. Scale bar 50 nm. (For interpretation of the references to color in this figure legend, the reader is referred to the web version of the article.)

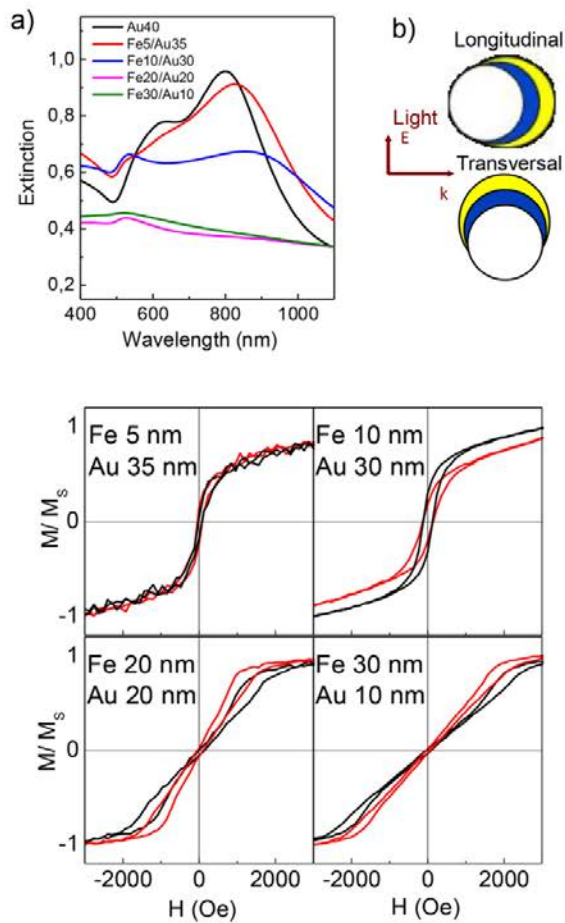


Fig. 2. Optical and magnetic properties of the MP nanodomes. (a) Experimental vis-NIR spectra for MP nanoparticles with different Fe and Au ratios. (b) Schematic of the two main optical configurations of the MP nanodomes, i.e. longitudinal and transversal configurations. (c) Vibrating sample magnetometer magnetization loops of MP nanodomes with different Fe and Au ratios for in-plane (black) and out-of-plane (red) applied fields. (For interpretation of the references to color in this figure legend, the reader is referred to the web version of the article.)

since the optical heating is only related to absorption and not to scattering, high optical heating efficiency can be still expected even with high Fe ratios, as we demonstrate below.

Interestingly, the MP nanodomes also offer tunable ferromagnetic properties by modifying the Fe thickness. Vibrating sample magnetometer measurements show that the MP nanodomes exhibit a ferromagnetic behavior at room temperature in all the studied Fe thicknesses (Fig. 2c). Nanodomes with 5 nm Fe thickness present single domain-like hysteresis loop with small coercivity, which substantially increases for the 10 nm Fe thickness. Interestingly, a magnetic vortex is formed in the nanodomes with 20 nm and 30 nm Fe thickness showing near zero remanence hysteresis loops, as expected from the size and thickness of the Fe layer [35,36]. This magnetic behavior explains the observed high colloidal stability in all the MP nanodomes, even for high Fe content. Namely, when the magnetic vortex is formed, the magnetostatic interaction in the absence of external magnetic field is negligible. On the other hand, the magnetic dipole-dipole interactions of the nanodomes with 5 nm and 10 nm Fe thickness are drastically reduced due to the large thickness of the Au layer and the strong electrostatic repulsion between particles.

We have analyzed the photothermal response of MP nanodomes for the different Fe/Au ratios, with concentrations ranging from 3×10^9 up to 1.2×10^{11} nanodomes/mL (Fig. 3b). A typical heating curve is shown in Fig. 3a, which displays the temperature rise in the nanodomes suspension when the laser is switched on, until the thermal equilibrium, due to the equal balance of absorbed and dissipated energy by the sample, is reached. The suspension slowly recovers the initial room temperature level once the laser is switched off.

As expected, the temperature increase follows a linear dependence with the colloidal concentration for low concentration levels. However, the temperature increase saturates at a concentration of 3×10^{10} nanoparticles/mL due to the complete absorption of the laser light along the 1 cm thick cuvette for higher nanodomes concentrations. Nevertheless, the most remarkable result is the almost identical optical heating efficiency for all nanodome configurations, regardless of the Fe/Au ratio (Fig. 3b). The reason behind this striking behavior can be inferred from Fig. 3c. Gold nanodomes are highly anisotropic structures showing fourfold difference in their absorption cross section for the longitudinal and transversal configurations at 800 nm wavelength. Consequently, only Au nanodomes that are longitudinally oriented with respect to the incident light polarization are efficiently heated. In contrast, the optical anisotropy is reduced as the Fe content increases, as Fig. 3c

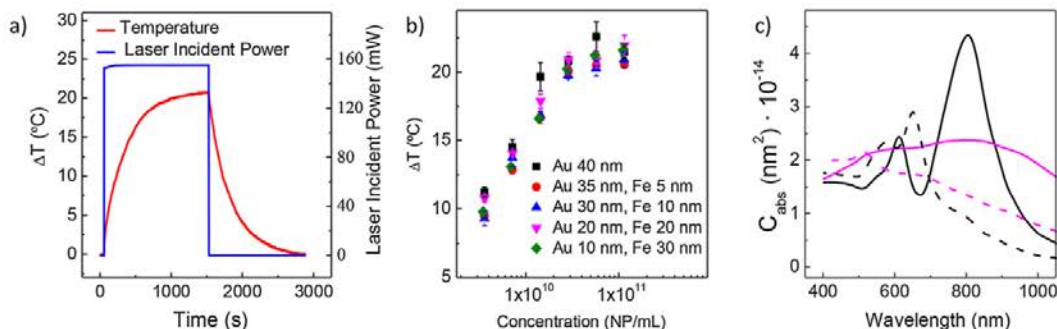


Fig. 3. Photothermal analysis. (a) Example of laser heating experiment showing the temperature increase, ΔT , and decrease when the incident laser power is on or off, respectively. (b) Temperature increase for MP nanodomes with different Fe and Au ratios and different concentrations (166 mW of incident laser power). (c) Theoretical absorption cross-section of Au 40 nm (black) and Au 20 nm/Fe 20 nm nanodomes (magenta) when the incident light polarization is in the longitudinal (continuous lines) or transversal (dashed lines).

shows for the 20 nm of Fe and 20 nm of Au nanodomies. Interestingly, the decrease in the absorption efficiency of Fe/Au nanodomies with respect to Au nanodomies in the longitudinal configuration is partially compensated by a higher efficiency in the transversal configuration. In addition, the heating efficiency of nanodomies with high Fe content benefits from their low scattering cross section (Fig. S4), thereby minimizing the back-scattered radiation that does not contribute to nanodomies heating. As a result, all the MP nanodomies achieve similar temperature increments for a given laser power and particle concentration. Interestingly, even at rather low particle concentrations (in the 10^9 nanodomies/mL range), temperature increments for therapeutic applications (from 5 °C to 8 °C) can be easily achieved. At this point, it is worth analyzing the photothermal conversion efficiency of the MP nanodomies with different Fe/Au ratios compared to state-of-the-art plasmonic nanoheaters, such as Au nanorods and Au nanoshells showing plasmonic resonances close to 810 nm. The photothermal conversion efficiency, η , is calculated by [37]:

$$\eta = \frac{hS\Delta T_{\max} - Q_{\text{dis}}}{I(1 - 10^{-A_{808}})} \quad (1)$$

where h is the heat transfer coefficient, S is the laser irradiating area, ΔT_{\max} is the optically induced temperature change when the thermal equilibrium is reached, Q_{dis} is the heat dissipation from the experimental set-up, I is incident laser power (166 mW), and A_{808} is the absorbance of the nanoparticles at 808 nm. The value hS is given by:

$$hS = \frac{m_{\text{water}}C_{\text{water}}}{\tau_s} \quad (2)$$

where m_{water} and C_{water} are the mass and heat capacity of deionized water (0.4 g and 4.2 J/g, respectively), and τ_s is the set-up time constant (250 ms), i.e. the time required to recover a temperature increase equal to ($\Delta T_{\max}/e$) in the set up once the light source is switched off and the sample cools down. The value of Q_{dis} (3.36 mW) was measured using a plastic cuvette containing deionized water (400 μ L). The photothermal efficiency results are gathered in Table 1, together with the A_{808} and ΔT_{\max} values experimentally obtained from the different nanoparticle dispersions.

As can be observed in Table 1, the Fe/Au nanodomies efficiency is clearly higher than that of Au nanodomies and is equal to that of the Au nanorods, which are the most efficient plasmonic nanoheaters. Such a high efficiency in the Fe/Au nanodomies is due to their minimized scattering cross section of the Fe/Au nanodomies and low optical anisotropy, as it was discussed below. The combination of both effects enables a deeper light penetration and a more uniform heating of the colloidal dispersion in the case of Fe/Au nanodomies. In addition, the heating efficiency is much larger than that of nanoshells, which are nanostructures that exhibit a large scattering cross section, and lower absorption cross section in the near infrared.

In addition to the higher photothermal conversion efficiency, the Fe layers confer the nanodomies with the unique capacity to magnetically control and amplify photothermal therapies. To experimentally assess such ability, we have first analyzed their magnetic trapping efficiency via magnetophoretic forces, by attaching a cylindrical FeNdB magnet (6 mm diameter, 10 mm length,

with a 2.5 kOe field at the surface) at the lateral side of the cuvette that is parallel to the light path (see Fig. S2). To compare the magnetophoretic forces among nanodomies, we have quantified the time that is required to achieve the 95% of the transmitted laser power (taking 100% as a water sample without particles), as a method to determine when the majority of the nanodomies are magnetically trapped at the cuvette wall. Magnetic trapping takes more than 1 h for nanodomies with only 5 nm of Fe. In contrast, the trapping time is reduced to 6 min for 10 nm Fe nanodomies, and less than 2 min for 20 nm and 30 nm Fe nanodomies (Fig. 4a). The large trapping time for 5 nm Fe nanodomies is due to their weak magnetic dipole moment and large mass given by the thick of Au layer. Increasing the Fe content to 10 nm, induces a 9-fold enhancement of the nanodomies magnetization (Fig. S6), probably due to a reduced magnetization at the Fe/Au interface [38,39], whose net magnetic effect is more pronounced for thin Fe films. The larger mass of the 5 nm Fe nanodomies and, consequently, their lower acceleration caused by the magnetic force can account for the 11-fold rise of the trapping time of 5 nm thick Fe nanodomies compared to that of 10 nm thick Fe. The increase of the Fe thickness to 20 nm and 30 nm induces an additional 4-fold reduction of the trapping time. Such reduction is the result of the larger magnetic moment and lower mass of the nanodomies with high Fe ratio. The only slight reduction of the trapping time in the 30 nm Fe nanodomies compared to that in the 20 nm Fe nanodomies is due to the more tilted hysteresis loop in the former ones (see Fig. 2c), which compensates their higher Fe content and lower mass.

To highlight the strength of the magnetic manipulation it is worth comparing the magnetic dipole (m) that can be generated in the nanodomies and in standard colloidal stable SPIONs. The maximum magnetic dipole that can be generated in the nanostructures is given by $m = M_s V_p$, where M_s is the saturation magnetization and V_p is the volume of the magnetic element. In the case of nanodomies with 20 nm Fe thickness, the maximum magnetic dipole is ca. 630-fold larger than that of FDA (US Food and Drug Administration)-approved SPIONs with 12 nm diameter, and almost three orders of magnitude larger for Fe 30 nm nanodomies. This huge difference is due to the 3-fold higher M_s of metallic iron compared to that of iron oxide (i.e., 1716 emu/cm³ for Fe versus 476 emu/cm³ for Fe₃O₄) and the much larger volume of the Fe layer in the nanodome. As a result, the nanodomies can act as very strong nanomagnets in the presence of a magnetic field (thus, reacting quickly to them), although they can keep high colloidal stability in the absence of magnetic fields due to their near zero remanence (given by their magnetic vortex state). Actually, mild sonication can easily disperse the magnetically trapped nanodomies and fully recover the homogeneous colloidal dispersion once the magnet is removed.

Interestingly, the efficient magnetophoretic manipulation can be used to locally amplify the optical heating efficiency by increasing the particle concentration at the illumination region. This effect is demonstrated for Fe 20 nm/Au 20 nm nanodomies in Fig. 4b, in which an 85% enhancement in the temperature rise is observed when particles are magnetically concentrated at the region that blocks the laser path in the cuvette wall (see Fig. S2). As we show below, this effect is especially valuable to locally enhance the photothermal treatments for efficiently killing tumor cells.

In addition to the significant fabrication cost reduction with respect to pure plasmonic nanoparticles and the magnetically enhanced photothermal effects, the Fe layer in the MP nanodomies provides an intense NMR contrast for imaging. To maximize the NMR signal we focus the NMR analysis on the MP nanodomies with the largest magnetic dipole, i.e. 30 nm of Fe. We have studied the relaxation rates ($R_1 = 1/T_1$ and $R_2 = 1/T_2$) as a function of the Fe molar concentration in samples of MP nanoparticles dispersed in agar gel (Fig. 5a). While we do not observe any significant T_1

Table 1
Values of the photothermal conversion efficiency of the Au and Fe/Au nanodomies compared to Au nanorods and Au nanoshells.

	A_{808}	ΔT_{\max}	η
Au 40 nm NDs	0.45	9.5	0.56
Fe 20 nm/Au 20 nm ND	0.54	12.0	0.65
Au nanorods	0.74	14.0	0.67
Au nanoshells	0.56	6.1	0.31

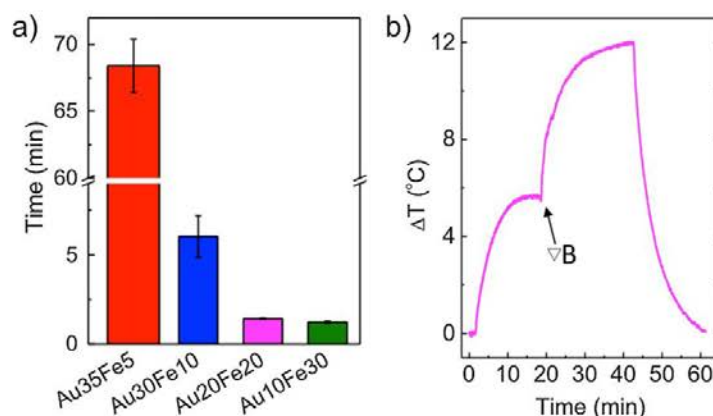


Fig. 4. Magnetic actuation and photothermal amplification analysis. (a) Time required to achieve 95% light transmission for MP nanodomains with different Fe and Au ratios due to the magnetic trapping by a permanent magnet that is attached to the cuvette wall. (b) Temperature increment amplification by magnetically increasing the particle concentration of the Fe 20 nm/Au 20 nm nanodomains in the laser path. The initial particle concentration is 2.4×10^9 particles/mL.

contrast, which is a consequence of the presence of the diamagnetic Au layer in contact to water molecules, we detect very high T_2 contrast. The slope of the R_2 curve as a function of Fe concentration reveals that the relaxivity r_2 is $266 \pm 27 \text{ mM}^{-1} \text{ s}^{-1}$. This relaxivity is between 1.5- and 2-fold larger than that of superparamagnetic iron oxide nanoparticles that have been commercially available as T_2 contrast agents, like Feridex ($105 \text{ mM}^{-1} \text{ s}^{-1}$ at 47 kOe) or Resovist ($176 \text{ mM}^{-1} \text{ s}^{-1}$ at 47 kOe) [40]. Even though these values correspond to slightly lower fields than in our case, substantial increase in their T_2 from 47 kOe to 70 kOe is not expected [40]. Therefore, compared to, for example, the Resovist nanoparticles (50 nm diameter), the larger size and higher density of metallic iron in the MP nanodomains enable packing a much higher amount of Fe atoms per particle. In addition, the Fe atoms in a metallic state induce higher relaxivity than oxidized iron atoms. The sum of both effects makes that the net relaxivity per particle of MP nanodomains is approximately 15-fold higher than that of Resovist particles, highlighting their high potential as T_2 NMR contrast agent. Notably, the nanodomains concentration range necessary to observe sizable T_2 effects is similar to that required for the photothermal treatments, which paves the way for efficient NMR-imaging guided photothermal therapies.

Moreover, the Au layer in the MP nanodomains is a very efficient contrast agent for X-ray imaging. We have exploited this capacity to visualize the internalized nanodomains by synchrotron-based soft X-ray transmission microscopy operating in the water window energy range (520 eV). By employing cryogenic conditions, the soft X-ray microscope enables operating in an environment close to the hydrated physiological conditions. Thus, soft X-ray microscopy can also yield 3D structural information of the entire cell without the need of fixation, dehydration, embedding and sectioning of the samples. The resolution of the soft X-ray microscope is about 40 nm, which is sufficient to visualize individual MP nanodomains at different cellular planes and to map their interaction with the cellular compartments. The X-ray images of Fig. 5b clearly show the individual MP nanodomains internalized by the cells. The movie included in the supporting information enables visualizing the MP nanodomains at different z-planes inside the cell. In addition, for reference, Fig. S9 displays some nanodomains which are outside the cells, since they are added after the cell freezing process to help in the image reconstruction process, showing similar morphology and X-ray absorption. These results highlight the potential of the MP nanodomains as contrast agents in X-ray computed tomography.

Further, MP nanodomains with fluorescent cores provide additional valuable imaging functionalities to understand their *in vitro* behavior and internalization pathways. We have integrated this functionality by fabricating the nanodomains on fluorescent polystyrene nanobeads (excitation at 570 nm and emission at 610 nm), yielding similar surface density on the wafer and colloidal stability. We have employed Fe 20 nm/Au 20 nm nanodomains with fluorescent cores to visualize their interaction and internalization by HeLa cancer cells via 3D confocal microscopy reconstructions and cross-section projections (Fig. 5c and d). Although the Fe/Au bilayer induces a 5-fold reduction of the fluorescent intensity with respect to the bare polymer particles, due to the high absorption cross section of the nanodomains, the fluorescent Fe/Au nanodomains can still be easily visualized by confocal microscopy. To discern internalized from not internalized MP nanodomains, the plasma membrane was labeled (white) to establish the cell boundaries. The nuclei were stained (blue) to determine whether MP nanodomains were able to translocate to the nucleus. Images obtained at different focal planes confirmed that, in the absence of magnetic field, the MP nanodomains could be fully internalized, rather than resting on the cell surface, as it can be seen in the orthogonal cross-sections (Fig. 5d). Discrete red spots, corresponding to MP nanodomains trapped in endosomes/lysosomes can be observed inside the cytoplasm, but not inside the nucleus due to their large size (100 nm in diameter), which prevents crossing the nuclear porous complex [41]. Probably, MP nanodomains are internalized via pinocytosis, forming endosomes that can be visualized as discrete points.

To assess the biomedical potential of the MP nanodomains, we finally tested the effect of photothermal treatments in HeLa cells in challenging conditions of low particle concentration and mild laser intensity (Fig. 6). We used glass bottom dishes with a thickness of 0.17 mm to facilitate light irradiation, where cells were seeded only in the glass region. Cells were incubated for 3 h with cell culture medium containing a concentration of either $10 \mu\text{g/mL}$ or $100 \mu\text{g/mL}$ of Fe 20 nm/Au 20 nm nanodomains.

We have compared the photothermal treatment efficiency either with or without magnetic field concentration of the nanodomains at the illumination region. After the incubation time, the cell culture medium with nanoparticles was replaced by 1 mL of fresh medium to leave only the particles in contact or inside the cells. The cell monolayer was irradiated with a laser at 808 nm emission wavelength during 30 min with an incident intensity

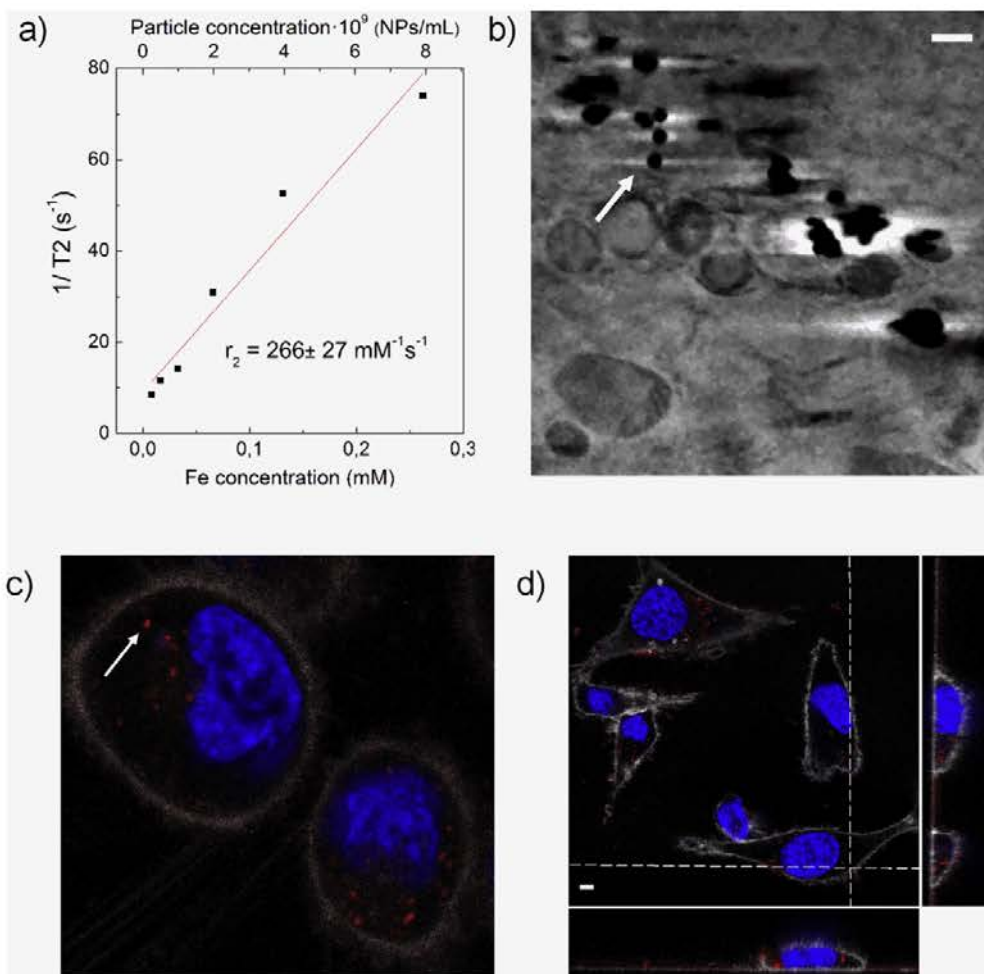


Fig. 5. MP nanodomains as contrast agents for imaging (a) NMR R_2 ($1/T_2$) values of the MP nanodomains with Fe 30 nm/Au 10 nm in agar gel as a function of Fe concentration. (b) Transmission X-ray microscopy image showing the internalized Fe 20 nm/Au 20 nm MP nanodomains as black dots (white arrow). The black diffused regions correspond to nanodomains in different focal planes (see Video S1). (c) Confocal optical image of HeLa cells that have internalized Fe 20 nm/Au 20 nm MP nanodomains with fluorescent core, seen as red dots in the image (white arrow). The plasma membranes are shown in white and the nuclei in blue. (d) Confocal image (middle) and its orthogonal projections of the z-stack reconstructions (right and bottom) of consecutive focal planes (0.5 μm each). Discrete red spots corresponding to MP nanodomains trapped in endosomes/lysosomes can be observed. Scale bars: 5 μm . (For interpretation of the references to color in this figure legend, the reader is referred to the web version of the article.)

of 5 W/cm^2 . Due to the limited irradiated area (laser spot diameter of 6 mm), we analyzed cell viability using a colorimetric assay (LIVE/DEAD[®]), which enables quantifying live (green) and dead (red) cells according to their esterase activity and membrane integrity, respectively (Fig. 6a–c). In these assays we compared the light treatment effect in control samples without nanodomains and in samples with two different initial concentrations of nanodomains (10 $\mu\text{g/mL}$ and 100 $\mu\text{g/mL}$), either in the absence of magnetic field or with magnetic concentration at the illumination region by a spherical FeNdB magnet (12 mm in diameter, 2.5 kOe at the surface) (see Fig. S8). Firstly, the results show that irradiated cell cultures without MP nanodomains do not exhibit statistically significant differences with the non-irradiated control (Fig. 6a), i.e. the laser actuation does not cause cytotoxicity. Secondly, we evaluated the effect of the MP nanodomains in cell cultures with and without magnetic concentration, showing that the presence of MP nanodomains does not induce a significant viability decreases, even for high nanodomains concentration (100 $\mu\text{g/mL}$) under magnetic concentration

conditions (Fig. 6a). Finally, we assessed the effect of light irradiation in cells containing MP nanodomains. The results show a minimal decrease in the cell viability without magnetic concentration for a nanodomains concentration of 10 $\mu\text{g/mL}$. The concentration must be increased up to 100 $\mu\text{g/mL}$ to observe a significant viability reduction in the absence of magnetic concentration. In contrast, a viability reduction of nearly 100% after the light treatment is observed in the case of magnetic concentration at the illumination region for both initial nanodomains concentrations of 10 $\mu\text{g/mL}$ and 100 $\mu\text{g/mL}$ (Fig. 6a). Interestingly, such drastic viability reduction is observed 24 h after the treatment for the initial 100 $\mu\text{g/mL}$ concentration, whereas it takes 48 h to get the near 100% reduction when the initial concentration is 10 $\mu\text{g/mL}$. The different light effect on the cancer cells can be clearly observed in the scanning electron microscopy images of Fig. 6d–f. For magnetically concentrated samples with initial 100 $\mu\text{g/mL}$ concentration, a clear loss of cell membrane integrity is observed, thereby reflecting the unfavorable fast necrotic cell death that is caused by the very intense

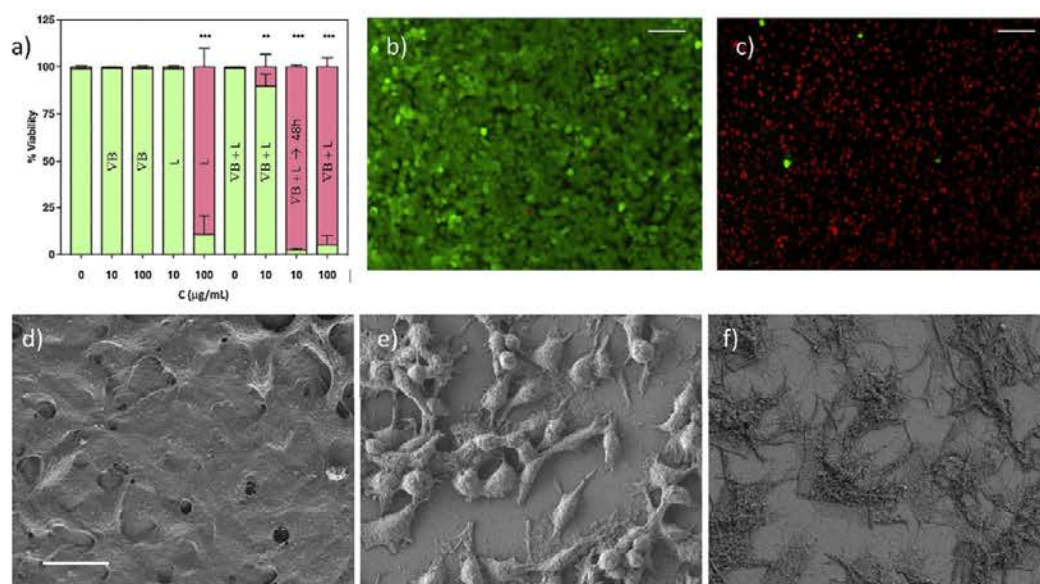


Fig. 6. Effects of photothermal treatment *in vitro*. (a) Results of the *in vitro* photothermal treatments in HeLa cells under different concentrations of MP nanodomers (C), magnetic manipulation (∇ B) and light actuation (L) conditions. The viability assays were performed 24 h after the treatment, except for the nanodomers with concentration of 10 $\mu\text{g}/\text{mL}$ under magnetic manipulation and light treatment (∇ B+L), in which the assays were carried out both after 24 h and 48 h. (b) and (c) Typical fluorescent images of live (green) and dead (red) cells of a sample with non-irradiated cells, and a sample of cells after the light treatment, respectively, for an initial concentration of 10 $\mu\text{g}/\text{mL}$ of nanodomers with magnetic concentration (scale bars 100 μm). (d)–(f) Scanning electron microscopy images of the HeLa cells for the control (d), and after the magnetic concentration and light treatment for initial nanodomers concentrations of 10 $\mu\text{g}/\text{mL}$ (e) and 100 $\mu\text{g}/\text{mL}$ (f). Scale bar: 20 μm . (For interpretation of the references to color in this figure legend, the reader is referred to the web version of the article.)

photothermal actuation under these conditions. On the contrary, for the initial concentration of 10 $\mu\text{g}/\text{mL}$, the cell membrane disruption is not perceived, although there is a clear morphological change in the cancer cells. The longer time to generate the viability reduction suggests a more controlled cell death pathway, which is desirable for the photothermal treatments. Importantly, the magnetic concentration at the light treatment region enables at least a 10-fold reduction of the quantity of injected particles to achieve the nearly 100% therapeutic efficacy, which can be highly relevant to reduce the therapy cost and the bioaccumulation of the nanoparticles in other organs.

The comparison of our results with other nanoparticles for photothermal therapies is not straightforward, since different composition, surface functionalization and concentration of particles have been employed, in addition to different irradiation conditions, and cell types [42]. Nevertheless, some trends can be found regarding particle concentration and exposure conditions. Studies that use high nanoparticle concentration (from 100 to 250 $\mu\text{g}/\text{mL}$) apply low or mild exposure conditions (from 0.1 to 10 W/cm^2), while studies using low nanoparticles concentration (from 6.6 to 36.5 $\mu\text{g}/\text{mL}$) typically need higher exposure conditions (from 15.3 to 250 W/cm^2) to obtain good efficiencies on cell death. In the present work, MP nanodomers have demonstrated to be a good candidate for photothermal treatments using low initial concentration (10 $\mu\text{g}/\text{mL}$) and mild incident intensity (5 W/cm^2) compared to other published studies [43]. This laser intensity is higher than the recommended clinical safety values (0.3 W/cm^2), but our *in vitro* assays with cell monolayers are much more demanding from the optical perspective than *in vivo* conditions, in which light can be efficiently absorbed along several millimeters. In contrast, the light absorption region is thinner than 10 μm in a 2D cell culture with nanoparticles only in the cell monolayer. The generated heat in the cell monolayer rapidly diffuses toward the cell medium and

the glass substrate due to the generated temperature difference between the cell monolayer and both the cell media and the substrate, thereby forcing the need of a higher light intensity to achieve temperature increments with sufficient therapeutic effect.

Finally, it is worth mentioning that, although the magnetic manipulation is a powerful tool to locally control the photothermal effects, the nanodomers could offer additional cell targeting by exploiting their straightforward functionalization with specific antibodies, proteins such as transferrin (see Fig. S2), and molecules such as folate [44], musuin7 [41], RGD peptide [42] or other specific molecules capable of preferentially binding the MP nanodomers to cancer cells overexpressing particular membrane receptors.

4. Conclusion

We have shown that MP nanodomers can have high potential for therapeutic and diagnostic applications. Compared to other magnetic, plasmonic or magneto-plasmonic nanoparticles fabricated by chemical synthesis, our fabrication process enables easier control in the magnetic and optical properties. The capacity to functionalize the MP nanodomers on the substrate and their direct dispersion in water or buffer represent also significant advantages with respect to chemically synthesized nanoparticles, yielding highly stable colloidal dispersions during months. Compared to state-of-the-art plasmonic nanoparticles for photothermal therapies, MP nanodomers offer higher heating efficiency at lower cost given by their strong manipulation *via* magnetophoretic force, very high contrast for NMR and X-ray imaging, and easy incorporation of fluorophores in the polymer core. Compared to iron oxide nanoparticles used in magnetic hyperthermia, the high heating efficiency of MP nanodomers enables local thermal treatments at much lower particle concentration [45]. Moreover, MP nanodomers show much higher T_2 contrast per particle for NMR imaging than that of

commercial iron oxide nanoparticles. Demonstration of both low cytotoxicity and magnetically enhanced efficiency for photothermal therapy at low particle concentrations and mild light intensity encourages the transfer of this nanotechnology to *in vivo* therapies. The high optical heating efficiency of the nanodomains could be also applied to develop temperature responsive drug delivery systems that could be magnetically controlled and visualized *via* computed X-ray tomography, NMR imaging, or fluorescence. The optical anisotropy in nanodomains with low Fe ratio and their capacity to efficiently rotate in the liquid under an alternating magnetic field can also provide interesting tools for the development of nanobiosensors and nanothermometers [46].

4.1. Data availability

The raw/processed data required to reproduce these findings cannot be shared at this time due to technical or time limitations.

Acknowledgements

Zhi Li and Antonio Aranda-Ramos contributed equally to this work. This work is supported by Spanish Ministry of Economy, Industry and Competitiveness (MINECO) and European Regional Development Fund (FEDER) (Projects number: MAT2013-48628-R, MAT2016-77391-R, MAT2017-86357-C3-1-R and MAT2017-86357-C3-3-R). Generalitat de Catalunya (2017-SGR-292) is acknowledged. ICN2 is funded by the Centres de Recerca de Catalunya (CERCA) Programme/Generalitat de Catalunya. ICN2 also acknowledges support from the Severo Ochoa Program (MINECO, Grant SEV-2013-0295). Zhi Li acknowledges the Chinese Scholarship Council Program (201506950059) for financial support. The ALBA Synchrotron is acknowledged for the provision of beamline, and the MISTRAL beamline staff is acknowledged for their help during the X-ray microscopy measurements. Jordi Sort acknowledges the financial support by the European Research Council (SPIN-PORICS 2014-Consolidator Grant, Agreement N° 648454).

Appendix A. Supplementary data

Supplementary data associated with this article can be found in the online version, at doi:10.1016/j.apmt.2018.07.008.

References

- [1] G.J. Kim, S. Nie, Targeted cancer nanotherapy, *Mater. Today* 8 (2005) 28–32, [http://dx.doi.org/10.1016/S1369-7021\(05\)71034-8](http://dx.doi.org/10.1016/S1369-7021(05)71034-8).
- [2] R. Bardhan, S. Lal, A. Joshi, N.J. Halas, Theranostic nanoshells: from probe design to imaging and treatment of cancer, *Acc. Chem. Res.* 44 (2011) 936–946, <http://dx.doi.org/10.1021/ar200023x>.
- [3] S.D. Jo, S.H. Ku, Y.Y. Won, S.H. Kim, I.C. Kwon, Targeted nanotheranostics for future personalized medicine: recent progress in cancer therapy, *Theranostics* 6 (2016) 1362–1377, <http://dx.doi.org/10.7150/thno.15335>.
- [4] G. Chen, I. Roy, C. Yang, P.N. Prasad, Nanochemistry and nanomedicine for nanoparticle-based diagnostics and therapy, *Chem. Rev.* 116 (2016) 2826–2885, <http://dx.doi.org/10.1021/acs.chemrev.5b00148>.
- [5] X.H. Huang, I.H. El-Sayed, W. Qian, M.A. El-Sayed, Cancer cell imaging and photothermal therapy in the near-infrared region by using gold nanorods, *J. Am. Chem. Soc.* 128 (2006) 2115–2120, <http://dx.doi.org/10.1021/ja057254a>.
- [6] S. Lal, S.E. Clare, N.J. Halas, Nanoshell-enabled photothermal cancer therapy: impending clinical impact, *Acc. Chem. Res.* 41 (2008) 1842–1851, <http://dx.doi.org/10.1021/ar800150g>.
- [7] C.M. Hessel, V.P. Pattani, M. Rasch, M.G. Panthani, B. Koo, J.W. Tunnell, B.A. Korgel, Copper selenide nanocrystals for photothermal therapy, *Nano Lett.* 11 (2011) 2560–2566, <http://dx.doi.org/10.1021/nl201400z>.
- [8] L. Cheng, K. Yang, Y. Li, J. Chen, C. Wang, M. Shao, S.T. Lee, Z. Liu, Facile preparation of multifunctional upconversion nanoprobe for multimodal imaging and dual-targeted photothermal therapy, *Angew. Chem. Int. Ed.* 50 (2011) 7385–7390, <http://dx.doi.org/10.1002/anie.201101447>.
- [9] Z. Sun, H. Xie, S. Tang, X.F. Yu, Z. Guo, J. Shao, H. Zhang, H. Huang, H. Wang, P.K. Chu, Ultrasmall black phosphorus quantum dots: synthesis and use as photothermal agents, *Angew. Chem. Int. Ed.* 54 (2015) 11526–11530, <http://dx.doi.org/10.1002/anie.201506154>.
- [10] W. Zhang, Z. Guo, D. Huang, Z. Liu, X. Guo, H. Zhong, Synergistic effect of chemo-photothermal therapy using PEGylated graphene oxide, *Biomaterials* 32 (2011) 8555–8561, <http://dx.doi.org/10.1016/j.biomaterials.2011.07.071>.
- [11] H. Liu, D. Chen, L. Li, T. Liu, L. Tan, X. Wu, F. Tang, Multifunctional gold nanoshells on silica nanorattles: a platform for the combination of photothermal therapy and chemotherapy with low systemic toxicity, *Angew. Chem. Int. Ed.* 50 (2011) 891–895, <http://dx.doi.org/10.1002/anie.2011002820>.
- [12] W. Guo, F. Wang, D. Ding, C. Song, C. Guo, S. Liu, TiO_{2-x} based nanoplatform for bimodal cancer imaging and NIR-triggered chem/photodynamic/photothermal combination therapy, *Chem. Mater.* 29 (2017) 9262–9274, <http://dx.doi.org/10.1021/acs.chemmater.7b03241>.
- [13] J.C. Yang, Y. Chen, Y.H. Li, X.B. Yin, Magnetic resonance imaging-guided multi-drug chemotherapy and photothermal synergistic therapy with pH and NIR-stimulation release, *ACS Appl. Mater. Interfaces* 9 (2017) 22278–22288, <http://dx.doi.org/10.1021/acsami.7b06105>.
- [14] A. Li Volsi, C. Scialabba, V. Vetri, G. Cavallaro, M. Licciardi, G. Giammona, Near-infrared light responsive folate targeted gold nanorods for combined photothermal-chemotherapy of osteosarcoma, *ACS Appl. Mater. Interfaces* 9 (2017) 14453–14469, <http://dx.doi.org/10.1021/acsami.7b03711>.
- [15] J.R. Cole, N.A. Mirin, M.W. Knight, G.P. Goodrich, N.J. Halas, Photothermal efficiencies of nanoshells and nanorods for clinical therapeutic applications, *J. Phys. Chem. C* 113 (2009) 12090–12094, <http://dx.doi.org/10.1021/jp900359z>.
- [16] X. Huang, M.A. El-Sayed, Gold nanoparticles: optical properties and implementations in cancer diagnosis and photothermal therapy, *J. Adv. Res.* 1 (2010) 13–28, <http://dx.doi.org/10.1016/j.jare.2010.02.002>.
- [17] R. Weissleder, A clearer vision for *in vivo* imaging, *Nat. Biotechnol.* 19 (2001) 316–317, <http://dx.doi.org/10.1038/86684>.
- [18] J.W. Nichols, Y.H. Bae, Odyssey of a cancer nanoparticle: from injection site to site of action, *Nano Today* 7 (2012) 606–618, <http://dx.doi.org/10.1016/j.nantod.2012.10.010.Odyssey>.
- [19] S. Schrittwieser, B. Pelaz, W.J. Parak, S. Lentijo-Mozo, K. Soulatia, J. Dieckhoff, F. Ludwig, T. Altantzis, S. Bals, J. Schotter, Homogeneous protein analysis by magnetic core-shell nanorod probes, *ACS Appl. Mater. Interfaces* 8 (2016) 8893–8899, <http://dx.doi.org/10.1021/acsami.5b11925>.
- [20] E.C. Ximenes, W.Q. Santos, U. Rocha, U.K. Kagola, F. Sanz-Rodríguez, N. Fernández, A.D.S. Gouveia-Neto, D. Bravo, A.M. Domingo, B. Del Rosal, C.D.S. Brites, L.D. Carlos, D. Jaque, C. Jacinto, Unveiling *in vivo* subcutaneous thermal dynamics by infrared luminescent nanothermometers, *Nano Lett.* 16 (2016) 1695–1703, <http://dx.doi.org/10.1021/acs.nanolett.5b04611>.
- [21] G. Armelles, A. Cebollada, A. García-Martín, J.M. García-Martín, M.U. González, J.B. González-Díaz, E. Ferreiro-Vila, J.F. Torrado, Magnetoplasmonic nanostructures: systems supporting both plasmonic and magnetic properties, *J. Opt. A: Pure Appl. Opt.* 11 (2009) 114023, <http://dx.doi.org/10.1088/1464-4258/11/11/114023>.
- [22] M. Donolato, P. Antunes, R.S. Bejhed, T. Zardán Gómez De La Torre, F.W. Österberg, M. Strömberg, M. Nilsson, M. Strømme, P. Svedlindh, M.F. Hansen, P. Vavassori, Novel readout method for molecular diagnostic assays based on optical measurements of magnetic nanobead dynamics, *Anal. Chem.* 87 (2015) 1622–1629, <http://dx.doi.org/10.1021/ac503191v>.
- [23] C. Peters, O. Ergeneman, P.D.W. García, M. Müller, S. Pané, B.J. Nelson, C. Hierold, Superparamagnetic twist-type actuators with shape-independent magnetic properties and surface functionalization for advanced biomedical applications, *Adv. Funct. Mater.* 24 (2014) 5269–5276, <http://dx.doi.org/10.1002/adfm.201400596>.
- [24] X.Z. Chen, M. Hoop, N. Shamsudhin, T. Huang, B. Özkale, Q. Li, E. Siringil, F. Mushtaq, L. Di Tizio, B.J. Nelson, S. Pané, Hybrid magnetoelectric nanowires for nanorobotic applications: fabrication, magnetoelectric coupling, and magnetically assisted *in vitro* targeted drug delivery, *Adv. Mater.* 29 (2017), <http://dx.doi.org/10.1002/adma.201605458>.
- [25] J.B. González-Díaz, A. García-Martín, J.M. García-Martín, A. Cebollada, G. Armelles, B. Sepúlveda, Y. Alaverdyan, M. Käll, Plasmonic Au/Co/Au nanosandwiches with enhanced magneto-optical activity, *Small* 4 (2008) 202–205, <http://dx.doi.org/10.1002/sml.200700594>.
- [26] B. Sepúlveda, J.B. González-Díaz, A. García-Martín, L.M. Lechuga, G. Armelles, Plasmon-induced magneto-optical activity in nanosized gold disks, *Phys. Rev. Lett.* 104 (2010) 147401, <http://dx.doi.org/10.1103/PhysRevLett.104.147401>.
- [27] G. Armelles, A. Cebollada, A. García-Martín, M.U. González, Magnetoplasmonics: magnetoplasmonics: combining magnetic and plasmonic functionalities, *Adv. Opt. Mater.* 1 (2013) 10–35, <http://dx.doi.org/10.1002/adom.201370002>.
- [28] A. Espinosa, M. Bugnet, G. Radtke, S. Neveu, G.A. Botton, A. Claire-Wilhelm, Abou-Hassan, Can magneto-plasmonic nanohybrids efficiently combine photothermia with magnetic hyperthermia? *Nanoscale* 7 (2015) 18872–18877, <http://dx.doi.org/10.1039/c5nr06168g>.
- [29] M. Abdulla-Al-Mamun, Y. Kusumoto, T. Zannat, Y. Horie, H. Manaka, Au-ultrathin functionalized core-shell (Fe₃O₄@Au) monodispersed nanocubes for a combination of magnetic/plasmonic photothermal cancer cell killing, *RSC Adv.* 3 (2013) 7816–7827, <http://dx.doi.org/10.1039/c3ra21479f>.
- [30] I. Uribe, C. Muñoz, L. Gomez, C. Marquina, V. Sebastian, M. Arruebo, J. Santamaria, Magneto-plasmonic nanoparticles as theranostic platforms for magnetic resonance imaging, drug delivery and NIR hyperthermia applications, *Nanoscale* 6 (2014) 9230–9240, <http://dx.doi.org/10.1039/c4nr01588f>.

- [31] Z. Xu, Y. Hou, S. Sun, Magnetic core/shell $\text{Fe}_3\text{O}_4/\text{Au}$ and $\text{Fe}_3\text{O}_4/\text{Au}/\text{Ag}$ nanoparticles with tunable plasmonic properties, *J. Am. Chem. Soc.* 129 (2007) 8698–8699, <http://dx.doi.org/10.1021/ja073057v>.
- [32] W. Dong, Y. Li, D. Niu, Z. Ma, J. Gu, Y. Chen, W. Zhao, X. Liu, C. Liu, J. Shi, Facile synthesis of monodisperse superparamagnetic Fe_3O_4 core@hybrid@Au shell nanocomposite for bimodal imaging and photothermal therapy, *Adv. Mater.* 23 (2011) 5392–5397, <http://dx.doi.org/10.1002/adma.201103521>.
- [33] E. Fantechi, A.G. Roca, B. Sepúlveda, P. Torruella, S. Estradé, F. Peiró, E. Coy, S. Jurga, N.G. Bastús, J. Nogués, V. Puntès, Seeded growth synthesis of $\text{Au}-\text{Fe}_3\text{O}_4$ heterostructured nanocrystals: rational design and mechanistic insights, *Chem. Mater.* 29 (2017) 4022–4035, <http://dx.doi.org/10.1021/acs.chemmater.7b00608>.
- [34] P. Hanarp, D.S. Sutherland, J. Gold, B. Kasemo, Control of nanoparticle film structure for colloidal lithography, *Colloid Surf. A* 214 (2003) 23–36, [http://dx.doi.org/10.1016/S0927-7757\(02\)00367-9](http://dx.doi.org/10.1016/S0927-7757(02)00367-9).
- [35] J.I. Martín, J. Nogués, K. Liu, J.L. Vicent, I.K. Schuller, Ordered magnetic nanostructures: fabrication and properties, *J. Magn. Magn. Mater.* 256 (2003) 449–501, [http://dx.doi.org/10.1016/S0304-8853\(02\)00898-3](http://dx.doi.org/10.1016/S0304-8853(02)00898-3).
- [36] S.H. Chung, R.D. McMichael, D.T. Pierce, J. Unguris, Phase diagram of magnetic nanodisks measured by scanning electron microscopy with polarization analysis, *Phys. Rev. B: Condens. Matter Phys.* 81 (2010) 024410, <http://dx.doi.org/10.1103/PhysRevB.81.024410>.
- [37] D.K. Roper, W. Ahn, M. Hoepfner, Microscale heat transfer transduced by surface plasmon resonant gold nanoparticles, *J. Phys. Chem. C* (2007) 3636–3641, <http://dx.doi.org/10.1021/jp064341w>.
- [38] L. Uba, A. Polewko, S. Uba, R. Gontarz, A.N. Yaresko, V.N. Antonov, Determination of the interfacial magneto-optical properties in sputtered Fe/Au multilayer structures, *Phys. Stat. Sol. A* 196 (2003) 145–148, <http://dx.doi.org/10.1002/pssa.200306428>.
- [39] D. Regatos, D. Fariña, A. Calle, A. Cebollada, B. Sepúlveda, G. Armelles, L.M. Lechuga, $\text{Au}/\text{Fe}/\text{Au}$ multilayer transducers for magneto-optic surface plasmon resonance sensing, *J. Appl. Phys.* 108 (2010) 054502, <http://dx.doi.org/10.1063/1.3475711>.
- [40] M. Rohrer, H. Bauer, J. Mintorovitch, M. Requardt, H.J. Weinmann, Comparison of magnetic properties of MRI contrast media solutions at different magnetic field strengths, *Invest. Radiol.* 40 (2005) 715–724, <http://dx.doi.org/10.1097/01.Rii.0000184756.66360.D3>.
- [41] S. Huo, S. Jin, X. Ma, X. Xue, K. Yang, A. Kumar, P.C. Wang, J. Zhang, Z. Hu, X.J. Liang, Ultrasmall gold nanoparticles as carriers for nucleus-based gene therapy due to size-dependent nuclear entry, *ACS Nano* 8 (2014) 5852–5862, <http://dx.doi.org/10.1021/nn5008572>.
- [42] J. Beik, Z. Abed, F.S. Ghoreishi, S. Hosseini-Nami, S. Mehrzadi, A. Shakeri-Zadeh, S.K. Kamrava, Nanotechnology in hyperthermia cancer therapy: from fundamental principles to advanced applications, *J. Control. Release* 235 (2016) 205–221, <http://dx.doi.org/10.1016/j.jconrel.2016.05.062>.
- [43] I.M.M. Paino, V.S. Marangoni, R. de, C.S. de Oliveira, L.M.G. Antunes, V. Zucolotto, Cyto and genotoxicity of gold nanoparticles in human hepatocellular carcinoma and peripheral blood mononuclear cells, *Toxicol. Lett.* 215 (2012) 119–125, <http://dx.doi.org/10.1016/j.toxlet.2012.09.025>.
- [44] O. Penon, T. Patiño, L. Barrios, C. Nogués, D.B. Amabilino, K. Wurst, L. Pérez-García, A new porphyrin for the preparation of functionalized water-soluble gold nanoparticles with low intrinsic toxicity, *ChemistryOpen* 4 (2015) 127–136, <http://dx.doi.org/10.1002/open.201402092>.
- [45] A. Espinosa, R. Di Corato, J. Kolosnjaj-Tabi, P. Flaud, T. Pellegrino, C. Wilhelm, Duality of iron oxide nanoparticles in cancer therapy: amplification of heating efficiency by magnetic hyperthermia and photothermal bimodal treatment, *ACS Nano* 10 (2016) 2436–2446, <http://dx.doi.org/10.1021/acsnano.5b07249>.
- [46] Z. Li, A. Lopez-Ortega, A. Aranda-Ramos, J.L. Tajada, J. Sort, C. Nogue, P. Vavassori, J. Nogue, B. Sepulveda, Simultaneous local heating/thermometry based on plasmonic magneto-chromic nanoheaters, *Small* 14 (2018) 1800868, <http://dx.doi.org/10.1002/sml.201800868>.

Supporting Information

Magnetically amplified photothermal therapies and multimodal imaging with magneto-plasmonic nanodomains

Zhi Li,^{a,d} Antonio Aranda-Ramos,^b Pau Güell-Grau,^a José Luis Tajada,^a Laia Pou-Macayo,^b Silvia Lope Piedrafita,^c Francesc Pi,^d Alejandro Gómez Roca,^a María Dolors Baró,^d Jordi Sort,^{d,e} Carme Nogués,^b Josep Nogués,^{a,e} and Borja Sepúlveda^{a,*}

^a Catalan Institute of Nanoscience and Nanotechnology (ICN2), CSIC and BIST, Campus UAB, Bellaterra, 08193 Barcelona, Spain

^b Departament de Biologia Cel·lular, Fisiologia i Immunologia, Facultat de Biociències, Universitat Autònoma de Barcelona, Bellaterra, 08193 Barcelona, Spain.

^c Servei de Ressonància Magnètica Nuclear, Universitat Autònoma de Barcelona, Bellaterra, 08193 Barcelona, Spain, and Centro de Investigación Biomédica en Red en Bioingeniería, Biomateriales y Nanomedicina (CIBER-BBN).

^d Departament de Física, Facultat de Ciències, Universitat Autònoma de Barcelona, Bellaterra, 08193 Barcelona, Spain.

^e ICREA, Pg. Lluís Companys 23, 08010 Barcelona, Spain.

Table S1. Results of the mass spectrometry analysis from several wafers dispersed in 1 mL of water. These measurements confirm that the Au/Fe ratio corresponds to the nominal evaporated one.

Nanodomos	Fe (mg/L)	Error of Fe (%)	Au (mg/L)	Error of Au (%)	Particle concentration (10 ⁹ NPs/mL)
Fe 20nm, Au 20 nm	169	4.3	444	2.7	140
Fe 20nm, Au 20 nm	171	2.4	396	2.0	134
Fe 30nm, Au 10 nm	251	1.6	213	2.0	138
Fe 30nm, Au 10 nm	234	1.8	198	2.3	128

Figure S1. Schematic drawing of the fabrication steps of the MP nanodomains

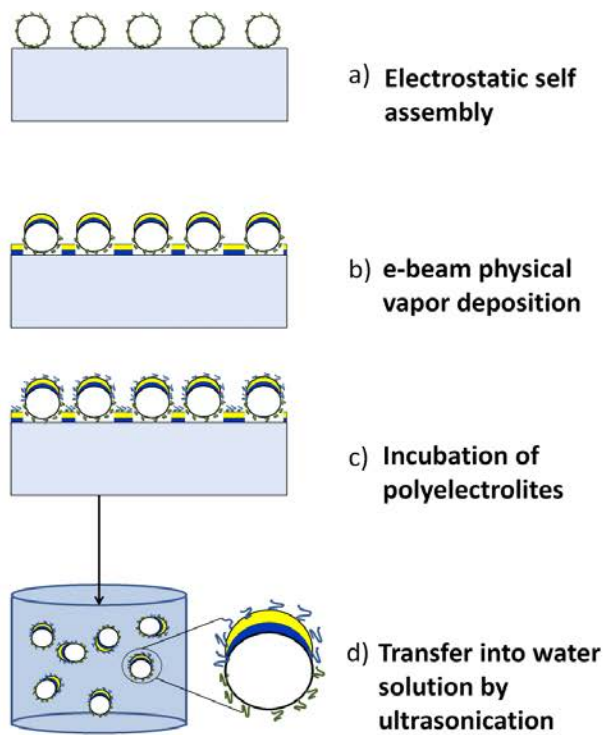


Figure S2. Fourier transform infrared (FTIR) analysis of the biofunctionalization with transferrin protein on the Fe/Au nanodomes surface on the substrate. a) Schematic picture of the transferrin directly linked to the bare Au film of the nanodomes on the wafer. b) FTIR analysis of the transferrin and transferrin/PSS layers showing that the PSS does not displace the transferrin from the surface. c) FTIR signal of the attached transferrin under different conditions of incubation time and ionic strength, showing highest efficiency after incubation in water for 1h.

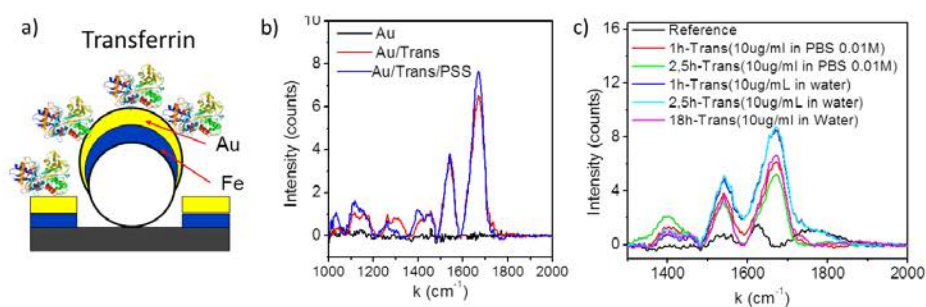


Figure S3. Schematic drawings of the experimental set-ups to analyze the photothermal effects of the MP nanodomains and the magnetic manipulation *via* magnetophoretic forces. a) Lateral view of the set-up to measure the temperature variations with the infrared (IR) thermometer and the transmitted light power. b) and c) Top view of the set-up to measure the magnetophoretic forces and the magnetically amplified photothermal effects, respectively

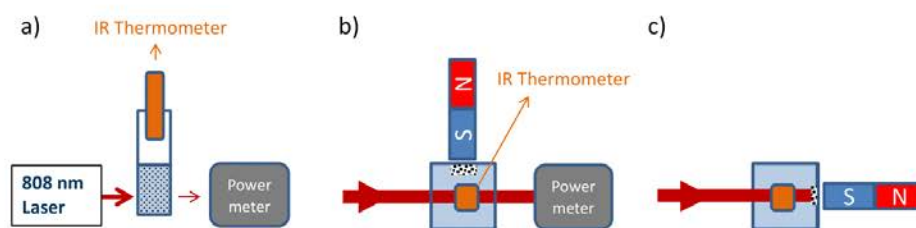


Figure S4. FDTD calculations of the scattering cross section C_{sc} and absorption cross section C_{ab} for MP nanodomes with different Au/Fe ratios in the longitudinal and transversal configurations.

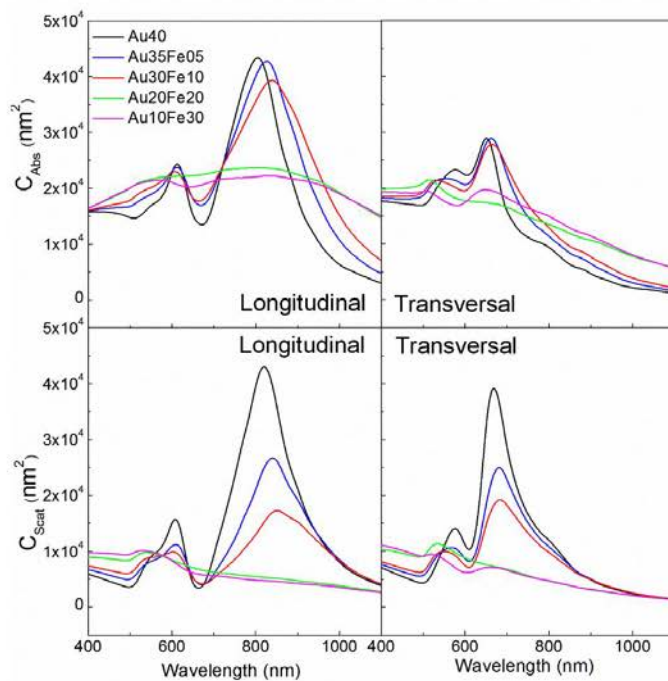


Figure S5. Experimental UV-vis spectra of Au nanodomes with different Au thickness.

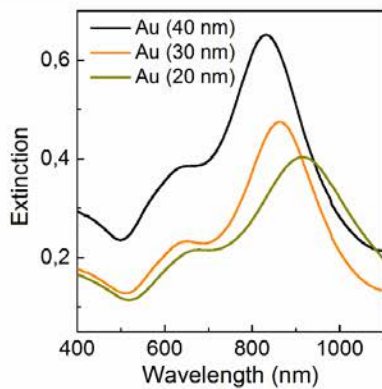


Figure S6. Comparison of the VSM hysteresis loops for MP nanodomes with 5 nm and 10 nm of Fe for equal surface coverage and sample size.

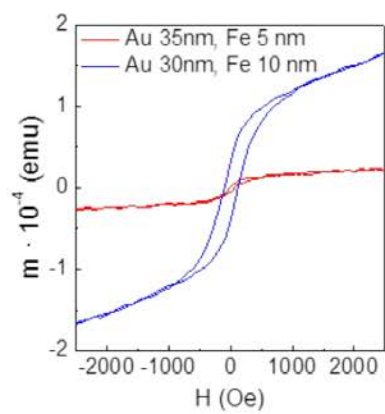


Figure S7. Experimental comparison of the heating efficiency in Fe 20 nm / Au 20 nm MP nanodomains, Au nanorods, and Au nanoshells for: a) equal mass concentration (10 $\mu\text{g/mL}$), and b) equal particle concentration ($2.4 \cdot 10^9$ particles/mL).

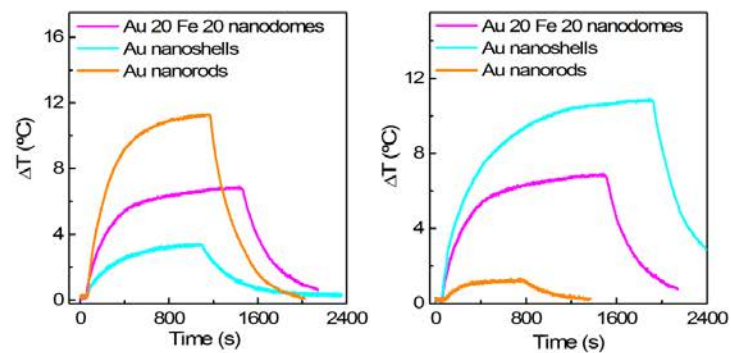


Figure S8. Schematic drawing of the experimental set-up for the *in vitro* assessment of the photothermal therapies under magnetic concentration, which involves two steps: a) magnetic concentration with a 12 mm diameter FeNdB magnet, and b) light treatment for 30 min.

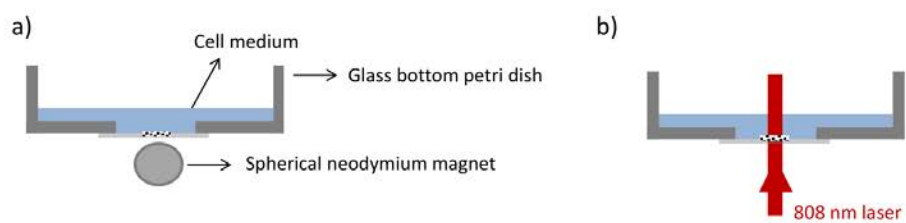
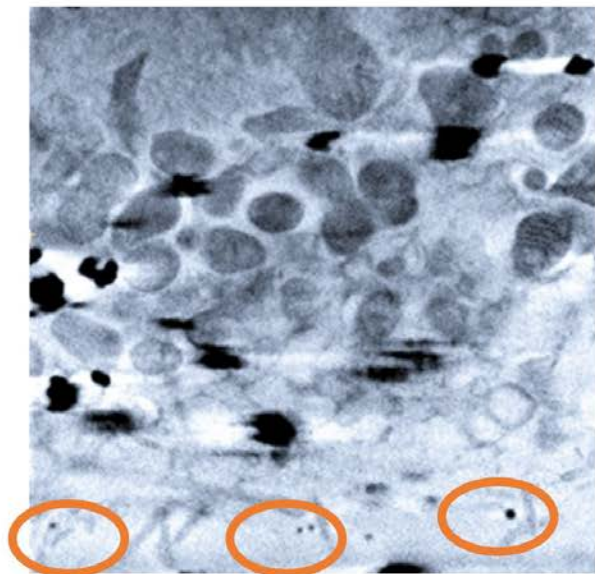
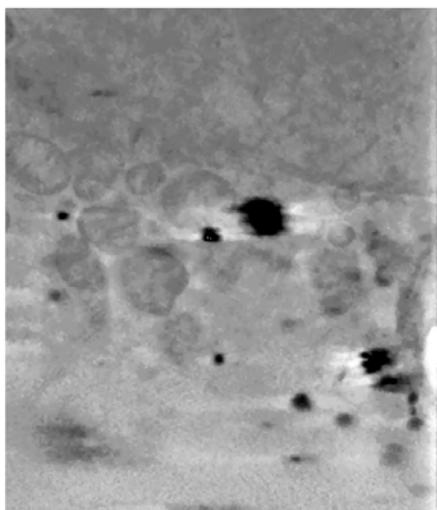


Figure S9. X-ray microscopy image showing the MP nanodomains outside of the cells, which are introduced on the samples after the freezing process.



Movie 1. X-ray microscopy video showing the MP nanodomes internalized at different depths inside the HeLa cells.



Chapter 2

2.1 Simultaneous local heating/thermometry based on plasmonic magnetochromic nanoheaters

The motivation for Chapter 2 came from a very relevant detail of the *in vitro* tests in Chapter 1. The magnetically amplified photothermal therapy with 100 $\mu\text{g}/\text{mL}$ of nanodomes induced a near 100% cell death after 24h. In contrast, the sample with 10 $\mu\text{g}/\text{mL}$ nanodomes showed a “delayed” cell death, with a cell viability reduction from 90% after 24h to 0% after 48h. This interesting behaviour indicates a regulated apoptosis rather than a severe necrosis, under these conditions. This result highlighted the necessity to locally detect and control the induced temperature changes during optical heating to control the condition to favour the apoptosis pathway. Therefore, in Chapter 2 we focused on developing the nanodomes and the detection tools to integrate in the same nanostructure the capabilities of efficient photothermal heating and temperature self-monitoring.

The initial work of Chapter 2 was motivated by the interesting magnetochromic effects, i.e. the change in the optical spectra under a homogeneous magnetic field, of the magneto-plasmonic nanodomes.

The structural asymmetry of the nanodomes generate intense optical anisotropy due to the presence of different optical resonances along two orthogonal orientations of the nanodomes with respect to light polarization. Therefore, different resonance bands can be excited when the orientation of the plane of semishells is parallel or perpendicular with the polarization of the incident light. As the nanodomes in solution can be aligned with their magnetization parallel to the external magnetic field, intense spectral changes can be magnetically induced when the incident light is linearly polarized.

To maximize the optical changes under an external magnetic field, we exploited our hybrid nanofabrication strategy to design (Co/Au) nanodomes merging unprecedented out-of-plane magnetization and maximized optical anisotropy in the NIR in an almost spherical structure. This unique combination permitted the very efficient rotation of the nanodomes under low external alternating magnetic field, and the generation frequency

dependent strong opto-magnetic modulation. This strong modulation could even be observed in very diluted dispersions which were undetectable by high-end UV-Vis spectrometers.

A custom-made opto-magnetic characterization setup enabled us analyzing and monitoring in real-time the nanodomains rotation as a function of the magnetic frequency. In particular, the phase lag between the applied magnetic field and the optical signal is highly dependent on the fluid viscosity, which in turn has a strong dependence on the temperature, especially for water solutions. Therefore, quantification of such phase-lag was employed to monitor the viscosity reduction in the surrounding fluid of the nanodomains during optical heating, as the novel simultaneous nano-heating/thermometry concept, by using a single NIR light beam for actuation and detection.

This nanothermometers exhibited a detection limit around 0.05 °C, which is comparable to the state-of-art luminescent nanothermometers, but using a much simpler and cost-effective detection system. The capacity to integrate efficient heating and nanothermometry in a single nanostructure and using a single light beam are additional relevant advantages.

To demonstrate the capability to work in practical biomedical conditions, *in vitro* tests were done in highly concentrated cell dispersions (6×10^6 cells mL⁻¹), showing a detection limit of 0.15 °C, despite the strong and dynamic scattering interferences caused by the moving cells. Moreover, to avoid the concerns of Co toxicity, we proved that 5 nm Fe/ 35 nm Au nanodomains with in-plane magnetization and high optical anisotropy could be also employed as nanothermometer probes showing a detection limit of 0.08 °C.

In conclusion, the unprecedented capacity to merge high photothermal heating and local temperature detection sensitivity in low-cost and scalable nanostructures and with a simple detection set-up highlight the great biomedical potential of this nanotechnology.

2.2 Personal Contribution

Due to the complex theoretical and experimental work, this article is accomplished by multiple collaborations. Thus, it is important to mention which were my contributions for this article.

My independent work included: **i)** Co/Au nanodomains fabrication, **ii)** characterizations of physicochemical properties (lithography pattern, size, surface charge) using scanning electron microscopy (SEM) and dynamic light scattering (DLS) and optical properties (extinction spectra) using vis-near infrared spectroscopy, **iii)** photothermal heating measurements using a custom-made optical system (built in collaboration with Borja Sepúlveda), **iv)** opto-magnetic modulation measurements using a custom-made magnetic-optical combined system (built in collaboration with Borja Sepúlveda), **v)** simultaneous nanoheating/thermometry with the nanodomains in water and cell dispersions, **vi)** fast optical heating and thermal detections in microfluidic channel.

I participated in other experiments, where the tests were carried out mainly by some colleagues, but I was personally involved in the experiments. These include **i)** high-resolution transmission electron microscopy (HR-TEM) and energy-dispersive X-ray (EDX) (Alberto Lopez-Ortega, CIC nanoGUNE), magnetization characterization using vibrating sample magnetometer (VSM; Jordi Sort, Universitat Autònoma de Barcelona), **ii)** theoretical calculations of optical properties using finite domain time domain (FDTD) method (Borja Sepúlveda).

Some experiments were carried out by collaborators, although I provided with the necessary nanodome samples. These include **i)** cell cultures (Antonio Aranda, Carme Nogués, Bioscience Faculty of Universitat Autònoma de Barcelona), **ii)** LabVIEW software programming for opto-magnetic detections (Borja Sepúlveda).



Simultaneous local heating/thermometry based on plasmonic magnetochromic nanoheaters

Zhi Li,^{1,4} José Luis Tajada,¹ **Josep Nogues**,¹ and **Borja Sepulveda**,^{1*}

Alberto Lopez-Ortega,^{2*} Vavassori, Paolo²

Antonio Aranda-Ramos,³ Carme Nogues,³

Jordi Sort⁴

¹*Catalan Institute of Nanoscience and Nanotechnology (ICN2), CSIC and BIST, Campus UAB, Bellaterra, 08193 Barcelona, Spain*

²*CIC nanoGUNE, E-20018 Donostia-San Sebastian, Spain*

³*Departament de Biologia Cel·lular, Fisiologia i Immunologia, Facultat de Biociències, Universitat Autònoma de Barcelona, Bellaterra, 08193 Barcelona, Spain.*

⁴*Departament de Física, Facultat de Ciències, Universitat Autònoma de Barcelona, Bellaterra, 08193 Barcelona, Spain.*

Simultaneous Local Heating/Thermometry Based on Plasmonic Magneto-chromic Nanoheaters

Zhi Li, Alberto Lopez-Ortega,* Antonio Aranda-Ramos, José Luis Tajada, Jordi Sort, Carme Nogues, Paolo Vavassori, Josep Nogues, and Borja Sepulveda*

A crucial challenge in nanotherapies is achieving accurate and real-time control of the therapeutic action, which is particularly relevant in local thermal therapies to minimize healthy tissue damage and necrotic cell deaths. Here, a nanoheater/thermometry concept is presented based on magnetoplasmonic (Co/Au or Fe/Au) nanodomains that merge exceptionally efficient plasmonic heating and simultaneous highly sensitive detection of the temperature variations. The temperature detection is based on precise optical monitoring of the magnetic-induced rotation of the nanodomains in solution. It is shown that the phase lag between the optical signal and the driving magnetic field can be used to detect viscosity variations around the nanodomains with unprecedented accuracy (detection limit 0.0016 mPa s, i.e., 60-fold smaller than state-of-the-art plasmonic nanorheometers). This feature is exploited to monitor the viscosity reduction induced by optical heating in real-time, even in highly inhomogeneous cell dispersions. The magneto-chromic nanoheater/thermometers show higher optical stability, much higher heating efficiency and similar temperature detection limits (0.05 °C) compared to state-of-the-art luminescent nanothermometers. The technological interest is also boosted by the simpler and lower cost temperature detection system, and the cost effectiveness and scalability of the nanofabrication process, thereby highlighting the biomedical potential of this nanotechnology.

effects in real time and with high precision. Relevant examples are optical hyperthermia for cancer treatments and temperature-activated drug delivery. These therapies typically exploit the plasmon-enhanced light absorption in plasmonic nanoparticles at their resonant wavelength to locally produce heat for generating the therapeutic effect. Photothermal therapies require accurate control over the optically induced temperature changes to avoid healthy tissue damage and to minimize unwanted necrotic cell deaths. Thereby, the efficient light-heat conversion requires simultaneous accurate measurement of the local temperature at the irradiated site. While efficient optical heating can be easily achieved with a variety of noble-metal nanoparticles, precise and simultaneous noncontact local thermometry remains an issue due to the low accessibility of the irradiated regions. Current approaches to achieve noncontact and minimally invasive nanothermometry are mainly based on the detection of radiometric or emission lifetime variations in luminescent probes.^[1–10]

A current strategic goal to improve the efficacy of nanotherapies is achieving externally controlled and localized therapeutic actions and, simultaneously, monitoring their induced therapeutic

effects in real time and with high precision. Relevant examples are optical hyperthermia for cancer treatments and temperature-activated drug delivery. These therapies typically exploit the plasmon-enhanced light absorption in plasmonic nanoparticles at their resonant wavelength to locally produce heat for generating the therapeutic effect. Photothermal therapies require accurate control over the optically induced temperature changes to avoid healthy tissue damage and to minimize unwanted necrotic cell deaths. Thereby, the efficient light-heat conversion requires simultaneous accurate measurement of the local temperature at the irradiated site. While efficient optical heating can be easily achieved with a variety of noble-metal nanoparticles, precise and simultaneous noncontact local thermometry remains an issue due to the low accessibility of the irradiated regions. Current approaches to achieve noncontact and minimally invasive nanothermometry are mainly based on the detection of radiometric or emission lifetime variations in luminescent probes.^[1–10]

Z. Li, J. L. Tajada, Prof. J. Nogues, Dr. B. Sepulveda
Catalan Institute of Nanoscience and Nanotechnology (ICN2)
Consejo Superior de Investigaciones Científicas (CSIC) and Barcelona
Institute of Science and Technology (BIST)
Campus UAB, Bellaterra 08193, Barcelona, Spain
E-mail: borja.sepulveda@icn2.cat

Z. Li, Prof. J. Sort
Departament de Física
Facultat de Ciències
Universitat Autònoma de Barcelona
Bellaterra 08193, Barcelona, Spain

Dr. A. Lopez-Ortega, Prof. P. Vavassori
CIC nanoGUNE
E-20018 Donostia-San Sebastian, Spain
E-mail: a.lopezortega@nanogune.eu

A. Aranda-Ramos, Dr. C. Nogues
Departament de Biologia Cel·lular
Fisiologia i Immunologia
Facultat de Biociències
Universitat Autònoma de Barcelona
Bellaterra 08193, Barcelona, Spain

Prof. J. Sort, Prof. J. Nogues
Institució Catalana de Recerca i Estudis Avançats (ICREA)
Pg. Lluís Companys 23, 08010 Barcelona, Spain

Prof. P. Vavassori
IKERBASQUE
Basque Foundation for Science
E-40013 Bilbao, Spain

 The ORCID identification number(s) for the author(s) of this article can be found under <https://doi.org/10.1002/sml.201800868>.

DOI: 10.1002/sml.201800868

in vivo can be hampered by the large absorption and scattering by physiological tissues of the ultraviolet and visible light typically involved in the luminescent nanothermometry. To maximize light penetration, luminescent probes with absorption and emission bands in the near infrared (NIR)^[11,12] have been proposed.^[13–15] However, an additional drawback of ratiometric and lifetime luminescence nanothermometers is the cost and complexity of the detection systems. In addition, none of these aforementioned approaches targets the strategic nanotherapeutic goal of enabling local heating and simultaneous real-time temperature detection. Although this approach remains technologically challenging, as an example in this direction, luminescent nanothermometers have been attached to plasmonic nanostructures to enable local heating and detection of the induced temperature variations.^[11,16] Nevertheless, the temperature detection suffers the same limitations of luminescent thermometry, in addition to the potential quenching or absorption of the emitted light by the plasmonic nanostructures, or the necessity of using different light sources for thermometry and heating. Nanoparticles based on Ln^{3+} cations have also shown heating and thermometry capacity using NIR fluorescence absorption and emission bands, although the simultaneous heating and detection can only be achieved at different wavelengths.^[11] Besides, their optical heating efficiency is substantially lower than that of plasmonic nanoparticles.

Here we present a novel and cost effective local (down to the μm^3 range in spatial resolution) heating/thermometry concept based on magneto-chromic nanoheaters, which are magnetoplasmonic nanodomains composed of 100 nm diameter polystyrene beads partially coated with a ferromagnetic/Au multilayer. In particular, we have studied nanodomains coated with $[\text{Co}-1 \text{ nm}/\text{Au}-6 \text{ nm}] \times 5/\text{Au}-5 \text{ nm}$ or $[\text{Fe}-5 \text{ nm}/\text{Au}-35 \text{ nm}]$ multilayers (Figure 1a–c). Their nanofabrication, based on a combination of electrostatic self-assembly of the polystyrene beads and highly directional electron beam evaporation (Figure S1, Supporting Information), enables creating nanoparticles that merge strong optical and magnetic anisotropies with a nearly spherical shape (see Methods in the Supporting Information). These magnetoplasmonic nanodomains embody very high thermoplasmonic heating efficiency and allow very accurate, stable, and fast detection of the local temperature variations. The local thermometry is achieved by optically tracking the viscosity-dependent rotation dynamics of the nanodomains activated by a weak external AC magnetic field. The magnetic rotation of the nanodomains results in an intense modulation of the transmitted light owing to their strong magneto-chromic effect, i.e., the large spectral change of the colloidal dispersion when a magnetic induction B is applied. Indeed, we show that ultraprecise local thermometry, potentially with a diffraction-limited spatial resolution, is achieved while optically heating the nanodomains through an innovative analysis

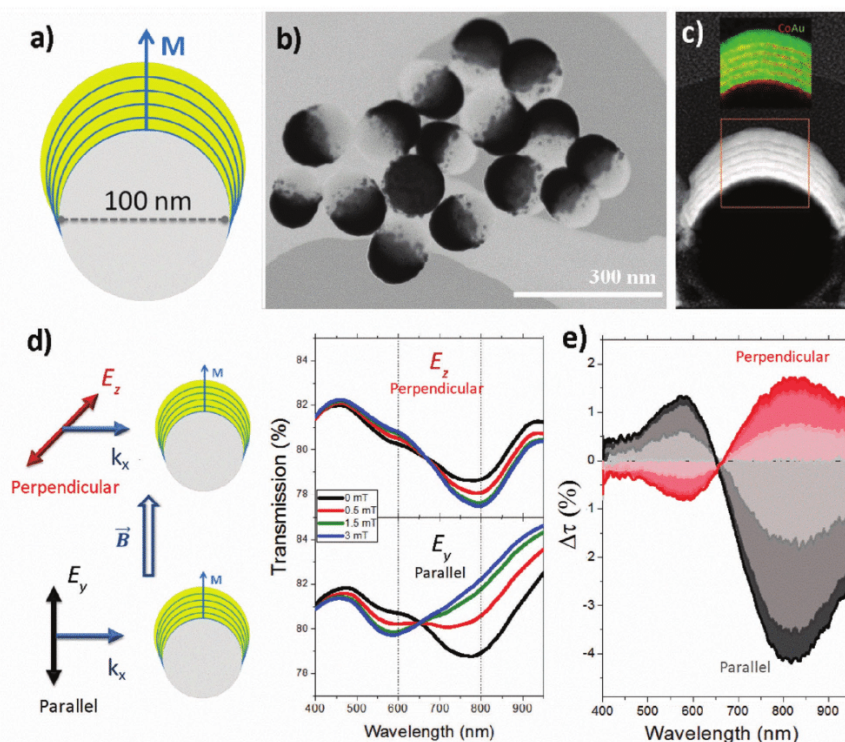


Figure 1. a) Schematic of the Co/Au nanodomains with out-of-plane magnetization. b,c) High-resolution TEM images and energy-dispersive X-ray elemental mapping (inset in panel (c)) of the nanodomains with the [Co/Au] multilayers. d) Transmission, τ , spectra of nanodomains in water under a static B when the light polarization E is either perpendicular or parallel to B , and the light wave vector k is perpendicular to B , as shown schematically. e) Spectra of the transmission variations ($\Delta\tau = \tau(B) - \tau(0)$) induced by the static B for the perpendicular (red curves) and the parallel (black curves) polarizations.

of the temperature-induced viscosity changes of the liquid surrounding the nanodomains. Such intense magnetochromic effect, together with the fast rotation speed of the nanodomains and their high heating efficiency, enables the simple and highly sensitive simultaneous plasmonic heating and temperature detection, even for low particle concentrations and in highly inhomogeneous media (e.g., tissues or physiological fluids).

High-resolution transmission electron microscopy (TEM) and energy-dispersive X-ray (EDX) elemental mapping images of Figure 1b,c clearly show the half magnetoplasmonic shell made of alternating layers with different composition and the nearly spherical shape of the nanodomains. The magnetoplasmonic multilayer provides the highly anisotropic magnetic and optical properties. The set of intercalated Co nanolayers exhibits an out-of-plane magnetic anisotropy, as indicated by the hysteresis loops of Figure S2 in the Supporting Information.^[17] In addition, the optical anisotropy is given by the existence of two localized plasmonic resonances with different resonant wavelengths along two different and orthogonal axes of the nanodomains (Figure 1d and Figure S3, Supporting Information). According to the finite difference time domain (FDTD) analysis, these resonances are located at 600 and 800 nm (Figure S3, Supporting Information) and are excited when the polarization E of the incident light is either parallel (wavelength 800 nm) or perpendicular (wavelength 600 nm) to the plane of the [Co/Au] multilayer. These resonances are in excellent agreement with the spectral features marked with dashed lines in the measured transmission spectral dips in Figure 1d.

This combination of features is crucial for attaining intense magnetochromic effects (Figure 1d), which can be rapidly modulated by inducing a rotation of the particles under the action of an external magnetic field (at hundreds of Hz). As a result of the magnetic anisotropy, the nanodomains that are initially randomly oriented in solution can be aligned with their M parallel to the applied magnetic induction, B , via magnetic torque. Such alignment enables a very accurate control of the excited plasmonic resonance with a linearly polarized light beam. The magnetochromic effect can be clearly observed in Figure 1d, which shows the strong changes in the transmission spectrum through a diluted colloidal dispersion (concentration of 1×10^9 nanodomains mL^{-1}) as a function of the amplitude of B for the light propagation wave vector (k) perpendicular to B , and the polarization E either parallel or perpendicular to B . In the parallel configuration, i.e., light polarization E parallel to B , a dip in the transmission at 600 nm is observed, whereas the dip is located at 800 nm in the perpendicular configuration, i.e., light polarization E perpendicular to B , as predicted by the FDTD simulations. Interestingly, a B amplitude as low as 2 mT allows toggling between the parallel and perpendicular resonances located at 600 and 800 nm. As a result, the transmission spectrum can be continuously tuned between the two resonances by modifying B amplitude (Figure 1d), with the largest spectral variation at ≈ 810 nm (Figure 1e). The intense 4% transmission variation ($\Delta\tau = \tau(B) - \tau(0)$) at 810 nm can be drastically amplified by increasing particle concentration. Although sizable magnetochromic effects can be obtained by applying the magnetic field in different directions (Figure S4, Supporting Information), we focus on the configuration with B parallel to E (Figure 2a), which is the one producing the largest

magnetochromic effect at 810 nm. In addition, this optimal wavelength is within the tissues transparent window and is spectrally close to commercially available and low-cost laser diodes with emission at 808 nm, as the one used in this study.

The application of a low amplitude (2 mT) alternating B with frequency ω induces the rotation of the nanodomains (Figure 2a), which results in an intense modulation of the transmitted intensity of the 808 nm linearly polarized laser beam. Importantly, the necessary B can be easily generated by a small coil, and the nanodomains rotation detection only requires a single linearly polarized light beam with 808 nm wavelength to maximize the magnetochromic effect, and a conventional photodiode (see the Supporting Information).

The right panel in Figure 2a depicts the dependence of the magnetochromic effect for incident light with 808 nm wavelength under an alternating B . If the B frequency is low (<100 Hz) the majority of the particles are oriented parallel to B when the magnetic induction is at its maximum amplitude $\pm B_{\text{max}}$ (Figure 2a). In these conditions light can only excite the plasmonic resonance located at 600 nm wavelength and, therefore, the transmitted intensity is maximized for the incident light with 808 nm wavelength (see Figure 1d). When the magnetic induction transitions between $+B_{\text{max}}$ and $-B_{\text{max}}$, the particles flip their orientation (Figure 2a). During the transition the resonance located at ≈ 800 nm is excited, thereby efficiently absorbing and scattering the incident beam. As a result, a large decrease of the transmitted intensity is observed (Figure 2a). As the extinction cross-section of the Co/Au nanodomains for $\pm B_{\text{max}}$ orientations is completely equivalent, an alternating B with ω frequency generates a light transmission modulation at frequency 2ω (see Figure 2a).

The periodic transmittance variation enables using the fast Fourier transform (FFT) analysis to extract both the amplitude and phase lag with respect to B for the different harmonics of the transmittance (Figure S5, Supporting Information). Since the nanodomains are dispersed in a viscous medium, the magnetochromic modulation amplitude and phase lag strongly depend on the frequency of B . Figure 2b represents the frequency dependence of the amplitude ($A2\omega$) and phase lag ($\phi2\omega$) of the second harmonic (2ω). In this analysis, the amplitude $A2\omega$ is normalized by the DC component of the FFT to eliminate the influence of the intensity fluctuations in the incident light, and it is therefore dimensionless. $A2\omega$ has the typical bell-like shape of resonant phenomena, which is due to the Brownian relaxation in this case.^[18,19] The maximum of $A2\omega$ is observed at 700 Hz, and for higher frequencies $A2\omega$ presents a monotonic decrease, which manifests the difficulty of nanodomains to follow B due to the viscous damping. The influence of the viscosity is also evident in the phase lag plot, $\phi2\omega$ (Figure 2b), showing a monotonic increase of the phase difference as ω increases, being almost 2π at 2 kHz.

Interestingly, moderate particle concentrations (3×10^{10} particles mL^{-1}) show huge transmittance modulation amplitudes, close to 90% (i.e., $A2\omega \approx 0.9$), which is orders of magnitude larger than those achieved in magneto-optic effects in magnetoplasmonic nanoparticles,^[20–23] and requires a much lower B amplitude. A key consequence of the strong magnetochromic modulation is the effectiveness to detect extremely low nanodomain concentrations (Figure 2c), even below 10^7 particles mL^{-1} (i.e., well below the

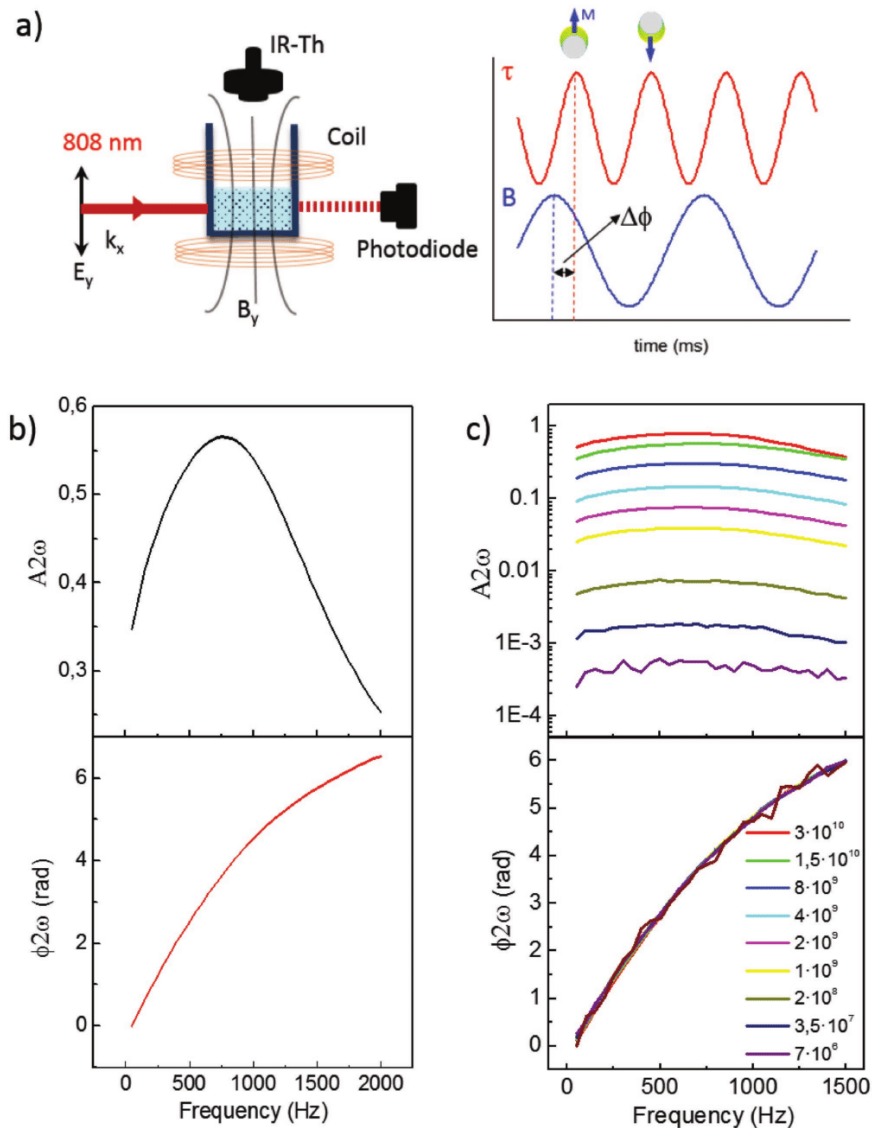


Figure 2. a) Left: Schematics of the experimental setup and right: Rotation of the Co/Au nanodomains under an alternating B and the induced light transmission (τ) modulation. b) Variation in the amplitude $A_{2\omega}$ and phase lag $\phi_{2\omega}$ of the transmitted intensity second harmonic (2ω) with ω . c) Nanodomains concentration dependence of $A_{2\omega}$ and $\phi_{2\omega}$ as a function of ω .

detection limit of high-end UV–vis spectrometers; Figure S6, Supporting Information), by using a very simple and cost-effective setup. Nevertheless, probably the most interesting and relevant feature for sensing applications is the complete independence of $\phi_{2\omega}$ on the nanodome concentration (Figure 2c).

Since $\phi_{2\omega}$ depends only on the viscous damping, the quantification of the $\phi_{2\omega}$ changes is an appealing approach to detect local viscosity variations around the nanoparticles. As expected, $\phi_{2\omega}$ approaches 2π at lower frequencies as the viscosity η (and thus, the damping) increases (Figure 3a). This effect is accompanied by a shift in the $A_{2\omega}$ maximum to lower frequencies (Figure S7a, Supporting Information). For small viscosity

changes ($\Delta\eta < 1$ mPa s) the phase lag variation at a given frequency, $\Delta\phi_{2\omega}$, is approximately linear. The induced $\Delta\phi_{2\omega}$ in this small η range is maximized at a $\omega = 600$ Hz, when $B = 2$ mT (Figure S7b, Supporting Information). Therefore, the sensitivity to detect the local viscosity variations, which is defined as $S_\eta = \Delta\phi_{2\omega}/\Delta\eta$, is also maximized at 600 Hz, giving a value of 0.95 rad $\text{mPa}^{-1} \text{s}^{-1}$ for $\Delta\eta < 1$ mPa s. For larger viscosity changes, $\phi_{2\omega}$ displays a nonlinear relationship with respect to the liquid viscosity (Figure 3b).

The detection of $\Delta\phi_{2\omega}$ at a fixed frequency has the additional advantage of enabling real-time monitoring of local viscosity changes (Figure 3c). Considering the signal-to-noise

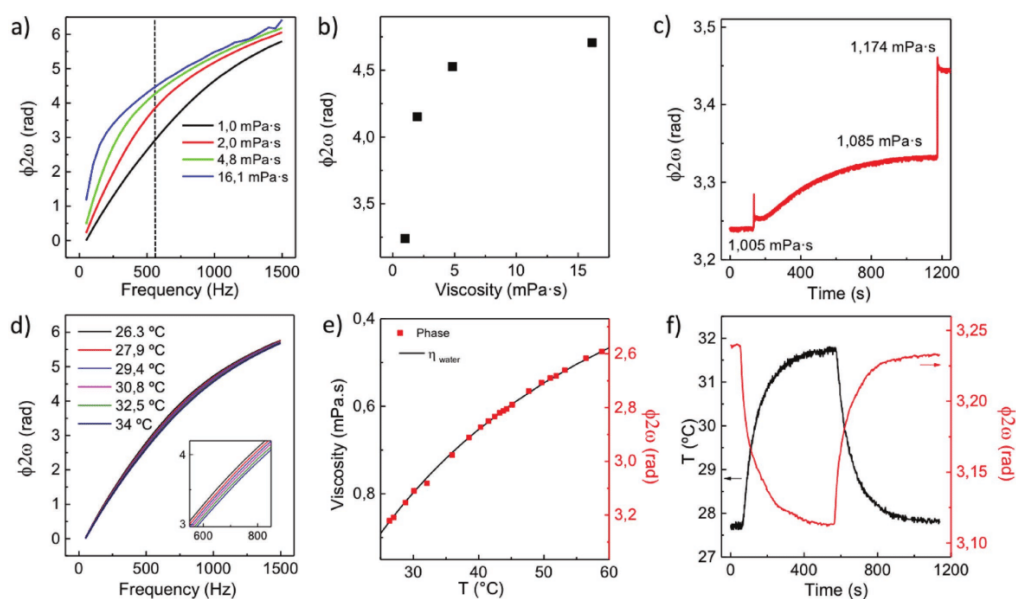


Figure 3. a) Frequency dependence of $\phi_{2\omega}$ for water/glycerol solutions of different viscosities. b) $\phi_{2\omega}$ for the same water/glycerol solutions at fixed 600 Hz actuation frequency ($B = 2$ mT). c) Real-time detection of small viscosity variations. d) Frequency dependence of $\phi_{2\omega}$ for different water temperatures (Inset: zoom of $\phi_{2\omega}$ for 600–800 Hz). e) Temperature calibration curve of the nanothermometers, showing the variations of $\phi_{2\omega}$ measured at 700 Hz as a function of the water T , compared to the tabulated water viscosities as a function of T . f) Real-time detection of the temperature variation induced by an external Peltier heater by monitoring $\phi_{2\omega}$ at 700 Hz modulation (particle concentration: 6×10^9 nanodomcs mL $^{-1}$).

ratio of $\phi_{2\omega}$, we can determine that the detection limit (LOD) of the viscosity variations, defined as $\text{LOD}_{\eta} = 3\sigma/S_{\eta}$ (where σ is the noise; Figure S8, Supporting Information), is as low as 0.0016 mPa s. This detection limit is 60-fold smaller than that of state-of-the-art plasmonic nanorheometers.^[24] Besides the strong magneto-chromic effect, this exceptional LOD value is also due to the high rotation frequency of our nanodomcs at the sensitivity maximum, which reduces the detrimental effects of low frequency noise, especially the $1/f$ noise. This is a clear advantage with respect to micrometer-sized particles^[25] or long magnetic nanorods, which cannot rotate at such a high frequency,^[26,27] and highlights the importance of the spherical geometry and small size of the nanodomcs. Importantly, the introduction of electronic filters or lock-in amplifiers could reduce even further this detection limit. As it can be observed in Figure 3b, there is a large decrease in the sensitivity to detect the viscosity variations for large liquid viscosities ($\eta > 5$ mPa s). As a result, we can establish that upper viscosity limit of the magneto-chromic nanodomcs as nanorheometers is 5 mPa s. Such upper limit is adequate for the biomedical applications since the viscosity of physiological fluids is generally lower than 2 mPa s.

The highly sensitive optical detection of the viscosity variations opens the path to monitor the local temperature (T) changes by exploiting the reduction of water viscosity when T increases. For calibration purposes, we first measured $\phi_{2\omega}$ at different water T by heating the nanodomcs dispersion with a Peltier-heater (Figure 3d–f) and we monitored the ΔT with a calibrated IR-thermometer (Figure 2a). In this case the variation of $\phi_{2\omega}$ with T shows a maximum at $\omega \approx 700$ Hz for $B = 2$ mT

(Figure S9, Supporting Information). The small frequency shift of the maximum sensitivity with respect to the viscosity measurements is due to the small nonlinearity of $\phi_{2\omega}$ dependence on viscosity. From Figure 3e we can estimate that the maximum sensitivity in the detection of temperature changes, ΔT , defined as $S_T = \Delta\phi_{2\omega}/\Delta T$, corresponds to -0.028 rad °C $^{-1}$ for small ΔT (<10 °C) around room temperature.

The calibration curve of Figure 3e enables direct conversion between $\phi_{2\omega}$ and the fluid temperature to obtain quantitative determination of the temperature changes. Even though the water viscosity is not a linear function of T (Figure 3e), $\phi_{2\omega}$ shows an almost linear dependence in the interesting T range for biomedical applications (i.e., from 37 to 45 °C). To quantify larger T changes (>20 °C), the variation of the sensitivity with T should be considered, as pointed out in the calibration curve of Figure 3e. For large water temperatures ($T > 60$ °C), the decrease in the sensitivity to detect small T changes (i.e., 2.8-fold from 25 to 60 °C) can be compensated by the capacity to induce the particle rotation at higher frequencies by exploiting the substantially lower fluid viscosity. The faster optomagnetic modulation enables reducing the noise in $\phi_{2\omega}$, thereby compensating the lower sensitivity and minimizing the increase in the detection limit.

Similarly, we can use $\phi_{2\omega}$ at a fixed frequency, 700 Hz, to monitor in real-time the temperature variations. Figure 3f compares the $\phi_{2\omega}$ variation generated by the ΔT with the measurements of the calibrated IR-thermometer, showing that both temperature curves exhibit a similar temporal evolution. Considering the sensitivity and noise of $\phi_{2\omega}$ at 700 Hz (Figure S8, Supporting Information), we can establish a limit of

detection of temperature variations $\text{LOD}_T = 0.05 \text{ }^\circ\text{C}$, which is in the same range as that of state-of-the-art luminescent nanothermometers^[1,2,16] although using a much simpler and lower cost detection system.

The viscosity of liquid water ranges from 1.7 mPa s near 0 °C to 0.3 mPa s close to 100 °C, thereby being below the upper viscosity limit of the nanodomains as nanorheometers. Even though we have not analyzed the temperature changes for $T < 20 \text{ }^\circ\text{C}$, since the water viscosity is below 5 mPa s in that temperature range, we can determine that the working T range of the nanodomains as nanothermometers in water is from close to 0 °C to at least 60 °C. The upper T limit is currently imposed by our experimental setup, which does not enable us extending the calibration curve for temperatures higher than 60 °C due to the water vapor condensation in the IR thermometer.

Another relevant advantage of the nanodomains is their capacity to detect ΔT by using the very same NIR light beam employed for heating via thermoplasmonic effects. Indeed, Figure 4a shows that the nanodomains are also excellent thermoplasmonic heaters in the NIR, showing heating efficiencies in the same range as those of state-of-the-art optical nanoheaters,^[28–30] such as Au nanorods and nanoshells.^[31–33] Remarkably, the magnetic modulated rotation of the nanodomains only induces a weak 4% reduction of the heating efficiency compared to the randomly oriented nanodomains. Therefore, the combined strong optical absorption efficiency and high sensitivity to detect local viscosity variations can be exploited to achieve the nanotherapeutic strategic goal of

simultaneously inducing local optical heating and detecting the ΔT caused by the same NIR light beam at the illuminated region. Figure 4b demonstrates this ability by displaying the frequency dependence of $\phi 2\omega$ at different laser powers, once the equilibrium T in the colloidal dispersion measured by the IR-thermometer is reached after 20 min. As in the Peltier heating case, the maximum sensitivity to detect ΔT occurs at 700 Hz, and it has a value of $-0.028 \text{ rad } ^\circ\text{C}^{-1}$ (Figure S9, Supporting Information). Moreover, Figure 4c displays the real-time detection of the ΔT extracted from $\phi 2\omega$ at 700 Hz for a sudden power increase (from 25 to 315 mW) of the collimated 808 nm laser beam (spot diameter 2 mm), compared to the IR-thermometer measurements. A steeper ΔT is observed during the first 2 s in the $\phi 2\omega$ measurements when the laser power abruptly increases (Figure S10a, Supporting Information), clearly showing that the nanodomains detect earlier the ΔT due to their local sensitivity, while the IR-thermometer only detects the averaged ΔT at the liquid surface.

Remarkably, this latter feature enables accessing the fast (millisecond) ΔT dynamics caused by the local laser-induced thermoplasmonic heating of the nanodomains (within the illuminated volume), which cannot be observed by conventional IR noncontact thermometers. The faster and local response of $\phi 2\omega$ to ΔT can be further appreciated by noting the substantially more pronounced differences in the detection of dynamic ΔT between the nanodomains and the IR-thermometer when the laser is focused in a small spot ($\approx 0.5 \text{ mm}$ in diameter) (Figure 4d,e). Whereas the IR-thermometer shows a similar

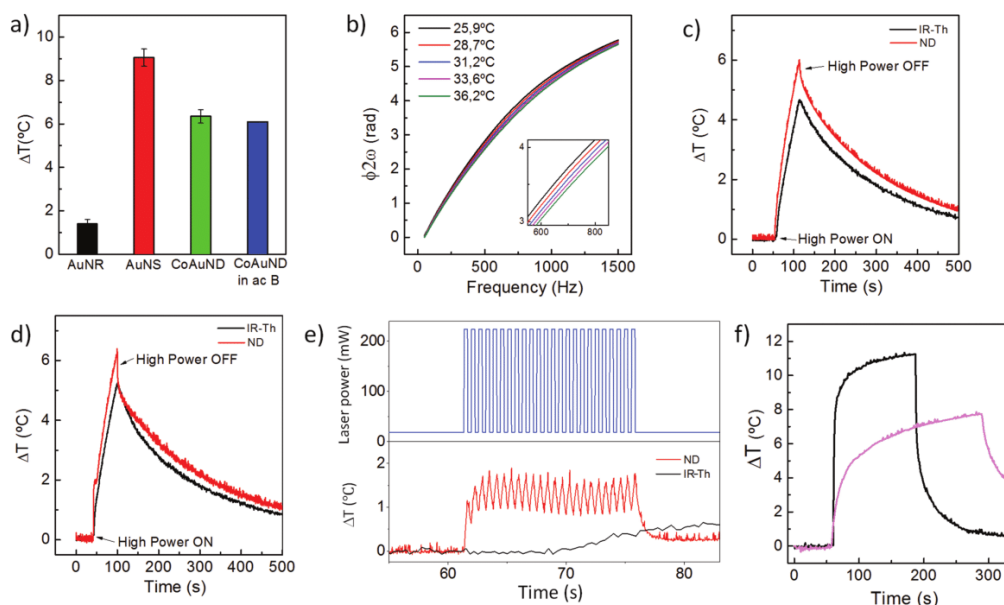


Figure 4. a) Comparison of the optical heating efficiency of Co/Au nanodomains (CoAuND), Au nanorods (AuNR), and Au nanoshells (AuNS), having resonances at $\approx 800 \text{ nm}$ wavelength under a linearly polarized laser (808 nm, 315 mW). b) $\phi 2\omega$ as a function of ω for different liquid T induced by plasmonic heating using increasing laser power (25, 75, 125, 175, and 225 mW). c) Comparison of the real-time detection of the ΔT by $\phi 2\omega$ at 700 Hz and the IR-Th induced by a sudden increase in laser power (from 25 to 315 mW) of a collimated laser beam and d) of a focused laser beam. e) Detection of fast ΔT by the focused laser with pulsed laser power of 600 ms period. The ΔT detected by the nanodomains is extracted from $\Delta T = \Delta\phi 2\omega/S_T$. (Particle concentration $6 \times 10^9 \text{ nanodomains mL}^{-1}$). f) Comparison of the simultaneous local optical heating and temperature detection inside a microfluidic channel by a focused light beam (black curve) and a large light beam (magenta curve) under a laser power increase from 15 to 185 mW.

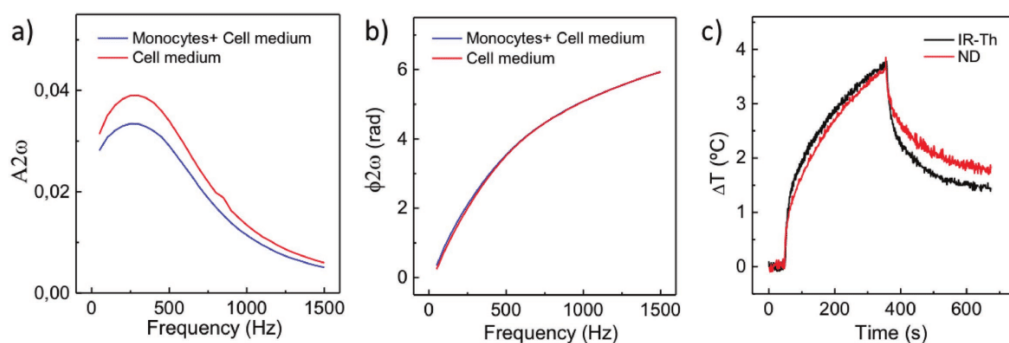


Figure 5. a,b) Frequency dependence of $A_{2\omega}$ and $\phi_{2\omega}$, respectively, for 1.7×10^9 nanodomes mL^{-1} in a cell medium and in a monocyte dispersion with 6×10^6 cells mL^{-1} . c) Comparison of the real-time detection of ΔT induced by a 225 mW increase of the 808 nm laser power by the nanodomes $\phi_{2\omega}$ ($\Delta T = \Delta\phi_{2\omega}/S_T$) and the IR-thermometer in the monocytes dispersion.

ΔT curve as that in Figure 4c under an identical abrupt laser power change, the local temperature around nanodomes suffers an even steeper increase than in Figure 4c, within the first 500 ms (Figure S10b, Supporting Information), which is followed by a sudden reduction in the slope during the following 7 s. We attribute the very sharp initial increase to the detection of the fast temperature increase in the liquid surrounding the particles at the beam waist, where we have the highest light intensity. Such localized heating triggers a convective flow process,^[34–36] which ejects the hot particles and liquid from the focus. The ejected hot particles are then substituted by colder particles and liquid, thereby explaining the sudden reduction of the slope when the convection process starts. Once the convection is stabilized, a process that takes ≈ 7 s, the temperature acquired by the nanodomes and the IR-thermometer start exhibiting similar slopes. Likewise, when the laser power suddenly decreases, a steep temperature decrease is observed within the first second due to the local cooling triggered by the convection process, which cools down the focal point inside the liquid before the surface of the liquid dispersion that is monitored by the IR-thermometer.

The capacity to detect fast local ΔT at the laser beam waist is also corroborated in Figure 4e, which shows the temperature detection by nanodomes under a pulsed laser excitation with square shape and 600 ms period. The fast acquisition (31 measurements per second in this experiment) enables us to clearly observe the millisecond-scale temperature oscillations in the focus under the modulated laser power, which cannot be detected in the IR-thermometer.

To highlight the local character of the nanodomes heating/thermometry concept we analyze in Figure 4f the optical heating and temperature detection inside a microfluidic channel with 0.8 mm height, which is not accessible to the non-contact IR-thermometer. We have compared the temperature changes induced by a 1 mm diameter light beam and a focused light beam by a microscope objective with a numerical aperture of 0.6 in air, which yields a beam waist of $\approx 25 \mu\text{m}^2$ with a depth of focus (length within which the cross section of the beam is less than two times that of the waist) of $\approx 15 \mu\text{m}$ inside the microfluidic channel. This corresponds to a heated volume of the solution of $\approx 375 \mu\text{m}^3$. As it can be observed, the focused light beam generates a much faster local temperature increase

due to the higher light intensity at the beam waist. The faster cooling process induced by the large temperature gradient also evidences the localized heating and temperature detection that can be achieved with the nanodomes.

To demonstrate the potential of the magnetochromic nano-heater/thermometers in biomedical applications, we show their capability to simultaneously heat and detect the temperature variations in concentrated monocyte dispersions. Notably, such cell dispersions show very strong light scattering to mimic the challenging optical conditions of physiological tissues. Indeed, the monocyte dispersions are an even more challenging optical media than tissues composed of adherent cells due to the dynamic and random perturbations in light scattering caused by free cell movement and cell sedimentation with time.

We first analyze the features and the stability of the magnetochromic modulation in the cell medium. The frequency dependence of $A_{2\omega}$ shows the maximum at 300 Hz (Figure 5a), which reflects both the higher viscosity of the cell medium compared to that of water, and the increase of the mass and hydrodynamic radius of the particles due to the unspecific adsorption of proteins at the nanodomes surface. Remarkably, the nanodomes show very high stability in cell medium, as it is demonstrated by the high stability of $A_{2\omega}$ and $\phi_{2\omega}$ measurements at 300 Hz for more than 2 h (Figure S11, Supporting Information).

Next, we introduce a concentration of 1.7×10^9 nanodomes mL^{-1} (equivalent to $10 \mu\text{g mL}^{-1}$ of nanodomes) in a monocyte dispersion with high cell concentration (6×10^6 cells mL^{-1}). The total transmitted light intensity through the monocytes dispersion shows a 20-fold decrease with respect to that in water due to the large light scattering generated by the cells. Despite such intensity reduction, both $A_{2\omega}$ and $\phi_{2\omega}$ can be easily detected (Figure 5a,b). These measurements show that the $A_{2\omega}$ maximum is located at the same frequency as in the case of the cell medium without monocytes, i.e., 300 Hz, thereby implying similar viscosities, as expected since the internalization of nanodomes by the cells is negligible during the assay time (20 min). Likewise, the temperature variations caused by the laser can be detected and monitored in real time, as shown Figure 5c. Despite the 20-fold reduction in the transmitted intensity, the noise of $\phi_{2\omega}$ only shows a

threefold increase, thereby yielding a detection limit of 0.15 °C of the temperature variations in the concentrated cell dispersion, which is sufficient for controlling the therapeutic effect in photothermal therapies. Such small increase in the detection limit is remarkable considering the low concentration of the nanodomains and the strong light scattering of the cell dispersion. In the case of tissues composed of adherent cells and for larger particle concentrations, a smaller detection limit (closer to 0.05 °C) is expected.

Although the Co content in the nanodomains might raise toxicity concerns for biomedical applications, the cytotoxicity is expected to be minimal due to the low Co amount, and its protection by the thick Au films. Nevertheless, to minimize any potential toxicity, we have demonstrated that the simultaneous nanoheating/thermometry can also be achieved with nontoxic Fe/Au nanodomains. The optical heating efficiency of the Fe/Au nanodomains is similar to that of the [Co/Au] nanodomains and, although the magneto-optical amplitude $A2\omega$ is threefold smaller due to the in-plane magnetization in the Fe layer (Figure S12a,b, Supporting Information), we can monitor ΔT with similar sensitivity ($-0.025 \text{ rad } ^\circ\text{C}^{-1}$) and a detection limit of 0.08 °C in water (Figure S12c, Supporting Information), thereby highlighting the biomedical potential of this nanotechnology.

Although the magneto-optical nanodomains cannot simultaneously determine the absolute values of the temperature and the fluid viscosity, we believe that this will not be a limitation for the control of the temperature during photothermal therapies. The strategy for T control in vivo will be to determine first the frequency dependence of both $A2\omega$ and $\phi2\omega$ at low optical power (i.e., negligible heating). These measurements will determine the magnetic frequency that maximizes both the optomagnetic signal and the sensitivity to detect the ΔT . Taking such $\phi2\omega$ value as reference, then the optical power will be increased to generate the local temperature increase. The usual duration of the optical treatments is between 10 and 30 min, which is short compared to the physiological responses (typically in the hours range). As a consequence, it can be assumed that any change in the viscosity during the optical treatment will be only the result of the temperature increase and not due to any physiological effect. Hence, the observed $\phi2\omega$ reduction will be only due to the local temperature increase. Moreover, high local viscosity variations are not expected due to the nanoscale size of the probes.^[24] As the nanodomains are much smaller than the cells, they are only sensitive to the viscosity variations of the interstitial fluid, which is mainly composed of water, salts, proteins, and carbohydrates. This effect is clearly observed in Figure 5a, which shows that the frequency dependence of $A2\omega$ and $\phi2\omega$ are exactly similar in the case of the cell medium and in the monocyte dispersion with high cell concentration ($6 \times 10^6 \text{ mL}^{-1}$).

Summarizing, we have demonstrated a new integrated magneto-optical heating/thermometry concept, which simultaneously shows very high heating efficiency and sensitivity in the detection of temperature variations. The noncontact optomagnetic detection allows for local thermometry, potentially with a diffraction-limited spatial resolution. The integrated concept is based on the innovative detection of tiny viscosity variations around magnetoplasmonic (Co/Au and Fe/Au) nanodomains when they are optically heated, by exploiting the intense magneto-optical modulation conferred by their concurrent high

magnetic and optical anisotropies. The cost-effectiveness and the fabrication scalability, together with the simplicity and low cost of the detection system add more relevance to this powerful tool to detect low temperature variations in highly inhomogeneous media with low accessibility. Remarkably, the magneto-optical nanoheater/thermometers have been able to merge detection limits in temperature variations similar to the best luminescent nanothermometers, but with a much simpler and cost-effective setup, and optical heating efficiencies comparable to that of state-of-the-art plasmonic nanoheaters.

The spherical shape and small size of the nanodomains confers them a low invasiveness and the capacity to rotate at high frequencies, which represents important advantages with respect to other possible nanoheater/thermometer approaches. As a result, the magnetoplasmonic nanodomains have a high potential for controlling and real-time monitoring photothermal therapies and optically triggered drug delivery systems. The nanodomains could also be interesting for miniaturized bioassays in biosensing applications.^[19]

Experimental Section

Fabrication of the Nanoheater/Thermometers: A schematic drawing of the different fabrication steps of the Co/Au and Fe/Au nanodomains can be seen in Figure S1 in the Supporting Information. Briefly, two-inch silicon wafers (Siegert Wafer GmbH) previously cleaned with oxygen plasma (PS210, PVA Tepla America, Inc.) were used as substrates for the electrostatic self-assembly of polystyrene nanospheres. The self-assembly started by incubating the wafer surface with a solution containing positively charged polyelectrolyte [poly(diallyldimethylammonium chloride, PDDA, Sigma-Aldrich) at 2% concentration for 1 min. Then the wafer was rinsed with osmotized water and blow dried with N_2 gas, thereby yielding a monolayer of PDDA on the surface. Next, the modified wafer surface was incubated with the dispersion of sulfate functionalized polystyrene beads (100 nm diameter, concentration 0.2%, Life Technologies) for 2 min, followed by rinsing with water and drying with N_2 flow to obtain a self-assembled monolayer of nanospheres. The self-assembly process yielded homogeneous particle monolayers with short-range order and surface density of $1.6 \times 10^9 \text{ spheres cm}^{-2}$, i.e., about 3.1×10^{10} particles per wafer.

The nanospheres on the wafer were then coated with Co or Fe and Au layers using an electron beam evaporator (ATC-8E Orion, AJA International Inc) to form the multilayers [(Co 1 nm/Au 6 nm) \times 5/Au 5 nm] or (Fe 5 nm/Au 35 nm) semi-shells with a total thickness of 40 nm. The thickness of the deposited layers was monitored with Å precision by a quartz crystal microbalance during the evaporations. Finally, the coated nanoparticles were incubated, while still on the surface of the wafer, with a negatively charged polyelectrolyte [poly(sodium 4-styrenesulfonate, PSS, Sigma-Aldrich) at 2% concentration for 3 min to deposit a monolayer of PSS on the Au surface, thereby increasing the surface charge and their hydrophilicity. The wafer was rinsed with water to remove the excess of PSS and was dried with N_2 flow. The Co/Au nanodomains were then magnetized out-of-plane by placing the wafer on a strong 7 cm diameter disk-shape NdFeB magnet. To disperse the particles in water, the wafer together with 10 mL of water is put into an ultrasonic bath for 1 min. The nanodomains were finally concentrated and redispersed through centrifugation (4000 rpm, 5 min), followed by ultrasonication to achieve highly stable dispersions at the required concentrations. The Si wafers could be reused after cleaning for 10 min in aqua regia, which efficiently dissolved the Co, Fe, and Au layers.

Morphological, Optical, Magnetic, and Colloidal Characterization: To study the size and distribution of nanodomains on the Si wafers, scanning electron microscopy (SEM) studies were performed using Quanta SEM 650 Field Electron and Ion Company (FEI) at 20 kV.

The TEM sample preparation was carried out on a Helios 450S SEM/focus ion beam (FIB) DualBeam (FEI, Eindhoven, The Netherlands) instrument. For x-section lamellae preparation the layer of spheres on the Si wafer was covered by ≈ 200 nm of electron beam deposited Pt followed by ≈ 2 μm ion beam deposited Pt. The thickness of the cross-section was intended to be no more than 20–30% of the diameter of the latex spheres in order to observe the layered structure on the curved surfaces.

The scanning transmission electron microscopy (STEM) study was performed on a Titan 60-300 TEM/STEM (FEI, Netherlands) instrument equipped with an EDX detector. The STEM imaging and the EDX mapping was carried out in STEM mode at 300 kV with a scan step (pixel size) of 1 nm and pixel dwell time 20 ms for imaging and 200 ms for mapping.

The UV–vis spectroscopy studies of the magneto-plasmonic (MP) nanodomains dispersions were carried out using Lambda 25 (PerkinElmer). For the optical measurements, the optical spectra ranged from 400 to 1100 nm, which covered visible light and near infrared region.

The magnetic characterization of the nanodomains was performed on monolayers of nanodomains that were transferred to adhesive tapes to eliminate the magnetic signal from the multilayer that is deposited on the wafer surface. Hysteresis loops were acquired at room temperature using a vibrating sample magnetometer (MicroSense) with a maximum applied field of $\mu_0 H = 2$ T. The measurements were performed by applying the field perpendicular or parallel to the plane of the sample, i.e., in an out-of-plane configuration.

Combined Optical Heating and Magneto-chromic Analysis Setup: A custom-made optomagnetic analysis system was used to determine the magneto-chromic and photothermal effects of the nanodomains in liquid (see Figure 2a), which consisted of: i) an NIR laser diode with emission wavelength at 808 nm (L808P500MM, THORlabs) driven by a laser diode controller (LDC240C, THORlabs) and a temperature controller (TED240C, THORlabs), ii) an optical collimating and aligning system, iii) a Helmholtz coil, iv) a signal generator (SDG1025, Siglent) and a modulated power supply (TS200, ACCEL Instruments), v) a Si photodiode (PDA36A-EC, THORlabs), vi) an infrared thermometer (MLX90614), and vii) data acquisition card (National Instruments) and computer for acquisition and processing with Labview.

The NIR laser was linearly polarized after the optical collimating and aligning system, which enabled the control of laser spot size at the sample (minimum diameter: 0.5 mm). The magnetic induction applied to the sample was generated by a Helmholtz coil with diameter of 3 cm to maximize the homogeneity of the field. In the experiment either static or sinusoidal magnetic induction, with tunable frequency (0–2 kHz), and strength (0–2 mT) was used. The transmitted light intensity was acquired and then processed via FFT analysis in a Labview program. The parameters extracted from the FFT analysis, i.e., amplitude ($A2n\omega$) and phase ($\phi2n\omega$), were real-time recorded. The time interval of data analysis was 250 ms, except for the high speed measurements of Figure S11 in the Supporting Information, in which the time interval was 31 ms.

For the analysis, samples in different solutions (water, glycerol, and cell media) with different concentration of nanodomains but with constant volume (≈ 400 μL) were prepared. The experimental photothermal efficiency comparison with Au nanorods (71 nm long axis and 20 nm short axis) and Au nanoshells (120 nm diameter of SiO_2 core and 16 nm Au shell thickness) was carried out using commercial Au particles (Nanocomposix). The temperature of the solution and the power transmitted through the sample were continuously monitored by the infrared thermometer and the photodiode. The time interval of data recording for the acquired temperature was 0.25 s during the assays.

Supporting Information

Supporting Information is available from the Wiley Online Library or from the author.

Acknowledgements

This work was supported by the Spanish Ministry of Economy, Industry and Competitiveness (MINECO) projects MAT2013-48628-R, MAT2016-77391-R, and PCIN-2016-093 (H2020 M-ERA.NET). Z.L. acknowledges the Chinese Scholarship Council (CSC) Program (201506950059) for financial support. The 2017-SGR-292 project of the Generalitat de Catalunya is acknowledged. The ICN2 was funded by the Centres de Recerca de Catalunya (CERCA) programme/Generalitat de Catalunya. The ICN2 was supported by the Severo Ochoa programme (MINECO, No. SEV-2013-0295). A.L.-O. and P.V. acknowledge funding from the Basque Government (No. PI2015_1_19), MINECO and the European Regional Development Fund (FEDER) (No. FIS2015 64519 R). A.L.-O. acknowledges the support from Juan de la Cierva grant. This work was also supported by MINECO under the Maria de Maeztu Units of Excellence (MDM-2016-0618). J.S. acknowledges the financial support by the European Research Council (SPIN-PORICS 2014-Consolidator Grant, Agreement No. 648454).

Conflict of Interest

The authors declare no conflict of interest.

Keywords

magnetoplasmonics, nanoheating, nanomagnetism, nanoplasmonics, nanothermometry, photothermal actuation

Received: March 5, 2018

Revised: April 4, 2018

Published online: May 14, 2018

- [1] X. Wang, O. S. Wolfbeis, R. J. Meier, *Chem. Soc. Rev.* **2013**, *42*, 7834.
- [2] C. D. S. Brites, P. P. Lima, N. J. O. Silva, A. Millán, V. S. Amaral, F. Palacio, L. D. Carlos, *Nanoscale* **2012**, *4*, 4799.
- [3] D. Ross, M. Gaitan, L. E. Locascio, *Anal. Chem.* **2001**, *73*, 4117.
- [4] J. Feng, K. Tian, D. Hu, S. Wang, S. Li, Y. Zeng, Y. Li, G. Yang, *Angew. Chem., Int. Ed.* **2011**, *50*, 8072.
- [5] G. W. Walker, V. C. Sundar, C. M. Rudzinski, A. W. Wun, M. G. Bawendi, D. G. Nocera, *Appl. Phys. Lett.* **2003**, *83*, 3555.
- [6] J. M. Yang, H. Yang, L. Lin, *ACS Nano* **2011**, *5*, 5067.
- [7] C. H. Hsia, A. Wuttig, H. Yang, *ACS Nano* **2011**, *5*, 9511.
- [8] L. H. Fischer, G. S. Harms, O. S. Wolfbeis, *Angew. Chem., Int. Ed.* **2011**, *50*, 4546.
- [9] C. D. S. Brites, A. Millán, L. D. Carlos, in *Handb. Phys. Chem. Rare Earths*, Elsevier **2016**, pp. 339–427.
- [10] J. Rocha, C. D. S. Brites, L. D. Carlos, *Chem. - Eur. J.* **2016**, *22*, 14782.
- [11] L. Marciniak, A. Pilch, S. Arabasz, D. Jin, A. Bednarkiewicz, *Nanoscale* **2017**, *9*, 8288.
- [12] E. C. Ximenes, W. Q. Santos, U. Rocha, U. K. Kagola, F. Sanz-Rodríguez, N. Fernández, A. D. S. Gouveia-Neto, D. Bravo, A. M. Domingo, B. Del Rosal, C. D. S. Brites, L. D. Carlos, D. Jaque, C. Jacinto, *Nano Lett.* **2016**, *16*, 1695.
- [13] R. Weissleder, *Nat. Biotechnol.* **2001**, *19*, 316.
- [14] C.-H. Quek, K. W. Leong, *Nanomaterials* **2012**, *2*, 92.
- [15] J. V. Frangioni, *Curr. Opin. Chem. Biol.* **2003**, *7*, 626.
- [16] A. Benayas, B. Del Rosal, A. Pérez-Delgado, K. Santacruz-Gomez, D. Jaque, G. A. Hirata, F. Vetrone, *Adv. Opt. Mater.* **2015**, *3*, 687.

- [17] F. J. A. Den Broeder, D. Kuiper, A. P. Van De Mosselaer, W. Hoving, *Phys. Rev. Lett.* **1988**, *60*, 2769.
- [18] P. C. Fannin, S. W. Charles, *J. Phys. D: Appl. Phys.* **1989**, *22*, 187.
- [19] M. Donolato, P. Antunes, R. S. Bejjed, T. Zardán Gómez De La Torre, F. W. Østerberg, M. Strömberg, M. Nilsson, M. Strømme, P. Svedlindh, M. F. Hansen, P. Vavassori, *Anal. Chem.* **2015**, *87*, 1622.
- [20] K. Lodewijks, N. Maccaferri, T. Pakizeh, R. K. Dumas, I. Zubritskaya, J. Åkerman, P. Vavassori, A. Dmitriev, *Nano Lett.* **2014**, *14*, 7207.
- [21] G. Armelles, A. Cebollada, A. García-Martín, J. M. García-Martín, M. U. González, J. B. González-Díaz, E. Ferreiro-Vila, J. F. Torrado, *J. Opt. A: Pure Appl. Opt.* **2009**, *11*, 114023.
- [22] B. Sepúlveda, J. B. González-Díaz, A. García-Martín, L. M. Lechuga, G. Armelles, *Phys. Rev. Lett.* **2010**, *104*, 147401.
- [23] V. Bonanni, S. Bonetti, T. Pakizeh, Z. Pirzadeh, J. Chen, J. Nogués, P. Vavassori, R. Hillenbrand, J. Åkerman, A. Dmitriev, *Nano Lett.* **2011**, *11*, 5333.
- [24] H. H. Jeong, A. G. Mark, T. C. Lee, M. Alarcon-Correa, S. Eslami, T. Qiu, J. G. Gibbs, P. Fischer, *Nano Lett.* **2016**, *16*, 4887.
- [25] C. J. Behrend, J. N. Anker, B. H. McNaughton, R. Kopelman, *J. Magn. Magn. Mater.* **2005**, *293*, 663.
- [26] J.-F. Berret, *Nat. Commun.* **2016**, *7*, 10134.
- [27] K. Keshoju, H. Xing, L. Sun, *Appl. Phys. Lett.* **2007**, *91*, 123114.
- [28] H. H. Richardson, M. T. Carlson, P. J. Tandler, P. Hernandez, A. O. Govorov, *Nano Lett.* **2009**, *9*, 1139.
- [29] G. Baffou, R. Quidant, *Laser Photonics Rev.* **2013**, *7*, 171.
- [30] O. Neumann, A. S. Urban, J. Day, S. Lal, P. Nordlander, N. J. Halas, *ACS Nano* **2013**, *7*, 42.
- [31] L. R. Hirsch, R. J. Stafford, J. A. Bankson, S. R. Sershen, B. Rivera, R. E. Price, J. D. Hazle, N. J. Halas, J. L. West, *Proc. Natl. Acad. Sci. USA* **2003**, *100*, 13549.
- [32] A. M. Gobin, M. H. Lee, N. J. Halas, W. D. James, R. A. Drezek, J. L. West, *Nano Lett.* **2007**, *7*, 1929.
- [33] S. Lal, S. E. Clare, N. J. Halas, *Acc. Chem. Res.* **2008**, *41*, 1842.
- [34] V. Garcés-Chávez, R. Quidant, P. J. Reece, G. Badenes, L. Torner, K. Dholakia, *Phys. Rev. B* **2006**, *73*, 85417.
- [35] X. Miao, B. K. Wilson, L. Y. Lin, *Appl. Phys. Lett.* **2008**, *92*, 124108.
- [36] J. S. Donner, G. Baffou, D. McCloskey, R. Quidant, *ACS Nano* **2011**, *5*, 5457.



Supporting Information

for *Small*, DOI: 10.1002/sml.201800868

Simultaneous Local Heating/Thermometry Based on
Plasmonic Magnetochromic Nanoheaters

Zhi Li, Alberto Lopez-Ortega, Antonio Aranda-Ramos, José Luis Tajada, Jordi Sort, Carme Nogues, Paolo Vavassori, Josep Nogues, and Borja Sepulveda**

Supporting Information

SIMULTANEOUS LOCAL HEATING/THERMOMETRY BASED ON PLASMONIC MAGNETOCHROMIC NANOHEATERS

Zhi Li, Alberto Lopez-Ortega*, Antonio Aranda-Ramos, José Luis Tajada, Jordi Sort, Carme Nogues, Paolo Vavassori, Josep Nogues, and Borja Sepulveda*

Figure S1. Schematic drawing of the fabrication steps of the nano-heater-thermometers (NHTs).

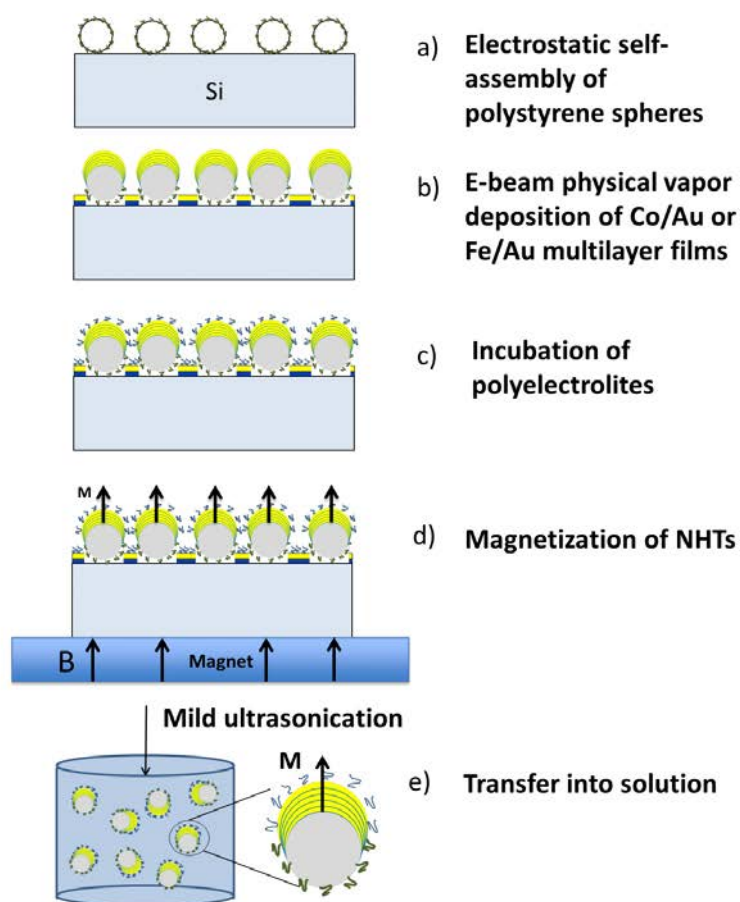


Figure S2. Room temperature out-of-plane hysteresis loop for the Co/Au nanodomes.

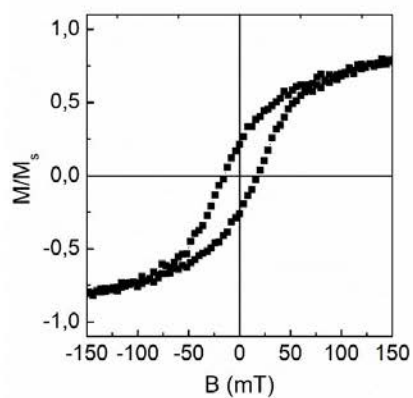


Figure S3. FDTD (Finite-difference time-domain) calculations of the extinction cross section C_{ext} of the Co/Au nanodomes in the perpendicular and parallel configurations of Figure. 1d.

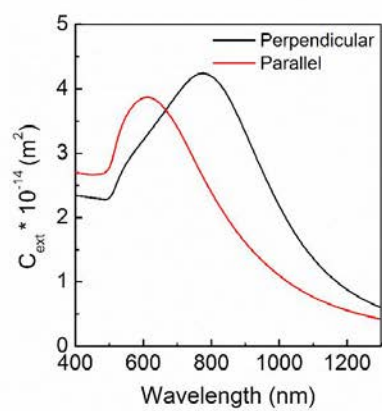


Figure S4. Differences in optical transmittance, $\Delta\tau$, of the Co/Au nanodombs for different combinations of magnetic induction B direction and light polarization TM and TE. The particle concentration of colloidal dispersion is $1 \cdot 10^9$ nanodombs/mL.

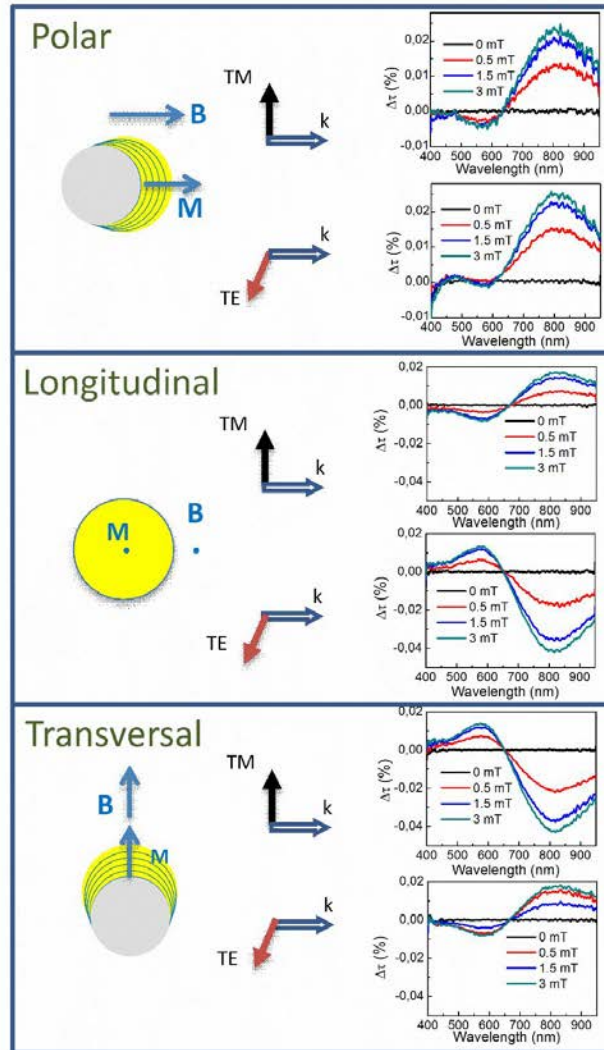


Figure S5. Amplitude ($A_{2n\omega}$) and phase ($\phi_{2n\omega}$) of the magneto-chromic signal, for different harmonics up to $n = 3$, as a function of the frequency of the ac magnetic induction with an rms amplitude of $B = 2$ mT. The particle concentration of colloidal dispersion is $1.5 \cdot 10^{10}$ nanodomains/mL.

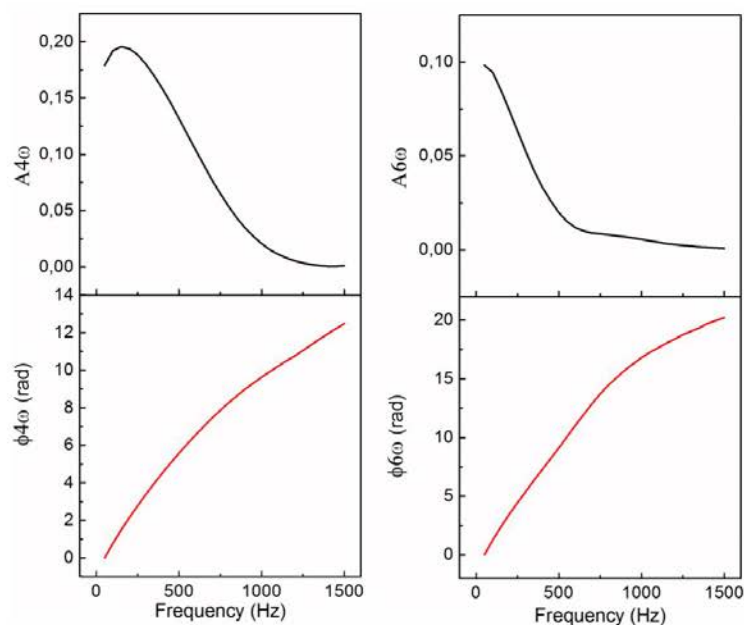


Figure S6. (a) UV-vis spectrum and (b) amplitude ($A_{2\omega}$) of second harmonic of the magneto-chromic signal under an alternating magnetic induction (2 mT) for different concentrations of nanodomains.

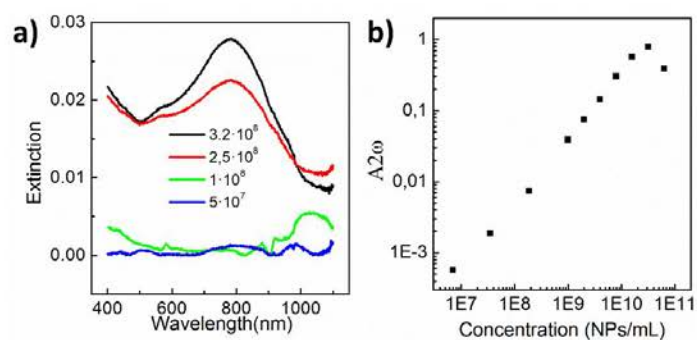


Figure S7. (a) Frequency dependence of $A2\omega$ for different liquid viscosities. Note the shift of the $A2\omega$ maxima to lower frequencies as the viscosity increases. (b) Determination of the sensitivity to changes of liquid viscosity, calculated as the phase lag change ($\Delta\phi2\omega$) per viscosity variation ($\Delta\eta$) (from 1 to 2 mPa·s) as a function of the magnetic induction frequency. ($B=2$ mT).

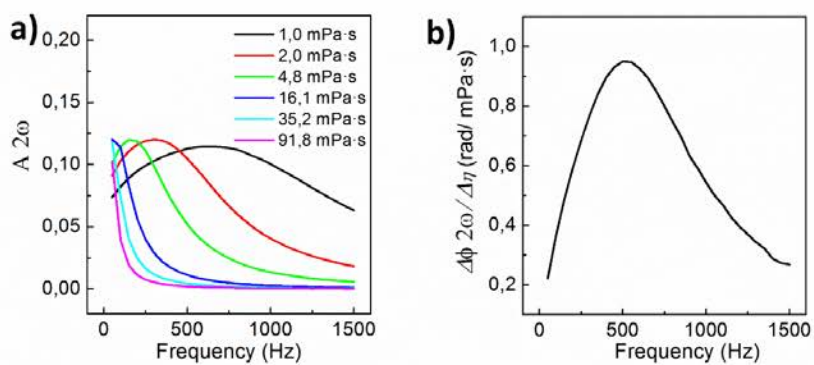


Figure S8. Analysis of the noise of the experimental setup during a real-time test of the phase ($\phi2\omega$) under an ac magnetic induction (700Hz, 2mT). The standard deviation of the data is $5.3 \cdot 10^{-4}$ rad.

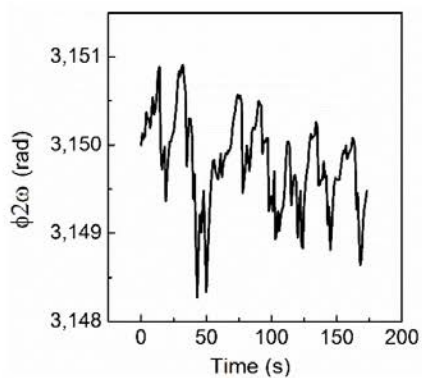


Figure S9. Sensitivity in the detection of temperature changes: variation of the phase lag ($\Delta\phi_{2\omega}$) induced by a temperature change (ΔT) as a function of the frequency (at $B = 2\text{mT}$) during Peltier heating (a), and optical heating (b) of the nanodomes.

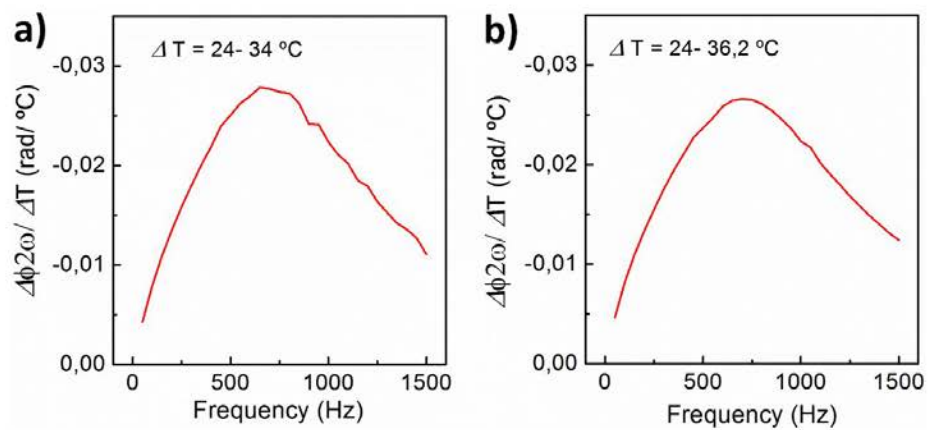


Figure S10. Comparative of the derivatives of the temperature with respect time (dT/dt) in the IR thermometer (IR Th) and nanodomains (ND) measurements when abrupt changes in the laser power from 25 mW to 315 mW and back to 25 mW are introduced, for either a collimated laser (left) or a focused laser (right).

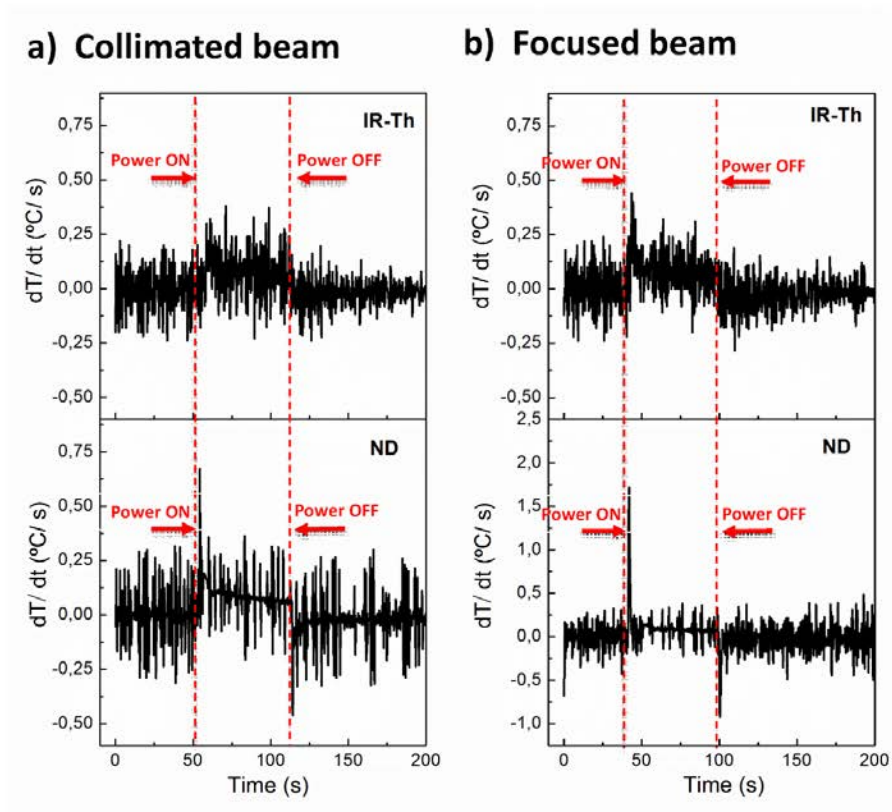


Figure S11. Long term stability test of the Co/Au nanodomains dispersed in cell medium (concentration $1.7 \cdot 10^9$ nanodomains/mL). Time dependence of the temperature (T) measured by the IR thermometer, and the phase ($\phi_{2\omega}$) and amplitude ($A_{2\omega}$) of magneto-chromic signal under an alternating magnetic induction ($\omega = 300$ Hz, $B = 2$ mT).

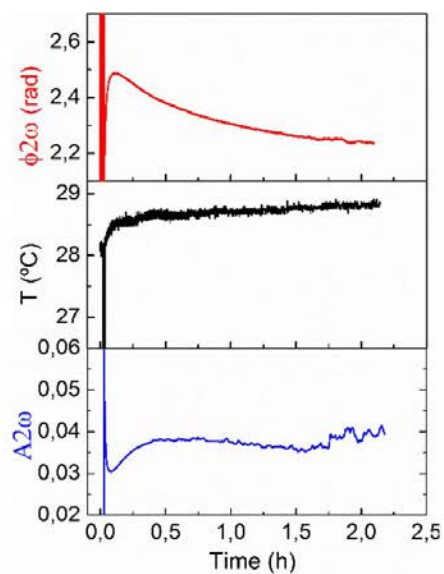
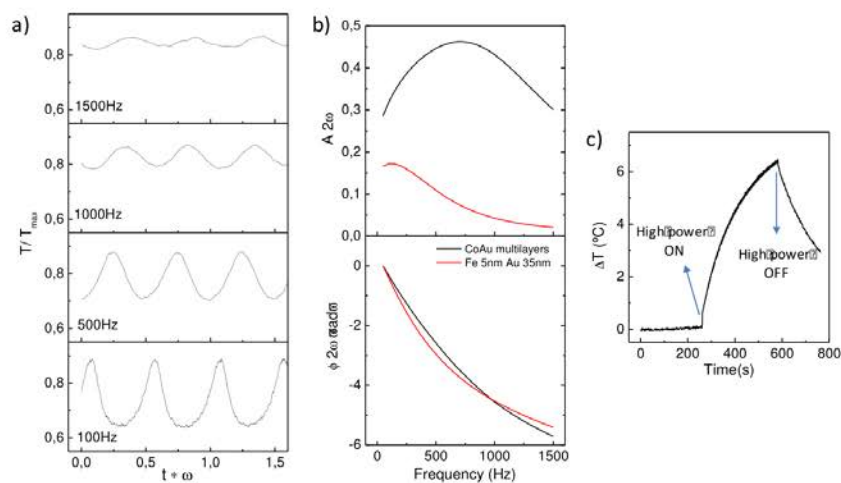


Figure S12. Demonstration of the simultaneous nano-heating/thermometry by Fe(5nm)/Au(35nm) nanodomains. a) Intensity modulation of the FeAu nanodomains at increasing magnetic induction frequencies ($B = 2\text{mT}$). b) Comparative of the amplitude ($A_{2\omega}$) and phase ($\phi_{2\omega}$) for Co/Au and Fe/Au nanodomains, showing the lower magneto-chromic effect in the latter due to their in-plane magnetization. c) Demonstration of the real-time detection of temperature variations induced by the 808 nm laser beam (noise 0.026°C , i.e. detection limit of 0.08°C) by the Fe/Au nanodomains.



Chapter 3

3.1 Biodegradable ferromagnetic-plasmonic nanocapsules for externally controlled and non-invasively monitored nanotherapies

The aim of this part was to merge the actuating and sensing capabilities demonstrated in the previous articles and to maximize the biomedical translatability by developing fully biodegradable ferromagnetic-plasmonic nanocapsules loaded by anticancer drugs. This combination will enable magnetically controlled drug concentration, controlled drug release, chemotherapy and co-adjuvant photothermal therapy, non-invasive visualization and multisensing (nanothermometry and biosensing).

To achieve these goals in Chapter 3 we incorporated a biodegradable PLGA polymer core encapsulating the antitumor drug Paclitaxel, and a Fe/SiO₂ semi-shell to obtain fully degradable ferromagnetic-plasmonic nanocapsules. The PLGA core was chosen due to its biocompatibility, hydrolysis based degradability, and high drug loading capacity. The fabrication of the drug loaded PLGA nanoparticles was undertaken by our collaborators from Institute for Drug Research in Jerusalem.

One of the main challenges of this work was optimizing the self-assembly of the loaded PLGA nanoparticles, which involved careful adjustment of the nanoparticles size and charge, their water stability and the substrate surface charge density. The PLGA hydrolysis also imposed a tight synchronization with our colleagues to prevent their degradation before the self-assembly and ensure the reproducibility. In addition, due to the lower glass transition temperature of PLGA with respect to polystyrene, the material electron-beam evaporation conditions should be carefully controlled to minimize overheating. To maximize the dispersibility in water, the thickness of Fe/SiO₂ was slightly reduced, while the size of the PLGA (150 nm) was increased. The low evaporation temperature of Fe and SiO₂ also helped in the dispersibility.

The PLGA nanoparticles exhibited large drug loading efficiency (32%), and a controlled release of 40% during the first 4 days and the rest during the full degradation of the PLGA which takes *ca.* 1 month.

The Fe/SiO₂ semi-shell enabled increasing the magneto-phoretic manipulation efficiency due to the decrease of the particle mass. The observed high magnetic trapping efficiency (30% per single pass at flow rates 1000 μL/min) in microfluidic channels mimicking blood circulating conditions highlights their capacity for strong magnetic control of the drug transport. In addition, Fe/SiO₂ semi-shell showed very intense T_2 contrast in nuclear magnetic resonance with improved relaxivity $r_2 = 368 \text{ s}^{-1} \text{ mM}^{-1}$.

On the other hand, the highly damped plasmonic behaviour of the Fe layer endowed the nanocapsules intense broadband optical absorption and minimized scattering. These features are crucial to keep very high photothermal conversion efficiencies in the first and second biological windows (63% and 67% for 808 nm and 1064 nm lasers, respectively).

The results from *in vitro* tests showed that the PLGA@Fe/SiO₂ nanocapsules possess very low toxicity in long-term cell cultures and strong label-free contrast in confocal imaging to assess the internalization by the cultured cells. Importantly, the preliminary results from *in vivo* tests confirmed the minimal toxicity of the nanocapsules in mice after tail vein injection. The high T_2 signal allowed non-invasively visualizing the accumulation of the free circulating capsules in the liver, and the almost total recovery of the signal 4 days after the intravenous injection.

Finally, the significant optical and magnetic anisotropies of the Fe/SiO₂ semi-shell could also be exploited for opto-magnetic sensing to integrate the simultaneous nano-heating/thermometry concept and the biosensing application to monitor the formation biofilms or to detect specific biomolecules at the nanocapsules surface, even under complex optical conditions.

To summarize, the PLGA@Fe/SiO₂ nanocapsules could retain the magneto-plasmonic properties for efficiently merging magnetic concentration, controlled drug release, photothermal therapy, non-invasive visualization and sensing. In addition, their lower cost, biocompatibility and biodegradability contributed to highlight the great potential as a multifunctional biomedical platform.

3.2 Personal Contribution

This manuscript is based on a project with international collaborators, thus the results should be attributed to the collaboration among all the collaborators. Thus, it is important to mention which were my personal contributions for this manuscript.

My independent work, which included i) PLGA@Fe/SiO₂ nanocapsules design, fabrication and optimization, **ii)** characterizations of physiochemical properties (lithography pattern, size, surface charge) using scanning electron microscopy (SEM) and dynamic light scattering (DLS) and optical properties (extinction spectra) using vis-near infrared spectroscopy, **iii)** photothermal heating efficiency measurements, **iv)** opto-magnetic modulations, **v)** simultaneous nanoheating/thermometry, **vi)** degradation process evaluation of nanocapsules by monitoring the optical extinction variations, **vii)** magnetic trapping efficiency measurements.

I participated in other experiments, where the tests were carried out mainly by some colleagues, but I was personally involved in the experiments. These include **i)** transmitted electron microscopy (TEM; Belen Ballesteros, ICN2), magnetization characterization using vibrating sample magnetometer (VSM; Jordi Sort, Universitat Autònoma de Barcelona), **ii)** theoretical calculations of optical properties using finite domain time domain (FDTD) software (Borja Sepúlveda), **iii)** *in vitro* cytotoxicity using Alamar Blue dyes under confocal imaging (Carme Nogués, Bioscience Faculty of Universitat Autònoma de Barcel), **iv)** *in vivo* cytotoxicity and distribution using T_2 signal in nuclear magnetic resonance (NMR Service at Universitat Autònoma de Barcelona).

Some experiments were carried out by collaborators, although I provided with the necessary nanodome samples. These include **i)** cell cultures and cell viability tests (Carme Nogués, Bioscience Faculty of Universitat Autònoma de Barcelona), **ii)** biosensing of polydopamine coating on the surface of nanocapsules (Aritz Lafuente, master student in ICN2); **or scientific services i)** transmission electron microscopy (TEM Service at Universitat Autònoma de Barcelona), **ii)** mass concentration tests using inductively coupled plasma mass spectrometry (ICP-MS Service at Instituto de Ciencia de Materiales de Madrid), **iii)** T_2 contrast signal detection using nuclear magnetic resonance (NMR) machine (NMR Service at Universitat Autònoma de Barcelona).

Biodegradable ferromagnetic-plasmonic nanocapsules for externally controlled and non-invasively monitored nanotherapies

Zhi Li,^{1,5} Josep Nogués,¹ and Borja Sepúlveda,^{1*}

Carme Nogués,²

Arnon Fluksman,³ Ofra Benny,³

Silvia Lope Piedrafita,⁴

Jordi Sort⁵

¹ Catalan Institute of Nanoscience and Nanotechnology (ICN2), CSIC and BIST, Campus UAB, Bellaterra, 08193 Barcelona, Spain

²Departament de Biologia Cel·lular, Fisiologia i Immunologia, Facultat de Biociències, Universitat Autònoma de Barcelona, Bellaterra, 08193 Barcelona, Spain.

³Faculty of Medicine, School of Pharmacy, Hebrew University; Institute for Drug Research, Jerusalem, 91120, Israel

⁴Servei de Resonància Magnètica Nuclear, Universitat Autònoma de Barcelona, Bellaterra, 08193 Barcelona, Spain, and Centro de Investigación Biomédica en Red en Bioingeniería, Biomateriales y Nanomedicina (CIBER-BBN).

⁵Departament de Física, Facultat de Ciències, Universitat Autònoma de Barcelona, Bellaterra, 08193 Barcelona, Spain.

Biodegradable ferromagnetic-plasmonic nanocapsules for externally controlled and non-invasively monitored nanotherapies

Abstract

Current nanotherapies require new tools to enhance their efficacy and to externally control their therapeutic effects, especially in cancer therapies. These critical needs could be achieved by developing nanomaterials enabling the external control of their accumulation at the site of action, as well as non-invasive visualization and detection of the actuation strength to tune the therapeutic effects. Here we present novel biodegradable hybrid (organic/inorganic) ferromagnetic-plasmonic drug loaded nanocapsules. This multi-active nanocapsules, composed of poly-lactic-co-glycolic-acid (PLGA) core loaded with paclitaxel anticancer drug and partially coated by a Fe/SiO₂ semishell (PLGA@Fe/SiO₂), combine high drug loading efficiency with strong ferromagnetic response, colloidal stability, extremely high optical heating efficiency, intense NMR contrast for *in vivo* visualization, and complete biodegradability.

The strong ferromagnetism of the PLGA@Fe/SiO₂ nanocapsules enables efficient concentration by external magnetic field gradients *via* magnetophoretic forces. A high magnetic trapping efficiency (> 30%) per single pass is demonstrated in microfluidic channels mimicking blood circulation conditions. Their high magnetization also provides very intense T_2 contrast in nuclear magnetic resonance (relaxivity $r_2 = 368 \text{ s}^{-1} \text{ mM}^{-1}$). The Fe semi-shell also presents a highly damped plasmonic behaviour leading to intense broadband optical absorption and minimized scattering. These properties are crucial to achieve high photothermal conversion efficiencies in the first and second biological windows (63% and 67% for 808 nm and 1064 nm lasers, respectively).

The evolution of the optical and magnetic properties of the nanocapsules during the PLGA degradation can be exploited as internal sensors to non-invasively monitor the nanocapsules degradation by optical spectroscopy or NMR imaging. The nanocapsules have demonstrated low *in vitro* toxicity in long-term cell cultures and strong label-free contrast in confocal imaging. Preliminary results *in vivo* have shown minimal toxicity effects in mice. Their high T_2 contrast has allowed visualizing the accumulation of the free circulating capsules in the liver, and the almost total recovery after 4 days.

Finally, the opto-magnetic analysis of the nanocapsules rotation under low amplitude and low frequency magnetic fields enables monitoring the changes in their external environment. We have demonstrated the application of the opto-magnetic detection for nanothermometry to monitor in real-time the induced temperature increase by laser heating (detection limit 0.15 °C), and for biosensing to monitor the formation of biofilms under complex optical conditions.

All these features are highly promising for developing advanced externally controlled, biodegradable, nanotherapeutic agents with enhanced therapeutic efficacy by merging efficient magnetic concentration, photothermal therapy, non-invasive visualization and sensing.

1. Introduction

Nanotherapies based on organic nanoparticles (*e.g.* liposomes, dendrimers, micelles, polymer particles) with linked or encapsulated drugs have emerged with the aim of overcoming the side effects of chemotherapies by increasing both circulation time and accumulation of the drug inside solid tumours by exploiting their high drug loading capacity and the Enhanced Permeability and Retention (EPR) effect in leaky tumour neovasculature. However, they have not fulfilled the high therapeutic expectations due to the passive delivery of the nanoparticles, which impedes achieving high nanoparticle concentrations inside solid tumours and efficient drug delivery in tumour cells.^[364,365] The main obstacles that nanoparticles face in clinical therapies are: hepatic, renal or immune system clearance that can drastically reduce the probability to target tumours; inherent elevated hydrostatic pressure in solid tumours that inhibits nanoparticle extravasation; poor diffusion inside solid tumours due to the dense extracellular matrix, or intracellular trapping of the nanoparticles in endosomes, which hampers the drug delivery to the sites of action in the cytoplasm or nucleus.^[365] These hurdles are behind the clinical approval of only very few nanotherapies to date, which have not demonstrated the high efficacy gains expected from the preclinical assays.^[366]

Magnetic nanostructures have been proposed to externally control and improve nanotherapies delivery.^[132,367-369] However, these nanostructures are mostly based on small superparamagnetic iron oxide nanoparticles that exhibit weak magnetic response, which severely hampers their efficient external actuation with magnetic fields, and due to their small size they have limited drug loading capacity. The use of small superparamagnetic nanoparticles for biomedical applications has been imposed by the difficulty to achieve strong and stable ferromagnetic nanoparticles by chemical synthesis, as result of the irreversible aggregation caused by their intense magnetic dipole-dipole interactions. Interestingly, nanoparticles combining plasmonic and iron oxide nanoparticles and for simultaneous light and magnetic actuations have also been proposed,^[132,368] but these systems show similar weak magnetic response and limited drug loading capabilities.^[369-372]

Therefore, there is a pressing need to develop novel drug vehicles with improved capacity of external control, as a way to achieve more efficient local release of the drug and enhanced therapeutic activity. In addition, the capacity to integrate therapeutic

actuation and sensing in the same nanostructure can open new technological pathways to gain more therapeutic control and to merge diagnosis and treatments.

Here we present novel biodegradable ferromagnetic nanocapsules which can merge high drug loading capacity with the following unique set of multi-actuation therapeutic and sensing capabilities: **i)** highly efficient magnetic manipulation and concentration *via* magnetophoretic forces and retained colloidal stability, **ii)** highly efficient and broadband optical heating in the two biological windows as adjuvant therapy, **iii)** opto-magnetic nanothermometry to control in real-time the optical heating, **iv)** intense label-free optical and magnetic resonance imaging to non-invasively visualize and track the nanocapsules and to monitor their degradation, and **v)** highly sensitive biosensing capabilities. This set of features together with the low *in vitro* and *in vivo* toxicity offer new externally actuated and monitored therapeutic-sensing nanovehicles with high potential to improve the local efficacy of nanotherapies.

2. Fabrication and structural properties

The active biodegradable ferromagnetic nanocapsules are composed of poly-lactic-co-glycolic-acid (PLGA) nanoparticles (diameter *ca.* 150 nm) loaded with the anticancer drug paclitaxel, which are partially covered by a metallic Fe (20 nm) and a SiO₂ (10 nm) layers (Figure 1a).

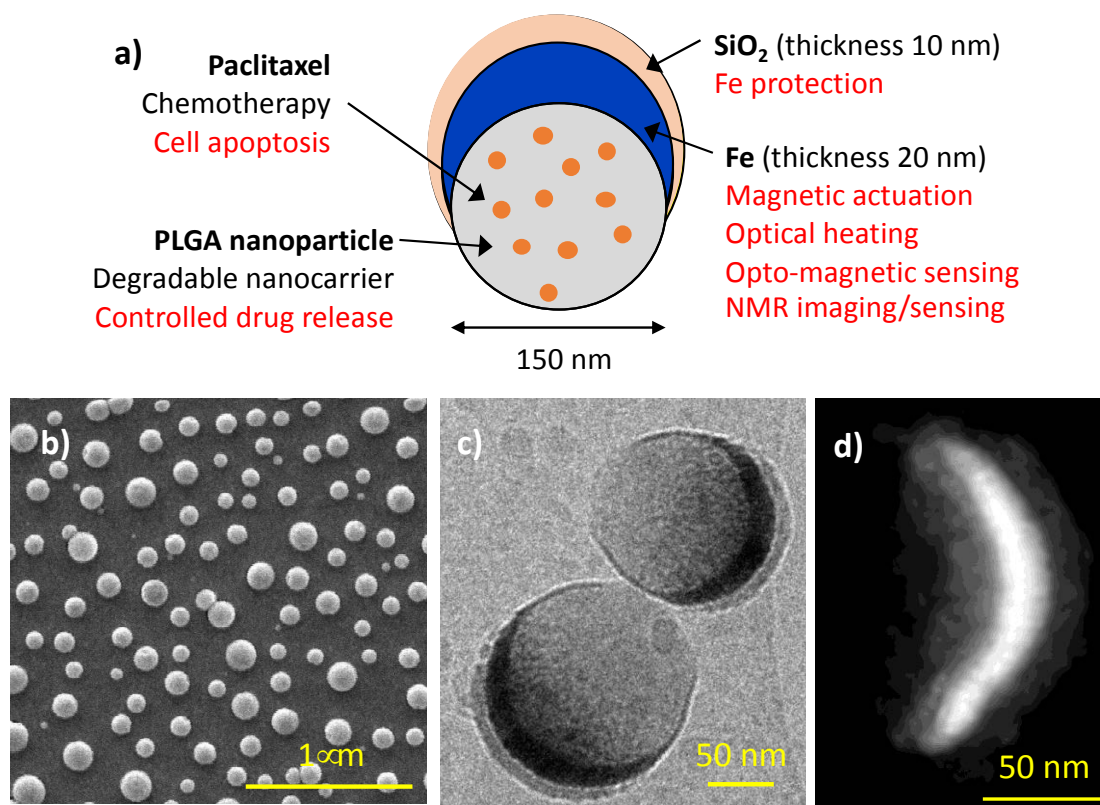


Figure 1. Structural properties. a) Schematic of the drug loaded ferromagnetic nanocapsules components and their functionalities. b) SEM image of the self-assembled PLGA nanoparticles evaporated with Fe (20 nm) and SiO₂ (10 nm). c) TEM images of the ferromagnetic nanocapsules after dispersion in water for 3 h. d) TEM image of the nanocapsule after 1 month degradation in water.

The fabrication of nanocapsules is based on a cost-effective and scalable combination of bottom-up and top-down processes, which can be divided in three steps. The first step is the synthesis of the drug loaded PLGA nanoparticles based on a nanoprecipitation method (Supporting Information experimental section). According to dynamic light scattering measurements, the PLGA nanoparticles exhibit an averaged hydrodynamic diameter of 200 nm (polydispersity index 0.04) and a zeta potential of -30 mV. The drug

loading efficiency, quantified by high performance liquid chromatography (HPLC) after dissolving the nanoparticles in acetonitrile, is 32%.

The second step consists of the electrostatic self-assembly of the drug loaded PLGA particles on a solid support (e.g. silicon wafers or plastic films), yielding a uniform monolayer of randomly distributed and well separated PLGA nanoparticles (Figure 1b). Finally, the Fe and SiO₂ layers are deposited by electron beam evaporation leading to a “nanodome” structure (Figure 1c). The metallic Fe layer provides the ferromagnetic and plasmonic properties, while the SiO₂ is used to protect the Fe from rapid oxidation and for future functionalization.

The ferromagnetic-plasmonic nanocapsules are finally dispersed in water or buffer by mild ultrasonication, giving rise to stable colloidal dispersions with zeta potential of -25 mV and average dynamic light scattering size of 200 nm. Once dispersed in water, the PLGA hydrolysis triggers the nanocapsule degradation and the release of the paclitaxel drug. According to HPLC measurements, approximately 40% of the drug is released within the first 4 days, and the rest is released during the full PLGA nanoparticle degradation, which nearly takes one month (Figure 1d).

3. Magnetic and optical properties

The diameter of the nanocapsules and the thickness of the Fe layer have been designed to achieve highly anisotropic magnetic and optical nanostructures with high magnetization saturation and intense optical absorbance.

The magnetic anisotropy is clearly observed in the in-plane and out-of-plane magnetization loops of Figure 2a, showing the predominant in-plane magnetization in the nanocapsules. Importantly, the in-plane magnetization reversal loop shows a vortex magnetic configuration (see Figure 2a inset) with near zero remanence and high $M(H)$ slope. As a consequence, the magnetic dipole moment and dipole-dipole interaction of the nanocapsules are negligible in the absence of magnetic field, which is crucial to keep stable colloidal dispersions. Moreover, the magnetization can be saturated with only 750 Oe, thereby enabling strong actuation with moderate magnetic field gradients. The high magnetization of the metallic iron layer also allows non-invasively imaging the

nanocapsules by nuclear magnetic resonance. The nanocapsules exhibit a very strong T_2 signal in NMR showing a relaxivity r_2 of $368 \text{ s}^{-1} \text{ mM}^{-1}$ (Figure 2b), which is much higher than that of commercial contrast agents based on iron oxides (*e.g.* Feridex and Resovist).

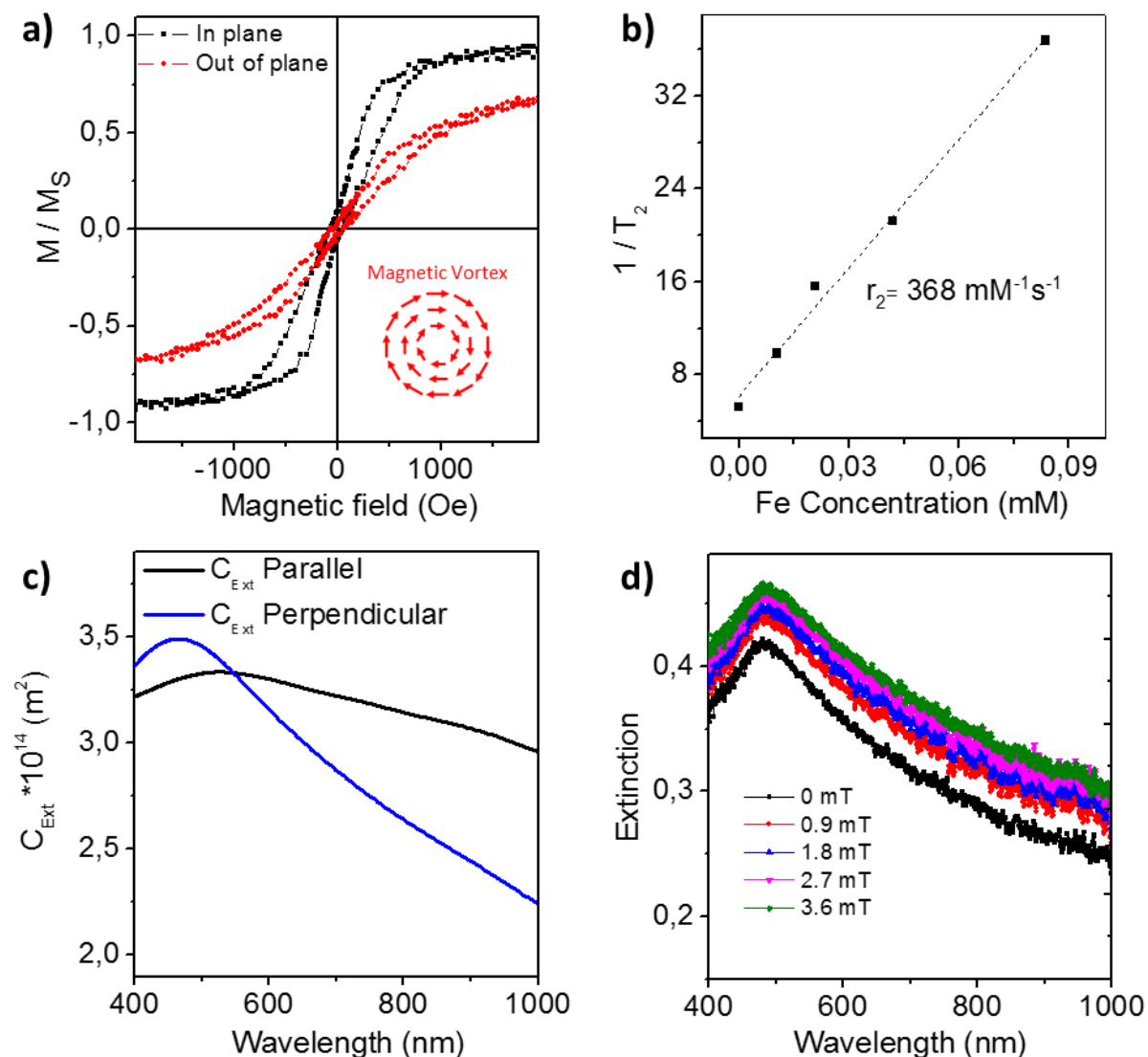


Figure 2. Magnetic and optical properties of the PLGA@Fe/SiO₂ nanocapsules. a) In plane and out-of-plane magnetization loops showing the ferromagnetic behaviour, the magnetic anisotropy and the vortex magnetic structure (inset image shows a schematic magnetic vortex configuration). b) Nuclear magnetic resonance T_2 contrast and r_2 relaxivity. c) Theoretical extinction cross section (C_{Ext}) for different orientations of the nanocapsules with respect to the polarization of the incident light. d) Experimental optical extinction of the nanocapsules in the presence of a static magnetic field H when light polarization is parallel to H .

The Fe layer also exhibits anisotropic optical properties, as observed in the finite difference time domain (FDTD) calculations of the extinction cross section of the nanocapsules for different orientations with respect to the light polarization (Figure 2c).

The combination of anisotropic optical and magnetic properties enables intense opto-magnetic effects, *i.e.*, changes in the extinction spectrum of the colloidal dispersions induced by static or alternating magnetic fields. In the absence of a magnetic field the particles are randomly oriented nanoparticles and the experimental extinction shows a very broad and flat spectrum (Figure 2d). The application of a static and homogeneous magnetic field H tends to align the nanocapsules with the plane of the Fe layer parallel to the magnetic field due to the generation of a magnetic torque. Interestingly, magnetic fields as low as 40 Oe are sufficient to align the colloidal ferromagnetic nanocapsules. The magnetic alignment results in a substantial absorbance increment in the whole visible-NIR spectrum when the light is polarized parallel to the magnetic field (Figure 2d), which is related to the higher extinction cross section of nanocapsules in this orientation. Such modulation of the optical extinction is highly relevant for the development of the sensing tools described below.

Remarkably, the highly damped plasmonic behaviour of the metallic iron semishell induces a large reduction of the scattering cross section of the nanocapsules, but keeping high and broadband absorption cross section (Supporting Information Figure S1), which are ideal features for achieving high photothermal conversion efficiencies.

4. External controls: magnetic manipulation and optical heating

The ferromagnetic vortex behaviour of the nanocapsules is ideal for external magnetic manipulation since it allows combining colloidal stability and the generation of strong magnetophoretic forces. To demonstrate the magnetic actuation strength of the nanocapsules *via* magnetophoretic forces we analyze the magnetic trapping efficacy by a magnet in a microfluidic channel mimicking the flow conditions in blood vessels. The experimental setup and more details about the experiments are included in supporting information (Figure S2). The percentage of trapped particles by the magnet is quantified by measuring the relative decrease of the absorbance ($\Delta A/A$) of the nanocapsules dispersions that are flowed through the microfluidic channel at controlled flow rates by using a syringe pump. As can be observed in Figure 3a, even in a single fluidic pass, an extremely high trapping efficiency (>30%) can be achieved for flow rates lower than 1

mL/min. For higher speeds the trapping percentage is stabilized at *ca.* 15% per pass. These results are highly promising for efficient magnetic trapping in small capillaries.

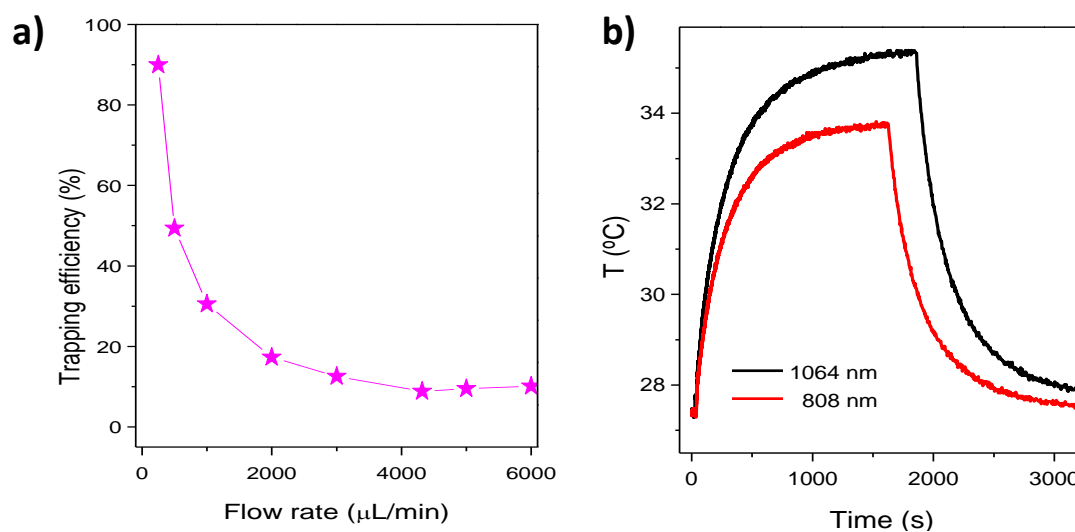


Figure 3. Magnetic and optical external actuation tools. a) Magnetic trapping efficiency in a microfluidic channel at increasing flow rates. b) Demonstration of the efficient optical heating in the first and second biological windows with 808 nm and 1064 nm lasers (incident light power 200 mW, nanocapsules concentration 9.75 μg/mL, and volume 600 μL).

On the other hand, the high absorption and reduced scattering cross sections of the nanocapsules (Figure S1) enable highly efficient optical heating in the near infrared spectral regions with the maximized penetration in tissues (Figure 3b). Indeed, the photothermal conversion efficiency in the first (wavelength 808 nm) and second biological windows (wavelength 1064 nm) are as high as 63% and 67% (Figure S3), respectively, which is comparable with state-of-the-art nanoplasmonic heaters.^[373,374] The slightly increased temperature variation at 1064 nm observed in Figure 3b is a consequence of the small water heating contribution at this wavelength.

5. Non-invasive and label-free monitoring of the nanocapsules degradation

Interestingly, as the PLGA@Fe/SiO₂ nanocapsules are degradable, the optical and magnetic properties of the Fe layer can evolve during the degradation process due to its tendency to oxidize. This evolution can be exploited to non-invasively detect and monitor the degradation process. To demonstrate it, we disperse the nanocapsules in an agar hydrogel (0.5% mass concentration) in PBS (1X) buffer solution to trap the nanoparticles

in the gel and to avoid concentration changes due to the nanoparticle sedimentation with time.

Regarding the optical properties (Figure 4a), the broadband absorbance spectrum of the nanocapsules initially shows a decrease in the whole vis-NIR range (first 7 days), which is followed with an increase of the absorbance in the ultraviolet and blue parts of the spectrum, and a reduction of the NIR range (day 7- day 31). This optical evolution is consistent with the partial transformation of the metallic iron into iron oxides.^[375]

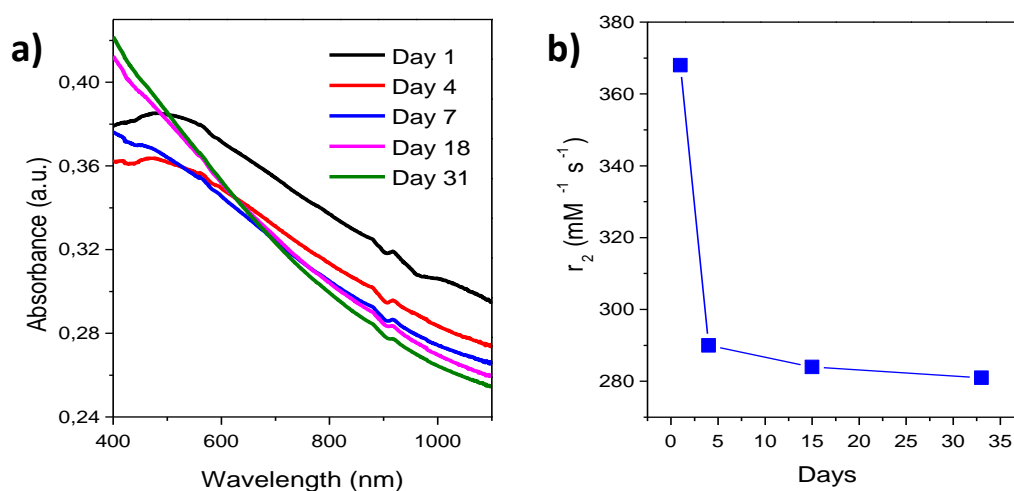


Figure 4. Non-invasive monitoring of the nanocapsules degradation. a) Evolution of the vis-NIR spectrum and b) magnetic resonance r_2 relaxivity evolves as the nanocapsules degrade in PBS.

The NMR tests of the PLGA@Fe/SiO₂ nanocapsules has also been conducted (supporting information section 3). The r_2 relaxivity also exhibits an interesting behaviour (Figure 4b). There is an abrupt decrease in the r_2 signal during the first 4 days, after which the relaxivity decreases at a slower rate. This behaviour can be exploited to efficiently visualize the *in-vivo* magnetic concentration of nanocapsules, to indirectly follow the drug release during the first days, and to finally track their long term biodistribution. The high r_2 value after one-month degradation proves that the nanocapsules can keep a high magnetic strength despite of their dispersion in a highly corrosive PBS environment.

6. *In vitro* cytotoxicity and label-free imaging

Another highly relevant aspect for biomedical applications is the necessity of minimizing the toxicity of the nanotherapeutic agents. To ensure the biomedical potential we have exposed SKBR3 cells to two different concentrations (10 $\mu\text{g}/\text{mL}$ and 40 $\mu\text{g}/\text{mL}$) of the unloaded PLGA@Fe/SiO₂ nanocapsules. (Supporting information section 6).

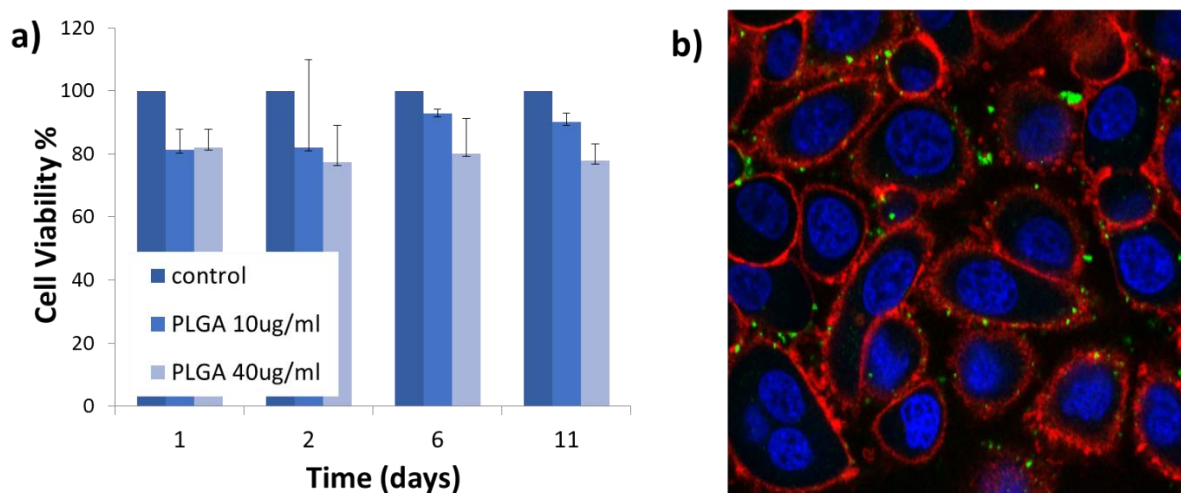


Figure 5. *In vitro* characterization. a) Long term viability of the SKBR3 cell exposed to 10 and 40 $\mu\text{g}/\text{mL}$ of the unloaded PLGA@Fe/SiO₂ nanocapsules. b) Confocal image of cells after incubating 3h with 40 $\mu\text{g}/\text{mL}$ nanocapsules. The white arrow shows the internalized nanocapsules (green).

We have analyzed the long-term cytotoxicity in SKBR3 cells by Alamar Blue assay cells during 11 days. The results show a minimal decrease in the cell viability with respect to the control sample, which confirms the expected low cytotoxicity of the PLGA@Fe/SiO₂ nanocapsules.

In addition, the intense and broadband optical extinction of the nanocapsules is able to serve as valuable label-free visualization tool. The large attenuation of the transmitted light by the nanocapsules enables accurate visualization by bright field and confocal microscopy (green dots in Figure 5b) in both transmission and reflection modes. In particular, confocal imaging can be used to assess *in vitro* cell internalization efficiency of the nanocapsules, as it can be easily combined with conventional cell fluorescence imaging (Figure 5b).

7. *In vivo* toxicity and MRI imaging and biodistribution analysis

Once the low cytotoxicity had been established, we analysed the *in vivo* toxicity and biodistribution in C57BL/6 mice by exploiting the intense T_2 contrast in magnetic resonance imaging. We have injected 5 mg/Kg (i.e. 100 μg) in mice (N=2) *via* tail vein injection, and we have monitored the nanocapsules distribution by T_2 weighted imaging at different times (Figure 6) in a 7 T magnet. (Supporting information section 3).

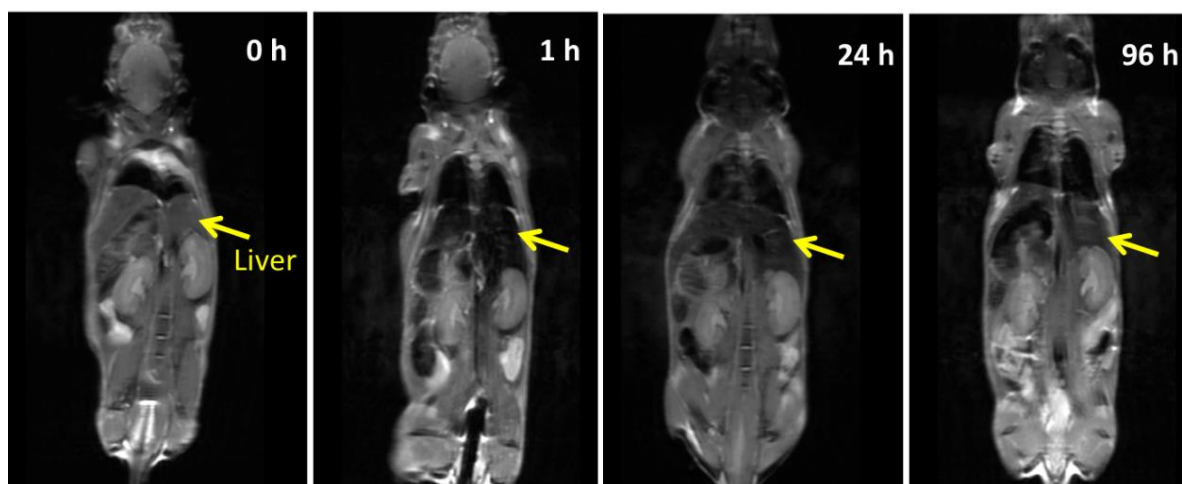


Figure 6. *In vivo* characterization. Magnetic resonance T_2 weighted images of C57BL/6 mice before and after tail vein injection of 5 mg/Kg (i.e. 100 μg) of unloaded PLGA@Fe/SiO₂ nanocapsules.

The NMR images show a very clear decrease in the T_2 signal in the liver 1 h after the injection, while there is not a significant decrease in other organs, such as kidneys, or muscle. The T_2 signal already increases at 24 h post-injection, and it is almost fully recovered after 96 h. The mice have not suffered any weight loss during the assay or any noticeable toxicity effects after 2 weeks. The secretion pathway *via* the liver is the expected route given the size and surface charge of the nanocapsules and their passive delivery. The overall low toxicity and the strong T_2 contrast *in vivo* are valuable features for future magnetically guided and concentrated nanocapsules at the site of action by external magnetic field gradient.

8. Sensing: simultaneous nanoheating/thermometry, and biosensing

In addition to the capabilities of external actuation and non-invasive monitoring of the internal changes, the PLGA@Fe/SiO₂ nanocapsules can also be employed as sensors to detect the changes in their surrounding environment by analyzing absorbance

measurements when rotating under low frequency and low amplitude alternating magnetic fields, which induce the nanocapsules rotation in the fluid.

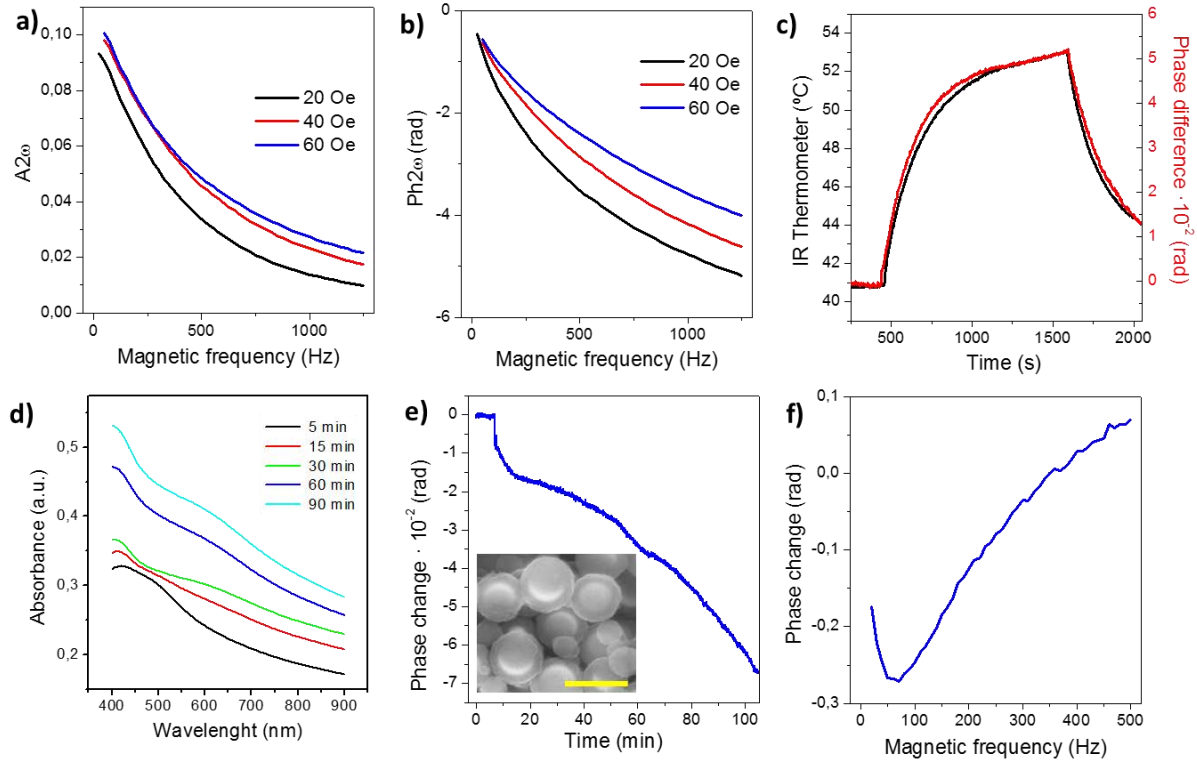


Figure 7. Opto-magnetic nanosensing. a) and b) Opto-magnetic rotation dynamics, amplitude $A_{2\omega}$ and phase $Ph_{2\omega}$, respectively, of the nanocapsules in an alternating magnetic field as a function of the magnetic frequency. c) Demonstration of simultaneous nano-heating/thermometry by measuring the variation of $Ph_{2\omega}$ as the nanoparticles are heated by the 808 nm laser. d) Absorbance spectra of the nanocapsules dispersion during the formation of a polydopamine over-layer on the nanocapsules. e) Phase variation induced by the polydopamine coating as a function of time during the coating formation at a magnetic frequency of 37 Hz. Inset SEM image shows clear surface coating (14 nm) of polydopamine around the nanodomains after 90 min reaction which reconfirms the corresponding phase change f) Phase variation as a function of the rotation frequency after 150 min reaction. All the measurements are acquired at $H = 40$ Oe.

The nanocapsules magnetic rotation generate intense opto-magnetic modulation of the transmitted light. Since the nanocapsules alignments for positive and negative H are optically equivalent, the opto-magnetic modulation exhibits a frequency (2ω) that is twice the applied magnetic frequency (ω). There are two parameters of the opto-magnetic modulation that can accurately describe the magnetic rotation of the nanocapsules: **i)** the amplitude ($A_{2\omega}$), and **ii)** the phase lag between the optical signal

and the magnetic field ($\text{Ph}2\omega$). Both parameters can be easily extracted by Fast Fourier Transform (FFT) analysis of the opto-magnetic modulation signal.^[376] For low particle concentrations, $A2\omega$ is proportional to the particle concentration and to the capacity to fully align the nanocapsules parallel to the magnetic field, which depends on the amplitude and frequency of the magnetic field. As the nanocapsules are dispersed in a viscous fluid, the particle rotation shows an increased damping with the magnetic frequency. As a result, the value of $A2\omega$ drops as the frequency increases (Figure 7a), which evidences that the nanocapsules cannot achieve a complete rotation. At the same time, the phase lag $\text{Ph}2\omega$ increases (Figure 7b). Importantly, the value of $\text{Ph}2\omega$ is independent on the particle concentration, but it is highly dependent on the fluid viscosity and the H amplitude. The rise of H produces an increase of $A2\omega$ and a reduction of $\text{Ph}2\omega$, as the stronger magnetic torque allows overcoming more efficiently the fluid friction. The $\text{Ph}2\omega$ parameter can be employed for sensing applications, to monitor the temperature increase generated by the nanocapsules induced optical heating and to detect with high sensitivity the attachment of biomolecules, as low cost nanobiosensors.

The combination of the NIR illumination and alternating magnetic fields enables using the magnetically actuated rotating nanocapsules as the recently developed simultaneous nano-heaters/thermometers.^[14] This application involves analyzing the light modulation signal of the nanocapsules dispersion at a fixed magnetic frequency, and monitoring the phase lag $\text{Ph}2\omega$ variations when the laser intensity is increased to induce the local heating. We exploit the water viscosity reduction as the temperature increases and, therefore, the related reduction of $\text{Ph}2\omega$ as the induced optical heating in the nanocapsules rises the temperature of their surrounding liquid. As shown in Figure 7c, $\text{Ph}2\omega$ follows the exact same tendency as the temperature curve acquired by an infrared thermometer. According to these measurements, the conversion factor is 0.009 rad/ °C, and the detection limit of the temperature variations is 0.15 °C. This value is slightly higher than that of Au/Co nanostructures,^[376] but it is sufficient for controlling the photothermal treatments. In contrast, the multifunctionality of the nanocapsules together with their simplicity and much lower cost are clear benefits over the Au/Co structures. Finally, the phase lag $\text{Ph}2\omega$ parameter can also be employed to develop highly sensitive biosensors. In this application we exploit the changes in $\text{Ph}2\omega$ as the hydrodynamic radius of the nanocapsules increase when biomolecules attach to their

surface. Such increase results in a higher viscous damping and, therefore, an increase in the phase lag between the nanoparticles rotation (optical signal) and the magnetic field. In order to demonstrate the power and versatility of this sensing scheme, we detected the formation of a polydopamine layer around the nanocapsules and the highly absorbing polydopamine nanoparticles in the solution. The complexity of this measurement can be witnessed in the visible-NIR spectra of the colloidal dispersion (Figure 7d) after the addition of the dopamine solution (0.5 $\mu\text{g}/\text{mL}$). After 30 min reaction the nanocapsule absorbance is almost hidden by the strong absorbance of the formed polydopamine nanoparticles in solution, and it is totally undistinguishable after 1 h reaction. In contrast, the opto-magnetic detection system enables extracting only the optical signal of the rotating magnetic particles inside of the complex absorbing medium. As the phase lag is totally independent of the medium absorbance, it enables detecting in real-time and without any interference the continuous formation of the polydopamine layer around the nanoparticles once the dopamine is added to the solution (Figure 7e). The total increase of the phase lag after 90 min reaction is approximately 0.1 rad, and corresponds to the formation of a 14 nm thick shell around the nanocapsules (Figure 7e inset). As the typical noise of the phase measurements is 0.002 rad, subnanometric layers can be easily detected even in an optically complex environment, and with a very cost-effective set up. The total phase change after stopping the reaction as a function the magnetic frequency shows that the highest sensitivity in the detection of the over-layer formation is achieved with a frequency of around 50 Hz (Figure 7f).

9. Conclusions

In conclusion, the biodegradable ferromagnetic nanocapsules constitute a novel nanotherapeutic concept that is able to merge externally controlled multi-therapies with non-invasive imaging and (bio)sensing capabilities. The high magnetic strength and colloidal stability are the key elements for enabling efficient external magnetic actuation via magnetophoretic force. Such strong magnetism also provides outstanding contrast for NMR imaging, showing the capacity to monitor the nanocapsules degradation. On the other hand, the high optical absorbance with minimal scattering enable highly efficient optical heating in both NIR biological windows. The change in the optical properties during the nanocapsule degradation is also appealing for monitoring their degradation.

The low toxicity *in vitro and in vivo*, and the capacity to non-invasively assess the nanocapsules biodistribution by magnetic resonance imaging add more biomedical potential and interest to this nanotechnology. Moreover, the combination of optical and magnetic actuation opens the path to develop highly sensitive opto-magnetic sensors, which can be applied to monitor the temperature changes during photothermal actuations or the specific attachment of biomolecules. The combination of all these features endow the ferromagnetic capsules a promising future as smart nanotherapeutic agents.

Reference

- [1] S. Wilhelm, A. J. Tavares, Q. Dai, S. Ohta, J. Audet, H. F. Dvorak, W. C. W. Chan, *Nat. Rev. Mater.* **2016**, *1*, 16014.
- [2] J. W. Nichols, Y. H. Bae, *Nano Today* **2012**, *7*, 606.
- [3] S. Mura, J. Nicolas, P. Couvreur, *Nat. Mater.* **2013**, *12*, 991.
- [4] K. C.-F. Leung, S. Xuan, X. Zhu, D. Wang, C.-P. Chak, S.-F. Lee, W. K. W. Ho, B. C. T. Chung, *Chem. Soc. Rev.* **2012**, *41*, 1911.
- [5] S. Shams, M. Ghazanfari, C. Schmitz-Antoniak, *Nanomaterials* **2019**, *9*, 97.
- [6] S. Stafford, R. Serrano Garcia, Y. Gun'ko, *Appl. Sci.* **2018**, *8*, 97.
- [7] I. Urries, C. Muñoz, L. Gomez, C. Marquina, V. Sebastian, M. Arruebo, J. Santamaria, *Nanoscale* **2014**, *6*, 9230.
- [8] S. Santra, C. Kaittanis, J. Grimm, J. M. Perez, *Small* **2009**, *5*, 1862.
- [9] S. Kayal, R. V. Ramanujan, *J. Nanosci. Nanotechnol.* **2010**, *10*, 5527.
- [10] P. Gangopadhyay, S. Gallet, E. Franz, A. Persoons, T. Verbiest, *IEEE Trans. Magn.* **2005**, *41*, 4194.
- [11] J. R. Cole, N. A. Mirin, M. W. Knight, G. P. Goodrich, N. J. Halas, *J. Phys. Chem. C* **2009**, *113*, 12090.
- [12] B. Li, Q. Wang, R. Zou, X. Liu, K. Xu, W. Li, J. Hu, *Nanoscale* **2014**, *6*, 3274.
- [13] J. Tang, M. Myers, K. A. Bosnick, L. E. Brus, *J. Phys. Chem. B* **2003**, *107*, 7501.
- [14] Z. Li, A. Lopez-Ortega, A. Aranda-Ramos, J. L. Tajada, J. Sort, C. Nogues, P. Vavassori, J. Nogues, B. Sepulveda, *Small* **2018**, *14*, 1800868.

Supporting information

Biodegradable ferromagnetic-plasmonic nanocapsules for externally controlled and non-invasively monitored nanotherapies

1. Nanomaterials preparation section

- **Nanoprecipitation synthesis process of drug loaded PLGA nanoparticles**

Firstly, an organic solution of PLGA (100 mg) and paclitaxel (2 mg) in acetonitrile (5 ml) containing 0.01% Tween80 are added to an aqueous solution (10 ml, 0.1%, solutol) at room temperature. Following 15 min of stirring, the acetonitrile is removed under reduced pressure using an evaporator and the loaded PLGA nanoparticles are collected.

- **Fabrication of PLGA@Fe/SiO₂ nanodomies**

The applied fabrication approach is adapted from the previous developed method in the Chapter 1. In particular, 2mg/ mL drug loaded PLGA in Tris (20 mM) was prepared for colloidal lithography. 20 nm Fe and 10 nm SiO₂ were deposited using electron beam evaporation on PLGA pattern wafer.

2. Morphological, optical, magnetic and colloidal characterization

- The morphology and distribution of the nanodomies on the Si wafer were studied through scanning electron microscopy (SEM) using Quanta SEM 650 (Field Electron and Ion Company (FEI)) at 5 kV. Transmission electron microscopy, TEM, images were performed in a FEI Tecnai F20.
- Zeta potential and hydrodynamic size of PLGA and nanodomies were obtained through dynamic light scattering using Zetasizer Nano ZS (Malvern Instruments Ltd.).

- The mass concentration of Fe in the nanodomes dispersions was determined by inductively coupled plasma atomic emission spectroscopy (ICP-OES; Perkin Elmer mod. Optima 2100DV).
- The visible-near infrared (vis-NIR) spectroscopy studies of the nanodomes dispersions were carried out using Lambda25 (PerkinElmer). For the optical measurements, the optical spectra ranged from 400 nm to 1100 nm, which covered visible light and near infrared region.
- The magnetic characterization of the nanodomes was performed on monolayers that were transferred to a 1 cm polydimethylsiloxane (PDMS) substrate to eliminate the magnetic signal from the bilayer that is deposited on the wafer surface. Magnetization loops were acquired at room temperature using a vibrating sample magnetometer (MicroSense, LOT QuantumDesign) with a maximum applied field of 20 kOe. The measurements were performed by applying the field either parallel or perpendicular to the sample, i.e., in-plane or out-of-plane conditions.

3. Nuclear Magnetic Resonance

¹H-magnetic resonance imaging (MRI) studies were performed in a 70 kOe Bruker BioSpec 70/ 30 USR (Bruker BioSpin GmbH, Ettlingen, Germany) system equipped with a mini-imaging gradient set (4000 Oe/m) and using a linear volume coil with 72 mm inner diameter. Magnetic resonance data were acquired and processed on a Linux computer using Paravision 5.1 software (Bruker BioSpin GmbH, Ettlingen, Germany). For the relaxivity measurements of PLGA@Fe/SiO₂ nanodomes, phantoms containing various nanodomes concentrations in 1% agarose and PBS (1X) mixture were prepared. Magnetic resonance images were obtained from two 2.5 mm slice thickness coronal sections with a field of view (FOV) of 9×6 cm². Only transverse relaxation time (T_2) measurements have been performed, a multi-slice multi-echo sequence was used, with TR = 3 s, TE values between 10 and 600 ms in steps of 10 ms, and MTX= 128×128. Data were fitted to exponential curves to obtain the T_2 relaxation times, respectively. Transverse relaxivity values, r_2 , were obtained as the slope of the linear regression of the relaxation rates (R), as the inverse of the relaxation times ($R_2 = 1/T_2$) versus Fe concentration.

A similar approach was used to image T_2 contrast in nuclear magnetic resonance signal of the PLGA@Fe/SiO₂ nanodomains *in-vivo* in mice. In detail, the unloaded PLGA@Fe/SiO₂ nanocapsules were injected *via* tail vein with a total volume of 100 μ L with a concentration at 1mg/mL to reach a total mass of 100 μ g for a standard *in vivo* test condition of mice (5 mg/Kg). The magnetic resonance imaging tests were conducted in different time (0h (right after), 1h, 24h and 48h) after the injection.

4. Magnetic trapping in the microfluidic channel

Magnetic trapping experiments were performed by setting a spherical 19 mm diameter FeNdB permanent magnet (7.1 kOe at the surface) attached to a narrow microfluidic channel (3 mm in diameter). A nanodomains dispersion (total volume of 1mL) was controllably flowed by a syringe pump through the microfluidic channel at different flow rates. Experimental setup shown in Figure S2. Optical spectra of the sample before and after the trapping experiments were carried out to establish the concentration of particles in the dispersion.

5. Photothermal heating efficiency measurement

An identical experimental setup employed in Chapter of the Thesis has been applied to evaluate the photothermal heating efficiency of PLGA@Fe/SiO₂ nanodomains under 808 nm and 1064 nm laser illumination. A comprehensive calculation process has been described in article 1 and more information about this calculation can be found in Appendix (at the end of the Thesis). The incident power of 808 nm and 1064 nm lasers were set to be identical at 200 mW. The total volume of the nanodomains dispersion is 600 μ L. The extinction values of the PLGA@Fe/SiO₂ nanodomains dispersion at 808 nm and 1064 nm were measured to be 0.2192 and 0.1837 (Figure S3a), respectively. The constant time of the system was determined as 280 s, as shown in Figure S3b.

6. Cell culture

Human breast cancer cells (cell line SK-BR-3) were seeded in 4-well plates with a density of 3×10^4 cells/ml. After 48 hours incubation at constant 37 °C with 5%CO₂, 10

and 40 $\mu\text{g/ml}$ PLGA@Fe/SiO₂ were added to the cell culture. Cell viability was checked after an incubation time of 1, 2, 6 and 11 days to evaluate their cytotoxicity.

Alamar blue assay was used to check the cell viability. In particular, cells were washed with HEPES-Buffered Saline three times before adding the fresh media with 10% of Alamar blue. After 5 hours of staining, the cell samples were measured by spectrophotometry.

7. Sensing

A custom-made opto-magnetic analysis system was used to determine the opto-magnetic modulation of nanodomes in liquid. Detailed information about the setup has been elaborately described in Chapter 2.

8. Figures

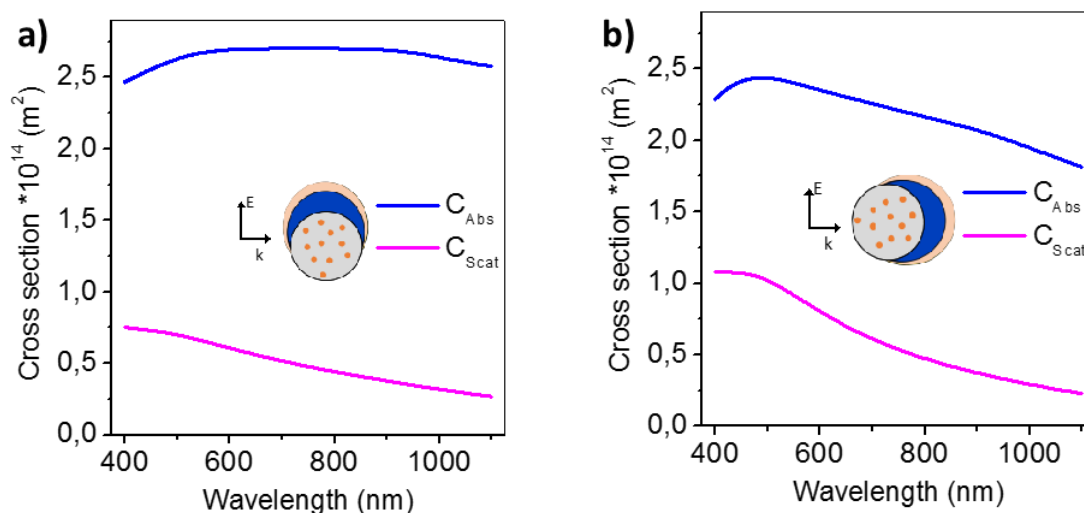


Figure S1. a) and b) Theoretical simulations through finite domain time domain (FDTD) of scattering (C_{scat}) and Absorption (C_{abs}) cross sections of the nanocapsules for different orientations of the nanocapsules with respect to the polarization of the incident light.

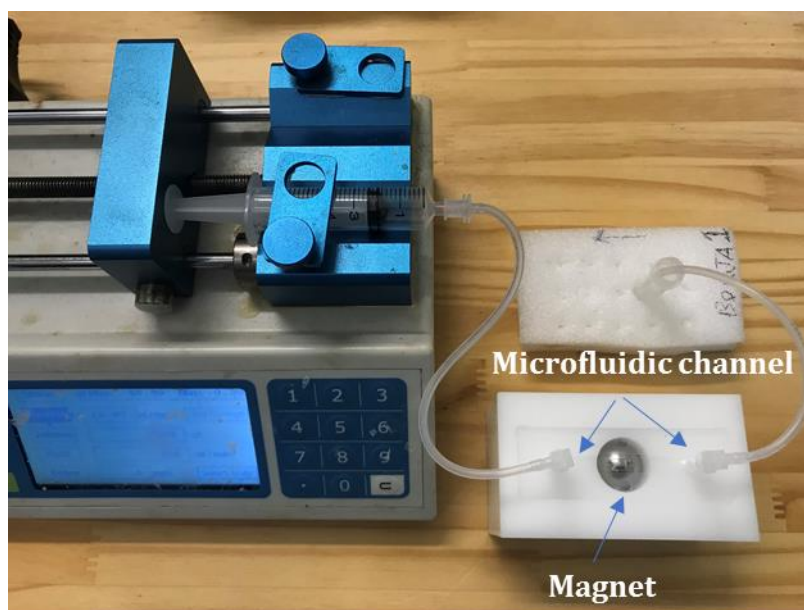


Figure S2. Experimental setup for magnetic trapping experiments with magnetic fluidic channel.

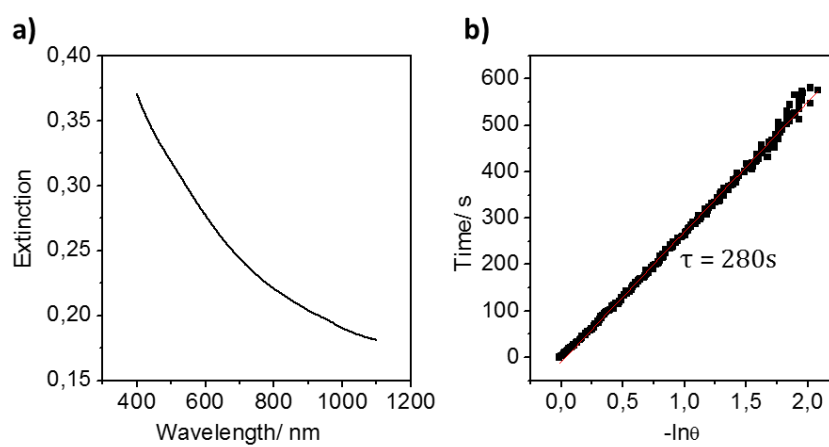


Figure S3. a) Extinction curve of the PLGA@Fe/SiO₂ nanodomains dispersion for measuring the optical heating efficiencies under 808 nm and 1064 nm laser illumination, b) The time constant for heat transfer of the system is determined to be $\tau = 280$ s.

Chapter 4: General discussion

This Thesis was motivated by the necessity to develop new tools for externally improving and controlling the therapeutic effects of nanotherapies, special for cancer treatments. Magnetically and optically actuated nanotherapies are becoming appealing alternatives for local treatments due to their non-invasiveness, high efficiency, multiple applications and the versatility of the nanomaterial candidates. However, merging these two actuation capacities in nanomaterials and fine tuning their properties for nanotherapy uses is challenging by standard chemical synthesis. **Therefore, the main goal of this Thesis has been to develop novel magneto-plasmonic nanomaterials by using non-conventional nanofabrication strategies to enable efficient combined optical and magnetic nanotherapy activation, amplification and control. In this Thesis we have demonstrated that the combination of bottom-up and top-down nanofabrication strategies** could be an ideal route to gain benefits from both approaches and to minimize their drawbacks. In particular, colloidal self-assembly and physical vapor deposition have been combined to easily merge ferromagnetic and optical nanomaterials and to fine-tune their properties by their size and composition.

As a demonstration of the powerful capabilities of this combined fabrication method, Fe/Au nanodomes were initially developed due to their capabilities of merging strong ferromagnetic and plasmonic properties for combined optical and magnetic therapeutic actuations. Due to the magnetic dipole-dipole interactions between nanodomes, one of the challenges was obtaining strong but colloidally stable ferromagnetic nanoparticles. The colloidal stability was achieved either by the distance between the magnetic layers of neighbouring particles (i.e., thick Au shells and the polymeric core) or by the in-plane magnetic vortex configuration (Fe > 20 nm) to minimize their magnetic attraction.

From the optical perspective, there were concerns related to the potential reduction of the nanoparticles absorption due to the Fe layer, which damps the plasmonic behaviour. However, as a highly relevant, and somehow unexpected result, we showed that Fe layer provides highly suppressed light scattering but intense absorption due to its highly dumped plasmonic behaviour. This behaviour enabled

keeping very high photothermal conversion efficiencies even for high Fe contents. Therefore, owing to the highly tunable core-semishell structure, the **excellent ferromagnetic and optical properties of the Fe/Au could be merged.**

The merged magneto-plasmonic properties of the Fe/Au nanodomes were exploited for bioimaging and nanotherapies externally actuated by magnetic fields and light. **The large X-ray attenuation of the Au layer, high T_2 signal in nuclear magnetic resonance of Fe layer, and the fluorescence polymer core could endow the nanodomes multimodal imaging capacities of X-ray computed tomography, magnetic resonance imaging and fluorescence imaging.**

On the other hand, the large magnetization, good colloidal stability and strong NIR absorption were promising for therapeutic applications including magnetic in magnetically enhanced photothermal therapies. We achieved **high photothermal conversion efficiency (ca. 65%) which is comparable to typical photothermal therapy nanoagents** (*e.g.* Au nanorods and nanoshells). However, the efforts for exploiting Fe/Au nanodomes for magnetic hyperthermia failed. The main reasons were the heavy mass and relatively small area of the magnetic hysteresis loop of the nanodomes.

Nevertheless, the **strong magnetophoretic forces that could be exerted nanodomes under external magnetic field gradient enabled their directed guidance and concentration at the site of action for amplifying the photothermal effects.** The *in vitro* results showed very low cytotoxicity and could confirm the magnetic amplification of the photothermal therapeutic effects by the magnetic concentration of the nanodomes at the illumination region.

These *in vitro* therapeutic assays evidenced the necessity to carefully control the local temperature increase during the optical actuation for controlling the cell death pathway. The very limited capacity to combine efficient nanoheating and local thermometry by current technologies, encouraged us to find ways to merge these two capacities in the nanodomes. The idea arose when analyzing the opto-magnetic properties of the rotating nanodomes under alternating magnetic fields. This analysis showed that we could very accurately monitor phase lag between the magnetic field and the optical signal, which is highly dependent on the local viscosity and completely

independent on the light intensity and particle concentration. These features enabled monitoring in real-time the induced viscosity decrease in water around the nanodomes by the increase of the laser power.

In order to generate efficient magnetic rotation and to maximize the resultant optical modulation of nanodomes, we exploited the nanofabrication strategy to develop nanodomes with a high out-of-plane magnetization and a maximized optical anisotropy in the near infrared, by using a Co/Au multilayer [Co-1nm/Au-6nm] \times 5/ Au-5nm on a polymer core (100 nm). These features enabled merging very efficient optical heating and simultaneous accurate detection of the optical induced temperature changes by the same incident laser beam. Importantly, the intense opto-magnetic modulation enabled the detection of the temperature changes in very complex optical media of highly concentrated cell dispersion, which gives rise to strong dynamic fluctuations in the transmitted light. It is also worth mention, that it is not necessary to use such a complex magneto-plasmonic Co/Au structure, since Fe/Au nanodomes with a large in-plane magnetization and a high optical anisotropy showed equivalent heating efficiency and detection sensitivity for self-monitoring the optical heating effects, thereby boosting the biomedical interest.

After showing the capacities of magnetic amplification and control (nanothermometry) of the photothermal therapies by the magneto-plasmonic nanodomes, our final aim was to **maximize their nanotherapeutic potential by fully exploiting and integrating their sensing and actuating capabilities, and maximizing the multi-therapeutic efficacy in fully biodegradable nanostructures.**

To achieve this goal we first substituted the inert and inactive polystyrene core, by a drug (Paclitaxel) loaded biodegradable PLGA nanoparticle. This change required and intense optimization of the PLGA composition and tuning of the colloidal self-assembly conditions to achieve correctly nanoparticles monolayers on solid substrates. In addition, the lower glass transition temperature of the PLGA imposed a slight increase of the particle size to enable an efficient dispersion of the nanocapsules after the electro-beam evaporation process. Moreover, to improve the biodegradability and to reduce the cost of the nanocapsules we substituted the Au layer by a protective SiO₂ layer, and we kept the metallic Fe with low evaporation temperature, as the

ferromagnetic-plasmonic element to provide outstanding magnetic and optical properties to the nanocapsules.

High drug loading efficiency (32%) and hydrolysis controlled sustainable drug release was achieved in the drug loaded PLGA@Fe/SiO₂, showing a total degradation of the PLGA after 1 month.

The Fe/SiO₂ layer enabled improving the magnetophoretic actuation strength compared to Fe/Au by reducing the total mass per particle but keeping similar in plane vortex-magnetization. Moreover, a 50% increase in the nuclear magnetic resonance relaxivity r_2 was achieved for highly efficient T_2 imaging. The **strong and broadband optical absorption contributed to maintain their high photothermal conversion efficiency in both NIR optical windows (ca. 63- 67%)**, which confirmed that metallic Fe is an excellent magneto-plasmonic nanomaterial.

Interestingly, the evolution of the optical and magnetic properties of the Fe layer enabled the **non-invasive visualization of the degradation process as internal sensing feature**. We could also demonstrate that the anisotropic magnetic and optical properties of PLGA@Fe/SiO₂ nanocapsules can be used to develop **opto-magnetic sensors for integrating simultaneous nanoheating/thermometry concept, and for biosensing** to detect with high sensitivity attachment of biomolecules at their surface.

The *in vitro* analysis demonstrated the **low long-term cytotoxicity** of the unloaded nanocapsules as well as the capacity of **label-free confocal imaging** to assess their internalization by tumor cells.

Finally, the preliminary *in vivo* tests have confirmed their **minimal toxicity effects in mice** and their biodistribution after intravenous injection by exploiting their very strong T_2 in MRI. We could **non-invasively observe by MRI** the accumulation of nanocapsules in the liver and the almost total recovery of the signal after 4 days. The treated mice did not show any noticeable toxicity effect during 3 weeks after injection.

Therefore, the drug loaded biodegradable PLGA@Fe/SiO₂ nanocapsules have demonstrated great capacities to merge efficient magnetic concentration, photothermal therapy, non-invasive visualization and sensing together, which encourage their **further development for future advanced nano-multi-therapies**.

Chapter 5: Conclusion

Intense efforts have been devoted in this Thesis to develop new nanotools for externally improving and controlling the therapeutic effects for cancer treatment. To end the Thesis, a brief but comprehensive list of the main conclusions is presented here.

1. The hybrid top-down (colloidal self-assembly) and bottom-up (electron beam evaporation) nanofabrication approach is a simple, scalable, cost-effective and controllable method to enable the development of highly tunable magneto-plasmonic core-semi-shell nanostructures.
2. The metallic Fe layer does not strongly reduce the optical absorption, but heavily suppresses the scattering, which endows the nanodomes great capacity for merging outstanding ferromagnetic and photothermal properties.
3. The ferromagnetic behaviour of the nanostructures can be tuned by controlling the thickness of the Fe layer and the diameter of the dielectric core from single domain to vortex, keeping high colloidal stability.
4. A very high photothermal conversion efficiency in both biological windows (63- 67%) has been obtained after completely eliminating the Au layer to minimize the light scattering and to achieve intense broadband absorbance. This value is comparable with the best plasmonic nanoheaters.
5. Co/Au multilayers, e.g. [Co-1nm/Au-6nm] \times 5/Au-5nm, can be employed to achieve anisotropic out-of-plane magnetization and to maximize the optical anisotropy in the nanodomes for opto-magnetic sensing applications.
6. The combination of optical and magnetic anisotropies with the high optical heating efficiency of the nanodomes has enabled the development of the novel simultaneous nano-heating/thermometry concept with a single NIR laser. The lowest detection limit (0.05 °C) is obtained for the Co/Au multilayers, but biomedically relevant resolution (0.15 °C) can be achieved even for the nanodomes with a single Fe layer.
7. The nanodomes exhibit multiparametric bioimaging capabilities. The Au layer provides strong X-ray absorption, and the Fe layer high T_2 contrast in magnetic resonance imaging. The highest NMR r_2 relaxivity (368 s⁻¹ mM⁻¹) has been achieved

for the Fe/SiO₂ nanodomains, whose value is much higher than that of commercial iron oxide contrast agents. The Fe can also generate intense absorption contrast for label-free confocal imaging, and the polymer core can incorporate fluorophores for fluorescent imaging and flow cytometry.

8. The nanodomains have shown very low cytotoxicity *in vitro* even in the cases of local magnetic enrichment and long-term cell cultures.
9. The *in vivo* biodistribution analysis by magnetic resonance imaging shows preferential accumulation in the liver and almost total recovery of the signal 4 days after the intravenous injection.
10. The drug loaded PLGA@Fe/SiO₂ nanocapsules show very promising features for controlled multi-therapies by merging: high biodegradability, efficient magnetic concentration, high photothermal conversion efficiency (63-67%), strong label-free confocal imaging contrast, very high T_2 contrast for magnetic resonance imaging, simultaneous nano-heating/thermometry, highly sensitive biosensing, and low *in vitro* and *in vivo* toxicities.

Chapter 6: Future Perspectives

Although very promising features have been demonstrated on the novel highly tunable nanodomains, many research efforts must be made to translate this nanotechnology to the clinic:

1. **Nanofabrication scaling-up.** The nanodomains yield of current fabrication method is less than 400 μg per wafer (4 inch), which is currently limited by our e-beam evaporation system. This quantity is enough for *in vivo* assays in mice. The quantity can be scaled up by achieving higher polymer particle surface density, by the use of industrial evaporation systems that allow multiple and bigger size samples to be loaded and evaporated sequentially and automatically. However, this is not enough for widespread biomedical application in humans. The large-scale production could be achieved by combining spray drying of the polymer nanoparticles and *in situ* sputtering in the same column, together with roll-to-roll technology to recover the evaporated particles in plastic rolls, thereby enabling easy preservation and direct dispersion in water based solutions.
2. **Biodegradability control.** The NMR and TEM analysis have shown that the Fe/SiO₂ shell is slowly degraded. The longer-term degradability of PLGA@Fe/SiO₂ should be tracked for times longer than 1 month. The degradation rate could be increase by reducing the thickness of the SiO₂ layer and/or increasing its porosity.
3. **Drug release control.** The capacity of the ferromagnetic-plasmonic nanocapsules to control the drug release rate by photothermal heating or magnetic rotating should be evaluated for achieving enhanced and externally controlled drug release.
4. **Surface functionalization for *in vivo* application.** The functionalization of the PLGA@Fe/SiO₂ nanodomains with antifouling agents (e.g. PEG) and specific ligands (e.g. antibodies) should be optimized, to improve the circulation time and the cell targeting abilities.

5. **The capacity of multiple nanotherapeutic application** by the loaded PLGA@Fe/SiO₂ nanocapsules, merging chemotherapy, magnetically amplified and controlled photothermal therapy and magneto-mechanical therapy, should be demonstrated *in vitro* and *in vivo*.

6. **The biosensing applications** based on the opto-magnetic modulation could be exploited for intracellular interaction sensing and for distinguishing the cell death pathways after therapeutic actuation.

7. **Novel functionalities** could be incorporated by using other cores, such as porous silica or metal organic frameworks (MOFs), with large pores for drug delivery with large loading efficiency. Photodynamic agents could be included either at the surface, inside the nanoporous cores or embedded as a part of the structure to permit magnetically controlled photodynamic therapies.

8. Novel magneto-electric, photo-electric and electro-chemically active nanodomains could be achieved by changing the composition of the semishell.

Chapter 7: Appendix

Photothermal conversion efficiency calculation

A general introduction of the calculation process of photothermal conversion efficiency of nanoparticles in liquid is introduced here by following Roper's report. Take the nanoparticles dispersion as a system, light irradiation and system dissipation could work as power input and output respectively and nanoparticles act as energy translator. The energy balance of this system could be expressed by Eq 1:

$$\sum_i m_i C_{p,i} \frac{dT}{dt} = Q_{laser} - Q_{dis} \quad (1)$$

, where m and C_p are the mass and heat capacity of nanoparticles solution respectively, T is the solution temperature, t is time, Q_{laser} is the energy inputted by light irradiation and Q_{dis} is heat dissipating energy from solution system to surrounding air. The laser induced heat input item Q_{laser} consists of two heating sources Q_{water} and Q_{NP} . The item Q_{water} represents the water heat induced by light irradiating, which is a constant value and easy to be obtained through heating pure water without nanoparticles under the equivalent experimental conditions. And Q_{NP} represents the heat translated by nanoparticles from laser irradiation at a certain wavelength, which could be determined according to Beer-Lambert law:

$$Q_{NP} = I(1 - 10^{-E_\lambda})\eta \quad (2)$$

, where I is the incident laser power, η is the light-to-heat photothermal conversion efficiency, and E_λ is the light extinction of nanoparticles at wavelength of λ . The item Q_{dis} represents the output power by the heat dissipation from the nanoparticles dispersion, which is nearly proportional to the linear thermal driving force:

$$Q_{dis} = hS(T - T_{amb}) \quad (3)$$

, where h is the heat transfer coefficient between the nanoparticles dispersion and the ambient surrounding, S is the surface area of the nanoparticles dispersion container, and T is the real-time temperature of the nanoparticles dispersion, T_{amb} is the ambient temperature of the surrounding. Once the laser power is defined, the heat input ($Q_{water} + Q_{NP}$) will be finite. The heat output (Q_{dis}) is related to the

changing temperature according to the Eq. 3. Then it is necessary to analyze the temperature evaluation process of the nanoparticles dispersion.

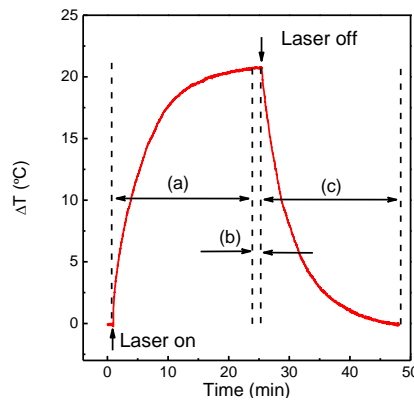


Figure 1. Typical optical heating curve comprised of heating up (a), thermal stabilization (b) and cooling down(c) processes.

Figure 1 is a typical temperature evaluation curve with CW laser heating including heating up (a), thermal stabilization (b) and cooling down(c) processes.

Considering the case of (b) when the temperature of the nanoparticles dispersion reaches the maximum value, there is a thermal balance of laser laser input and heat loss:

$$Q_{laser} - Q_{dis} = Q_{NP} + Q_{water} - Q_{dis} = 0$$

$$I(1 - 10^{-E\lambda})\eta + Q_{water} = hS(T_{max} - T_{amb})$$

And photothermal conversion efficiency (η) with laser wavelength at λ can be derived as follows:

$$\eta = \frac{hS(T_{max}-T_{amb})-Q_{water}}{I(1-10^{-E\lambda})} \quad (4)$$

In order to get the value of η , hS for heat dissipating should be carried out.

Therefore, the cooling stage (c) will be further considered and analyzed. During the cooling process, there is no light irradiating while the temperature of the nanoparticles dispersion is decreasing down all the way until reaching T_{amb} :

$$\sum_i m_i C_{p,i} \frac{dT}{dt} = Q_{dis} = hS(T - T_{amb}) \quad (5)$$

Here for convenience reason, θ , a dimensionless parameter representing the relative driving force of cooling process could be defined:

$$\theta = \frac{T - T_{amb}}{T_{max} - T_{amb}} \quad (6)$$

To get rid of the integral heat energy during the process, τ_s as a system time constant during the cooling process will be introduced as:

$$\tau_s = \frac{\sum_i m_i c_{p,i}}{hS} \quad (7)$$

Therefore, summarized from Eq6 and Eq7, it could be concluded:

$$\frac{d\theta}{dt} = -\frac{1}{\tau_s} \theta \quad (8)$$

By setting the boundary condition when the cooling process starts: $t=0, \theta=1$, Eq8 could be solved as:

$$\theta = e^{-\left(\frac{t}{\tau_s}\right)}$$

$$\ln\theta = -\frac{1}{\tau_s} t \quad (9)$$

From Eq9, it will be easy to deduce that there is a linear relationship between $\ln\theta$ and the time starting from cooling process. The slope of the fitting curve is $\left(-\frac{1}{\tau_s}\right)$ value, from which the value of τ_s and hS could be obtained. And then substituted in Eq4, η can be finally acquired.